İTÜ

İSTANBUL TEKNİK ÜNİVERSİTESİ 1773

MTM

INTERNATIONAL MATERIALS TECHNOLOGIES AND METALLURGY CONFERENCE

2-3 OCTOBER 2025

Innovating Tomorrow's Materials Today

4th INTERNATIONAL MATERIALS TECHNOLOGIES AND METALLURGY CONFERENCE

2-3 October 2025

ITU SULEYMAN DEMIREL CONFERENCE CENTER

ISTANBUL - TÜRKİYE

www.imtmc.tr

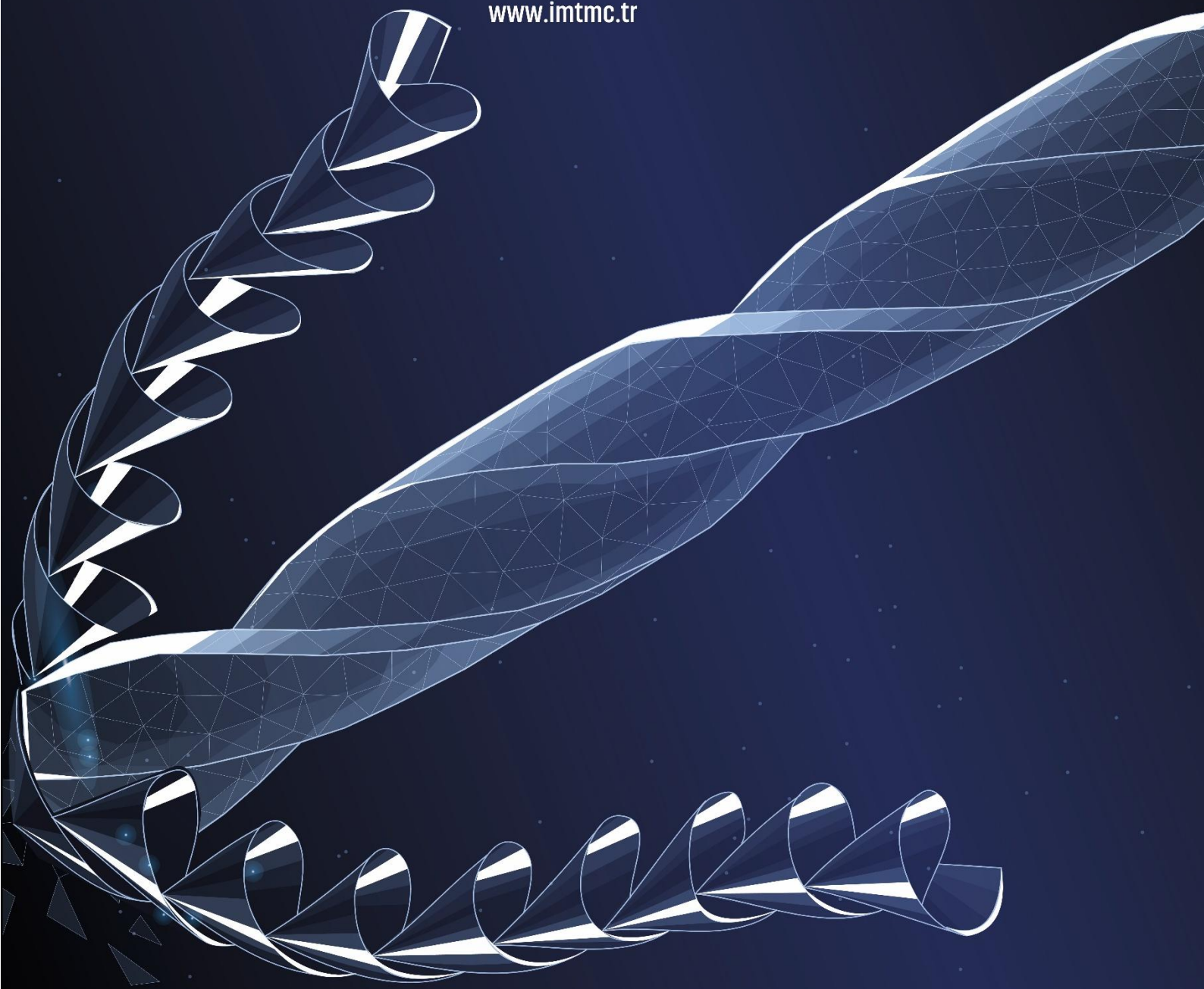

COMMITTEES

CONFERENCE CHAIRS

Prof. Dr. Gultekin Goller

Istanbul Technical University

Prof. Dr. Iulian Vasile Antoniac

University Politehnica of Bucharest

Assoc. Prof. Dr. Mustafa Guven Gok

Gaziantep University

Dr. Baris Yavas

University of Connecticut

EXECUTIVE COMMITTEE

Prof. Dr. Taner Albayrak

Piri Reis University

Prof. Dr. Sedat Alkoy

Gebze Technical University

Met. Eng. Erman Car

METEM - The Union of Metallurgical

and Materials Engineers Training Center

Assoc. Prof. Dr. Nermin Demirkol

Kocaeli University

Prof. Dr. Cihangir Duran

Yıldırım Beyazit University

Met. Eng. Serdar Erol

AVEKS International Trading Company

EXECUTIVE COMMITTEE

Prof. Dr. Hasan Gocmez

Dumlupinar University

Prof. Dr. Hakan Gur

Middle East Technical University

Prof. Dr. Sebahattin Gurmen

Istanbul Technical University

Prof. Dr. Cengiz Kaya

Yildiz Technical University

Prof. Dr. Figen Kaya

Yildiz Technical University

Prof. Dr. Ozgul Keles

Istanbul Technical University

EXECUTIVE COMMITTEE

Prof. Dr. Suleyman Can Kurnaz

Sakarya University

Prof. Dr. Burc Mısırlıoglu

Sabancı University

Assoc. Prof. Dr. Ozden Ormanci

Mimar Sinan Fine Art University

Prof. Dr. Esra Ozkan Zayim

Istanbul Technical University

Prof. Dr. Filiz Sahin

Istanbul Technical University

Met. Eng. Huseyin Savas

METEM - The Union of Metallurgical and Materials Engineers Training Center

EXECUTIVE COMMITTEE

Prof. Dr. Eda Tahir Turanlı

Acıbadem University

Doç Dr. Ebru Turkoz Acar

Yeditepe University

Prof. Dr. Onuralp Yucel

Istanbul Technical University

INTERNATIONAL SCIENTIFIC COMMITTEE

Prof. Dr. Iulian Vasile Antoniac
Polytechnic University of Bucharest

Dr. Csaba Balázsi
Centre for Energy Research of Hungarian Academy of Sciences

Prof. Dr. Simona Cavalu
University of Oredea

Assoc. Prof. Dr. Burcak Ebin
Chalmers University of Technology

Prof. Dr. -Ing. Bernd Friedrich
RWTH Aachen University

Prof. Dr. Gilson Khang
Chonbuk National University

Prof. Dr. Corrado Piconi
National Research Council of Italy

Prof. Dr. Julietta V. Rau
ISM-CNR Istituto di Struttura della Materia

Prof. Dr. Julia Mirza Rosca
University of Las Palmas de Gran Canaria

Associate Professor Dr. Srecko Stopic
IME-RWTH Aachen

Prof. Dr. Petrica Vizureanu
Technical University Iasi

Prof. Dr. -Ing Bengi Yagmurlu
TU-Clausthal

NATIONAL SCIENTIFIC COMMITTEE

Assoc. Prof. Dr. Duygu Agaogullari
Istanbul Technical University

Dr. Burcu Apak
Sisecam

Asst. Prof. Dr. Fahir Arisoy
Istanbul Technical University

Prof. Dr. Murat Baydogan
Istanbul Technical University

Assoc. Prof. Dr. Mehmet Buğdaycı
Yalova University

Prof. Dr. Huseyin Cimenoglu
Istanbul Technical University

Prof. Dr.Sibel Çekim Dağlılar
Yıldız Technical University

Dr. Erçin Çağan Duran
Istanbul Technical University

Prof. Dr. Miray Çelikbilek Ersundu
Yıldız Technical University

Prof. Dr. Alpagut Kara
Eskisehir Technical University

Prof. Dr. Ferhat Kara
Eskisehir Technical University

Dr. Muhammet Karabaş
Kırklareli University

Prof. Dr. İpek Akın Karadayı
Istanbul Technical University

Assoc. Prof. Dr. Billur Deniz Karahan
Istanbul Technical University

Prof. Dr. Ali Arslan Kaya
Mugla Sitki Kocman University

Prof. Dr. Kursat Kazmanli
Istanbul Technical University

NATIONAL SCIENTIFIC COMMITTEE

Dr. Fatıh Kırbıyık
Adıyaman University

Prof. Dr. Hasan Mandal
Istanbul Technical University

Asst. Prof. Dr. Faiz Muhaffel
Istanbul Technical University

Dr. Kübra Onbaşlı
Istanbul Technical University

Asst. Prof. Cem Ornek
Istanbul Technical University

Prof. Dr. Burak Ozkal
Yurtbay Seramik

Asst. Prof. Dr. Nuri Solak
Istanbul Technical University

Prof. Dr. Servet Timur
Istanbul Technical University

Assoc. Prof. Dr. Ahmet Turan
Yeditepe University

Assoc. Prof. Dr. Aytekin Uzunoğlu
Istanbul Technical University

Prof. Dr. Suat Yilmaz
Istanbul Cerrahpasa University

Prof. Dr. Bihter Zeytuncu
Istanbul Technical University

Prof.Dr. Hüseyin Kızıl
Istanbul Technical University

Prof. Dr. Ebru Mensur
Gebze Technical University

Dr. Burak Cagri Ocak
Surface Technologies, Sisecam Turkey

Prof. Dr. Gokhan Orhan
Istanbul Cerrahpasa University

Prof. Dr. M. Lutfi Ovecoglu
MEF University

Assoc. Prof. Dr. Guldem Kartal Sireli
Istanbul Technical University

Assoc. Prof. Dr. Mehmet Seref Sonmez
Istanbul Technical University

Prof. Dr. Servet Turan
Eskisehir Technical University

Assoc. Prof. Dr. Necip Unlu
Istanbul Technical University

Asst. Prof. Dr. Ayten Kubra Yagiz
Nigde Omer Halisdemir University

Met. Eng. Hikmet Yumurtacı
Termo Cam San ve Tic Ltd Şti.

Advanced Ceramics and Composites

High-Entropy-Alloy Doping's Effect on B4C Ceramic's Mechanical and Electrochemical Properties

Alberto Daniel Rico-Cano[1], Julia Claudia Mirza-Rosca[1], Burak Cagri Ocak[2], Gultekin Goller[2],

1. Universidad de Las Palmas de Gran Canaria

2. Istanbul Technical University

The objective of this study is to assess and contrast the mechanical and electrochemical characteristics of four novel materials made of monolithic B4C doped with different volumes of CoCrFeNiMo High-Entropy Alloy (HEA) and their comparison with monolithic B4C fabricated under the same conditions

The Spark Plasma Sintering (SPS) method was used to create all five samples under study. Using a Vickers microhardness test and Scanning Electron Microscopy (SEM), the materials' hardness and microstructure were examined. Tests for corrosion potential, corrosion rate and Electrochemical Impedance Spectroscopy (EIS) were performed to ascertain the samples' electrochemical behavior under an artificial corrosive marine environment

As HEA content increase, a denser microstructure and smaller grain size were attained, the denser microstructure was found on the 3% HEA content sample. All electrochemical test revealed that higher HEA content increase samples corrosion resistance, in a two-step chemical interaction, influenced by the presence of the Warburg element. According to the Vickers measurements, every sample showed a normal distribution, with the highest hardness found in the 3% HEA content sample.

HEA adition implies a denser microstructure, increasing the composites microhardness. All test revealed that higher HEA content translates into improved corrosion resistance and mechanical characteristics.

Keywords: B4C, HEA, EIS, Corrosion, SEM

Synthesis And Consolidation of BN Nanoplate Reinforced B4C Composites

Yiğit TAZEGÜL[1], Suna AVCIOĞLU[1], Figen KAYA[1], Cengiz KAYA[1], Ali ÇELİK[2], Alpagut KARA[3],

1. YILDIZ TECNICAL UNIVERSITY

2. ESKISEHIR TECHNICAL UNIVERSITY

3. SABANCI UNIVERSITY

Although boron carbide (B_4C) exhibits outstanding properties such as high hardness, low density, and excellent ballistic resistance, its application is limited by its low fracture toughness and poor resistance to crack propagation. The primary objective of this study is to enhance the mechanical and functional properties of boron carbide (B_4C)-based composite materials.

To achieve this, nano-hybrid composite powders comprising B_4C and boron nitride (BN) nanoplates were synthesized at low temperatures via the sol-gel method. These powders were subsequently consolidated using Spark Plasma Sintering (SPS). The resulting hybrid composites are expected to exhibit improved mechanical performance, particularly in terms of fracture toughness.

The synthesized composites were characterized using XRD, SEM, and mechanical testing methods, including Vickers hardness and fracture toughness measurements. XRD analysis revealed a phase evolution with increasing BN content, transitioning from a single-phase B_4C structure to a dual-phase composition containing approximately 15 wt.% BN. SEM investigations showed that BN nanoplates were primarily located along the grain boundaries of the B_4C matrix, contributing to microstructural refinement and potential toughening mechanisms.

With increasing BN incorporation, a slight decrease of approximately 3% in Vickers hardness was observed, while fracture toughness exhibited a significant improvement of nearly 48%, indicating the effective role of BN nanoplates in hindering crack propagation and promoting energy dissipation.

Keywords: B_4C-BN composite, fracture toughness

IMPACT OF LASER POWER ON SURFACE TOPOGRAPHY AND MATERIAL RESPONSE DURING THE LASER TEXTURING OF TUNGSTEN CARBIDE

Buse Ortac Bastekeli, Haci Abdullah Tasdemir, Emin Orhun Bastekeli

Istanbul Technical University, Faculty of Mechanical Eng., Mechanical Eng. Dep., 34437, İstanbul, Turkiye

Keywords: Tungsten Carbide, Laser Surface Texturing, Laser Power

Abstract

Tungsten carbide (WC) is widely used in high-performance industrial applications due to its exceptional hardness, wear resistance, and thermal stability. Enhancing its surface functionality—such as friction reduction, improved adhesion, and wettability control—has become increasingly important, particularly through micro and nanoscale surface texturing. Among the available surface modification techniques, laser surface texturing (LST) offers notable advantages in terms of precision and applicability to hard materials like tungsten carbide. This study investigates the effect of laser power on the surface texturing of tungsten carbide, focusing on material removal behavior, surface morphology, and process optimization. Ten different laser power levels were selected and applied to determine the power values in which dimples could be formed on the material surface without causing thermal damage. For the first time in the literature, the relationship between laser power and texture formation on tungsten carbide using a 1064 nm nanosecond pulsed fiber laser was systematically examined. The results aim to provide a valuable data resource for researchers working on laser-based surface modification of hard materials.

1. Introduction

Cobalt-cemented tungsten carbide (WC-Co) is a composite material widely recognized for its exceptional hardness and outstanding wear resistance [1, 2]. This material is composed of rigid tungsten carbide (WC) particles embedded in a tough cobalt (Co) matrix, effectively merging the beneficial characteristics of both ceramics and metals [3, 4]. In this composite, cobalt serves as a metallic binder, significantly enhancing the ductility and fracture toughness of the otherwise brittle polycrystalline WC phase [4, 5]. Due to its adaptability and superior performance characteristics, WC-Co is extensively utilized in high-demand applications such as cutting tools, aerospace components, and wear-resistant engineering parts [6, 7]. Although WC-Co exhibits superior mechanical properties, its inherent high hardness imposes substantial challenges during conventional machining processes, including excessive tool wear and significantly reduced tool life [8]. As a result, non-conventional machining methods—such as laser machining and electrical discharge machining (EDM)—have gained widespread adoption for processing WC-Co components, owing to their effectiveness in handling hard and difficult-to-machine materials [9, 10].

Laser-based systems have gained considerable importance in recent years, primarily due to their high versatility. These systems are particularly well-suited for machining hard-to-process materials such as hardened steels, ceramics, and other advanced engineering materials that present challenges for conventional machining techniques [11]. Laser beams can be employed in a wide range of material removal operations, including turning, milling, high-speed cutting, and other high-precision manufacturing processes [4]. In addition, laser technologies are applicable to various surface modification methods such as texturing, melting, and hardening, thereby enabling both functional and structural enhancement of component surfaces [12].

In recent years, research on surface texturing has gained significant momentum [13]. The primary objectives of creating surface textures are to reduce adhesion and the contact area between sliding surfaces, decrease the coefficient of friction, and trap wear debris generated during operation [14]. Due to its ability to improve tribological properties, surface texturing has found widespread application in systems involving relative motion between components. Examples of such applications include piston–cylinder assemblies, cutting tools, bearings, hydraulic motors, prosthetic devices, and dental implants. Various techniques are available for generating surface textures, including laser beam processing, electrical discharge machining (EDM), chemical etching, sandblasting, micro-grinding, and micro-casting [15]. Among these methods, laser-based surface texturing is particularly preferred due to its high precision, rapid processing capability, and suitability for creating complex surface geometries [16]. Laser surface texturing can be applied to a variety of cutting tools. Studies in the literature have demonstrated its use on drill bits [17, 18], turning inserts [19], and milling cutters [20]. The textures created on material surfaces can exhibit a wide range of shapes and geometries. These include dimples [21, 22], parallel or perpendicular grooves [23, 24], engraved patterns composed of geometric shapes or letters [25, 26], as

well as biomimetic structures inspired by natural forms [27, 28].

This research explores how varying laser power influences the surface texturing of tungsten carbide, with particular emphasis on material removal mechanisms, surface characteristics, and process efficiency. Ten distinct laser power values were calculated and applied to identify the range within which dimples can be generated on the material surface without inducing thermal damage. For the first time in the existing literature, a systematic investigation was conducted into the correlation between laser power and texture formation on tungsten carbide using a 1064 nm nanosecond pulsed fiber laser. The aim of this study is to investigate the behavior of dimples formed on tungsten carbide using different laser power levels.

2. Experimental Procedure

In the current study, cylindrical tungsten carbide specimens with a cobalt binder, having a diameter of 12 mm and a height of 8 mm, were used. SEM images of the material at 2 mm and 1 µm scales are shown in Figure 1.

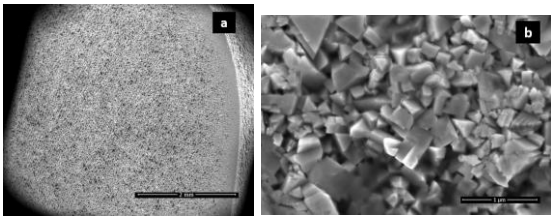

Figure 1. SEM images of the WC-Co specimen at 2 mm (a) and 1 µm (b) scales.

A nanosecond Q-switched solid-state laser system was utilized, specifically a Neodymium-doped Yttrium Aluminum Garnet (Nd:YAG) laser (Wuhan Raycus Fiber Laser Technologies Co., Ltd.), operating at a wavelength of 1064 nm with an average output power of 50 W. The laser beam was focused onto the specimen surface using an f-theta lens with a focal length of 160 mm. The system operates in the fundamental transverse electromagnetic mode (TEM_{00}), and the beam quality is characterized by an M^2 value of 1.6, indicating a near-Gaussian beam profile. During the experiments, the laser spot diameter was maintained at approximately 50 µm. All processing was carried out in ambient atmospheric conditions, without the use of a shielding or inert gas environment. A schematic representation of the Q-switched Nd:YAG laser setup is shown in Figure 2, while the technical specifications of the laser source are presented in Table 1.

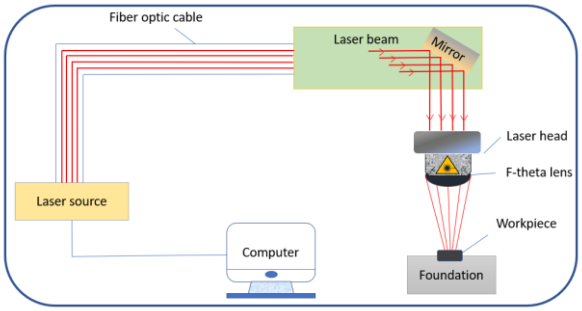

Figure 2. Schematic representation of the Q-switched Nd:YAG laser setup.

Table 1. Technical specifications of the Nd:YAG fiber laser system used in laser machining processes.

Laser type	Nanosecond laser
Mode of operation	Q-switched (pulsed)
Wavelength (nm)	1060~1085
Mode of laser beam	TEM_{00} - Fundamental mode
Pulse duration (ns)	120~150 @ kHz
Average output power (W)	50

To investigate the effect of laser power during the experiments, the laser scanning speed and frequency were kept constant at 10 mm/s and 20 kHz, respectively, while the laser power was varied for each set of 10 dimples. Subsequently, the dimples were numbered from S1 to S10. The diameter of each produced dimple is 200 µm. The specimen numbers and the laser power values applied during processing are listed in Table 2. The dimples produced by laser processing were observed using an optical microscope and SEM, and corresponding analyses and interpretations were carried out.

Table 2. Specimen numbers and the corresponding laser powers.

Specimen ID	Laser Power- P (W)	Specimen ID	Laser Power- P (W)
S1	5	S6	30
S2	10	S7	35
S3	15	S8	40
S4	20	S9	45
S5	25	S10	50

The descriptions of several critical primary laser parameters relevant to laser processing operations are provided below.

Laser power: The amount of energy delivered by the laser per unit time, typically measured in watts (W).

Laser scanning speed: The rate at which the laser beam moves across the material surface, usually expressed in millimeters per second (mm/s).

Laser frequency (or **pulse repetition rate**): The number of laser pulses emitted per second, typically measured in kilohertz (kHz).

Nanosecond laser ablation involves complex interactions between laser pulses and material surfaces, governed primarily by photothermal mechanisms. When a nanosecond laser pulse irradiates a material, the energy is absorbed and converted into heat, leading to rapid temperature rise, melting, and subsequent vaporization or ejection of material [30]. Due to the relatively long pulse duration (compared to femtosecond or picosecond lasers), heat diffusion into the surrounding material becomes significant, often resulting in a larger heat-affected zone (HAZ) and potential thermal damage [31]. Additionally, plasma formation and recoil pressure contribute to the removal of molten material, influencing both ablation efficiency and surface quality. The overall ablation behavior depends strongly on material properties and laser parameters such as power, wavelength, and pulse repetition rate. In addition, the material ablation process is also influenced by the transverse electromagnetic (TEM) mode of the laser. For instance, in the case of the fundamental mode (TEM₀₀), the temperature distribution exhibits a Gaussian profile, as illustrated in the Figure 3. This intensity profile leads to a highly localized energy concentration at the beam center, which significantly affects the thermal gradient and ablation characteristics.

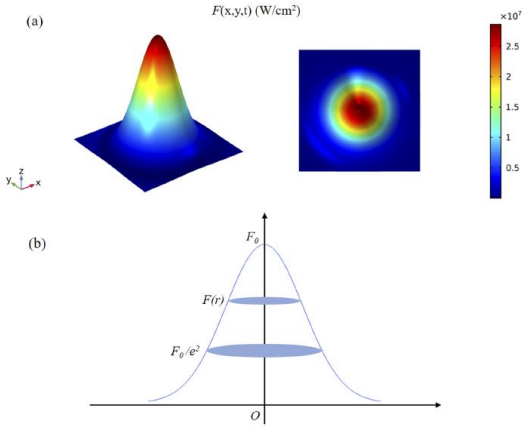

Figure 3. Gaussian profile of the laser beam: 3D representation of energy density distribution and (a), cross-sectional views of the energy density (b) [32].

3. Results and Discussion

Dimples with a diameter of 200 microns were fabricated at ten different laser power levels and subsequently examined using an optical microscope and SEM. While optical microscope images of the dimples are shown in Figure 4, the observed changes in surface morphology are presented in Figure 5.

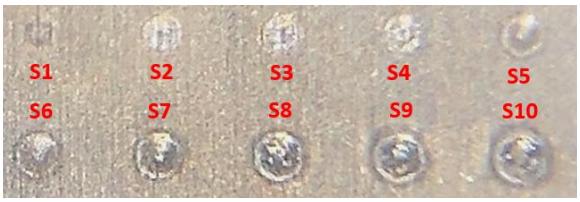

Figure 4. Optical microscope images of the dimples.

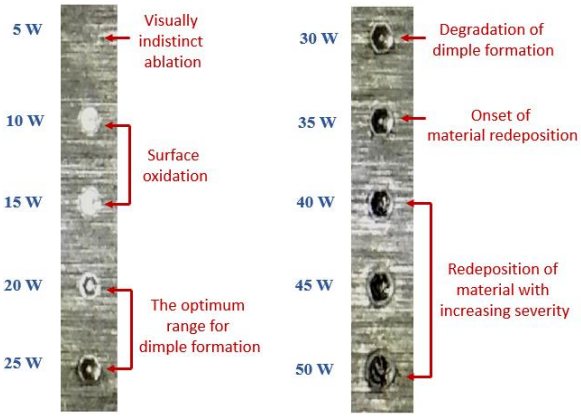

Figure 5. Morphological features and their interpretation.

At the lowest power level of 5 W, a barely visible ablation area was observed, indicating minimal material interaction. When the laser power was increased to 10 W and 15 W, faint marks appeared on the surface; however, these were attributed to surface oxidation rather than actual material removal. The white marks observed at 10 W and 15 W in Figure 5 are shown in the SEM images presented in Figure 6. As can be seen from the SEM images, a surface oxidation layer has formed, while no dimple formation has occurred.

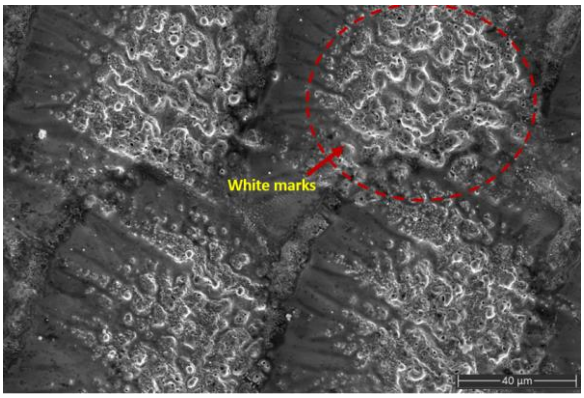

Figure 6. Surface oxidation resulting from 10–15 W laser texturing.

Within the 5–15 W range, the laser power was insufficient to produce well-formed dimples under the current processing parameters. At 20 W, a shallow dimple structure began to form, while at 25 W, an optimal dimple morphology was achieved. Therefore, it can be concluded that 20–25 W represents the most suitable laser power range for dimple formation under the given conditions. At 30 W, surface degradation and distortion of the dimple shape were observed. The power level of 35 W marked the onset of material deposition. Between 40 W and 50 W, progressively increasing material debris was noted, resulting in significant surface damage. Based on these observations, the threshold power required for initiating dimple formation was determined to be 20 W. Additionally, as the laser power increased, the size of the surrounding heat-affected zones (HAZ) and the accumulation of residual material along the dimples became more pronounced. An increase in the heat-affected zone with rising laser power is observed in Figure 7.

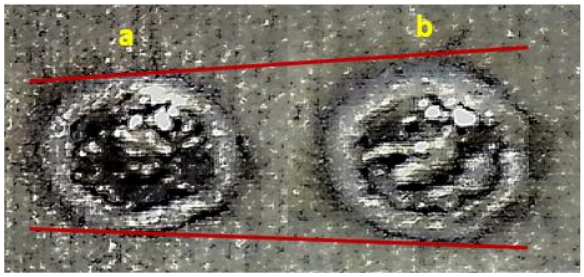

Figure 7. HAZ expansion in dimples created at 45 W (a) and 50 W (b).

4. Conclusion

Dimples were created on tungsten carbide–cobalt (WC–Co) material using a nanosecond Nd:YAG laser with a wavelength of 1064 nm at ten different laser fluence and laser power levels, and the resulting surface features were examined using optical microscopy. The key findings are summarized below.

Dimples were formed at laser power levels of 5 and 50 W; however, at 5 W, the dimples were barely distinguishable to the naked eye. At 10 and 15 W, the energy delivered to the surface was insufficient for dimple formation, and only surface oxidation was observed. The most well-defined and uniform dimples were obtained at fluence levels of 20 and 25 W. When the laser power increased to 30 W distortions in dimple geometry and termal effects began to appear. At 35 W, initial signs of material accumulation were detected on the surface. As the power exceeded 40 W, this accumulation intensified, leading to the formation of a burn-like layer. Additionally, the heat-affected zone, debris formation, and material accumulation on the surface were visualized in a manner consistent with the temperature distribution of the laser's TEM_{00} mode.

Acknowledgment

This work was financially supported by Istanbul Technical University Scientific Research Projects Coordination Unit (ITU BAP Koordinasyon Birimi, No. MGA-2023-45222).

References

[1] C. Chen, Z. Guo, S. Li, Y. Xiao, B. Chai, and J. Liu, "Microstructure and properties of WC-17Co cermets prepared using different processing routes," Ceramics International ,vol. 45 (7), pp. 9203-9210, 2019.
[2] Z. Z. Fang, M. C. Koopman, and H. Wang, Cemented tungsten carbide hardmetal-an introduction, 2014.
[3] I. Konyashin and B. Ries, Cemented carbides. Elsevier, 2022.
[4] K. E. Hazzan, M. Pacella, and T. L. See, "Understanding the surface integrity of laser surface engineered tungsten carbide," The International Journal of Advanced Manufacturing Technology, vol. 118 (3), pp. 1141-1163, 2022.
[5] G. S. Upadhyaya, "Materials science of cemented carbides—an overview," Materials & Design, vol. 22 (6), pp. 483-489, 2001.
[6] T. Schwanekamp, J. Gussone, and M. Reuber, "Impact of laser irradiation on microstructure and phase development of tungsten carbide-cobalt," Procedia CIRP, vol. 94, pp. 239-242, 2020.
[7] K. F. Wang, X. L. Tang, S. Jiao, K. C. Chou, and G. H. Zhang, "A short and facile process to synthesize WC-Co cemented carbides," International Journal of Refractory Metals and Hard Materials, vol. 92, p. 105288, 2020.
[8] S. Marimuthu, J. Dunleavey and B. Smith, "High-power ultrashort pulse laser machining of tungsten carbide," Procedia CIRP, vol. 94, pp. 829-833, 2020.

[9] G. Eberle, S.C.D. Huber, B. Frei and C. Pluess, "Ultrashort-pulsed laser processing of hard and ultrahard helical cutting tools," 10th CIRP Conference on Photonic Technologies [LANE 2018], 2018.

[10] M. Jahan, M. Rahman, and Y. Wong, "A review on the conventional and micro-electrodischarge machining of tungsten carbide," Int. J. Mach. Tools Manuf. vol. 5, pp. 837–858, 2011.

[11] J. Steyn, K. Naidoo, and K. J. Land, "Improvement of the surface finish obtained by laser ablation with a Nd: YAG laser on pre-ablated tool steel," 2007.

[12] K. E. Hazzan, M. Pacella, and T. L. See, "Understanding the surface integrity of laser surface engineered tungsten carbide," The International Journal of Advanced Manufacturing Technology, vol. 118 (3), pp. 1141-1163, 2022.

[13] J. Marczak, "Micromachining and pattering in micro/nano scale on macroscopic areas," Archives of Metallurgy and Materials, vol. 60, 2015.

[14] J. Nagpal, R. Rana, R. Lal, R. M. Singari, and H. Kumar, "A brief review on various effects of surface texturing using lasers on the tool inserts," Materials Today: Proceedings, vol. 56, pp. 3803-3812, 2022.

[15] A. Roushan, "Influence of laser parameters on the machining performance of textured cutting tools," Optics & Laser Technology, vol. 165, p. 109569, 2003.

[16] A. Arslan, H. H. Masjuki, M. A. Kalam, M. Varman, R. A. Mufti, M. H. Mosarof, L. S. Khuong, and M. M. Quazi, "Surface texture manufacturing techniques and tribological effect of surface texturing on cutting tool performance: a review," Critical Reviews in Solid State and Materials Sciences, vol. 41 (6), pp. 447-481, 2016.

[17] B. Mao, A. Siddaiah, Y. Liao, and P.L. Menezes, "Laser surface texturing and related techniques for enhancing tribological performance of engineering materials: A review," Journal of Manufacturing Processes, vol. 53, pp. 153-173, 2020.

[18] E. Öztürk and K. Kaya, "Drilling performance of micro-textured twist drill bit for TI-6AL-4V alloy: Validated FEM and statistical approaches," Journal of Manufacturing Processes, vol. 115, pp. 342-351, 2024.

[19] S. Niketh and G.L. Samuel, "Surface texturing for tribology enhancement and its application on drill tool for the sustainable machining of titanium alloy," Journal of cleaner production, vol. 167, pp. 253-270, 2017.

[20] N. Kawasegi, H. Sugimori, H. Morimoto, N. Morita, and I. Hori, "Development of cutting tools with microscale and nanoscale textures to improve frictional behavior," Precision Engineering, vol. 33 (3), pp. 248-254, 2009.

[21] T. Sugihara and T. Enomoto, "Improving anti-adhesion in aluminum alloy cutting by micro stripe texture," Precision Engineering, vol. 36 (2), pp. 229-237, 2012.

[22] G. Vignesh, D. Barik, P. Ragupathi, and S. Aravind, "Experimental analysis on turning of AISI 4340 steel using non-textured, dimple textured and MoS_2 coated dimple textured carbide cutting inserts at the rack surface," Materials Today: Proceedings, vol. 33, pp. 2616-2620, 2020.

[23] I. Etsion, "Improving tribological performance of mechanical components by laser surface texturing," Tribology letters, vol. 17, pp. 733-737, 2004.

[24] R. Baumann, Y. Bouraoui, U. Teicher, E. Selbmann, S. Ihlenfeldt, and A.F. Lasagni, "Tailored laser structuring of tungsten carbide cutting tools for improving their tribological performance in turning aluminum alloy Al6061 T6," Materials, vol. 16 (3), p. 1205, 2023.

[25] D. Bhaduri, S. Dimov, and S. L. Soo, "Laser texturing of tungsten carbide tools: the effects on tribological performance when machining Ti-6Al-4V alloy," In Euspen's 16th International Conference & Exhibition, UK, 2016.

[26] D. Maldonado-Cortés, L. Peña-Parás, N.R. Martínez, M.P. Leal, and D.I.Q. Correa, "Tribological characterization of different geometries generated with laser surface texturing for tooling applications," Wear, vol. 477, p. 203856, 2021.

[27] P. Sreedath, S. Bhat, and N. Arunachalam, "Evaluation and characterization of deterministic laser textured surfaces using machine vision," Measurement, vol. 135, pp. 537-546, 2019.

[28] A. Fatima and P.T. Mativenga, "On the comparative cutting performance of nature-inspired structured cutting tool in dry cutting of AISI/SAE 4140," Proceedings of the Institution of Mechanical Engineers, Part B: Journal of Engineering Manufacture, vol. 231 (11), pp. 1941-1948, 2017.

[29] P. Ranjan and S.S. Hiremath, "Influence of texture parameters of the bio-inspired crescent textured tool on machining performance of martensitic stainless steel," CIRP Journal of Manufacturing Science and Technology, vol. 39, pp. 70-90, 2022.

[30] C. Chu, Q. Zhang, H. Zhuo, Z. Zhang, Y. Zhu, and Y. Fu, "Investigation on the ablation behavior of cemented tungsten carbide by a nanosecond UV laser," Journal of Manufacturing Processes, vol. 71, pp. 461-471, 2021.

[31] B. Nagarajan, J. Han, S. Huang, J. Qian, J. Vleugels, and S. Castagne, "Femtosecond laser processing of cemented carbide for selective removal of cobalt," Procedia CIRP, vol.113, pp. 576-581, 2022.

[32] D. Jian, Z. Hou, C. Wang, M. Zhuo, D. Xiao, and X Wu, "Fabrication of fused silica microstructure based on the femtosecond laser," AIP Advances, vol. 11(9), 2021.

Biomaterials, Biotechnology and Drug Delivery Systems

EFFECTS OF Nanoparticles, Seawater, and BiocideS on the ANTIFOULING Composites

Ahmet Furkan Akın [1], Deniz Fıstıkçı[2], Büşra Osma [3], Alper Ekinci [4] Gülşen Akın Evingür4, Önder Pekcan [1]

[1]Kadir Has University, 34083 Cibali, Istanbul, Türkiye

[2] High School of Alkev, 34535, Büyükçekmece, Istanbul, Türkiye

[3]Yıldız Technical University, 34349 Beşiktaş, Istanbul, Türkiye

[4]Piri Reis University, 34940 Tuzla, Istanbul, Türkiye

Antifouling composites are widely employed to protect submerged ship surfaces by preventing the settlement of marine organisms, thereby improving operational efficiency and reducing environmental impacts such as invasive species transfer and excess fuel consumption. In this study, polymer-based antifouling composites were developed through the incorporation of various nanoparticles and biocidal agents. Their diffusion behaviour and elastic properties were investigated under different seawater conditions using immersion experiments. Fluorescence spectroscopy (Perkin Elmer LS 55) was employed to monitor the diffusion process, and diffusion coefficients were determined based on Fick's law. Elasticity was assessed through compression testing. The results demonstrate that both the type of incorporated agents and the characteristics of the seawater significantly influence the diffusion kinetics and mechanical properties of the composites. These findings highlight the importance of tailored material design for enhancing the durability and performance of antifouling systems in marine environments.

Keywords: Antifouling composites; nanoparticles; seawater; biocides; Diffusion coefficients; modulus

ANTIBACTERIAL CELLULOSE ACETATE/GELATIN NANOFIBERS ENRICHED WITH *HYPERICUM PERFORATUM* ESSENTIAL OIL

Aysen Akturk[1]

[1]Istanbul Technical University, Faculty of Chemical & Metallurgical Engineering, Chemical Eng. Dep., 34469, İstanbul, Turkiye

Keywords: Electrospinning, Nanofiber, Composite, Essential oil, Wound dressing

Abstract

The development of electrospun nanofibrous scaffolds represents a promising material for wound healing because they possess high porosity and adjustable fiber structure and mimic the extracellular matrix. In this study, nanocomposite scaffolds were obtained by incorporating *Hypericum perforatum* essential oil (HPO), which is known for its therapeutic potential, into the cellulose acetate (CA)/gelatin (GT) chitosan electrospun nanofibers for wound healing applications. The effects of HPO concentrations between 10–30 wt% on nanocomposite morphological properties and structural integrity and antibacterial performance were evaluated. The SEM images showed that all nanofibers maintained uniform structures with diameters between 1.44 and 2.16 µm and achieved high porosity levels above 83% which supports tissue regeneration. FTIR spectroscopy showed that HPO successfully incorporated into the polymer matrix through specific absorption bands. The antibacterial tests showed that Escherichia coli and Staphylococcus aureus growth was completely inhibited when HPO loading reached 20% and 30%. This research demonstrates that CA/GT/HPO nanofibers show promise as wound dressing materials because they maintain structural stability while providing bioactive properties.

1. Introduction

Nanofiber and nanoscaffold dressings prepared with electrospinning have received considerable attention in various fields including regenerative medicine, tissue engineering, biomedical applications, wound healing, and controlled drug delivery because of their sophisticated physicochemical properties and complex architectures [1]. Electrospun nanofibrous scaffolds possess unique characteristics such as a high surface-area-to-volume ratio, specific pore sizes, and particular fiber diameters that make them ideal for tissue engineering applications. These characteristics enable them efficient in imitating the functions of the extracellular matrix (ECM) [2]. The combination of nanofibers with other nanoparticles (NPs) and/or active biomaterials also enables the enhancement of their functional properties. As a result, different types of electrospun nanofibrous scaffolds with a distinctive architecture that resembles the extracellular matrix morphological structure and composites of mixed biomaterials have been developed for a variety of applications [1].

Since infection is the most common complication that can occur during wound healing, dressing systems containing antiseptic agents are essential to delay or inhibit the growth of microorganisms [3]. For this reason, a wide range of bioactive compounds with antimicrobial activities have been incorporated into the structure of wound dressings to prevent the penetration of bacteria into the wound and at the same time promote the healing process [4]. It was demonstrated that essential oils (EOs), typically extracted from diverse aromatic plants, possess inherent antibacterial, antifungal, and insecticidal characteristics. EOs offer advantages over other synthetic antimicrobial agents because they are widely available natural compounds with a low degree of toxicity. Moreover, they can be efficiently combined with polymeric matrices to form composite materials with exceptional antimicrobial properties [3].

Gelatin (GT) serves as a popular wound dressing material because it possesses excellent biocompatibility together with non-immunogenicity and biodegradability [5]. The application of GT is restricted because it lacks strong mechanical properties and has rapid degradation rate [6]. The electrospinability of GT also remains poor because its strong hydrogen bonding results in low-quality electrospun nanofibers. The combined use of GT with natural or synthetic biopolymers improves its spinnability and enhances the mechanical, physicochemical, and biological properties of electrospun nanofibers [7]. The interest in cellulose-derived fibers has increased significantly during recent years because they offer low cost and light weight properties together with easy processability and good mechanical and barrier characteristics and recyclability [8]. The derivative cellulose acetate (CA) demonstrates efficient processing capabilities to create membranes and films and fibers from solution or melt states [5]. The drug release

regulation properties of CA nanofibers make them suitable for electrospun drug delivery systems [6]. From this perspective, several researchers developed different composite structures for wound dressing applications by electrospinning using the combination of CA and GT [5,6,9,10].

Along with the structural requirements, a functional wound dressing should contain an active ingredient to either improve the healing process or even offers the antibacterial characteristics. Different kinds of chemical, biological, and natural components have used to provide biological functions to the dressings [9]. Hypericum perforatum essential oil (HPO, St. John's wort) is known for its antimicrobial and therapeutic activities. It was reported that its phytoconstituents enhance collagen deposition, decrease inflammation, and modulate the immune response, thereby accelerating the wound healing process [11].

The present study focuses on the development of nanocomposites by employing electrospinning method to combine cellulose/acetate polymer blend and HPO. The effects of HPO incorporation on the morphological, structural, and antimicrobial, properties of the nanocomposites were investigated. It was demonstrated that the fibrous composite scaffolds produced in this study effectively inhibited the growth of both *E. coli* and *S. aureus*. As a result, it can be said that the combination of the CA/GT polymer matrix with HPO could have potential for the biomedical applications

2. Experimental Procedure

2.1. Materials

Cellulose acetate (CA, Mn = 30,000, Sigma Aldrich), bovine gelatin (GT, 220 Bloom Alfasol), 1,1,1,3,3,3-hexafluoro-2-propanol (HFIP, purity ≥99, Sigma Aldrich) and organic St. John's wort essential oil (Florame) were used to prepare electrospun nanocomposites.

2.2. Electrospinning

CA and GT with a weight ratio of 3:4 was dissolved in HFIP to obtain a final polymer concentration of 14% w/v. HPO was added to the polymer solutions at weight ratios of 10, 20, and 30% w/v with respect to the total polymer amount. Electrospinning was performed in a single nozzle setup (Nanospinner 24 Touch, Inovenso Co.) under ambient conditions. The applied voltage, tip-to-collector distance, and flow rate were 20 kV, 130 mm, and 3 $mL.h^{-1}$, respectively. The obtained nanofiber membranes were named as CA/GT, CA/GT/HPO10, CA/GT/HPO/20, and CA/GT/HPO30, based on HPO concentration.

2.3 Morphological and chemical characterisation of the nanofibers

The fiber diameter and morphology of the nanocomposite fibers were analyzed using Scanning Electron Microscopy (SEM). A FEI Quanta 250 FEG microscope was used, operating in high vacuum mode with an acceleration voltage set at 20 kV. A thin coating of gold-palladium was achieved using the Quorum SC7620. SEM images were analyzed using ImageJ to calculate fiber diameter distribution. Surface porosity and pore size of nanocomposites were determined by using their gray scale SEM images by setting a threshold value in ImageJ. The ratio of dark pixels to total pixels was then calculated to measure the surface porosity. To find the pore size, an elliptical was fitted into the pores, and the larger sizes of 30 pores were taken into account [12, 13]. FTIR (Jasco FT/IR 4700, 4000–500 cm^{-1}) was used to identify and confirm the presence of specific functional groups within the nanofibers.

2.4 Antibacterial activiy of the nanofibers

The optical density (OD) method was used to measure the antibacterial activity of nanofibers against Gram-negative Escherichia coli ATCC 25923 and Staphylococcus aureus ATCC 25922. Ten microliters of a bacterial solution (105 CFU/mL) and 50 mg of nanofiber samples were mixed into 10 mL of fresh Luria Bertani broth and incubated at 37°C with agitation at 100 rpm. After incubation, a UV–vis spectrophotometer (BioTek Technologies, Winooski, VT, USA) was used to evaluate the suspension's optical density at 600 nm.

3. Results and Discussion

SEM micrograph were used to evaluate the morphology of the CA/GT and HPO loaded CA/GT nanofibers (Figure 1). The nanofibers displayed uniform morphology together with a smooth surface and porous structure. The average diameters of CA/GT, CA/GT/HPO10, CA/GT/HPO20 and CA/GT/HPO30 PCL/GT/FL40 nanofibers were measured as 1.69 ± 1.05, 1.94 ± 0.89, 2.16 ± 1.15, and 1.44 ± 0.42 µm respectively. The morphological characteristics of electrospun fibers play a crucial role in determining cell behavior. It is known that smaller fiber diameters, such as 700 nm, promote a more dispersed and elongated morphology in human skin fibroblasts. which can enhance cell migration. However, Gao et al. found that while smaller fibers support cell morphology, larger fibers (3000 nm) actually exhibit a higher migration speed and effective migration rate due to their reduced specific surface area and lower adhesion protein adsorption. Thus, the relationship between fiber diameter and cell migration is complex, with larger diameters showing enhanced migration capabilities [14]. Moreover, the porosity and pore size of electrospun

nanofibers play a significant role in scaffold designs and long-term success of biomaterials. The range of 60–90 % is recognized as the appropriate porosity for cell proliferation [13]. Surface porosity percentages of CA/GT, CA/GT/HPO10, CA/GT/HPO20 and CA/GT/HPO nanofibers were calculated as 83.70 %, 84.86 %, 84.17 %, and 83.06 %, respectively, showing that the nanofibers are highly porous and acceptable for tissue engineering applications. The pore sizes of CA/GT, CA/GT/HPO10, CA/GT/HPO20 and CA/GT/HPO nanofibers were found as 5.36 ± 4.51, 4.94 ± 1.40, 5.01 ± 1.54, and 5.67 ± 1.71 µm, respectively.

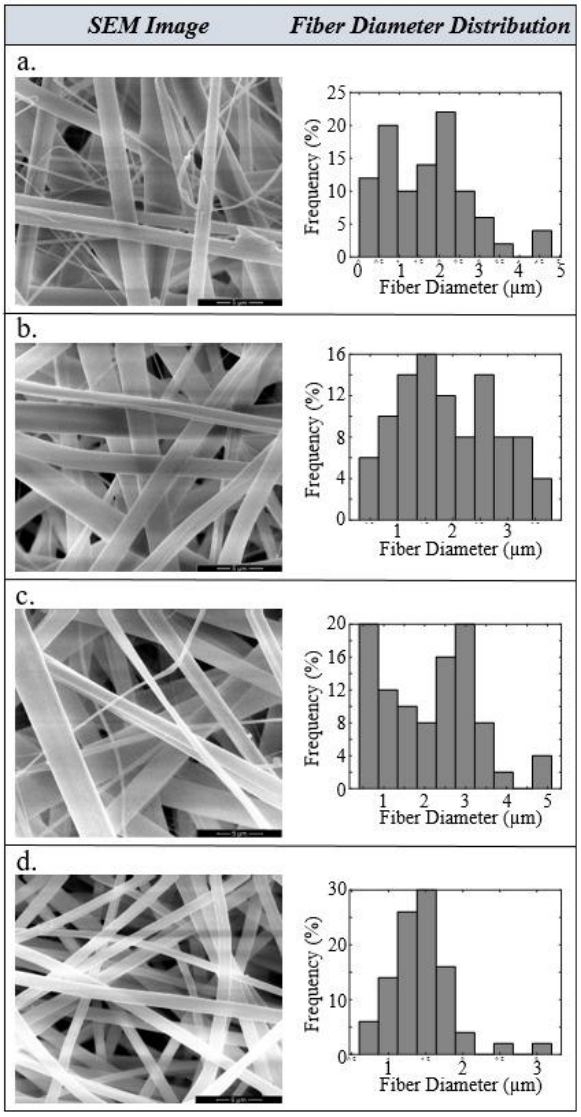

Figure 1. SEM images and fiber distributions of CA/GT (a), CA/GT/HPO10 (b), CA/GT/HPO20 (c), and CA/GT/HPO30 nanofibers

Pore diameters of 2-12 µm are ideal for the dermal layer, promoting cell migration, nutrient transport, ECM deposition, and skin structure organization [15].

The FTIR spectra of CA/GT and HPO loaded CA/GT nanocomposites were obtained and the spectrums are given in Figure 2. It can be said that the peaks at 1741, 1625, 1545, 1370, 1194, 1054 and 899 cm^{-1} belong to both of these polymers. CA indicated the characteristic bands attributed to the acetate group. The stretching bands of carbonyl (C═O stretching) at 1741 cm^{-1}, methyl bending at 1370 cm^{-1} (C–CH3 stretching), the alkoxyl stretch of the ester at 1194 cm–1 (C–O–C antisymmetric stretching ester group), and the C–O functional group in the absorption region of 1054 cm^{-1} were observed for the CA electrospun nanofibers [16]. On the other hand, the peaks at 1625 (amide I) and 1545 cm^{-1} (amide II), showing stretching vibrations of the C–O bond and the bending of the N–H bond and the stretching of the C–N bond, respectively, confirmed the presence of GT in the sample [17]. All membranes exhibited the characteristic peaks of polymers. Only with the addition of HPO, the intensity of the peaks at 2950 and 2857 cm^{-1} increased which are C-H stretching bands specific to HPO [18]. In this context, it can be concluded that HPO is integrated into the structure.

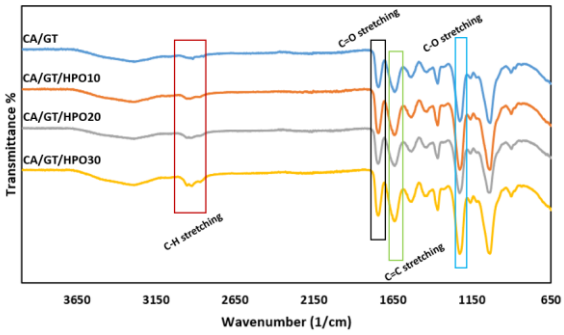

Figure 2. FTIR analysis of CA/GT and HPO loaded CA/GT nanofibers

Nanocomposites antimicrobial efficacy against two bacteria was evaluated by OD method and percent bacterial inhibitions are shown Figure 3. It was observed that the neat CA/GT membrane has an effect on both bacteria. The antibacterial effect observed in this membrane suggests that HFIP, used as a polymer solvent during the electrospinning process, was not completely removed from the membrane structure. Moreover, it can be seen that the addition of HPO has a positive effect on the antimicrobial activity of membranes. CA/GT/HPO20 and CA/GT/30 composites showed complete antimicrobial activity against both bacteria. CA/GT/HPO10 composite was more effective against *S. aureus* than *E. coli.* It was reported that HPO demonstrates superior effectiveness against gram-positive bacteria than against gram-negative bacteria. The outer membrane of gram-negative bacteria contains

lipopolysaccharides which prevent antibacterial agents from entering. Additionally, HPO components hypericin and hyperforin show better binding properties to peptidoglycan layers thus enabling better penetration and activity [18].

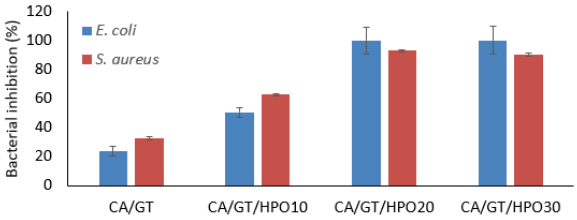

Figure 3. Antibacterial activity of HPO loaded CA/GT membranes against *E. coli* and *S. aureus*.

4. Conclusion

This research involved on the fabrication of cellulose acetate (CA)/gelatin (GT) nanofibers with Hypericum perforatum essential oil (HPO) through electrospinning for wound dressing applications. The composite membranes displayed smooth and porous structures which had suitable surface porosity and appropriate pore dimensions that supported cell attachment and proliferation. FTIR analysis confirmed HPO addition which strengthened the antibacterial properties of the nanofibers especially against S. aureus. The CA/GT/HPO20 and CA/GT/HPO30 samples showed complete bacterial inhibition because HPO displayed powerful antimicrobial activity. The combination of biocompatible polymers with natural bioactive oil presents a promising approach to develop advanced wound dressings.

References

[1] R. Abdel-Sattar, S. S. Sharaf, and A. A. Gibriel, "Preparation, characterization and biomedical applications of electrospun cellulose acetate nanofiber dressing fabricated with silver and bioglass nanoparticles for efficient wound healing in streptozotocin induced diabetic rat," J Eng Fibers Fabr, vol. 19, p. 15589250241302430, 2024..

[2] K. T. Chaka, K. Cao, T. Tesfaye, and X. Qin, "Nanomaterial-functionalized electrospun scaffolds for tissue engineering," J Biomater Sci Polym Ed, vol. 36, no. 3, pp. 371–413, 2025.

[3] I. Liakos, L. Rizzello, H. Hajiali, V. Brunetti, R. Carzino, P. P. Pompa, and E. Mele, "Fibrous wound dressings encapsulating essential oils as natural antimicrobial agents," J Mater Chem B, vol. 3, no. 8, pp. 1583–1589, 2015.

[4] C. Mouro and I. C. Gouveia, "Electrospun wound dressings with antibacterial function: a critical review of plant extract and essential oil incorporation," Crit Rev Biotechnol, vol. 44, no. 4, pp. 641–659, 2024.

[5] H. Samadian, M. Salehi, S. Farzamfar, A. Vaez, A. Ehterami, H. Sahrapeyma, and S. Ghorbani, "In vitro and in vivo evaluation of electrospun cellulose acetate/gelatin/hydroxyapatite nanocomposite mats for wound dressing applications," Artif Cells Nanomed Biotechnol, vol. 46, sup. 1, pp. 964–974, 2018.

[6] T. Huang, Y. Zeng, C. Li, Z. Zhou, Y. Liu, J. Xu, and K. Wang, "Preparation and investigation of cellulose acetate/gelatin janus nanofiber wound dressings loaded with zinc oxide or curcumin for enhanced antimicrobial activity," Membranes, vol. 14, no. 5, p. 95, 2024. or curcumin for enhanced antimicrobial activity. Membranes, 14(5), 95.

[7] T. Li, M. Sun, and S. Wu, "State-of-the-art review of electrospun gelatin-based nanofiber dressings for wound healing applications," Nanomaterials, vol. 12, no. 5, p. 784, 2022.

[8] H. D. López-Calderón, H. Avilés-Arnaut, L. J. Galán-Wong, V. Almaguer-Cantú, J. R. Laguna-Camacho, C. Calderón-Ramón, and K. Arévalo-Niño, "Electrospun polyvinylpyrrolidone-gelatin and cellulose acetate bi-layer scaffold loaded with gentamicin as possible wound dressing," Polymers, vol. 12, no. 10, p. 2311, 2020.

[9] H. Samadian, S. Zamiri, A. Ehterami, S. Farzamfar, A. Vaez, H. Khastar, and M. Salehi, "Electrospun cellulose acetate/gelatin nanofibrous wound dressing containing berberine for diabetic foot ulcer healing: In vitro and in vivo studies," Sci Rep, vol. 10, no. 1, p. 8312, 2020.

[10] K. Lee and S. Lee, "Electrospun nanofibrous membranes with essential oils for wound dressing applications," Fibers Polym, vol. 21, no. 5, pp. 999–1012, 2020.

[11] B. Farasati Far, G. Gouranmohit, M. R. Naimi-jamal, E. Neysani, H. A. El-Nashar, M. El-Shazly, and K. Khoshnevisan, "The potential role of Hypericum perforatum in wound healing: A literature review on the phytochemicals, pharmacological approaches, and mechanistic perspectives," Phytother Res, vol. 38, no. 7, pp. 3271–3295, 2024.

[12] L. Ghasemi-Mobarakeh, D. Semnani, and M. Morshed, "A novel method for porosity measurement of various surface layers of nanofibers mat using image analysis for tissue engineering applications," J Appl Polym Sci, vol. 106, no. 4, pp. 2536–2542, 2007.

[13] M. R. Nejad, M. Yousefzadeh, and A. Solouk, "Electrospun PET/PCL small diameter nanofibrous conduit for biomedical application," Mater Sci Eng C, vol. 110, p. 110692, 2020.

[14] X. Gao, T. Hou, L. Wang, Y. Liu, J. Guo, L. Zhang, and M. Wen, "Aligned electrospun fibers of different diameters for improving cell migration capacity," Colloids Surf B Biointerfaces, vol. 234, p. 113674, 2024.

[15] F. Mukasheva, L. Adilova, A. Dyussenbinov, B. Yernaimanova, M. Abilev, and D. Akilbekova, "Optimizing scaffold pore size for tissue engineering: Insights across various tissue types," Front Bioeng Biotechnol, vol. 12, p. 1444986, 2024.

[16] A. Akturk, "Enrichment of cellulose acetate nanofibrous scaffolds with retinyl palmitate and clove essential oil for wound healing applications," ACS Omega, vol. 8, no. 6, pp. 5553–5560, 2023.

[17] A. Akturk, C. Erkoc, O. E. Tureyen, D. N. Dikmetas, A. Unal-Aslan, F. Karbancioglu-Guler, and M. Erol-Taygun, "Electrospun nanofibrous hybrids of algae, salicylic acid and zinc oxide nanoparticles for an antibacterial application," Fibers Polym, vol. 25, no. 9, pp. 3331–3342, 2024.

[18] N. Öztaş, E. Kara, D. Demir, D. Yetkin, S. Ceylan, and Z. İyigündoğdu, "Biologically active sodium pentaborate pentahydrate and Hypericum perforatum oil loaded polyvinyl alcohol: chitosan membranes," Int J Biol Macromol, vol. 269, p. 132133, 2024.

MULTI-WALLED CARBON NANOTUBE AND COPPER NANOPARTICLE DOPED THERMOPLASTIC POLYURETHANE ELECTROSPUN SCAFFOLD FOR SKELETAL MUSCLE TISSUE APPLICATION

Aysen Akturk[1], Ayşe Kübra Aydınalev[1], Mustafa Sertbas[1], Dilara Nur Dikmetas[2], Gökçen Gökçeli[3], Nilgün Karatepe[3], Funda Karbancioglu-Guler[2], Melek Erol-Taygun[1]

[1]Istanbul Technical University, Department of Chemical Engineering, Istanbul, 34469, Türkiye

[2]Istanbul Technical University, Department of Food Engineering, Istanbul, 34469, Türkiye

[3]Istanbul Technical University, Energy Institute, Renewable Energy Division, Istanbul 34469, Türkiye

Keywords: Electrospinning, Tissue Engineering, Thermoplastic Polyurethane, Multi-Walled Carbon Nanotube

Abstract

In the present study, thermoplastic polyurethane (TPU) nanocomposite structures containing copper nanoparticle (CuNP) and multi-walled carbon nanotube (MWCNT) were fabricated by using electrospinning method for skeletal muscle tissue engineering. TPU was used as the polymeric structure due to high mechanical strength. The enhancement in angiogenic properties and facilitation of cell signaling in muscle cells were aimed with the incorporations of CuNP and MWCNT into nanocomposite structure, respectively. The characterization studies, including scanning electron microscope (SEM), Fourier-transform infrared (FTIR), X-Ray Diffractometer (XRD) and ion release, demonstrated fabrication of nanofiber composite structures integrated with CuNPs and MWCNTs. Antibacterial activity was increased against *S. aureus* and thermogravimetric analysis (TGA) pointed out a slight elevation in thermal stability due to MWCNT and CuNP additions. Although the 1% CuNP-incorporated TPU/MWCNT nanocomposite exhibited enhanced properties compared with the other samples, further investigations will be conducted to optimize copper and MWCNT concentrations that may establish them as promising candidates for skeletal muscle tissue engineering applications.

1. Introduction

In recent years, electrospun scaffolds have been used effectively in tissue engineering applications. Electrospun polymeric micro/nanofiber scaffolds can incorporate various therapeutic additives into both synthetic and natural polymer structures, enabling the release of these additives for a variety of applications. Due to its excellent mechanical properties and good biocompatibility, synthetic thermoplastic polyurethane (TPU) is widely used in a variety of biomedical applications including skeletal muscle tissue engineering via electrospinning. Muscle tissues are required to respond to electrical signals for proper functioning of cellular signaling in the human body and this necessitates the use of conductive biomaterial in muscle tissue engineering [1]. Through the electrospinning technique, a nanofiber membrane was successfully fabricated using a polymer matrix combined with the selected reinforcements. Carbon nanotubes are conductive materials and their incorporation into electrospinning solution enables fabrication of conductive nanofiber scaffolds [2]. Copper nanoparticles possess inherent antibacterial and antimicrobial properties, making them particularly advantageous in muscle tissue engineering applications where infection risk is a concern [3]. The combination of TPU, CuNP and MWCNTs in the electrospun nanofibers offers a promising approach for developing advanced materials with tailored properties for tissue engineering applications. The detailed characterization and testing methodologies employed provide valuable insights into the morphological, structural, antimicrobial, and release properties of the nanocomposite material, which are essential considerations for its potential use in tissue engineering applications.

2. Experimental Procedure

2.1. Fabrication of MWCNT/TPU/CuNP electrospun scaffolds

TPU-based nanocomposites were fabricated by using MWCNTs in various ratios. MWCNT was added to the dimethyl formamide (DMF)/tetrahydrofuran (THF) (60/40 v/v) solution at 0.5%, 1%, 2%, 3%, 5% and 10% w/w of the TPU in the polymer solution. TPU polymer solution was added to this solution at 8% w/v. Subsequent to determination of optimum conditions (MWCNT ratio), the addition of CuNP into polymer solution was performed. CuNP addition was performed at 1% and 5% of polymer

content to the 3% MWCNT-doped TPU polymer composition. The synthesis of MWCNT and CuNP are described in the previous studies [4-5]. These polymer solutions were taken into 5 ml syringes and membrane fabrication was carried out by electrospinning device (Nanospinner 24 Touch, Inovenso) at 23 kV voltage, 1.5 ml/h flow rate and 160 mm tip-collector distance.

2.2. Characterization studies

The obtained nanofiber composites were characterized by using various analysis. The fiber morphology was analyzed using a scanning electron microscope (SEM, Quanta FEG 250), and ImageJ software was used to measure fiber diameters. The functional groups of the nanofibers were investigated by Fourier-transform infrared (FTIR, Perkin Elmer, Spectrum 100) spectroscopy. The characteristic phases and crystallinity of nanofibers were examined using X-Ray Diffractometer (XRD, Panalytical Xpert Pro). Analyses were conducted on samples at 2θ angles between 10° and 80°. TGA analyses were performed to determine the thermal properties of polymeric nanofiber membranes containing MWCNT and CuNP. TGA analyses were performed between 30 and 600°C using a TA Instruments SDT Q600 Model instrument at a heating rate of 10°C/min under a nitrogen atmosphere. To investigate copper ion release, samples were placed in phosphate buffer saline (PBS 7.4) for 2, 4, 6, and finally 24 hours in a shaking water bath at 37°C. The amount of copper ion released into the PBS after this period was measured using Inductively Coupled Plasma-Mass Spectrometry (ICP-MS, Perkin Elmer Optima 2100 DV). The antibacterial activities of the nanofiber membranes against *Staphylococcus aureus* and *Escherichia coli* were quantitatively analyzed using the OD technique [6].

3. Results and Discussion

The membrane morphology did not change significantly with the addition of different amounts of MWCNTs to the TPU polymer (Figure 1a-d). SEM images showed that the nanofibers were homogeneously distributed, and no bead-like structures formed on the fibers. It was observed from the SEM micrographs that the nanofibers were homogeneously distributed in the sample prepared with 3% MWCNT, but as the MWCNT content increased, the fiber structure deteriorated, and bead-like structures formed on the fibers (Figure 1e-g). Additionally, MWCNTs were detected on the fiber surfaces of the sample prepared with 3% MWCNT. The mean diameters of the nanofibers were determined using ImageJ software using SEM images and results were presented on each related images (Figure 1). The nanofiber diameters initially increased slightly with the addition of 0.5% MWCNT, but as the amount of MWCNT increased, the nanofiber diameters began to decrease. The decrease in nanofiber diameter is thought to be due to the conductive properties of MWCNT increasing the charge density on the polymer jet, resulting in easier fiber formation due to the fibers being more easily stretched and elongated. However, when the MWCNT content is 5%, the fiber diameter increases due to deterioration of nanofiber morphology. When MWCNTs were added above 3%, electrospinning becomes more difficult due to the increase in viscosity of the polymer solution, and a uniform nanofiber structure cannot be achieved. Based on the high-magnification SEM images of a nanofiber containing 3% MWCNT (Figure 2), the surface of the nanofibers was coated with uniformly placed MWCNTs. Therefore, it was decided to continue the study with samples containing 3% MWCNTs. MWCNT/TPU/CuNP nanocomposite structures were obtained by adding 1% and 5% CuNPs to the 3% MWCNT-added sample. Based on previous preliminary studies, it was decided to use 1% and 5% CuNPs as two different concentrations for electrospinning nanofiber fabrication. The mean diameters for the sample containing 1% and 5% CuNP were determined as 225 and 193 nm, respectively. The increase in CuNP content decreased the fiber diameter, resulting in a more porous structure. It is thought that the reason for the decrease in fiber diameter is that CuNP with a conductive structure, such as MWCNT, enable the fibers to stretch and elongate more easily.

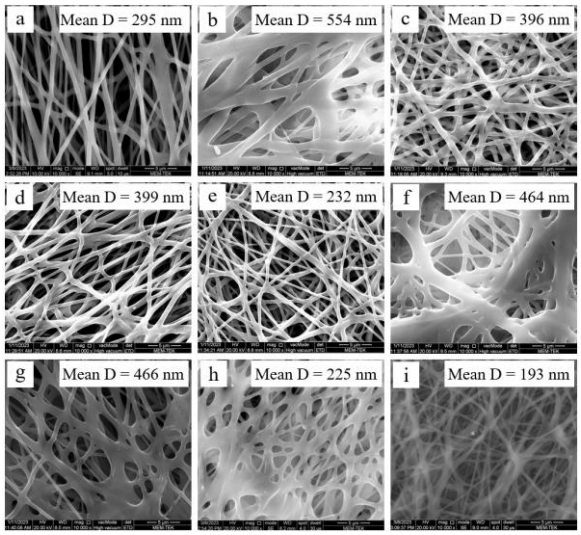

Figure 1. SEM images and mean fiber diameters of TPU Blank (a), TPU/%0.5MWCNT (b), TPU/%1MWCNT (c), TPU/%2MWCNT (d), TPU/%3MWCNT (e), TPU/%5MWCNT (f), TPU/%10MWCNT (g), TPU/%3MWCNT/%1CuNP (h), and TPU/%3MWCNT/%5CuNP (i)

Comparative FTIR analysis results of the obtained TPU Blank, TPU/MWCNT, TPU/MWCNT/1%CuNP, and TPU/MWCNT/5%CuNP nanofibers were given in Figure 3. The characteristic peaks of TPU show the NH stretching vibration at 3315 cm^{-1}, the C=O stretching at 1738 cm^{-1}, the C-N stretching and N-H bending at 1529 cm^{-1}, the

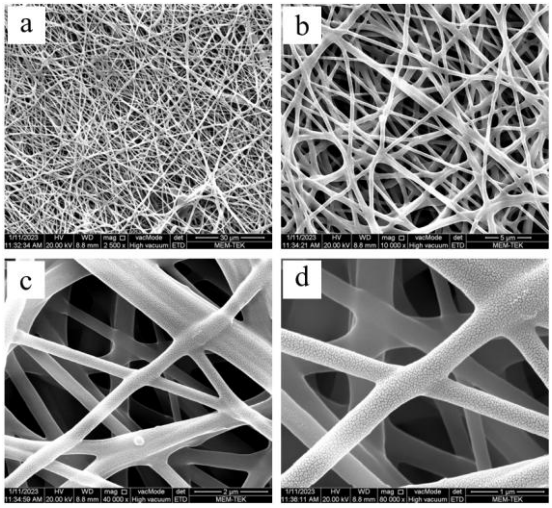

Figure 2. SEM images of nanofibers containing 3% MWCNT at high-magnification of 2500 x (a), 10 000 x (b), 40 000 x (c) and 80 000 x (d)

asymmetric C-O-C stretching at 1102 cm^{-1}. The absorption peaks observed at the wavelength of 3315 cm^{-1} indicate the -OH functional group present in MWCNT. Similarly, the absorption peaks observed at 3457 cm^{-1} correspond to the -NH functional group present in TPU. Intermolecular hydrogen bonding between -OH and -NH groups in MWCNT/TPU composite films leads to stretching vibration absorption. FTIR analysis results indicated that MWCNTs were successfully incorporated into the polymer matrix.

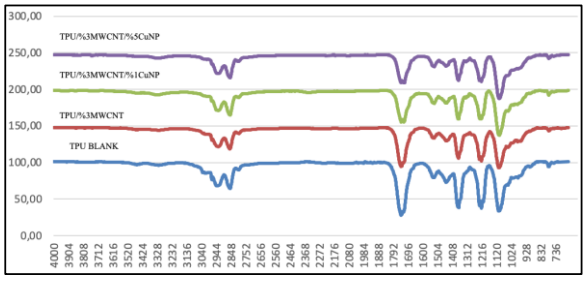

Figure 3. FTIR analysis of TPU Blank, TPU/%3MWCNT, TPU/%3MWCNT/%1CuNP, and TPU/%3MWCNT/%5CuNP

XRD analysis was performed for TPU Blank, TPU/3%MWCNT, TPU/3%MWCNT/1%CuNP, and TPU/3%MWCNT/5%CuNP (Figure 4). The carbon peak can be seen in Figure 4. It was observed that the carbon and copper peaks increased with increasing copper content. As can be seen in the comparative XRD patterns of all samples, carbon and copper peaks are visible in the graphs. This result showed that the copper nanoparticles were successfully incorporated into the structure.

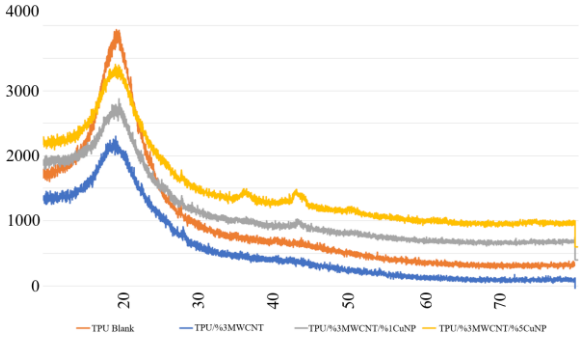

Figure 4. XRD analysis of TPU Blank, TPU/%3MWCNT, TPU/%3MWCNT/%1CuNP, and TPU/%3MWCNT/%5CuNP

E. coli and *S. aureus,* the most widely researched model microorganisms for biological materials [6], were used for the antibacterial analysis (Figure 5). When comparing samples with TPU and TPU/MWCNT nanofiber structures, the antibacterial activity increased against *S. aureus*, but no inhibition was obtained for *E. coli*. However, when comparing samples with the CuNP, the incorporation of this nanoparticle into the composite structure demonstrate antibacterial activity against both bacterial species. Studies examining the effectiveness of CuNP-added samples against *E. coli* and *S. aureus* showed that the samples were more effective against *S. aureus* due to the different composition of the cell wall structures of these bacteria.

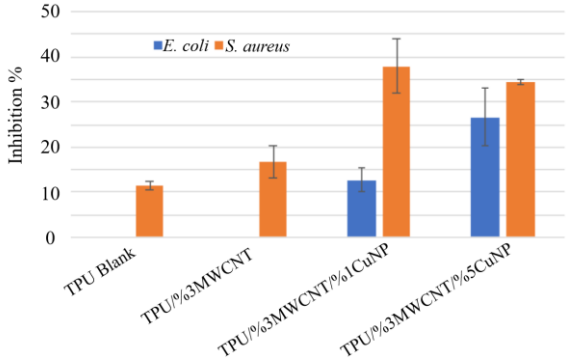

Figure 5. Antibacterial activity analysis of TPU Blank, TPU/%3MWCNT, TPU/%3MWCNT/%1CuNP, and TPU/%3MWCNT/%5CuNP

TGA analysis was performed on TPU blank, TPU/MWCNT, TPU/MWCNT/1%CuNP, and TPU/MWCNT/5%CuNP nanofiber membranes. An examination of all curves in the TGA graph (Figure 6) revealed that the nanofibers exhibited a weight loss of approximately 5% in the temperature range of 30-300°C. The weight loss in this region was due to the removal of physically adsorbed water molecules. The TGA curves of the samples indicated a weight loss behavior corresponding to the disruption of the polymer chains between 300 and 450°C.

When the DTG results were compared with the DTG curves of pure TPU, the results for both TPU/MWCNT and TPU/MWCNT/CuNP showed a decrease in the thermal degradation rate and increased stability. Thus, it was concluded that the addition of CuNP and MWCNT slightly increased the thermal stability of the TPU nanofiber structure.

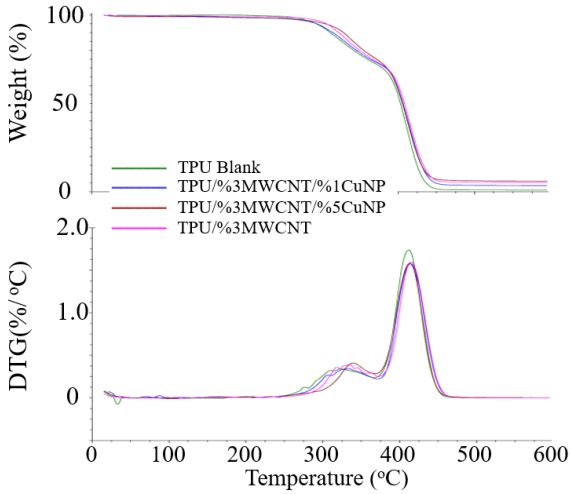

Figure 6. TGA (a) and DTG (b) analysis of TPU Blank, TPU/%3MWCNT, TPU/%3MWCNT/%1CuNP, and TPU/%3MWCNT/%5CuNP

The copper ion release results from nanofibers containing CuNPs were given in Figure 7. The copper ion release increased in a controlled manner for the nanofiber containing 1% Cu. However, it was determined that the copper ion release did not occur in a controlled manner for the nanofiber containing 5% Cu. This is thought to be due to the lack of a smooth nanofiber structure in the sample containing 5% CuNPs and the inhomogeneity of the nanofiber distribution.

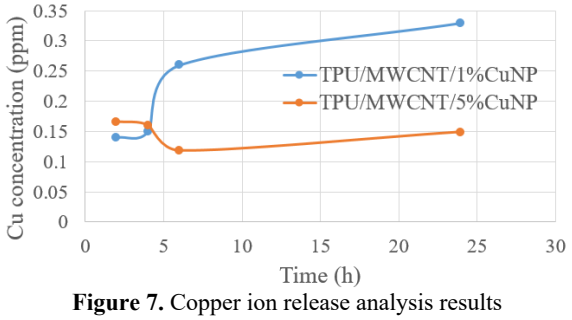

Figure 7. Copper ion release analysis results

4. Conclusion

In this study, an electrospun nanocomposite scaffold was fabricated from TPU doped with MWCNT and CuNP, and holding a potential as skeletal muscle tissue material. The characterization of the prepared nanocomposite membranes was investigated by using SEM, FTIR, XRD TGA, antibacterial and ion release tests. The optimal nanocomposite scaffold sample was determined to be 3% MWCNT. Fiber diameter and morphology changed with the addition of MWCNT and CuNP. FTIR graphs pointed out successful incorporation of MWCNTs into the TPU without altering the chemical structure of the polymer. XRD analysis indicated the CuNPs integration into the nanocomposite structure. It was observed that the incorporated CuNP imparted antibacterial properties to the nanocomposite samples. Copper ion release tests also revealed that the copper concentration was below the toxic level that would kill muscle cells. TGA and DTG results determined that the addition of MWCNTs and CuNPs increased the thermal stability of the nanocomposite samples. Although the 1% CuNP-added TPU/MWCNT nanocomposite sample showed better properties than those of the samples based on the obtained results, further analyses will be conducted to investigate the different concentrations of copper and MWCNT that may render them potential candidates for skeletal muscle tissue applications.

Acknowledgment

This work was supported by Istanbul Technical University Research Fund (Project Number: MGA-2021-43116).

References

[1] R. Dong, P. X. Ma, and B Guo, "Conductive biomaterials for muscle tissue engineering." Biomaterials, vol. 229, p. 119584, 2020.

[2] T. C. Suh, J. Twiddy, N. Mahmood, K. M. Ali, M. M. Lubna, P. D. Bradford, M.A. Daniele and J. M. Gluck, "Electrospun carbon nanotube-based scaffolds exhibit high conductivity and cytocompatibility for tissue engineering applications." ACS omega, vol. 7, pp. 20006-20019, 2022.

[3] M. E. Villanueva, A. M. D. R. Diez, J. A. González, C. J. Pérez, M. Orrego, L. Piehl, S. Teves, and G. J. Copello, "Antimicrobial activity of starch hydrogel incorporated with copper nanoparticles." ACS Applied Materials&Interfaces, vol. 8, pp. 16280–16288, 2016.

[4] A. Akturk, F. K. Güler, M. E. Taygun, G. Goller, and S. Küçükbayrak, "Synthesis and antifungal activity of soluble starch and sodium alginate capped copper nanoparticles," Materials Research Express, vol. 6, p. 1250g3, 2020.

[5] G. Gökçeli, and N. Karatepe, "Improving the properties of indium tin oxide thin films by the incorporation of carbon nanotubes with solution-based techniques," Thin Solid Films, vol. 697, p. 137844, 2020.

[6] A. Akturk, "Enrichment of Cellulose Acetate Nanofibrous Scaffolds with Retinyl Palmitate and Clove Essential Oil for Wound Healing Applications," ACS Omega, vol. 8, pp. 5553–5560, 2023.

Preliminary Research on Hydroxyapatite Depo-Sition on Ti Alloys by Aluminides Binding Zone Formation

Marian Miculescu[1], Ștefan Lăptoiu[1], Diana Enescu[1],

1. National University of Science and Technology Politehnica Bucharest

Given the promising but challenging nature of Ti-Al alloys, especially regarding their processing, this study employed EDM to explore innovative surface engineering strategies, aiming to enhance biocompatibility for medical applications..

Al was deposited on the Ti alloy through electrical impulse discharge, followed by a subsequent investigation of the results obtained for the deposition of hydroxyapatite using the same technique. The deposits were made under strictly identical conditions. The sample was subjected to thermal treatment at 600°C for 3 h, followed by controlled cooling for 12 h in an oven, and placed face-down in a layer of aluminum oxide. In parallel, a thermochemical treatment was applied using a mixture consisting of 30 g CON_2H_4, 3.4 g NH_3Cl, 40 g graphite, and 26.5 g Al_2O_3, followed by the same thermal regime.

The preliminary results derived from optical and electron microscopy (SEM, EDS) analyses confirmed the excellent adhesion between the deposited layers and titanium-based substrate. The formation of complex Ti–Al–V intermetallic compounds is observed both at the interface and within the coating layers, indicating successful diffusion and metallurgical bonding. The from rezollts we can spaculate the formation of intermetallic phases such as $TiAl_2$ and $TiAl_3$ suggests favorable reaction kinetics during the thermal and thermochemical treatments. Among the tested samples, thermochemical treatment demonstrated the most promising overall performance, exhibiting enhanced diffusion, good structural integrity, and a significant increase in surface hardness.

The findings support the viability of employing multilayer surface engineering approaches, particularly involving thermochemical treatments, to enhance the performance and durability of titanium-aluminum alloy components in advanced applications.

Keywords: electrical impulse discharge, hydroxyapatite, biocompatible

EXTRACTION OF CELLULOSE FROM AGRICULTURAL WASTES FOR APPLICATION IN BIOMATERIAL-BASED FORMULATIONS

Sila Kilic Cevirgel[1,2], Ebru Turkoz Acar[2], Gultekin Goller[1,†]

[1] Istanbul Technical University, Faculty of Chemistry & Metallurgy, Metallurgical and Materials Eng. Dep., 34469, İstanbul, Turkiye

[2] Yeditepe University, Faculty of Pharmacy, Department of Pharmaceutical Analytical Chemistry, 34755 Atasehir, Istanbul, Turkey.

Keywords: Biomaterials, Cellulose, Extraction, Agricultural waste.

Abstract

The demand for biocompatible, biodegradable, and economically sustainable raw materials has been steadily increasing for pharmaceutical formulations. Among these materials, cellulose, which is a naturally occurring polysaccharide, is a striking candidate due to its wide availability and physicochemical properties. In this study, cellulose was extracted from agricultural wastes of wheat and corn, and its potential application in plant-based biomaterial formulations was investigated. Extraction experiments involving alkali treatment, bleaching, and acid hydrolysis were performed in each experimental group by modifying a single parameter, such as solution concentration or temperature, in order to assess its specific impact on the quality of cellulose extraction. The extracted cellulose samples were characterized using Fourier Transform Infrared Spectroscopy (FTIR) and X-ray Diffraction (XRD) to assess their chemical and structural properties. Optimal extraction conditions were identified, and the applicability of the extracted cellulose in the development of pharmaceutical biomaterials was evaluated based on the characterization results.

1. Introduction

Cellulose is the most abundant biopolymer in nature and represents the primary structural component of plant cell walls, providing mechanical strength and stability (Gbenebor et al., 2023). Structurally, it is a linear homopolymer composed of β-(1→4)-linked D-glucose units with the general formula $(C_6H_{10}O_5)_n$. The hydroxyl-rich backbone facilitates extensive intra- and intermolecular hydrogen bonding, resulting in insolubility in water, a fibrous morphology, and high tensile strength. These characteristics make cellulose highly attractive for applications in composites, biofilms, coatings, and biomedical devices [1,2].

Plant cell walls are mainly composed of cellulose, hemicellulose, and lignin. While cellulose is the predominant fraction, hemicellulose consists of heterogeneous polysaccharides with various sugar units, and lignin is a cross-linked phenolic polymer that contributes to rigidity and hydrophobicity [3].

As a semi-crystalline polymer, cellulose contains both amorphous and crystalline domains, with their ratio varying according to plant species, geographical origin, and applied extraction methods. For instance, hardwoods typically contain 40–50% cellulose, softwoods about 40–45%, and cotton up to 90% [3]. Agricultural residues such as corn husks and wheat straw also exhibit relatively high cellulose contents (35–45%), together with hemicellulose, lignin, and minor organic constituents, thereby representing sustainable and cost-effective sources for high-quality cellulose biopolymer production [1,4].

Cellulose extraction typically involves three main steps: alkali treatment, bleaching, and acid hydrolysis. Alkali treatment with sodium hydroxide removes hemicellulose and part of the lignin, isolating cellulose. Bleaching further enhances purity and whiteness by eliminating residual lignin, hemicellulose, pectins, and waxes; this step is often repeated to optimize quality. Finally, acid hydrolysis selectively cleaves amorphous regions, yielding cellulose nanocrystals (CNCs) with high crystallinity, surface hydroxyl enrichment, and nanoscale dimensions. CNCs exhibit exceptional mechanical strength, biodegradability, and dispersibility, making them valuable for advanced applications such as drug delivery, nanocomposites, and sustainable packaging [2].

In this study, cellulose was extracted from wheat and corn agricultural residues using this multistep process, and the resulting samples were characterized to assess their potential as sustainable biomaterials.

2. Experimental Procedure

The corn husk and wheat straw were used as agro-wastes in extraction processes and they were obtained from local market (Eskişehir, Turkey). Sodium hydroxide (NaOH), hydrogen peroxide (H_2O_2) and hydrogen chloric acid (HCl) were purchased from Merck, Turkey. All other chemicals were of analytical reagent grade and used as received, without further purification. During the filtration and neutralization processes, distilled water was used.

Cellulose extraction has three main parts as alkali treatment, bleaching, and acid hydrolysis. The corn husks and wheat straws were used in the extraction processes to get cellulose. There are six experiment sets for waste type and each set which have different experiment parameters (Table 1). EXP1 and EXP6 are reference experiments for wheat and corn respectively. Based on these reference sets, one of the parameters was changed in other sets and this set was compared with reference set to observe effects of parameter changing.

Table 1. Parameters of experiment sets.

Agricultural waste	Exp. codes	Changing Exp. Parameter	α	ß	θ
Wheat Corn	EXP1 EXP6	Reference experiment	80 C°, (1:10), 2 hr, 4% w/v	70 C°, (1:10), 3 hr, 8% w/v	60 C°, (1:10), 1 hr, 10% w/v
	EXP2 EXP7	Bleaching repetation	-	70 C°, (1:10), 3 h, %8 w/v	-
	EXP3 EXP8	l/s ratio from 1:10 to 1:20	1:20	1:20	1:20
	EXP4 EXP9	Reaction time	3 hr	4 hr	2 hr
	EXP5 EXP10	Reaction temperature	100 C°	90 C°	100 C°

α: Alkali treatment, **ß:** Bleaching, **θ:** Acid hydrolysis

2.1. Alkali treatment (α)

The corn husk and wheat straw were washed with distilled water and dried at room temperature for 24 hours. After washing and drying processes, wastes were ground and sieved with grinder and stored at room temperature. The ground wastes were treated with 4% w/v sodium hydroxide (NaOH) alkali solution at defined temperature and duration of reaction that are indicated in Table 1. The solid was then filtered and washed several times in distilled water till the pH of filtrate was be neutralized.

2.2. Bleaching (ß)

Following alkali treatment, the bleaching treatment was carried out using 8% w/v hydrogen peroxide (H_2O_2) at defined temperature and duration of reaction that are indicated in Table 1. The mixture was allowed to cool and filtered using excess distilled water. For EXP2 and EXP7 experiment sets, this process was repeated to understand the effect of step repetition.

2.3. Acid hydrolysis (θ)

The acid hydrolysis treatment was conducted after alkali treatment and bleaching process using hydrogen chloric acid (HCl) concentration 10% w/v and indicated reaction temperature with a range of reaction time (60 and 120 minutes) under continuous stirring. The ratio of the obtained cellulose to liquor was changed according to Table 1. The hydrolyzed material was washed with distilled water to remove solvents residues till neutralization.

All extracted celluloses were grinded by homogenizer with 20.000 rpm and dried under the vacuum to obtain micro crystalline cellulose (MCC, γ).

2.4. Characterization

Fourier Transformation Infrared Radiation (FTIR)

Untreated, alkali-treated, bleached, and acid-hydrolyzed corn husk and wheat samples were analyzed (Figure 1a) using a Perkin- Elmer Fourier Transform Infrared spectrometer within the wavelength range of 4000–500 cm^{-1}. The analysis was performed using the Attenuated Total Reflectance (ATR) probe. The obtained spectra were considered reliable for identifying characteristic functional groups of the extracted materials.

X-Ray Diffraction (XRD)

The crystallinity of extracted celluloses was analyzed using a Rigaku Miniflex X-Ray Diffractometer equipped with Ni-filtered CuKα radiation in the step-scan mode with a 2θ angle ranging from 10 to 50° at a scan rate of 3°/min with a resolution of 0.02°. The operating voltage and current were 30 kV and 15 mA, respectively. The crystallinity index was calculated [5] with Eq. (1).

$$Cr = \frac{I002 - Iam}{Iam} \quad \textbf{(1)}$$

The XRD analysis further elucidated the crystalline structure of the nanocellulose. Prominent diffraction peaks at 2θ values of 16°, 22°, and 35° confirmed its crystalline nature. The Crystallinity Index (CrI), calculated using the Segal method by Eq 1.

Where Cr is the crystallinity index, I_{002} is the maximum intensity of the diffraction from the 002 plane, and I_{am} is the intensity of scattered by the amorphous part of the sample.

3. Results and Discussion

Spectroscopic analysis

Structural analyses were performed using FTIR spectroscopy, with particular attention to lignin removal, cellulose purification, and crystallinity.

When standard conditions were applied (EXP1 and EXP6), the FTIR spectra displayed persistent aromatic peaks at ~1619 cm^{-1}, indicating incomplete delignification and limited cellulose purity. This observation demonstrates that conventional processing is insufficient for achieving high-quality cellulose, regardless of the agricultural source.

The introduction of a second bleaching step (EXP 2 and EXP7) substantially improved structural purification. The suppression of aromatic C=C bands, accompanied by the emergence of a distinct β-glycosidic peak at ~896 cm^{-1}, confirmed more effective lignin removal. This result highlights that repeated oxidative treatment facilitates higher cellulose purity without altering other parameters, offering a straightforward strategy for process improvement.

Increasing the reagent volume (EXP3 and EXP8), achieved by adjusting the S/L ratio from 1:10 to 1:20 while maintaining constant concentrations, enhanced the efficiency of extraction. FTIR spectra revealed weaker aromatic signals and more symmetric C–H and C–O bands, suggesting improved reagent diffusion and more effective interaction with the biomass. This finding emphasizes the importance of sufficient reagent accessibility to the substrate and suggests scalability of the method for larger production volumes.

Extending the reaction times of extraction steps (EXP4 and EXP9) further contributed to cellulose quality. Prolonged treatments resulted in the complete disappearance of aromatic signals and significant intensification of the glycosidic C–O–C region (1050–900 cm^{-1}). These observations indicate that longer durations allow more thorough removal of lignin and hemicellulose, while simultaneously exposing crystalline cellulose domains. However, extended times may increase energy consumption, which should be considered in large-scale applications.

Elevated processing temperatures (EXP5 and EXP10) proved to be the most effective parameter in promoting rapid delignification and crystallinity. Treatment at 100 °C (alkali) and 90 °C (bleaching) resulted in complete suppression of aromatic peaks and pronounced intensification of crystalline cellulose bands, indicating accelerated structural ordering within shorter durations. Nevertheless, discoloration of samples during subsequent acid hydrolysis at 100 °C suggested partial thermal degradation.

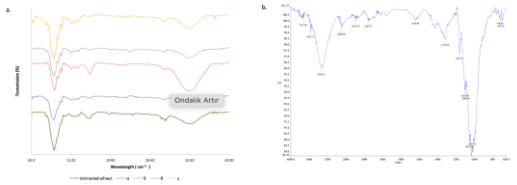

Figure 1. FTIR spectrum of nanocellulose in EXP 8 (a), Comparision of FTIR spectrums of each extraction step for EXP8 (b).

Overall, the results demonstrate that repeated bleaching, higher reagent volumes, extended reaction times, and elevated temperatures all contributed positively to cellulose purification, albeit with varying degrees of effectiveness. Among these, prolonged durations and high temperatures produced the most crystalline cellulose, whereas bleaching repetition and reagent volume adjustments provided practical and scalable improvements. The suppression of aromatic C=C (~1600–1650 cm^{-1}), narrowing of O–H stretching (~3300 cm^{-1}), and intensification of β-glycosidic C–O–C signals (1050–900 cm^{-1}) were consistent FTIR indicators of successful cellulose purification (Figure 1b) . These findings underline the necessity of parameter optimization to obtain high-purity cellulose suitable for pharmaceutical biomaterial applications.

X-Ray Diffraction (XRD)

Figure 2a presents the XRD patterns of untreated waste, alkali-treated, bleached, acid-hydrolyzed samples, and nanocellulose. The XRD patterns of the samples were analyzed using the X'Pert software, which enabled detailed evaluation of diffraction peaks and crystallinity parameters. The diffraction data were compared with the standard reference from the JCPDS database and the results confirmed that the diffraction peaks of the sample matched the characteristic JCPDS card number (*JCPDS: 00-050-2241*) of cellulose, thereby verifying its crystalline structure. The characteristic diffraction peaks observed at $2\theta \approx 16°$, 22°, and 35° correspond to the crystalline domains of cellulose I, confirming that the extracted nanocellulose retained its crystalline structure. The crystallinity index (CrI%) of each sample was calculated using the Segal method, and the best result was given in Table 2.

At the baseline conditions (EXP 1 and EXP6), where a single bleaching step was applied, the CrI values were relatively low. This outcome demonstrates that limited removal of lignin and hemicellulose from the amorphous regions is insufficient to enhance crystallinity, and highlights the inadequacy of a single bleaching treatment for complete purification.

When bleaching was applied twice (EXP2 and EXP7), a pronounced increase in crystallinity was observed. The additional oxidative step facilitated more effective removal

of residual lignin and hemicellulose, enabling the rearrangement of crystalline domains and producing sharper diffraction peaks. This finding indicates that repeated bleaching not only improves delignification but also contributes significantly to preserving the structural integrity of cellulose.

Adjusting the solid-to-liquid ratio from 1:10 to 1:20 (EXP3 and EXP8), while keeping reagent concentrations constant, also improved the CrI values. The increased liquid volume enhanced reagent diffusion and accessibility, thereby promoting more uniform interaction with the lignocellulosic matrix. As a result, cellulose chains were more effectively purified, and crystalline domains were better preserved. This highlights the importance of optimizing reagent accessibility for scalable and efficient cellulose extraction.

Table 2. Crystallinity Index (CrI %) values of EXP 8.

Exp. Codes	Raw waste	α	ß	ß-*repetition*	θ	Micro cellulose
EXP8	78,66	79,49	83,74		83,75	90,00

In contrast, extending the reaction durations (EXP4 and EXP9) did not yield further improvement in crystallinity. Instead, prolonged exposure to alkali and bleaching media led to relatively lower CrI values, suggesting partial depolymerization or degradation of cellulose chains. Although FTIR spectra confirmed enhanced removal of lignin and hemicellulose, the decline in crystallinity implies that excessively long treatments may compromise the structural order of cellulose.

Similarly, processing at elevated temperatures accelerated delignification, as evidenced by the disappearance of lignin-associated signals in FTIR spectra. However, XRD analysis revealed lower CrI values compared to optimized conditions. This reduction can be attributed to thermal degradation during high-temperature treatments (e.g., 100 °C alkali, 90 °C bleaching), which may induce chain scission or formation of disordered phases. The observed darkening of samples during acid hydrolysis further supports this interpretation.

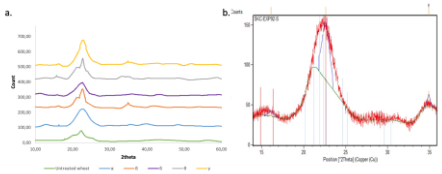

Figure 2. Comparision of XRD patterns of each extraction step for EXP8 (a), XRD pattern of EXP 8 (b).

Overall, the highest CrI values were obtained under conditions involving repeated bleaching and increased reagent volume. These results demonstrate that optimization of bleaching frequency and liquid-to-solid ratio plays a more critical role in preserving crystalline cellulose than either prolonged durations or elevated thermal treatments. Consistency between FTIR and XRD results—suppression of aromatic C=C (~1600–1650 cm^{-1}), narrowing of O–H stretching (~3300 cm^{-1}), and intensification of β-glycosidic C–O–C vibrations (1050–900 cm^{-1})—confirms that these optimized conditions produce high-purity, crystalline cellulose suitable for advanced biomaterial applications.

4. Conclusion

This work confirmed that cellulose can be extracted with comparable success from both corn husk and wheat straw when appropriate processing conditions are applied. FTIR analyses demonstrated that single-step treatments were insufficient for either source, while repeated bleaching cycles and higher solid-to-liquid ratios consistently improved cellulose purity in both cases. These modifications provided effective and scalable improvements without introducing additional complexity.

Similarly, extended treatment times and elevated temperatures enhanced crystallinity for both corn- and wheat-derived cellulose, indicating that parameter changes exert parallel effects regardless of biomass type. However, these conditions also carried drawbacks, including increased energy consumption and partial thermal degradation. Thus, while high temperatures and prolonged durations improved ordering, repeated bleaching and optimized reagent accessibility represent more sustainable strategies, equally effective for both agricultural residues.

References

[1] Chopra, L., & Manikanika, "Extraction of cellulosic fibers from the natural resources: A short review," Materials Today: Proceedings, vol. 48, pp. 1265–1270, 2021.

[2] Rathinavelu, R., Paramathma, B. S., Divkaran, D., & Siengchin, S., "Physicochemical, thermal, and morphological properties of microcrystalline cellulose extracted from Calotropis gigantea leaf. Biomass Conversion and Biorefinery", vol. 14(19), pp. 24455–24472, 2024.

[3] Gbenebor, O. P., Olanrewaju, O. A., Usman, M. A., & Adeosun, S. O., "Lignin from Brewers' Spent Grain: Structural and Thermal Evaluations," Polymers, vol.15(10), 2023.

[4] Kampeerapappun, P., "Extraction and Characterization of Cellulose Nanocrystals Produced by Acid Hydrolysis from Corn Husk. Journal of Metals," Materials and Minerals, vol. 25(1), pp. 19–26, 2015.

[5] Segal, L., Creely, J. J., Martin, A. E., & Conrad, C. M. (1952). "Opportunity for new developments in all phases of textile manufacturing. ' Literature Cited An Empirical Method for Estimating the Degree of Crystallinity of Native Cellulose Using the X-Ray Diffractometer," In Apparel Manufacturing, Vol. 43, 1952.

OPTIMIZATION OF SILICATE–ZRO_2 MICRO-ARC OXIDATION COATINGS ON AZ31 MAGNESIUM ALLOY FOR BIORESORBABLE IMPLANTS

Obada Abdülhalik[1], Faiz Muhaffel[1],

1. İstanbul Technical University, Department of Metallurgical and Materials Engineering, İstanbul

This study investigates the synthesis and optimization of silicate-based micro-arc oxidation (MAO) coatings reinforced with ZrO2 on AZ31 alloy, and the relationship between electrical parameters and coating structure and performance.

Micro-arc oxidation (constant-voltage regime, including mixed-pulse and continuous positive and constant-current modes), SEM analysis, XRD analysis, EDS analysis, and contact angle measurement.

Crater size and density increased with higher positive pulse proportions.-XRD analyses identified MgO and Mg2SiO4 as dominant phases in the MAO coating.-Coating thickness increased from 18.2 ± 4.3 μm (constant current) to 37.2 ± 6.2 μm (continuous positive).-Growth in average roughness from 1.5 to 4.5 μm.-EDS analyses confirmed the uniform incorporation of Si and Na, while Zr reached 24 wt.% in the thickest coating formed by the MAO process.-With increasing thickness, the static water contact angle decreased from 72° to 31°, which indicated enhanced hydrophilicity,

An apatite nucleation is expected to be accelerated by rough, hydrophilic surfaces, while substrate dissolution should be slowed by a denser oxide and ZrO2 enrichment.

Keywords: Magnesium, Micro-arc oxidation, Bioresorbable, Implant

Coatings

FABRICATION AND CHARACTERIZATION OF HIGH ENTROPY MoTiVWZr ALLOYS BY MAGNETRON SPUTTERING

ERKAN KAÇAR[1], CEM ÖRNEK[2],

1. Hakkari University

2. Istanbul Technical University

This study aimed to synthesize MoTiVWZr high-entropy alloy (HEA) thin films using magnetron sputtering from individual elemental targets, and to systematically investigate the influence of deposition parameters such as power and working pressure on their structural, mechanical, and electrochemical properties. The goal was to assess their potential for various engineering applications.

MoTiVWZr thin films were deposited via magnetron sputtering. Their structural and phase characteristics were then investigated using X-ray diffraction (XRD). Scanning electron microscopy (SEM) was utilized for analyzing the cross-sectional morphology. Mechanical performance was evaluated through nanoindentation tests using a Vickers-type diamond indenter. Additionally, the electrochemical behavior was assessed via potentiodynamic polarization tests in both 0.1 M NaCl and pH 4 H2SO4 solutions.

XRD analysis confirmed the formation of crystalline phases with broad peaks, indicating a fine grain structure and lattice distortions. SEM observations revealed consistent cross-sectional morphologies. The films exhibited good hardness values (7-8 GPa) as determined by nanoindentation. Furthermore, in both 0.1 M NaCl and pH 4 H2SO4 solutions, the coatings demonstrated stable passive behavior over a wide potential range and exhibited significantly lower current densities compared to both single elements and stainless steel.

Our results indicate that magnetron sputtering is a suitable method for producing compositionally complex MoTiVWZr coatings. These coatings possess tunable microstructural, mechanical, and electrochemical characteristics, making them highly promising for various engineering applications where enhanced surface properties, particularly superior corrosion resistance in diverse environments, are required.

Keywords: High-Entropy , MoTiVWZr, Magnetron Sputtering

Microstructural and Electrochemical Evaluation of APS-deposited Layers on Disk Harrow Agricultural Components

Corneliu Munteanu[1], *Bogdan Istrate*[1], Ramona Cimpoesu[1], Fabian Cezar Lupu[1], Gelu Ianuș[1], Iurie Melnic[2], Vlad-Nicolae Arsenoia [3],

1. "Gheorghe Asachi" Technical University of Iasi

2. Technical University of Moldova

3. University of Life Sciences Ion Ionescu de la Brad

The atmospheric plasma spray (APS) deposition technology is a well-established method for performing coatings on the surfaces of various metallic materials used in fields such as agriculture, automotive and others. The present study offers a comparative analysis of three different types of coatings from a microstructural and electrochemical evaluation perspective: W2C/WC12Co (Metco71NS), Cr2O3-4SiO2-3TiO (Metco136F), and Co25.5Cr10.5Ni7.5W0.5C (Metco45C-NS). The mentioned powders were deposited on a highly stressed agricultural component under working conditions: the disc harrow. Microstructural evaluation using optical microscopy and SEM of the obtained layers revealed the formation of uniform and adherent coatings to the base material, but with the presence of some micropores and a few cracks. The corrosion resistance of coating systems applied on steel substrates was evaluated by linear and cyclic polarisation tests, and by electrochemical impedance spectroscopy (EIS) in 3.5% NaCl solution. The electrochemical parameters determined - corrosion current density, corrosion potential, charge transfer resistance, interface capacitance and diffusive components - allowed a detailed characterisation of the effectiveness of the protective barriers, the stability of the protective layer and the behaviour in initiating of corrosion processes. The results obtained demonstrate that the deposition of the coatings significantly improved the electrochemical stability and corrosion resistance of the metal substrate, reflecting the effectiveness of the protective barriers. The assessment and improvement of corrosion resistance represent an important factor for the long-term use of all vital agricultural components, especially those such as the disc harrow.Acknowledgment:This work was supported by a grant of Ministery of Research, Innovation and Digitization, CNCS-UEFISCDI, project numberPN-IV-P8-8.3-ROMD-2023-0108, within PNCDI IV.

Keywords: APS, coatings, microstructure, corrosion resistance

Evaluation of The Cellulose-Acetate-Based Composite Used as Coatings for Biodegradable Magnesium Implants

Streza Alexandru [1], Antoniac Aurora[1], Voicu Ioan Stefan[1], Paltanea (Manescu) Veronica[1], Popescu Elena[1], Antoniac Iulian[1],

1. National University for Science and Technical POLITEHNICA Bucharest,

In this study, we developed a polymeric-based composite coating on biodegradable magnesium alloys to reduce the biodegradation rate: PC1 (cellulose acetate+5% hydroxyapatite), PC2 (cellulose acetate+5% Mg particles), PC3 (cellulose acetate + 5% hydroxyapatite + 5% Mg particles). A coating made of cellulose acetate was used as a reference (CA).

The composite coatings were evaluated using FTIR/RAMAN spectroscopy, scanning electron microscopy (SEM), and energy-dispersed X-ray spectroscopy (EDS). Degradation rate in PBS, and cytotoxicity tests MTT were also performed.

The obtained results demonstrated that coatings based on cellulose acetate and hydroxyapatite and/or magnesium particles could be obtained by the solvent evaporation method. The addition of hydroxyapatite and magnesium powders in the cellulose acetate polymer matrix influenced the composite samples' morphology. SEM images reveal pores on the surface of the composite coating, with irregular sizes, and distributed in regions of different densities. Reinforcing elements influence the degradation behavior and cytotoxicity tests of coatings differently, highlighted the positive effect of magnesium and hydroxyapatite particles when they are used alone.

Anyway, even these composite coatings have differentiated characteristics through a combination of the fillers, their biocompatibility and controllable degradation rate make them attractive materials for use as coatings materials for biodegradable Mg alloys.

Keywords: biomaterials, magnesium alloys, composite, coating

Investigation of Wear Resistance and Surface Characterization of Manganese Phosphate Coated Crankshafts Under Various Mnp Bath Conditions

Berfin Kaya[1], Rıdvan Gecü[1], Simge Tarkuç[2],

1. Yıldız Technical University

2. Beko Corporate

This study aims to systematically investigate the effects of manganese phosphate (MnP) bath parameters on wear resistance and surface properties of crankshaft components. Specifically, the research focuses on understanding how variations in bath temperature, pH level, immersion time, and accelerator concentration influence the final coating quality and tribological performance.

Crankshaft specimens were subjected to manganese phosphate coating under systematically varied bath conditions, including adjustments in temperature, pH levels, immersion durations, and accelerator concentrations. Following the coating process, surface characterization was conducted using scanning electron microscopy (SEM), energy-dispersive X-ray spectroscopy (EDS), and surface roughness measurements. Tribological evaluations were performed through semi-lubricated sliding wear tests to determine the relationship between coating parameters and wear resistance.

Results indicated that optimized manganese phosphate bath parameters significantly improved surface morphology, achieving a more uniform and dense crystal structure. The optimized coatings exhibited notably enhanced wear resistance, characterized by reduced wear rates during tribological testing.

The study provides practical insights highlighting that precisely controlled manganese phosphate coating parameters play a critical role in improving surface quality and extending the service life of crankshaft components. These findings underline the importance of bath optimization in achieving superior component durability and performance.

Keywords: Coatings, Tribology, Wear

Composite Materials

Extrusion Processing and Thermo-Mechanical Characterization of Polypropylene Composites Reinforced with Agricultural Waste

Zeynep KAYA[1], Hale BERBER[1], Şebnem BAYSEÇ GEMCİ[2],

1. Yıldız Technical University

2. Beko Corporate

In recent years, the environmental impacts of petroleum-based plastics and the increasing dependency on finite natural resources have prompted extensive research into sustainable material technologies. In this context, polymer composites reinforced with additives derived from agricultural waste have emerged as a promising alternative in terms of environmental sustainability, waste valorization, and material circularity. Among widely used polymers, polypropylene (PP) stands out due to its balanced mechanical performance, low cost, and broad applicability in industrial sectors. However, enhancing its functionality through eco-friendly reinforcements remains a critical research need. This study aims to develop agricultural waste-reinforced PP composites via melt extrusion and to evaluate their suitability for structural applications by characterizing their mechanical and thermal behavior. By doing so, it addresses the growing demand for cost-effective, environmentally benign materials, while contributing to the advancement of bio-based circular material systems.

In this study, waste materials derived from lemon peels, apricot kernels, and post-production lavender residues were dried, ground, and incorporated into a neat polypropylene (PP) matrix at concentrations ranging from 2.5% to 10% by weight using a twin-screw extrusion process. Prior to extrusion, all fillers were thoroughly dried to prevent moisture-induced degradation. The resulting granules were then shaped into test specimens via injection molding. The mechanical properties of the composites were evaluated through tensile, flexural, and impact tests, while their thermal and structural behaviors were characterized using Thermogravimetric Analysis (TGA), Differential Scanning Calorimetry (DSC), and Fourier-Transform Infrared Spectroscopy (FTIR).

Among the tested formulations, the 5 wt.% filler content exhibited the most balanced performance in terms of processability and composite properties. A 5% lavender addition increased the flexural modulus by 4% while causing a 10% reduction in impact strength. Lemon peel reinforcement significantly improved stiffness, increasing the flexural modulus by up to 77%. Apricot kernel addition led to enhanced impact strength, indicating improved toughness. TGA results confirmed that all agricultural fillers maintained thermal stability at processing temperatures (~200 °C), without signs of premature degradation. Overall, the composites preserved structural integrity and offered functional enhancements while reducing dependency on conventional fillers.

This study demonstrated that agricultural wastes such as lemon peel, lavender residue, and apricot kernel can be effectively utilized as eco-friendly fillers in polypropylene matrices to produce sustainable composite materials. 5 wt.% filler content provided optimal performance in terms of both processability and mechanical–physical properties. Based on the mechanical tests and thermal analyses, all three waste types were found to be compatible with PP at appropriate loading levels.All findings indicate that incorporating agricultural waste into polymer matrices not only contributes significantly to sustainability, but also enhances material performance through improved mechanical properties. These improvements validate the potential of such composites for use in various industrial applications.

Keywords: agricultural waste,extrusion, biocomposites, sustainability

THE EFFECT OF REINFORCEMENT ON THE MECHANICAL PROPERTIES OF POLYMER MATRIX COMPOSITE REINFORCED WITH PALM TREE FIBER

Aydın Bayram[1], Serkan Ateş[2],

[1]Department of Mechanical Engineering, Faculty of Engineering and Architecture, Burdur Mehmet Akif Ersoy University, Burdur, Türkiye 0009-0002-7958-8742

Aydinbyrm0@outlook.com

[2]Department of Mechanical Engineering, Division of Construction and Manufacturing, Faculty of Engineering and Architecture, Burdur Mehmet Akif Ersoy University, Burdur, Türkiye 0000-0002-5858-5190

sates@ogr.mehmetakif.edu.tr

Keywords: Polymer matrix composites, Palm fiber reinforcement, Mechanical properties, Natural fiber composites

Abstract

In this study, the potential use of abundantly available palm tree fibers as natural reinforcement in polyurethane-based polymer matrix composites was investigated. The primary objective is to develop environmentally friendly and sustainable composites and evaluate their mechanical behavior. Composite specimens were prepared by incorporating 1%, 3%, and 5% palm fibers into a two-component polyurethane matrix using a manual mixing and casting method. Mechanical properties were evaluated through tensile (ASTM D638), flexural (ASTM D790), and Charpy impact (ASTM D256) tests. Test results revealed that palm fiber significantly enhanced mechanical performance. Tensile strength reached 17.676 MPa with 3% fiber (35% increase); flexural strength reached 50.914 MPa with 5% fiber (86% increase); impact strength reached 43.632 kJ/m² with 5% fiber (57% increase). These findings show that palm fibers effectively improve strength and toughness in bio-based composites. The experimental results were also supported by ANSYS software.

1. Introduction

Today, increasing environmental concerns and limited resources necessitate sustainable solutions in the field of materials science. In this context, biodegradable, renewable, and eco-friendly materials have gained significant importance. Natural fiber-reinforced composites attract attention due to their light weight and economic advantages [1]. Composites can achieve superior performance by combining components with different properties; while the matrix phase ensures integrity, the reinforcement phase enhances strength [2,3]. To maintain the integrity of the matrix phase, polymer matrices can be preferred. Polymer matrix composites stand out with their wide range of applications and processability, while environmental concerns have encouraged the use of natural reinforcements [4]. Numerous studies in the literature have focused on the use of natural reinforcements as reinforcing agents. Research has shown that oil palm fibers improve the mechanical properties of composites [5], sugar palm fibers can enhance matrix compatibility through various chemical treatments [6,7,8], and Carica papaya fibers yield favorable results in epoxy matrices [9]. With advantages such as low density and recyclability, natural fiber composites are considered important for sustainable industrial applications [10]. In addition to fibers such as flax, jute, and sisal, palm tree fibers, with their high cellulose content and biodegradable structure, also stand out as potential reinforcements. As agricultural waste, these fibers provide both environmental and economic benefits; however, more studies are needed regarding their performance in composites [11]. Within the scope of this thesis, palm fibers were reinforced into a polyurethane matrix for the first time to produce composite material, and their mechanical properties were investigated. Experimental studies revealed significant improvements in tensile, flexural, and impact strengths at different fiber ratios; in particular, a 3% fiber ratio improved tensile strength by 35%, a 5% fiber ratio enhanced flexural strength by 86%, and impact strength by 57%.

2. Experimental Procedure

2.1. Mold Preparation

For the preparation of composite specimens, molds compliant with ASTM D638 (tensile), ASTM D790 (flexural), and ASTM D256 (impact) standards were modeled in SolidWorks and produced using a 3D printer. The models were placed on a flat surface and surrounded with cardboard plates to prevent silicone overflow. The silicone was mixed with 2% hardener at low speed for 18 minutes, poured onto the models, and left to cure for 48 hours. After curing, the hardened molds were removed and made ready for composite production.

Figure 1. Mold production process

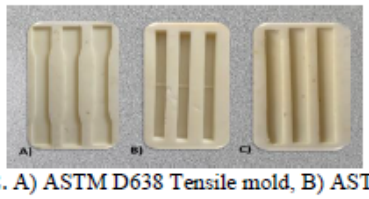

Figure 2. A) ASTM D638 Tensile mold, B) ASTM D256 Charpy impact test mold, C) ASTM D790 Three-point bending mold

2.2. Calculation of Ratios

In the experimental study, reinforcement ratios were determined as 0% (control), 1%, 3%, and 5%. For each ratio, three control specimens were prepared in accordance with ASTM D638, D790, and D256 standards. The composite components were calculated on a mass basis according to the targeted ratios.

Table 1. Material quantities used at different reinforcement ratios according to ASTM D256 Standard

Reinforcement Ratio (%)	Palm Fiber (g)	Polyurethane (g)	Total Mixture (g)
1	0,20	19,87	20,07
3	0,60	19,47	20,07
5	1,00	19,07	20,07

Table 2. Material quantities used at different reinforcement ratios according to ASTM D638 Standard

Reinforcement Ratio (%)	Palm Fiber (g)	Polyurethane (g)	Total Mixture (g)
1	0,10	10,23	10,33
3	0,31	10,02	10,33
5	0,52	9,81	10,33

Table 3. Material quantities used at different reinforcement ratios according to ASTM D790 Standard

Reinforcement Ratio (%)	Palm Fiber (g)	Polyurethane (g)	Total Mixture (g)
1	0,06	6,29	6,35
3	0,19	6,16	6,35
5	0,32	6,03	6,35

2.3. Production

Palm fibers, previously prepared and cut to approximately 10 mm in length, were weighed according to the reinforcement ratios specified in the experimental design (1%, 3%, and 5%). The weighed fibers were mechanically mixed with the A and B phases of a two-component polyurethane system. During the mixing process, the homogeneous dispersion of fibers within the matrix phase was ensured, thereby maintaining the structural integrity of the composite material. The prepared fiber–polyurethane mixture was carefully poured into the pre-fabricated silicone molds, and surface smoothness was ensured. The casting process was carried out at room temperature, and the composite specimens were left to cure for approximately 30 minutes. After curing, the specimens were carefully removed from the molds, surface burrs were cleaned, and the samples were made suitable for mechanical testing. In this way, structurally intact and testable composite specimens, compliant with standards, were obtained.

Figure 3. Composite specimens produced with 1%, 3%, and 5% fiber content

3. Results and Discussion

3.1. Tensile Test Results

The tensile tests demonstrated that palm fiber reinforcement had a positive effect on the tensile strength of polyurethane composites. As shown in Figure 4, neat polyurethane (PU) reached a maximum tensile stress of 13.107 MPa, while the specimen containing 1% PF achieved 16.164 MPa. The highest strength was recorded at 3% PF reinforcement, with a value of 17.676 MPa, whereas the specimen containing 5% PF exhibited 16.487 MPa, which was still superior to neat PU.

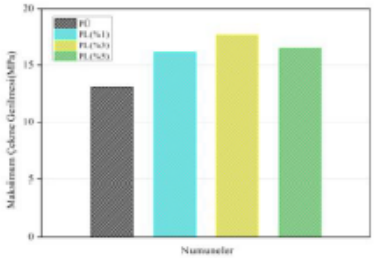

Figure 4. Maximum tensile stress (MPa) of composite specimens with different palm fiber contents

When the stress–strain curves in Figure 5 are examined, the neat PU specimen exhibited the highest strain capacity and demonstrated ductile behavior. In contrast, the reinforced specimens achieved higher stress values but fractured at lower strains. In particular, the specimen with 3% PF reinforcement displayed the highest stress capacity, indicating an improvement in strength.

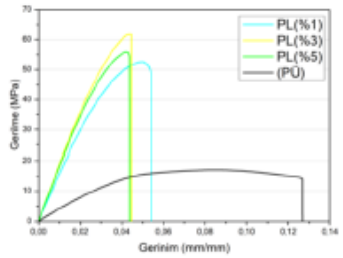

Figure 5. Stress–strain curves of composite specimens with different palm fiber contents

The findings obtained from the force–elongation curves in Figure 6 also support this situation. Although neat PU exhibited greater elongation, the force it could withstand was lower. In the reinforced specimens, particularly at 3% reinforcement, both the load-bearing capacity and stiffness of the material increased. However, the elongation capacity decreased slightly.

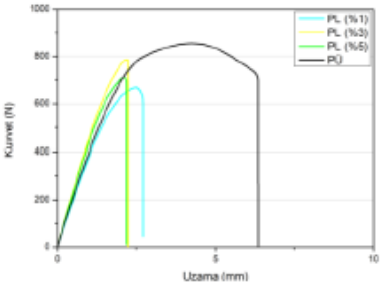

Figure 6. Force–elongation curves of composite specimens with different palm fiber contents

3.2. Three-point bending test

Three-point bending tests revealed that palm fiber reinforcement enhanced the flexural strength of the composites. As shown in Figure 7, the neat PU sample reached a flexural stress of 27.315 MPa, while this value increased to 39.981 MPa with 1% PF and 42.223 MPa with 3% PF. The highest value was obtained with 5% PF reinforcement, reaching 50.914 MPa. This increase indicates a significant improvement in flexural strength with higher fiber content..

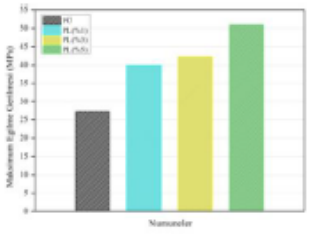

Figure 7. Maximum flexural stress (MPa) of composite specimens with different palm fiber contents

The force–elongation curves presented in Figure 8 illustrate the deformation behavior of the composites. While the neat PU sample exhibited ductile behavior with high elongation capacity, the reinforced samples withstood higher forces but fractured at lower elongation values. This indicates that fiber reinforcement increases stiffness while reducing ductility. In particular, the sample containing 5% PF carried the highest force during bending and reached the maximum stress level.

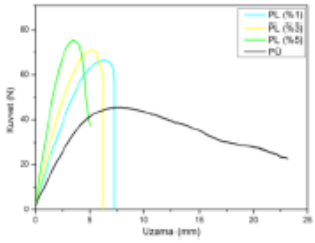

Figure 8. Bending test force–elongation curves of composite specimens with different palm fiber contents

3.3. Charpy Impact Test Results

Charpy impact tests demonstrated that palm fiber reinforcement enhanced the impact energy absorption capacity of the composites. As shown in Figure 9, the neat PU sample exhibited an impact strength of 27.317 kJ/m², which increased to 37.645 kJ/m² with 1% PF and 38.487 kJ/m² with 3% PF. The highest impact strength was obtained with 5% PF reinforcement, reaching 43.632 kJ/m².

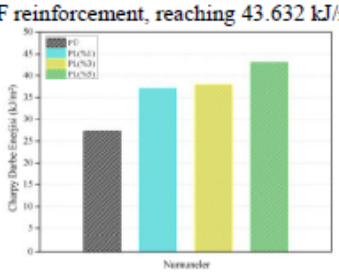

Figure 9. Charpy impact energy (kJ/m²) of composite specimens with different palm fiber contents

3.4. ANSYS simulation results

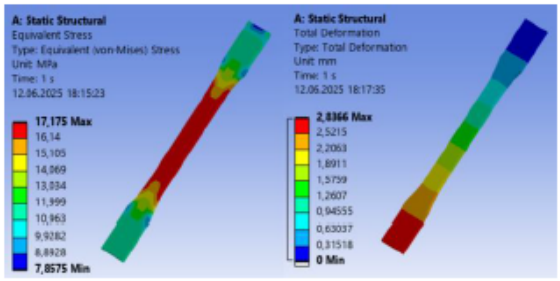

Figure 10. Equivalent stress (von Mises) and total deformation analysis of the tensile specimen reinforced with 3% palm fiber in ANSYS

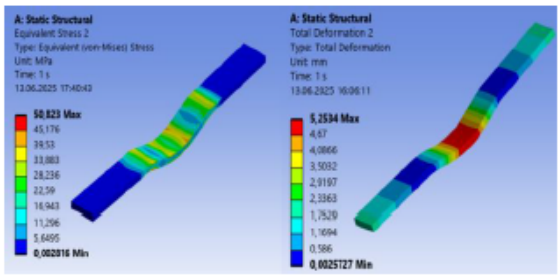

Figure 11. Equivalent stress (von Mises) and total deformation analysis of the 5% palm fiber-reinforced three-point bending specimen in ANSYS

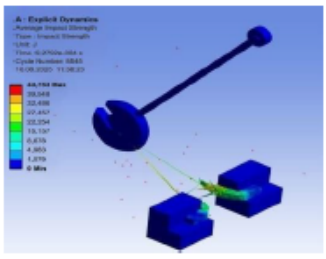

Figure 12.ANSYS Explicit Dynamics simulation of the Charpy impact test for the 5% palm fiber-reinforced composite specimen

4. Conclusion

In this study, aiming for sustainable and eco-friendly composite production, the usability of palm tree fibers as reinforcement in polyurethane-based polymer matrix composites was investigated through experimental and numerical methods. The effects of fiber contents (1%, 3%, and 5%) on mechanical properties were evaluated, and the findings were supported by ASTM standard tests and ANSYS analyses. Tensile tests revealed that the specimen with 3% fiber achieved the highest strength of 17.676 MPa, providing a 35% increase compared to neat polyurethane. Three-point bending tests showed that the specimen with 5% fiber reached 50.914 MPa, representing an 86% increase over the unreinforced sample. Charpy impact tests demonstrated that with 5% reinforcement, an energy absorption capacity of 43.632 kJ/m² was achieved, indicating a 57% higher impact strength compared to the neat sample.

References

[1] Karaca Uğural, B., "Gürültü bariyeri için çevre dostu alternatif: Doğal elyaf takviyeli kompozit malzemeler. " Avrupa Bilim ve Teknoloji Dergisi, vol. 32, pp. 1006–1010, 2021.
[2] Kaya, A. İ., "Kompozit malzemeler ve özellikleri. "Putech & Composite Poliüretan ve Kompozit Sanayi Dergisi, vol. 29, pp. 38(45), 2016.
[3] Çelik, O. "Karbon fiber kompozitlere alternatif olarak doğal fiber takviyeli hibrit kompozit malzemelerin özellikleri." Yüksek lisans tezi, Eskişehir Teknik Üniversitesi. 2020.
[4] Afgan, S., Ullah, N., Sulaiman, M., Ali, I., Iqbal, T., Younas, M., & Rezakazemi, M. "High strength insulating polymeric composite based on recycled/virgin polyethylene terephthalate (PET) reinforced with hydrous magnesium silicate (talc). " Journal of Materials Research and Technology, vol. 21, pp. 3579–3593, 2022
[5] Ishak, M. R., et al. ''Mechanical properties of oil palm fibre-reinforced polymer composites.''Journal of Natural Fibers, vol. 18-1, pp. 1(17), 2021.
[6] Muniandy, S. K., et al. ''Sugar palm lignocellulosic fiber reinforced polymer composite.'' Journal of Fibers and Polymer Composites, vol.1(1), pp. 1–19, 2022.
[7] Latiff, A. S. M., et al. ''Mechanical properties of benzoylation treated sugar palm fiber and its composite.'' International Journal of Recent Technology and Engineering, vol.8(5), pp. 4248–4252, 2020.
[8] Atiqah, A., et al. ''Effect of alkali and silane treatments on mechanical and interfacial bonding strength of sugar palm fibers with thermoplastic polyurethane.'' Journal of Natural Fibers, vol.15(2), pp. 251–261, 2018.
[9] Saravana, A., et al. ''Mechanical properties of alkali-treated Carica papaya fiber-reinforced epoxy composites.'' Journal of Natural Fibers, vol. 19(2), pp. 269–279, 2020.
[10] Kamarudin, S. H., et al. ''Natural fiber reinforced polymer composites (NFRPC) for sustainable industrial applications.''Polymers, vol. 14(17), pp. 3698, 2022.
[11] Thompson, C., González, C., & Llorca, J. ''Material extrusion fabrication of continuous metal wire-reinforced polymer–matrix composites.'' Composites Part A: Applied Science and Manufacturing, vol. 140, pp.106-171, 2021.

EVALUATION OF BRAZILIAN ESPRESSO WASTE AS A REINFORCEMENT MATERIAL IN THE PRODUCTION OF WOOD-LIKE POLYURETHANE MATRIX COMPOSITES

Kadir ASLAN[1], Lokman YÜNLÜ[2], Serkan ATEŞ[2]

[1] Department of Mechanical Engineering, Faculty of Engineering and Architecture, Burdur Mehmet Akif Ersoy University, Burdur, Turkey – 0009-0003-5453-4390

kadirraslaan16@mail.com

2 Department of Mechanical Engineering, Division of Construction and Manufacturing, Faculty of Engineering and Architecture, Burdur Mehmet Akif Ersoy University, Burdur, Türkiye 0000-0003-1625-995X
lyunlu@mehmetakif.edu.tr

2 Department of Mechanical Engineering, Division of Construction and Manufacturing, Faculty of Engineering and Architecture, Burdur Mehmet Akif Ersoy University, Burdur, Türkiye 0000-0002-5858-5190
sates@mehmetakif.edu.tr

ABSTRACT

Composite materials are multiphase engineering products obtained by combining at least two components with different properties. In this study, the utilization of organic waste generated from Brazil espresso production as a reinforcement material in wood-like polyurethane matrix composites was investigated. The waste, ground into fine powder, was mixed homogeneously with the polyurethane matrix at ratios of 5%, 10%, 15%, 20%, and 25% using a mechanical mixer, and the composite specimens were produced by casting into silicone molds. Mechanical tests revealed that the highest tensile, flexural, and impact strength values were achieved at the 5% reinforcement ratio. The carbon-based structure of the Brazil espresso waste and the flexibility of the polyurethane enhanced the mechanical performance of the composite system. This study offers significant contributions in terms of environmentally friendly material production and the valorization of industrial waste.

Keywords: Brazil Espresso, Polyurethane, Sustainability, Composite Material

1.INTRODUCTION

Industrialization and technological advancements have significantly increased energy and raw material consumption, leading to global challenges such as climate change, environmental pollution, and resource scarcity [1, 2]. In this context, the development of environmentally friendly, cost-effective, and recyclable materials in line with sustainability principles has gained critical importance. Composite materials stand out with advantages such as lightness, strength, and thermal resistance, while polymer matrix composites, particularly polyurethane (PU), are widely utilized due to their high mechanical and chemical durability [3].The innovative aspect of this study lies in the utilization of Brazilian espresso waste as a reinforcement material. Globally, millions of tons of coffee consumption generate substantial amounts of this by-product [4, 5]. Rich in cellulose and phenolic compounds, these wastes can be processed into functional reinforcement elements for composites [6]. Thus, both waste recovery and the production of sustainable, cost-efficient materials are achieved, while also contributing to domestic manufacturing strategies and the development of environmentally friendly alternatives.

2.MATERIALS AND METHODS

In this study, commercially available polyurethane resin was used as the matrix material, while Brazilian espresso waste served as the reinforcement. Based on the literature, reinforcement ratios were determined in the range of 5–25% with 5% increments; thus, composites were prepared with ratios of 95–5, 90–10, 85–15, 80–20, and 75–25, respectively.The Brazilian espresso waste obtained after brewing was naturally dried for one week at room temperature in a well-ventilated environment without any chemical treatment. This process aimed to remove free moisture, thereby improving interfacial bonding with the matrix and preventing defects during curing. The dried waste was sieved to achieve a homogeneous particle size and then mixed with the polyurethane matrix in the specified proportions.The molds for specimen preparation were designed in accordance with ASTM D638 (tensile), ASTM D790 (bending), and ASTM D256 (impact) standards using SolidWorks software

(Figure 1) and produced with a 3D printer (Figure 2). Silicone-based molds were subsequently fabricated from these prototypes.

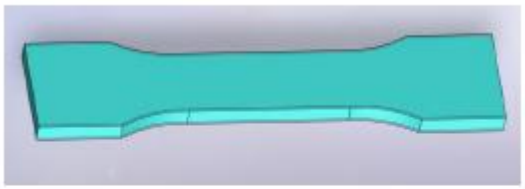

Figure 1. Mold design created using SolidWorks software.

The homogenized mixtures were cast into the silicone molds, and the specimens were kept at room temperature for 1 hour before demolding. They were then cured under ambient conditions for 10 days to ensure complete polymerization and enhanced mechanical properties. After curing, the specimens were prepared for mechanical testing in compliance with the relevant ASTM standards (Figure 3).

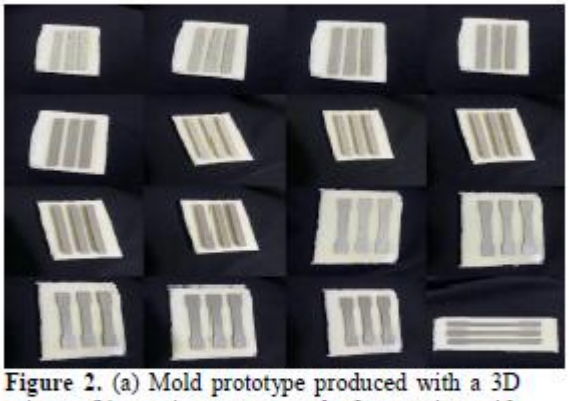

Figure 2. (a) Mold prototype produced with a 3D printer; (b) specimens prepared after casting with Brazilian espresso waste.

3. RESULTS AND DISCUSSION

Tensile Test

The tensile test is applied to evaluate the elastic–plastic behavior, strength, and ductility of materials. In this study, the specimens were prepared and tested in accordance with ASTM D638. During the experiments, the maximum tensile stress and elongation at break were determined, ensuring both the reliability of the results and their comparability with the literature.

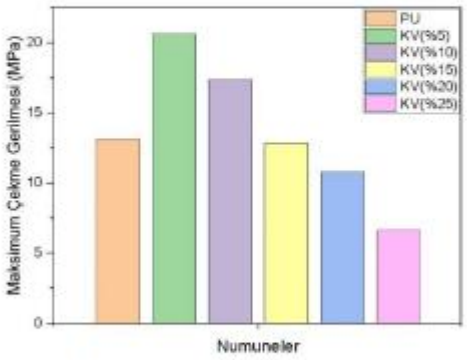

Figure 4. Graph of tensile test results for composite material reinforced with Brazilian espresso waste.

Stress–strain graph of composites reinforced with 5% Brazilian espresso waste.

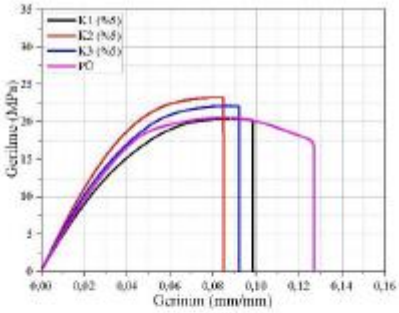

Figure 5. Stress–strain graph of composite reinforced with 5% Brazilian espresso waste.

Force–elongation graphs of composites reinforced with 5% Brazilian espresso waste.

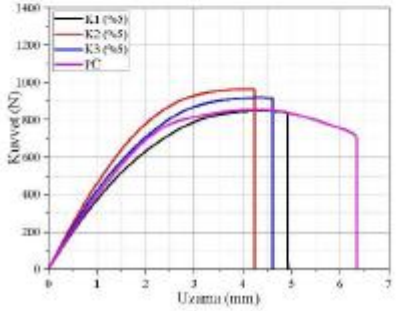

Figure 6. Force–elongation graph of composite reinforced with 5% Brazilian espresso waste.

Flexural Test

The three-point bending test is a mechanical testing method applied to determine the flexural strength of a material. In this study, the composite specimens were prepared in accordance with ASTM D790 and subjected to three-point bending tests. The specimens were cut to the standard dimensions, and the tests were performed accordingly. This procedure ensured the reliability of the obtained data and its comparability with the literature.

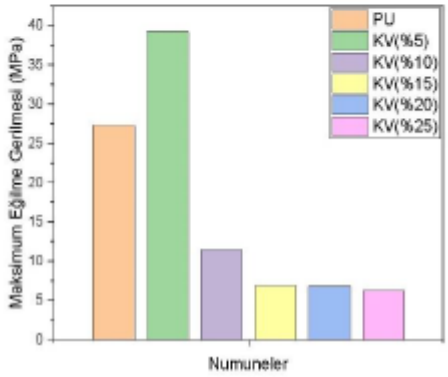

Figure 7. Flexural stress values of wood-like polyurethane matrix composites reinforced with Brazilian espresso waste at different reinforcement ratios.

Impact Test

The notched impact test is a mechanical testing method applied to determine the fracture resistance of a material under sudden and impact-type loadings. In this study, the specimens were prepared in accordance with ASTM D256 and subjected to notched impact testing. The specimens, notched to standard dimensions, were tested at room temperature. This test was conducted to evaluate the effect of quartz powder reinforcement on the impact performance of polyurethane matrix composites.

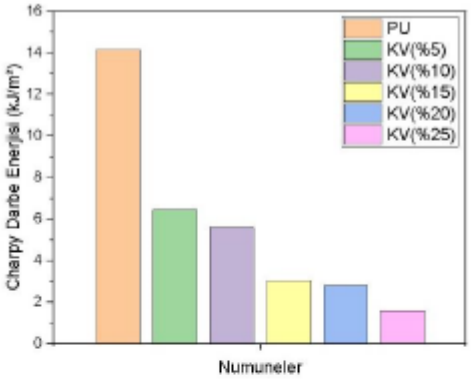

Figure 8. Impact energy values of wood-like polyurethane matrix composites reinforced with Brazilian espresso waste at different reinforcement ratios.

ANSYS Analysis Results

Tensile Test Analysis

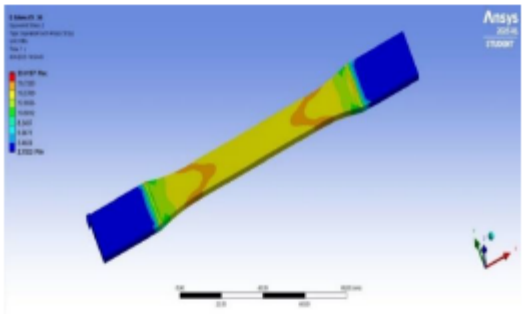

Figure 9. ANSYS analysis of composite material reinforced with 5% Brazilian espresso waste.

Three-Point Bending Test Analysis

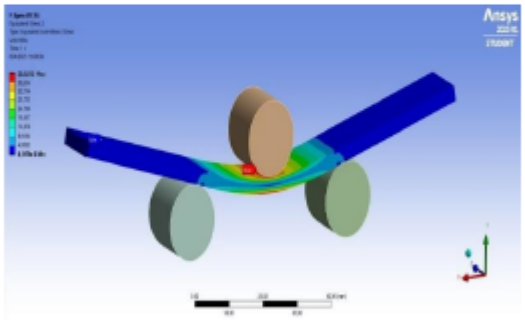

Figure 10. ANSYS analysis of composite material reinforced with 5% Brazilian espresso waste.

Analysis of Notched Impact Test

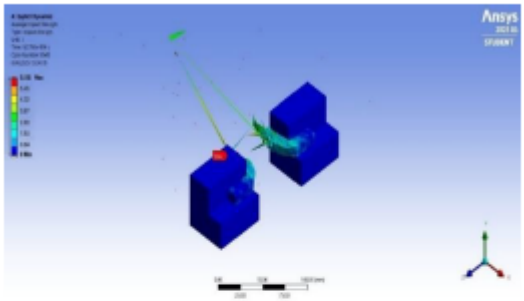

Figure 11. ANSYS analysis of composite material reinforced with 5% Brazilian espresso waste.

Comparison of Results

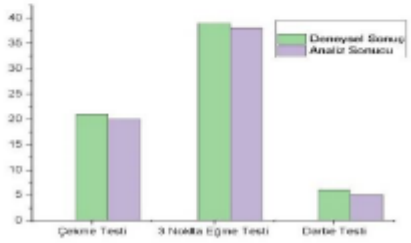

Figure 11. Comparison of results.

4.CONCLUSION

In this study, Brazilian espresso waste was used as a reinforcement material in wood-like polyurethane matrix composites. Specimens with reinforcement ratios of 5–25% were prepared and tested according to ASTM D638, ASTM D790, and ASTM D256 standards. The results showed that at 5% reinforcement, the tensile strength reached ≈21 MPa and the flexural strength ≈39 MPa; however, at higher reinforcement ratios, the mechanical performance decreased. At 25% reinforcement, the tensile strength dropped to ≈7 MPa and the impact energy to ≈1.5 kJ/m². These findings indicate that Brazilian espresso waste can improve composite performance at low contents, whereas higher amounts lead to brittleness and reduced strength.

Similarly, the literature reports that natural waste powders can enhance the mechanical properties of polymer composites. Prabhu [7] studied coconut shell powder, Salih et investigated rice husk ash, and Olaitan [8] examined peanut shell powder, all reporting the best performance at low to moderate reinforcement ratios. Thus, these findings also support the present study.

5.REFERENCES

1.Marmolejo, L. F., Díaz, L. F., Torres, P., & García, M. (2012). Perspectives for sustainable resource recovery from municipal solid waste in developing countries: Practices and alternatives. In Waste Management – An Integrated Vision (pp. 153–166).

2. Yücel, M., & Ekmekçiler, Ü. S. (2008). A holistic approach to the concept of environmentally friendly products: Clean production system, eco-label, and green marketing. Electronic Journal of Social Sciences, 7(26), 320–333.

3. Engels, H. W. (2013). Polyurethanes: Versatile materials and sustainable problem solvers for today's challenges. Angewandte Chemie International Edition, 52(36), 9422–9441.

4. Delavarde, A., Savin, G., Derkenne, P., Boursier, M., Morales-Cerrada, R., Nottelet, B., ... & Caillol, S. (2024). Sustainable polyurethanes: toward new cutting-edge opportunities. *Progress in Polymer Science*, *151*, 101805.

5. Barbero, S., & Fiore, E. (2015). The flavours of coffee grounds: The coffee waste as accelerator of new local businesses. *ANNALS of Faculty Engineering Hunedoara-International Journal of Engineering*, *13*(1), 57-63.

6. Ravindran, R., Desmond, C., Jaiswal, S., & Jaiswal, A. K. (2018). Optimisation of organosolv pretreatment for the extraction of polyphenols from spent coffee waste and subsequent recovery of fermentable sugars. *Bioresource Technology Reports*, *3*, 7-14.

7. Prabhu, R., Rahul, M. P., Aeilias, A., Sunny, B., Alok, J., & Bhat, T. (2017). Investigation of tribological property of coconut shell powder filled epoxy glass composites. *Ame J Mater Sci*, *7*(5), 174-184.

8. Olaitan, A. J., Terhemen, A., King, G., & Oluwatoyin, O. (2017). Comparative assessment of mechanical properties of groundnut shell and rice husk reinforced epoxy composites. *Am. J. Mech. Eng*, *5*(3), 76-86.

MECHANICAL PROPERTIES AND ENVIRONMENTAL AGING BEHAVIOR OF NANOCLAY REINFORCED POLYMER COMPOSITES

Deniz Aktas [1], Hacı Abdullah Tasdemir [1]

[1]Istanbul Technical University, Department of Mechanical Engineering, 34437, Istanbul, Turkiye

Keywords: Polymer nanocomposites, environmental aging, nanoclay reinforcement

Abstract

In this study, polycarbonate (PC), acrylonitrile butadiene styrene (ABS), and PC/ABS blends were reinforced with 1%, 3%, and 5% nanoclay via melt compounding. Mechanical properties were evaluated through Shore D hardness (unaged), three-point bending, and Charpy impact tests (on aged and unaged specimens). Chemical aging was simulated by immersing samples in methanol and sodium lauryl ether sulfate (SLES) for up to 240 hours. Compared to their neat counterparts, hardness increased consistently with nanoclay loading across systems. Aging led to distinct degradation trends depending on matrix type and environment. PC-based composites exhibited notable loss in impact strength and moderate changes in modulus under methanol exposure, while ABS composites maintained impact performance and partially recovered stiffness over time. PC/ABS blends demonstrated the most balanced aging resistance, especially at low nanoclay concentrations. The results highlight how matrix selection and nanofiller concentration govern the durability of polymer nanocomposites in aggressive environments.

1. Introduction

Polymer composites have become essential engineering materials in modern industries due to their high strength to weight ratio, tunable properties, and ease of processing. Among them, amorphous thermoplastics such as polycarbonate (PC), acrylonitrile butadiene styrene (ABS), and their blends (PC/ABS) are extensively used in automotive, electronic, and consumer applications. These polymers offer an excellent balance of stiffness, toughness, and dimensional stability, yet their long term performance can be significantly compromised under environmental factors such as chemical exposure or thermal oxidation [1,2]. One of the most critical degradation mechanisms in polymers is environmental aging. This process involves exposure to aggressive solvents, surfactants, or humid conditions, which can trigger plasticization, chain scission, and ultimately environmental stress cracking (ESC). For example, methanol or isopropanol can rapidly degrade polycarbonate (PC) and other glassy polymers such as poly(methyl methacrylate) and polystyrene, leading to micro-cracking and embrittlement under stress [3,4]. Blends such as PC/ABS and polymers like ABS also exhibit sensitivity to environmental degradation, especially when used in chemically demanding service conditions [5].

To mitigate the detrimental effects of environmental aging, recent research has highlighted the potential of nanofiller incorporation as an effective strategy. For instance, halloysite nanotube (HNT)-reinforced PA6 nanocomposites (≈4 wt% APTES-functionalized HNT) exhibited reduced water uptake and preserved molecular weight and visco-rheological properties even after prolonged hydrothermal aging (1680 h), thereby demonstrating improved durability under moisture-driven degradation [6]. Similarly, the introduction of organically modified montmorillonite (OMMT) into cross-linked polyethylene (XLPE) has been shown to mitigate water-tree aging, as evidenced by lower initiation probability and shorter tree lengths compared to neat polyethylene systems [7]. These findings confirm that nanofillers not only enhance the barrier performance of polymer matrices but also play a crucial role in extending service life under chemically and moisture-induced aging conditions.

The present study aims to provide a systematic evaluation of the mechanical performance and environmental aging behavior of nanoclay-reinforced PC, ABS, and PC/ABS composites. To this end, three different nanoclay loadings (1, 3, and 5 wt%) were incorporated into the matrices, and Shore D hardness, flexural strength, and Charpy impact tests were conducted on both unaged and chemically aged specimens. Aging environments included methanol and sodium lauryl ether sulfate (SLES), chosen to represent polar solvent and surfactant-induced degradation, respectively. By directly comparing different polymer matrices and nanoclay concentrations, this work seeks to clarify how filler loading influences stiffness and impact retention under aggressive environments. Through this approach, the study not only extends recent findings on nanofiller-assisted durability, but also provides new insights into the design of chemically robust nanocomposites for demanding industrial applications.

2. Experimental Procedure

2.1. Materials

Polycarbonate (PC), acrylonitrile butadiene styrene (ABS), and a commercial PC/ABS blend were employed as base matrices for nanocomposite preparation. The PC grade was SABIC's LEXAN™ EXL 9330 with a density of 1.19 g/cm³. The PC/ABS blend was Bayblend® T65 XF (Covestro) with a density of 1.13 g/cm³, and the ABS matrix was CYCOLAC™ MG47F (SABIC) with a density of 1.04 g/cm³. The nanofiller used in this study was EsanNANO 1-140 (Esan Eczacıbaşı Industrial Raw Materials, Turkey), an organically modified montmorillonite (MMT), was incorporated into these polymers at loading levels of 1, 3, and 5 wt%. All materials were used as received without further purification, and polymer granules were dried prior to compounding according to supplier recommendations to minimize moisture-induced degradation.

2.2. Nanocomposite Preperation

Nanocomposites based on PC, ABS, and PC/ABS matrices were prepared by melt compounding with a lab-scale twin-screw extruder (Gulnar Machine, Turkey; screw diameter 16 mm, L/D ratio 40). The extrusion process was performed at a screw speed of 150 rpm, with barrel temperatures set between 240 and 260 °C from the feeding zone to the die. Organically modified montmorillonite (MMT, EsanNANO 1-140) was incorporated at loading levels of 1, 3, and 5 wt%. Sample notations and compositions are defined in Table 1.

Table 1. Sample notation and compositions

Compositions	Sample Code	Nano filler ratio (wt%)
PC	1	0
	1B1	1
PC+MMT	1B3	3
	1B5	5
PC/ABS	2	0
	2B1	1
PC/ABS+MMT	2B3	3
	2B5	5
ABS	3	0
	3B1	1
ABS+MMT	3B3	3
	3B5	5

The granules were molded into standard test specimens using a Yuhdak vertical injection molding machine. Injection molding was conducted at a barrel temperature of 260 °C and a mold temperature of 50 °C, with an injection speed of 100 mm/s. Flexural, and notched Charpy impact specimens were prepared according to BS ISO 178, and BS ISO 179-1/2eA standards, respectively.

2.3. Chemical Aging Protocol

The aging behavior of the specimens was investigated by immersing them in two chemically aggressive media. Methanol was chosen as a representative polar solvent, widely recognized for its strong interaction with polymer chains and its ability to accelerate aging related degradation phenomena in glassy matrices. In parallel, an aqueous solution of sodium lauryl ether sulfate (SLES) was employed to simulate surfactant rich conditions, thereby reflecting environments relevant to detergent exposure and household cleaning applications. All specimens were fully immersed at ambient temperature for a maximum of 240 hours. At predetermined intervals (72, 120, and 240 hours), samples were carefully removed, dried to eliminate residual surface liquid, and subsequently subjected to mechanical characterization.

2.4. Mechanical Testing

The surface hardness of the specimens was evaluated with a MACRONA durometer according to ISO 868 standard. For each specimen, ten different points were measured across the sample surface, and the mean values were taken as representative.

Flexural strength was assessed through three-point bending tests using a universal testing machine (Shimadzu AG-X Plus) at room temperature. The crosshead displacement rate was maintained at 1.5 mm/min, with a support span of 64 mm. Stress–strain curves were obtained directly from the testing software, and flexural properties were determined in accordance with the relevant standards. A minimum of five replicates per composition were tested to ensure reproducibility, and averaged results are reported.

Impact behavior was determined using a Charpy impact tester (Devotrans DVT CD D 50IC, Turkey) with notched specimens prepared in accordance with ISO 179-1. The equipment was fitted with a pendulum having a drop angle of 150°, a maximum height of 755.7 mm, and an impact velocity of 3.8 m/s. A 6-J impact hammer was employed for precise measurements. The impact strength (a_{cN}, kJ/m²) was calculated from the absorbed energy during fracture using:

$$a_{cN} = \frac{W_c}{hb_N} * 10^3 \quad (1)$$

where W_c (J) is the corrected energy absorbed during fracture, h (mm) is the thickness of the specimen, and b_N (mm) is the remaining width of the specimen after notching.

3. Results and Discussion

3.1. Effect of Nanoclay on Hardness

Shore D hardness measurements on the unaged specimens revealed distinct responses of the three polymer systems to nanoclay incorporation. For the PC matrix, the addition of nanoclay led to a noticeable increase in hardness at 3 wt%, while a slight reduction was observed at 5 wt%, suggesting that moderate filler loadings promote effective reinforcement, whereas higher concentrations may induce partial agglomeration and limit chain packing. In the PC/ABS system, improvements were also evident at 1 and 3 wt% loadings, but the hardness dropped markedly at 5 wt%, indicating that excess filler can disturb the multiphase morphology and weaken interfacial compatibility. In the ABS matrix, the incorporation of nanoclay increased hardness compared to the neat polymer; however, values obtained at 1, 3, and 5 wt% were very close to each other, indicating that beyond the initial reinforcement effect, further additions of nanoclay did not produce a significant incremental change. This suggests that the stiffening effect in ABS may quickly reach a saturation level, after which additional filler does not meaningfully alter the surface rigidity.

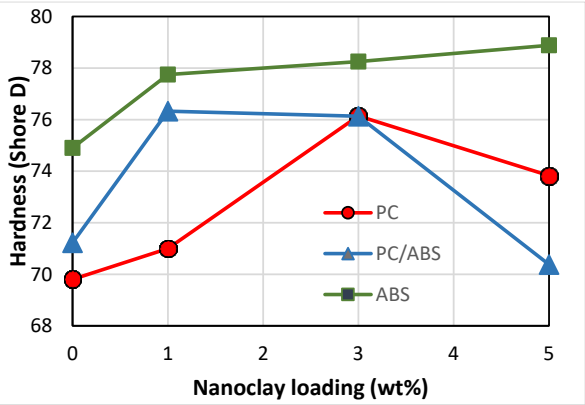

Figure 1. Shore D hardness of PC, ABS, and PC/ABS nanocomposites as a function of nanoclay loading.

3.2. Flexural Properties Before and After Aging

Three-point bending tests demonstrated that the incorporation of nanoclay enhanced the flexural modulus of all three polymer systems in their unaged state, with the most pronounced improvement observed in polycarbonate (PC) and PC/ABS blends. This outcome reflects the high stiffness of the PC rich matrices, where rigid clay platelets can more effectively restrict chain mobility and reinforce load transfer. The increase in modulus was accompanied, however, by a reduction in strain at yield, particularly at higher clay contents, indicating a stiffening effect at the expense of ductility.

When subjected to chemical aging, the response of the composites showed strong dependence on both the polymer matrix and the aging medium. In methanol, a pronounced deterioration in flexural properties was observed across all systems. PC-based samples, which initially exhibited the highest stiffness, suffered severe modulus loss together with a drastic reduction in yield stress and strain. The effect was particularly strong at higher nanoclay loadings, where instead of providing a barrier effect, the rigid filler appeared to accelerate embrittlement, most likely by promoting local stress concentrations and facilitating microcrack initiation under solvent induced plasticization. Interestingly, formulations containing 3 wt% nanoclay showed relatively less severe modulus loss compared to 1 wt% and 5 wt%, suggesting that a balance between barrier action and filler-induced brittleness may exist at intermediate loadings.

In contrast, aging in SLES solution produced milder effects. While reductions in modulus and yield stress were still detected, the magnitude of deterioration was smaller compared to methanol exposure. Moreover, certain ABS-based nanocomposites exhibited partial stabilization of flexural modulus with prolonged immersion, which may be attributed to mild surfactant induced swelling leading to stress relaxation or secondary ordering effects in the amorphous domains. Overall, SLES aging proved less aggressive, allowing nanoclay reinforcement to retain part of its mechanical benefit.

These results indicate that while nanoclay incorporation improves the flexural stiffness of amorphous thermoplastics in the unaged state, its effectiveness under chemical aging is highly environment and composition dependent. PC and PC/ABS systems benefited most from moderate clay additions, particularly under SLES exposure, whereas methanol immersion revealed the strong susceptibility of rigid, clay filled structures to solvent induced embrittlement. The detailed stress-strain responses together with the corresponding values of yield stress, yield strain, and Young's modulus for all compositions are presented in the following figures and tables.

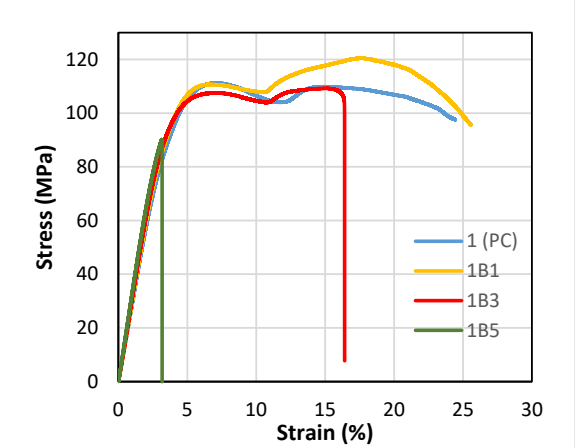

Figure 2. Stress–strain curves of neat PC and PC nanocomposites with 1, 3, and 5 wt% nanoclay in the unaged state.

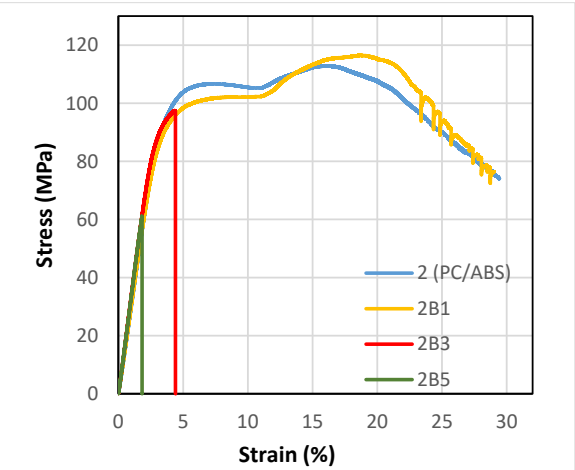

Figure 3. Stress–strain curves of neat PC/ABS and PC/ABS nanocomposites with 1, 3, and 5 wt% nanoclay in the unaged state.

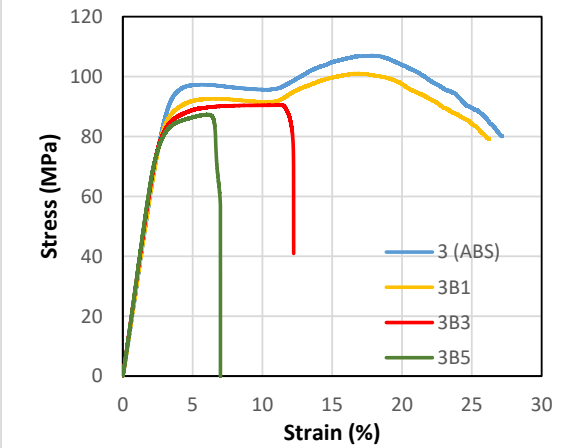

Figure 4. Stress–strain curves of neat ABS and ABS nanocomposites with 1, 3, and 5 wt% nanoclay in the unaged state.

Table 2. Mechanical properties of samples without chemical exposure

Samples	Young Modulus (GPa)	Strain at Yield (%)	Yield Stress (MPa)
1	1.88	6.0	110
1B1	1.96	6.0	111
1B3	1.98	5.7	108
1B5	2.46	3.0	86
2	1.98	6.13	105
2B1	1.93	6.2	101
2B3	2.10	3.9	95
2B5	2.55	1.7	53
3	1.98	5.3	97
3B1	1.89	5.1	93
3B3	1.80	5.0	88
3B5	1.77	4.2	85

Table 3. Mechanical properties of samples exposed to SLES aqueous solution for 72 hours.

Samples	Young Modulus (GPa)	Strain at Yield (%)	Yield Stress (MPa)
1	1.82	5.2	107
1B1	1.96	6.2	111
1B3	1.97	5.6	107
1B5	2.42	2.5	74
2	1.95	5.4	101
2B1	2.00	5.5	102
2B3	1.94	3.9	92
2B5	2.43	1.8	41
3	1.89	4.1	91
3B1	1.86	4.1	88
3B3	1.79	4.1	86
3B5	1.75	3.5	82

Table 4. Mechanical properties of samples exposed to SLES aqueous solution for 120 hours.

Samples	Young Modulus (GPa)	Strain at Yield (%)	Yield Stress (MPa)
1	1.89	6.4	109
1B1	1.99	5.8	109
1B3	2.07	3.9	101
1B5	2.50	1.9	64
2	1.99	5.3	102
2B1	1.96	5.2	100
2B3	2.54	2.9	87
2B5	2.57	1.8	58
3	1.92	4.6	93
3B1	1.87	4.4	90
3B3	1.79	4.0	85
3B5	1.75	3.4	82

Table 5. Mechanical properties of samples exposed to SLES aqueous solution for 240 hours.

Samples	Young Modulus (GPa)	Strain at Yield (%)	Yield Stress (MPa)
1	1.92	6.2	109
1B1	2.02	6.0	110
1B3	1.93	6.2	109
1B5	1.94	4.2	98
2	1.99	5.6	103
2B1	2.09	5.1	106
2B3	2.01	5.9	104
2B5	1.87	6.1	108
3	1.85	4.3	90
3B1	1.96	4.7	94
3B3	1.96	4.8	95
3B5	1.80	4.7	87

Table 6. Mechanical properties of samples exposed to methanol for 72 hours.

Samples	Young Modulus (GPa)	Strain at Yield (%)	Yield Stress (MPa)
1	1.70	6.5	100
1B1	1.66	4.8	89
1B3	1.64	3.5	64
1B5	1.38	2.3	37
2	1.71	6.1	91
2B1	1.56	5.1	81
2B3	1.74	3.0	59
2B5	1.65	1.8	41
3	1.24	5.1	62
3B1	1.25	5.5	62
3B3	1.21	5.1	59
3B5	1.16	5.0	57

Table 7. Mechanical properties of samples exposed to methanol for 120 hours.

Samples	Young Modulus (GPa)	Strain at Yield (%)	Yield Stress (MPa)
1	1.87	6.2	106
1B1	1.21	3.3	56
1B3	1.11	1.1	16
1B5	0.81	1.0	11
2	1.96	5.4	101
2B1	1.67	3.3	58
2B3	1.06	1.2	16
2B5	0.75	0.9	10
3	1.82	5.0	91
3B1	1.79	5.1	89
3B3	1.70	4.8	87
3B5	1.71	4.3	84

Table 8. Mechanical properties of samples exposed to methanol for 240 hours.

Samples	Young Modulus (GPa)	Strain at Yield (%)	Yield Stress (MPa)
1			
1B1	1.6	3.6	77
1B3	1.26	2.8	69
1B5	0.47	1.9	22
2	1.68	5.3	84
2B1	1.72	4.3	84
2B3	1.17	3.7	59
2B5	0.85	1.2	37
3	1.64	4.9	86
3B1	1.60	5.0	78
3B3	1.65	4.4	80
3B5	1.47	4.6	72

3.3. Charpy Impact Strength and Environmental Degradation

The impact strength results revealed a consistent reduction in toughness upon nanoclay incorporation across all three polymer systems. In PC, the loss was particularly severe at higher filler loadings, while in PC/ABS and ABS the decline was less pronounced but still significant. This behavior reflects the stiff, plate like nature of nanoclay, which constrains molecular mobility and introduces local stress concentrations, thereby suppressing energy dissipating mechanisms such as shear yielding and crazing. In the multiphase PC/ABS system, the deterioration is likely exacerbated by disruption of the rubber phase morphology, whereas in ABS the reduction tends to plateau beyond low filler levels, suggesting that the initial stiffening effect dominates and further additions provide diminishing influence. These observations are consistent with the well-known stiffness toughness trade-off in polymer nanocomposites [8].

Following 240 h of methanol exposure, all polymer systems exhibited an increase in impact toughness compared to their unaged state. This unexpected trend can be attributed to the pronounced plasticizing effect of methanol, which penetrates into the amorphous regions of the polymers, enhances chain mobility, and facilitates localized energy dissipation under impact. Even in the presence of nanoclay, where a stiffening effect is normally expected, the solvent induced plasticization dominated the mechanical response, leading to higher impact resistance than in the unaged samples. These findings highlight that prolonged solvent exposure does not always result in simple embrittlement, but under certain conditions may temporarily improve toughness due to molecular-level relaxation phenomena. This apparent recovery at 240 h reflects the competing effects of nanoclay-induced stress localization and methanol-driven plasticization.

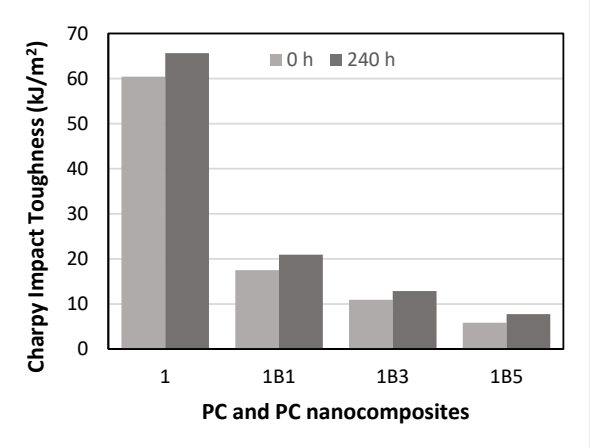

Figure 5. Charpy impact toughness of neat PC and PC nanocomposites in the unaged state and after 240 h of methanol immersion.

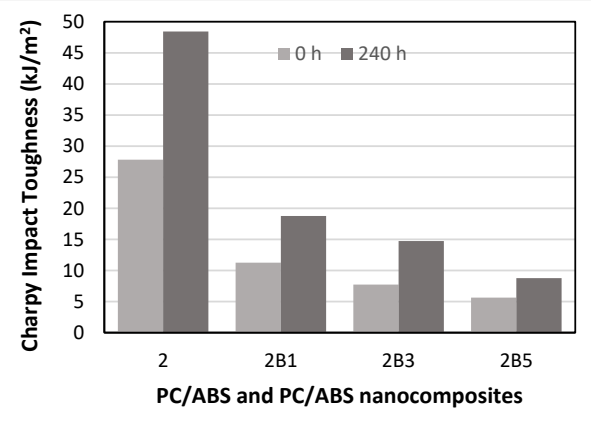

Figure 6. Charpy impact toughness of neat PC/ABS and PC/ABS nanocomposites in the unaged state and after 240 h of methanol immersion.

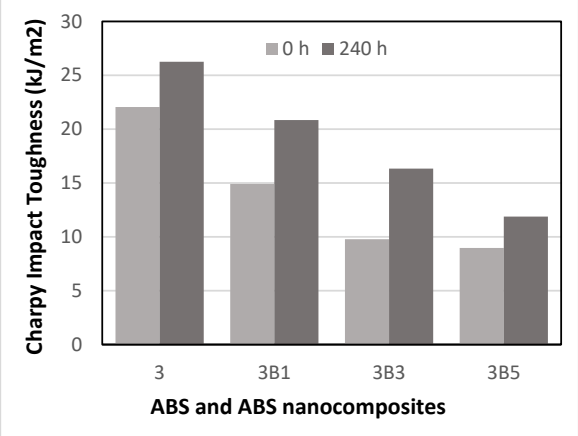

Figure 7. Charpy impact toughness of neat ABS and ABS nanocomposites in the unaged state and after 240 h of methanol immersion.

4. Conclusion

This study demonstrated that nanoclay reinforcement effectively enhanced the stiffness of PC, ABS, and PC/ABS matrices in their unaged state, although this improvement was accompanied by a reduction in ductility and impact toughness, consistent with the classical stiffness toughness trade-off in polymer composites. After 240 h of methanol exposure, an unexpected increase in impact toughness was recorded across all systems, a trend attributed to the plasticizing action of methanol, which enhances chain mobility and allows greater energy dissipation during impact. Overall, these results emphasize both the reinforcing potential and the limitations of nanoclay, while also highlighting the complex interplay between plasticization and filler-induced stress localization in governing the long-term reliability of polymer nanocomposites under environmental aging.

References

[1] N.-I. Kim, J.-M. Lee, J.-S. Moon, and J.-W. Wee, "Characterization and modeling of weathering degradation of PC/ABS blend in various temperature and humidity conditions," *Polym. Degrad. Stab.*, 2025.

[2] M. Konarzewski, T. Durejko, M. Lazinska, M. Czerwinska, P. Prasula, and R. Pnaowicz, "Thermo-oxidative aging of the polyoxymethylene (POM), acrylonitrile–butadiene–styrene (ABS) and polycarbonate (PC) polymers—A comparative study," *J. Polym. Res.*, vol. 29, p. 236, 2022.

[3] J. Nomai and A. K. Schlarb, "Environmental stress cracking (ESC) resistance of polycarbonate/SiO_2 nanocomposites in different media," *J. Appl. Polym. Sci.*, vol. 134, no. 43, p. 45451, 2017.

[4] L. M. Robeson, "Environmental stress cracking: a review," *Polym. Eng. Sci.*, vol. 53, no. 3, pp. 453–467, 2013.

[5] Y. N. Babu, M. V. Rao, and A. G. Krishna, "Characterization and evaluating the mechanical performance of halloysite nanotubes reinforced acrylonitrile butadiene styrene/polycarbonate composites exposed to aggressive environmental conditions," *Mater. Werkst. Tech.*, vol. 54, no. 1, pp. 81–89, 2023.

[6] V. Sabatini, T. Taroni, R. Rampazzo, M. Bompieri, D. Maggioni, D. Meroni, M. A. Ortenzi, and S. Ardizzone, "PA6 and halloysite nanotubes composites with improved hydrothermal ageing resistance: Role of filler physicochemical properties, functionalization and dispersion technique," *Polymers*, vol. 12, no. 1, p. 211, 2020.

[7] X. Li, Y. Yang, Q. Wang, Y. Gao, W. Zhang, and Z. Liu, "Study on the water-tree ageing characteristics of polyethylene/organic montmorillonite and crosslinked polyethylene/organic montmorillonite nanocomposites," *High Volt.*, vol. 7, no. 6, pp. 1074–1084, 2022.

[8] Aktas D., Tasdemir H.A., Alanalp M.B., and Durmus A., "Comparing the effects of halloysite nanotubes and precipitated calcium carbonate nanoparticles on the environmental stress cracking resistance and mechanical properties of polycarbonate," *Polymer. Composites*, 2025, doi: 10.1002/pc.28072.

Electronic, Magnetic and Optical Materials

Effect of Sintering Atmosphere on Eco Friendly Nbt-St Ceramics

Mustafa Yunus Kaya[1], Ayşe Berksoy Yavuz[2],

1. Bursa Technical University

2. Istanbul Gedik University

The importance and usage of electroceramics have increased significantly in electronic device applications year by year. Among these ceramics, lead-based compositions stand out due to their high electrical properties and stability over a wide temperature range, dating back to the 1950s. However, due to the hazardous effects on the environment and human health, the use and disposal of these materials are restricted by legal regulations, such as the EU 2002/95/EC directive. Subsequently, this situation has led to an increase in work on lead-free electro-ceramic materials. (1-x)(Na0.5Bi0.5Ti)O3-xSrTiO3 composition is considered a promising candidate due to its tunable electrical properties. In this study, compositions with different (1-x)NBT-xST ratios (x = 0.35-0.45-0.55) were synthesized using the solid-state calcination method, and the ceramics were produced via uniaxial pressing. The sintering was done under different sintering atmospheres (air and Argon), and the effects of it on the phase, structure, microstructure, and electrical properties were investigated.

Keywords: Lead-Free ceramics, NBT-ST, electrical properties

Investigation of The Effect of Doping on Dielectric Response and Energy Storage Performance of Lead-Free Nbt-Bt-St System

Ayse BERKSOY-YAVUZ[1], Deniz GÜNEŞ[2],

1. Istanbul Gedik University, Department of Materials Science and Nanotechnology Engineering, 34876 Kartal, Istanbul, Türkiye

2. Istanbul Gedik University, Department of Metallurgical and Materials Engineering, 34876 Kartal, Istanbul, Türkiye

Na0.5Bi0.5TiO3 (NBT)-based piezoceramics can be produced in binary or ternary solid solution form with BaTiO3 (BT) and/or SrTiO3(ST), and their piezoelectric properties can be easily regulated, making them an alternative to lead-based systems that are harmful to human health in the electronics industry. Moreover, the densification behaviour as well as the electrical properties of the NBT system can be optimized with additives such as CuO and Mn.

In this study, the structural and electrical properties of the antiferroelectric 0.70NBT-0.04BT-0.26ST system, synthesized with Mn doping at different molar ratios (0-1.0 mol%), which could serve as an alternative for energy storage applications, were investigated in detail. The 0.70NBT-0.04BT-0.26ST system with Mn doping in different molar ratios was sintered at a temperature range of 1150°C to 1200°C for 3 hours under atmospheric conditions. The dielectric constant and dielectric losses of these ceramics at various frequencies were taken from 25°C to 500°C.

All ceramics have a crystallized pure perovskite structure without any secondary phase. With increasing Mn doping ratio, an increase in grain size occurred in the 0.70NBT-0.04BT-0.26ST system.

Upon examination of the obtained data, it was observed that Mn doping significantly affected both the structural and electrical properties. According to these results, the Mn-doped 0.70NBT-0.04BT-0.26ST system is a potential alternative for compact pulse power capacitors in energy storage applications.

Keywords: Lead-Free, NBT-BT-ST, Mn-doping

DESIGN AND OPTIMIZATION OF INORGANIC MULTILAYER FILMS FOR TRANSPARENT RADIATIVE COOLING COATINGS

Habib Yazici [1], Osman Safa Cifci [2], Bihter Zeytuncu [1]

[1]Istanbul Technical University, Department of Metallurgical and Materials Engineering, 34469 Maslak, Istanbul, Turkiye

[2]Bogazici University, Department of Mechanical Engineering, 34342 Bebek, Istanbul, Turkiye

Keywords: Thin film design, transmittance, emissivity, radiative cooling, TMM, TPE, optimization

Abstract

This optimization study was initiated to develop transparent radiative cooling coatings exhibiting high reflectance across the solar spectrum and strong thermal emission through the mid-infrared atmospheric window. In this project, an inorganic multilayer thin-film design has been developed by conducting computational optimization study via Transfer Matrix Method and Tree-Structured Parzen Estimator. The 10-layer configuration demonstrates balanced performance with weighted reflectance of 0.662, emissivity of 0.636, and transmittance of 0.719 compared to 8 and 10 layer stacks. The findings reveal the potential of passive daytime radiative cooling coatings that use stable, earth-abundant and inorganic materials for window applications.

1. Introduction

As the global climate becomes a primary concern, the need for energy-free coating solutions is becoming more significant. Passive radiative cooling is a promising method that allows temperature reduction without external energy, combining solar reflectance through the mid-infrared band and emission through the atmospheric window [1].

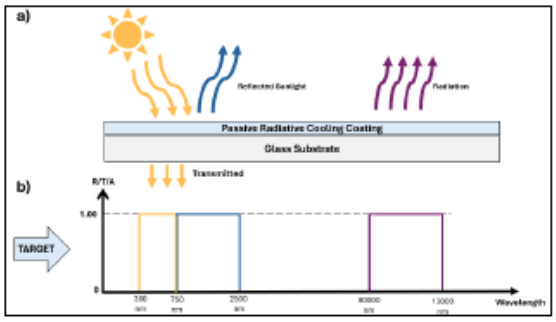

Figure 1. (a) Schematic of the passive radiative cooling mechanism (b) Target spectral response of the designed coatings

The fundamental strategy of passive radiative cooling is to achieve high emissivity within the atmospheric window (8–13 μm), allowing thermal radiation to escape into outer space and lowering the surface temperature. At the same time, high reflectance across the solar spectrum (0.3–2.5 μm) is required to avoid heating from incident sunlight. Therefore, most radiative coolers are designed to combine selective emissivity in the mid-infrared with strong solar reflectance from UV to NIR regions. However, initial designs of passive daytime radiative coolers (PDRC) appear opaque or silvery which is not desirable in some cases such as building windows. Very recently, transparent radiative cooling designs with high transmittance emerged in the literature [2]. Fig. 1a illustrates a transparent radiative cooling film and Fig. 1b demonstrates the spectral response of an ideal transparent radiative cooling design with unity transmittance in visible wavelengths, unity reflectance in NIR wavelengths, and unity emissivity in MIR wavelengths.

Broad research efforts have focused on different material systems to improve the design and performance of passive radiative cooling coatings. These designs utilize materials such as PDMS, silver or ITO, which raise environmental concerns and suffer from limited long-term stability. Besides, PDMS thicknesses in the designs reach up to 300 μm in some cases, which deviates the structure being a thin-film stack [3]. PDMS also suffers from yellowing, haze, and swelling.

Hence, this study aims to develop transparent radiative thermal cooling coatings via multilayered thin films by maximizing transmittance between the wavelength range of 380-780 nm, reflectance in the range of 780-2500 nm and emissivity between 3-25 μm without using critical materials or polymers.

2. Experimental Procedure

This study's transparent inorganic multilayer films were computationally designed and optimized for radiative cooling film applications. The spectral response of candidate stacks was modeled using the Transfer Matrix Method

(TMM). At the same time, layer configurations were optimized using the Optuna framework with a Tree-Structured Parzen Estimator (TPE) algorithm, which uses kernel density estimators that separate good and bad observations, and subsequently generate separate probability distributions to suggest the next design candidate [3]. Fourteen materials were added to the pool created for optimization (SiO_2, TiO_2, Al, ZnS, Al_2O_3, HfO_2, Cu, MgF_2, Si, SiC, Ni, Ta_2O_5, BaF_2, Nb_2O_5). The material selection criteria were criticality and cost-effectiveness, focusing on organic materials. The main target of the optimization study is to obtain maximum transmittance in the visible region, high reflectance within the near-infrared range, and superior thermal emissivity within the mid-infrared atmospheric window.

Spectral weighting methodology was applied in this study to obtain performance results that were close to realistic conditions. Because solar irradiance is not uniform, the calculated reflectance was weighted by the standard AM1.5D solar spectrum to quantify the rejection of solar heat accurately. Similarly, to evaluate the perceived transparency for a human observer, the visible transmittance was weighted against the CIE photopic luminosity function ($V(\lambda)$). Emissivity was evaluated against the downward atmospheric irradiance to conduct a realistic assessment. This allowed the optimization of high emissivity rates within the 8–13 µm atmospheric transparency window, where heat can escape into space.

The candidate design was discarded if the photopic transmittance was below 0.7, the minimum required threshold. Optimization studies were carried out for three configurations (8, 10, and 12 layers) using this methodology.

3. Results and Discussion

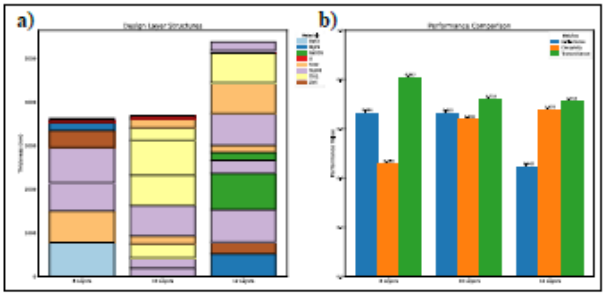

Figure 2. (a) Optimized layer structures for 8, 10, and 12-layer coatings with different material combinations (b) Comparison of reflectance, emissivity, and transmittance performance metrics for the three configurations

Optimized design for 8, 10, and 12 layer configurations, including material combinations with thicknesses, is illustrated in Figure 2a. Comparison of the reflectance, emissivity, and transmittance performance for the optimized designs is indicated in Figure 2b. The 8-layer stack demonstrates the worst performance in terms of emissivity (0.456). Because of that, the radiative cooling capability of the optimized 8-layer coating design is not sufficient. Even though transmittance and emissivity are relatively better for the 12-layer design, reflectance is less than 8 and 10 layer configurations.
Besides, increasing the layer number would increase the cost, time, and manufacturing errors in an experimental setting. In contrast, the 10-layer configuration exhibits high performance for each spectral property. The optimal design's reflectance, emissivity, and transmittance are 0.662, 0.636, and 0.719, respectively.

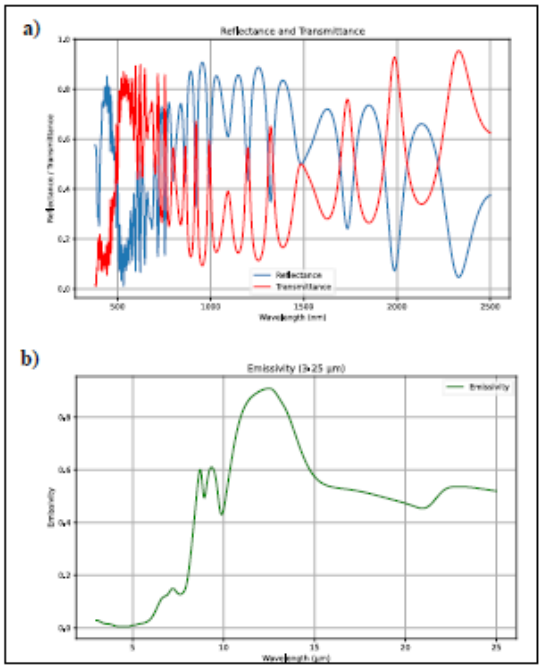

Figure 3. Spectral performance of the optimized multilayer coating: (a) reflectance and transmittance in the solar spectrum (0.38–2.5 µm), (b) emissivity in the mid-infrared region (3–25 µm) highlighting strong emission within the atmospheric window

The spectral performance of the 10-layer structure is presented in Figure 3. In the visible range (380-780 nm), transmittance is relatively high and reflectance remains low which is needed for achieving the desired transparency. Within the wavelength range of 780-2500 nm, while transmittance decreases, the reflectance increases. Subsequently, a significant reduction in solar heat gain can be observed in the NIR. Spectral selectivity enables that heat gain is blocked and visible transparency is provided. Total thickness of the coating is 3691.4 nm. In the Figure 3b, the emissivity performance of the coating is given. The graph indicates that firm emissivity peaks can be seen between the

wavelength of 8-13 μm. Such high emissivity in the thermal infrared region facilitates efficient radiative cooling by dissipating heat to outer space. Overall, the 10-layer configuration demonstrates a well-balanced spectral performance: high visible transmittance, strong NIR reflection, and pronounced mid-IR emissivity, making it an optimal candidate for radiative cooling window coatings.

4. Conclusion

Transparent passive radiative cooling coatings have primarily relied on multilayer films using materials such as PDMS, silver or ITO, which raise environmental concerns and suffer from limited long-term stability at thicknesses exceeding 100 μm. This work is designed to produce transparent coatings using stable, inorganic, and earth-abundant materials without exceeding 1 mm for each layer. A material pool of 14 different materials was created for the optimization study for 8, 10, and 12-layer configurations. As a result of the optimization study, the 10-layer configuration exhibits the most balanced performance regarding spectral properties. For the 10-layer configuration with a thickness of 3691.4 nm, AM1.5D-weighted reflectance, weighted hemispherical emissivity, and photopic transmittance are obtained as 0.662, 0.636, and 0.719, respectively.

For future work, cooling flux and temperature reduction will be calculated. In addition, increasing the material pool might enhance the performance by finding more suitable combinations. After design stage is completed, manufacturing and characterization of the optimum design will be conducted.

References

[1] Raman, A. P., Anoma, M. A., Zhu, L., Rephaeli, E., & Fan, S. (2014). Passive radiative cooling below ambient air temperature under direct sunlight. *Nature*, *515*(7528), 540–544.

[2] Kim, M., Lee, D., Son, S., Yang, Y., Lee, H., & Rho, J. (2021). Visibly Transparent Radiative Cooler under Direct Sunlight. *Advanced Optical Materials*, *9*(13), 2002226.

[3] Jin, Y., Jeong, Y., & Yu, K. (2023). Infrared-reflective transparent hyperbolic metamaterials for use in radiative cooling windows. *Advanced Functional Materials*, *33*(1), 2207940.

[4] Bergstra, J., Bardenet, R., Bengio, Y., & Kégl, B. (2011). Algorithms for Hyper-Parameter Optimization. *Neural Information Processing Systems; Curran Associates, Inc.*

Mechanical and Optoelectronic Response of Polyacrylamide-Graphene Oxide Composite Hydrogels

Büşra Osma [1], *Gülşen Akın Evingür*[2], *Bengü Özuğur Uysal*[3], *Önder Pekcan*[4]

[1]Yıldız Technical University, 34349 Beşiktaş, Istanbul, Türkiye
[2] Piri Reis University, 34940 Tuzla, Istanbul, Türkiye
[3]Altınbas University, 34218, Bağcılar, Istanbul, Türkiye
[4]Kadir Has University, 34083 Cibali, Istanbul, Türkiye

This study investigates the mechanical and optoelectronic behavior of polyacrylamide/graphene oxide (PAAm/GO) composite hydrogels in Black Sea seawater. Hydrogels were prepared with varying GO contents (107–250 µL) and evaluated under three conditions: pre-diffusion, post-diffusion, and post-release. Pyranine was incorporated as a fluorescent tracer to monitor gel dispersion in seawater. Optical performance was characterized using UV–Vis and FTIR spectroscopy, and dielectric constants were calculated in the visible and infrared regions. Mechanical properties were assessed through compression testing to evaluate elasticity and stability after seawater exposure. The results show that increasing GO content markedly enhances infrared absorption, decreases optical transmittance, and improves elastic strength, indicating a synergistic effect between optical and mechanical performance. These findings demonstrate the potential of PAAm/GO hydrogels as durable, multifunctional materials for infrared-absorbing marine coatings, with promising applications in naval technologies requiring both resilience and reduced infrared visibility.

Keywords: Composite hydrogels; spectroscopy; elasticity; marine coatings; naval applications

Metallurgy

HOT DEFORMATION BEHAVIOUR AND MICROSTRUCTURAL EVOLUTION OF AL-CU-LI ALLOYS PROCESSED UNDER VARYING THERMOMECHANICAL CONDITIONS

Şeydanur Kandöken [1], Beyza Karagül [1], Zeynep Yaren Toy [1],
Osman Halil Çelik [2], Faiz Muhaffel [1]

[1] Istanbul Technical University, Department of Metallurgical and Materials Engineering, 34469 Maslak, Istanbul, Turkey
[2] Turkish Aerospace Industry, Kahramankazan, Ankara, Turkey

Keywords: Third generation Al-Cu-Li alloy, Hot deformation, Mechanical properties, Microstructure, Heat Treatment

Abstract

The present study focuses on the hot deformation behavior and microstructural changes of aluminum-copper-lithium (Al-Cu-Li) alloys. Exceptional strength-to-weight ratios and enhanced corrosion resistance make these alloys very valuable in the aerospace industry. In this project, cylindrical samples were prepared from cast Al-Cu-Li alloy ingots. These samples were hot compressed at three different temperatures: 360 °C, 430 °C, and 500 °C. The deformation was applied at a constant strain rate of 0.05 s^{-1} with three different compression levels: 30%, 50%, and 70%. The test conditions were selected using FactSage 7.1 simulation software. Upon hot deformation, the samples were heat treated using the T6 process, which involved a solution treatment at 510 °C followed by water quenching and aging at 150 °C for 16 hours. The microstructure and Vickers microhardness of the samples were examined after hot compression and heat treatment. According to the results, the strength of the material increased with increasing temperatures and deformation levels. It was determined that this improvement was caused by the reduction of dislocations and the increase in grain size within the microstructure.

1. Introduction

In today's aviation applications, lightweight materials with high fatigue resistance and corrosion resistance are of great importance [1]. To meet these requirements, new generation Al-Cu-Li alloys, which have superior mechanical properties compared to other alloys, are preferred. However, to use these alloys effectively, it is necessary to systematically investigate the microstructural changes and mechanical behavior after hot deformation processes. While the literature highlights that Al-Cu-Li alloys offer numerous advantages in terms of grain orientation and precipitation behavior, data on their production parameters remains insufficient [2]. In our country, Turkey, the production of these alloys is supported by external sources. Reducing the use of external sources for defense industry and aerospace applications would provide a significant strategic advantage. One of the main objectives of the project is to thoroughly investigate the mechanical behavior of new-generation Al-Cu-Li alloys under hot deformation conditions. Within the scope of this project, the microstructural changes and mechanical behavior of the alloy have been analyzed in detail at different temperatures and deformation rates.

2. Experimental Procedure

In this project, third-generation Al-Cu-Li alloy was cast in ingot form. The chemical information of this alloy is shown in Table I. Before the hot deformation experiments, cylindrical samples with a diameter of 10 mm and a length of 15 mm were produced from the ingot-shaped alloy using a precision cutting method.

Table 1. Chemical composition of the samples

Element	Si	Fe	Cu	Mn	Mg	Zn	Li	Ag	Zr
Wt%	0.03	0.04	3.59	0.36	0.32	0.05	0.93	0.35	0.08

In order to prevent surface damage during the mechanical and thermal treatments to be performed on the samples, various surface treatments were applied to the surfaces of the samples and the surfaces were cleaned by grinding before

starting the experiment. The sample shape and pressing mechanism to be used during the experiment are shown in Figure 1.

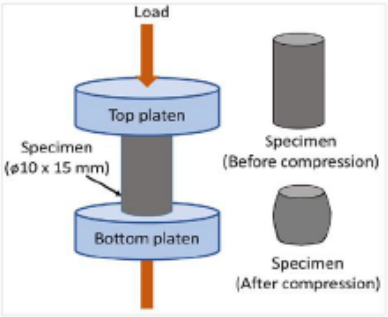

Figure 1. Hot compressing test setup and sample shape change

The aim was to determine the mechanical and deformation behaviors of the alloy when exposed to different temperatures and deformation rates through hot compressing experiments. For this purpose, the diagram shown in Figure 2 was drawn using the FactSage 7.1 program, and three different temperatures were determined based on this diagram. These temperatures are 360 °C, 430 °C, and 500 °C. Although the diagram below provides information about the thermodynamics of the alloy, it does not provide information about its kinetics because the diagram was drawn assuming an infinite diffusion time. For this reason, only information about the thermodynamic properties of the alloy can be obtained. At each temperature, plastic deformation was applied to the samples at rates of 30%, 50%, and 70%. A constant speed of 0.05 s^{-1} was used during the compression process. The samples were heated to the target temperatures using a Nabertherm laboratory furnace and held at these temperatures for 40 minutes to ensure homogeneous heating. After the hot pressing process, each sample was cooled in a controlled environment.

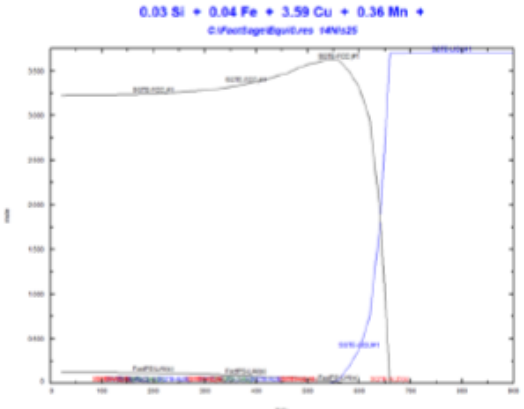

Figure 2. Phase diagram of Al-Cu-Li alloy plotted according to weigth percentages

After hot compressing, some samples were heat treated in accordance with T6 heat treatment standards. During the T6 heat treatment, the samples were solution treated at 510 °C for 30 minutes (in a KERR 999 model furnace), quenched in water at 25 °C, and subjected to artificial aging at 150 °C for 16 hours (in a BINDER GmbH brand furnace). The temperature-time graph for this process is shown in Figure 3. After the aging process, the samples were cooled to room temperature in a controlled manner within the furnace.

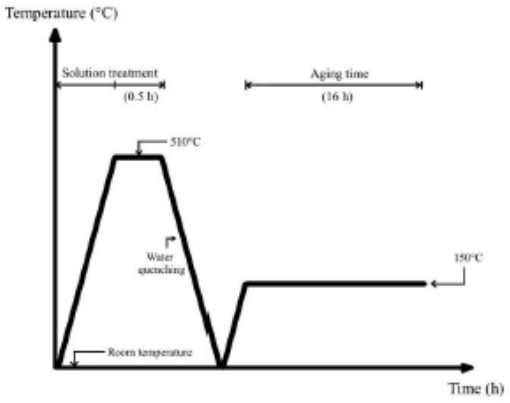

Figure 3. Hot compressing test setup and sample shape change

Metallographic preparation processes were carried out to accurately evaluate microstructural changes. Samples taken from cold bakelite were sanded with sandpaper with mesh numbers of 400, 600, 800, 1200, and 2500, respectively, and then polished. Subsequently, etching was performed using Keller's reagent. Microstructural examinations were conducted using a microscope, and the morphology of the grains and the distribution of secondary phases in the structure were evaluated. Microhardness measurements were taken from five different points on each sample using a Vickers hardness tester (HV 0.2) to determine the mechanical properties. The average of these values was calculated to determine the microhardness level. This allowed for a detailed examination of the alloy's mechanical properties, providing comprehensive data for its potential use in aerospace applications.

3. Results and Discussion

Samples subjected to 30%, 50%, and 70% deformation during the experimental procedure are shown in Figure 4,5, and 6. At the end of the experiment, microstructural images of samples subjected to hot deformation and T6 heat treatment were obtained.

Figure 4. Samples deformed at 360°C (from left to right: 30%, 50%, 70%)

Figure 5. Samples deformed at 430°C (from left to right: 30%, 50%, 70%)

Figure 6. Samples deformed at 500°C (from left to right: 30%, 50%, 70%)

Microstructural images of samples subjected to hot pressing at 360°C are shown in Figures 7 and 8. In Figure 8, T6 heat treatment was applied to the samples after hot pressing. Here, microstructural images of samples that underwent heat treatment and 70% deformation are shown [3].

Figure 7. Microstructures of specimens subjected to hot compression deformation at 360°C at rates of 30% (a), 50% (b), and 70% (c), respectively

Figure 8. Microstructures of specimens subjected to hot compression deformation at 360°C at rates of 30% (a), 50% (b), and 70% (c), respectively, and heated

Figures 9 and 10 show microstructural images of samples subjected to compression at 430 °C.

Figure 9. Microstructures of specimens subjected to hot compression deformation at 430°C at rates of 30% (a), 50% (b), and 70% (c), respectively

Figure 10. Microstructures of specimens subjected to hot compression deformation at 430°C at rates of 30% (a), 50% (b), and 70% (c), respectively, and heated

Figures11 and 12 show microstructural images of samples subjected to compression at 500 °C.

Figure 11. Microstructures of specimens subjected to hot compression deformation at 500°C at rates of 30% (a), 50% (b), and 70% (c), respectively

Figure 12. Microstructures of specimens subjected to hot compression deformation at 500°C at rates of 30% (a), 50% (b), and 70% (c), respectively, and heated

In terms of observing microstructural stability, the balance between temperature and deformation amount must be maintained [4]. Aluminum has a high tendency to recrystallize, so grain growth may occur in materials when high temperatures and deformation rates are applied. The resulting grain growth may cause a decrease in strength rather than an increase. This effect has been observed following thermal treatments conducted under various temperature and deformation conditions.

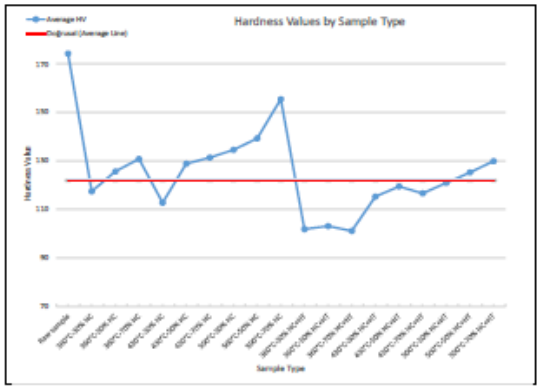

Figure 13. Sample-hardness graph

As can be seen from the graph in Figure 13, there is a direct correlation between temperature increase and strength [5]. According to the information in the literature, this situation has been observed as a result of the elimination of internal defects in the material during hot deformation. Up to a certain ratio of the solidus temperature, the increase in temperature has a positive effect on the increase in strength. However, when the temperature exceeds a certain level, the material's main phase (matrix) or some of the precipitates/intermetallic phases it contains may reach their melting temperature, resulting in changes in the size and morphology of the precipitate phases or grain growth. These developments cause a decrease in the material's strength.

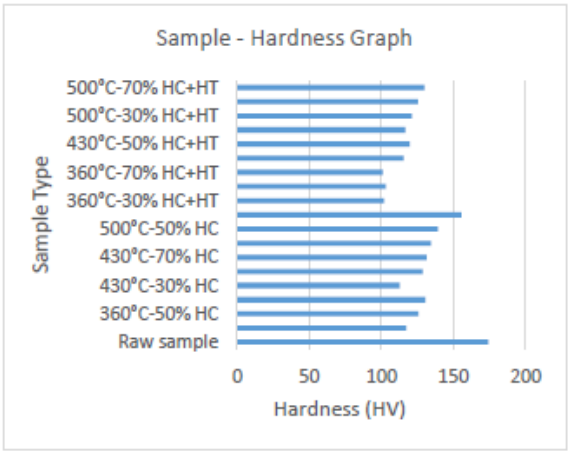

Figure 14. Sample-hardness values

Similarly, it has been observed that as the amount of deformation increases, the strength of the material also increases. With increasing deformation, the dislocation density also increases and atomic movements are impeded. As a result, the strength increases. As the amount of deformation increases, it becomes possible to obtain a finer microstructure [6]. The finer the grain structure, the greater the grain boundary, and the more dislocation movements are hindered. This is one of the factors that increases the mechanical strength of the material.

4. Conclusion

As a result, the effects of temperature and deformation variables on the microstructure and mechanical properties of the material were observed as a result of hot deformation and heat treatment. Up to a certain level, the increase in temperature increased the hardness and strength of the material, but as the solidus temperature was approached, a decrease in strength occurred as a result of grain growth. An increase in deformation positively affected strength, but under unbalanced conditions, grain growth and a decrease in hardness occurred. These results were confirmed by microstructure images, and it was concluded that the temperature-deformation balance is of critical importance.

Acknowledgment

We would like to thank TUSAŞ for enabling us to carry out this project under the LIFT-UP Program. We would also like to thank our industry advisor Dr. Osman Halil Çelik, our academic advisor Asst. Prof. Dr. Faiz Muhaffel, and TÜBİTAK for their valuable contributions throughout the process and for their financial support for our project.

References

[1] R. J. Rioja and J. Liu, "The evolution of Al–Li base products for aerospace and space applications," Metallurgical and Materials Transactions A, vol. 43, pp. 3325–3337, 2012, doi: 10.1007/s11661-012-1155-z.

[2] X. Xu et al., "Effects of heat treatment and pre-stretching on the mechanical properties and microstructure evolution of extruded 2050 Al-Cu-Li alloy," Materials Science and Engineering: A, vol. 845, p. 143236, 2022, doi: 10.1016/j.msea.2022.143236.

[3] Z. Li, X. Tang, L. Zhang, ve X. Tong, "Effects of Heat Treatment and Pre-stretching on the Mechanical Properties and Microstructure Evolution of Extruded 2050 Al–Cu–Li Alloy," Materials Science and Engineering A, cilt 845, s. 143236, Nisan 2022

[4] X. Zhu, Y. Zhang, X. Lu ve Y. Zhou, "Hot Workability and Microstructure Evolution of Homogenized 2050 Al-Cu-Li Alloy," Materials, cilt 17, no. 17, s. 4236, Ağu. 2024.

[5] Y. Cao et al., "Detailed Investigation on High Temperature Mechanical Properties of AA2050 Al–Cu–Li Alloy," Materials Science and Engineering A, cilt 845, s. 143236, Nisan 2022.

[6] Sheng, Z., Huang, Y., Zhao, Y., Fu, R., Wang, X., Fan, X., & Wu, F. (2024). Hot Workability and Microstructure Evolution of Homogenized 2050 Al-Cu-Li Alloy during Hot Deformation. Materials, 17(17), 4236. https://doi.org/10.3390/ma17174236

SUSTAINABLE EVALUATION OF ELECTRIC ARC FURNACE SLAGS VIA METALLOTHERMIC REDUCTION

İbrahim Yıldırım[1], Ali Atay Ellergezen[1], Zeynep Turan[1], Ege Baysal[1] , Çağdaş Ekin Zöhra[1], Selçuk Kan[1], Kağan Benzeşik[1], Onuralp Yücel*[1]

[1]Metallurgical and Materials Engineering Department, Faculty of Chemical and Metallurgical Engineering, Istanbul Technical University, 34469, Maslak, Istanbul, Turkey

*yucel@itu.edu.tr
Keywords: **:** Steel Slag, Aluminothermic Reduction, Circular Economy, Construction Raw Material, Sustainability, Recycling

Abstract

Steel making is an essential industrial activity and at every stage of it, various by-products are produced which include Electric Arc Furnace (EAF) slags. EAF is an iron-slag based material that is produced during steel making. This material is both beneficial and problematic from a sustainability perspective. From an environmental and resource management perspective, it is commercially important as its high iron content renders it unsuitable for wide-scale use in cement production. This research presents the design of a sustainable process for the use of EAF slag based on aluminothermic reduction. The main goal is to remove the iron from the slag so that it can be used in the production of cement and facilitate the principles of circular economy.

1. Introduction

In the context of modern steelmaking, Electric Arc Furnace (EAF) slag emerges as a substantial by-product, characterized by its high metal oxide content and considerable environmental footprint. While its complex composition poses challenges for direct reuse, the high iron content in EAF slag also presents a valuable opportunity for metal recovery and material valorization. With increasing emphasis on circular economy principles and sustainable industrial practices, transforming such metallurgical residues into secondary raw materials has become a vital research focus [1].

Among the various recovery techniques, metallothermic reduction particularly via aluminium is gaining attention due to its capability to extract valuable metals while improving slag characteristics for downstream applications such as cement production [2]. This method leverages the exothermic nature of aluminium-based reactions to facilitate the reduction of metal oxides, contributing to both waste minimization and resource efficiency [3].

This study explores the feasibility and optimization of EAF slag valorization through aluminothermic reduction, combining experimental studies using both induction and electric arc furnaces [4]. By utilizing waste aluminium beverage cans as the reducing agent and evaluating the process under varying conditions, the study aims to deepen the understanding of slag-metal separation dynamics, alloy formation behavior, and process thermodynamics [5].

2. Experimental Procedure

This study investigated the metallothermic reduction of electric arc furnace (EAF) slags using aluminium beverage cans as the primary reductant. The aim was both to recover valuable metals and to evaluate the potential of the resulting slag for reuse in the cement industry. The effects of aluminium content, furnace type and temperature, as well as additives such as ferrosilicon (FeSi), silica (SiO_2), and graphite on the process efficiency were systematically examined.

EAF slag, containing mainly FeO (32.6 wt%), CaO (26.3 wt%), and SiO_2 (12.3 wt%), was used as the base material. Aluminium beverage cans were prepared by washing, drying, and cutting into flakes. Their amount varied from 30–33 g in small-scale induction furnace tests to 350–430 g in large-scale EAF experiments. Additives included FeSi (900–1250 g), SiO_2 (300 g), and graphite (200 g), depending on the experimental series.

(a)  (b) 

Figure 1. (a)EAF Slag, (b) Al Beverage Cans.

The experiments were divided into two categories:

Induction furnace tests (TSII I–IV): Performed on a smaller scale (300 g slag). Aluminium input was gradually increased (30–33 g) while operating temperatures ranged from ~1320 to 1560 °C. Higher temperatures and aluminium contents improved reduction efficiency and metal yield, reaching ~109 g of metal in the final test.

Electric arc furnace tests (TSII V–XVI): Larger-scale experiments (15 kg slag) assessed the influence of aluminium, FeSi, SiO_2, and graphite. Casting methods varied between mold casting and water quenching to study cooling effects on slag structure. In general, increased aluminium and the addition of graphite enhanced reduction, while SiO_2 addition improved slag properties and phase separation.

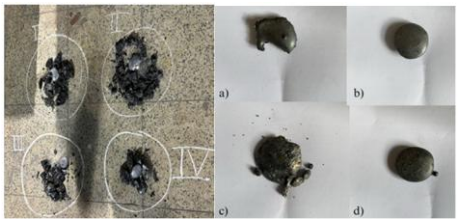

Figure 2. Images of Metals Recovered After Metallothermic Reduction Using Al Beverage Cans in Induction Furnace, a. TSII 1, b.TSII 2, c. TSII 3, d. TSII 4.

Figure 3. Metal slag mixed state of samples quenched in water TSII 6 and 7.

Figure 4. Reaction and casting in EAF.

3. Results and Discussion

3.1. Induction Furnace Experiments (TSII 1–4)

The first series of trials assessed the feasibility of using aluminium beverage cans as reductants for EAF slag in an induction furnace. Increasing both aluminium input and operating temperature enhanced metallothermic reduction, as confirmed by decreasing FeO content in slag and increasing metallic Fe in the recovered phase.

The obtained alloys contained Fe above 78 wt.% with Cr ranging from 0.8–2.6 wt.%, indicating the formation of Cr-bearing ferrous alloys. Carbon levels remained high (>4 wt.%), reflecting aluminium's role in reduction and alloy formation.

3.2. Electric Arc Furnace Experiments (TSII 5–16)

Large-scale experiments (15 kg slag per run) were performed in an EAF to better simulate industrial practice. Aluminium addition ranged from 350–430 g, with supplementary reductants including FeSi, FeSi+SiO_2, and FeSi+SiO_2+graphite. Water quenching of slag was introduced to promote amorphous phases suitable for cement applications.

Across all trials, Fe concentrations exceeded 85–90 wt.% with recovery efficiencies above 90%, while chromium recovery improved with auxiliary reductants and manganese recovery was highest using aluminium alone; silicon recovery increased when multiple reductants were applied. XRF analysis indicated that quenched slags contained less than 5 wt.% FeO, meeting requirements for cement production, and their Al_2O_3–CaO–SiO_2 ratios aligned closely with Portland cement compositions, with water quenching promoting glassy/amorphous structures favorable for cementitious use. The effect of basicity showed an optimum range of 0.90–1.00, achieving Fe recovery rates up to 98%, while deviations reduced efficiency, underlining the importance of moderate basicity for process optimization. XRD confirmed separation of iron-rich and silicate phases, and sieve analysis revealed coarse slag particles (>1 mm), though metal recovery remained high. Overall, the findings demonstrate that aluminium beverage cans are effective reductants for EAF slags, enabling Fe-rich alloy recovery and producing modified slags suitable for cement applications; auxiliary reductants enhanced element-specific recovery and amorphous slag formation, validating metallothermic reduction as a sustainable valorization route for EAF slags in both induction and arc furnace experiments.

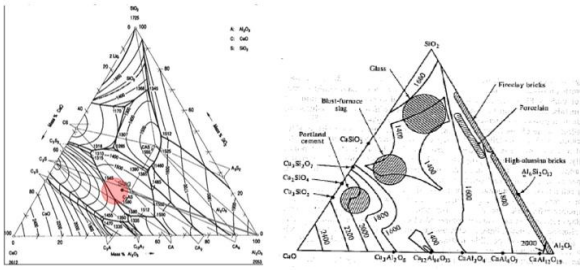

Figure 5. Average Composition in the 1200–1300°C Range left, Portland cement and Blast Furnace Slag composition in Ternary Phase Diagram.

As mentioned above, the average composition of the slag obtained by water quenching after casting at the achieved temperatures appears to be located near the Portland cement composition region in the Al_2O_3–CaO–SiO_2 ternary phase diagram. This indicates that the desired chemical properties have been closely approached.

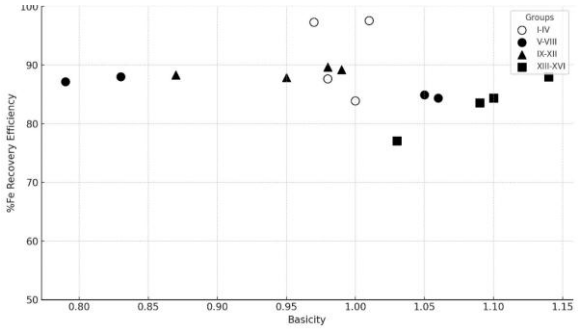

Figure 6. Metal Recovery Rates by Basicity.

The diagram demonstrates the correlation between two parameters: basicity and %Fe recovery efficiency across various experimental groups. Surprisingly, the most efficient iron recovery efficiencies of up to almost 98% are registered for basicity of 0.95 to 1.00. This suggests that a range of basicity could exist for the optimization of Fe recovery.

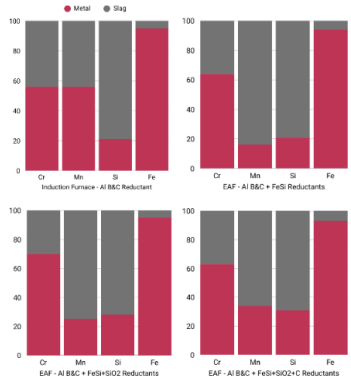

Figure 7. Recovery rates of experiments groups via used reductant materials.

4. Conclusion

This study shows that post-consumer aluminium beverage cans are an effective reductant for iron recovery from Electric Arc Furnace (EAF) slag. Pilot-scale induction furnace tests demonstrated that both aluminium dosage (30–33 g per 300 g slag) and smelting temperature (~1320–1560 °C) significantly increased recovery, nearly doubling metal yield from 51.6 g to 108.8 g (17–36 wt% Fe recovery). In larger EAF trials (15 000 g slag with 350–430 g cans), 3 476–4 747 g of metal was recovered, corresponding to 23–32 wt% Fe depending on process conditions.

Slag basicity and viscosity were found to be critical. The optimum CaO/SiO_2 ratio (0.90–1.00) enabled maximum FeO reduction, while lime addition reduced viscosity and improved separation. Co-reductants such as ferrosilicon and silica modified slag chemistry and further enhanced phase separation. Laboratory aluminothermic tests with pure aluminium achieved up to ~90 wt% Fe recovery, emphasizing the role of controlled flux chemistry.

Cooling methods influenced slag valorization. Mold casting produced crystalline slags with structural potential, while rapid water quenching yielded amorphous, glassy phases suitable as supplementary cementitious materials. XRD confirmed the reduced crystallinity of quenched slags.

Economically, using waste aluminium cans contributes to the circular economy by diverting waste and reducing CO_2 emissions compared to carbon-based reductants. Energy consumption of aluminothermic reduction in EAF compares favorably with conventional steelmaking stages, supporting industrial feasibility.

Future work should focus on optimizing Al/FeO ratios, co-reductant mixtures, and continuous feeding strategies, alongside detailed life-cycle and economic assessments. Mechanical and durability testing of slag products will guide their use in construction materials. Overall, aluminothermic reduction of recycled aluminium cans provides a sustainable route for iron recovery and slag valorization, offering a technically viable and environmentally friendly pathway for industrial application.

References

[1] World Steel Association, "World steel production report," 2023. [Online]. Available: https://worldsteel.org.
[2] Turkish Steel Producers Association, "Steel production statistics,"2022. [Online]. Available: https://www.dcud.org.tr.
[3] Z. Yildirim and M. Prezzi, "Chemical, mineralogical, and morphological properties of steel slag," Construction and Building Materials, vol. 24, no. 12, pp. 2540–2551, 2011.
[4] H. Shen and E. Forssberg, "An overview of recovery of metals from slags," Waste Management, vol. 23, no. 10, pp. 933–949, 2003.
[5] S. Serniabat, M. Hossain, and M. Karim, "Utilization of steel slag in construction materials," Procedia Engineering, vol. 95, pp. 188–194, 2014.

HYDROGEN REDUCTION OF EAF SLAG AND MILL SCALE

İrem Nur Ayar[1], Zehra Ergül[1], İlayda Doğan[1], Tolga Başakçı[1], Çağdaş Ekin Zöhra[1], Selçuk Kan[1], Onuralp Yücel[1]*

[1]Metallurgical and Materials Engineering Department, Faculty of Chemical and Metallurgical Engineering,

Istanbul Technical University, 34469, Maslak, Istanbul, Turkiye

*yucel@itu.edu.tr

Keywords: Mill scale, slag, hydrogen reduction, sustainability, iron-steel

Abstract

This study focuses on the design and development of a sustainable, energy-efficient, and low-emission recycling route for iron (Fe) -rich industrial wastes such as mill scale and slag, which are generated in significant quantities during iron and steel production processes. Despite their high metal content, these wastes are often underutilized or discarded, leading to both economic loss and environmental harm. To address this issue, gas-phase hydrogen reduction was employed as an alternative to conventional carbon (C)-based methods to produce high-purity Fe powders. This approach significantly reduces carbon emissions and eliminates the need for agglomeration or high-temperature carbothermic reduction. In this study, EAF (electric arc furnace) slag and 2 different mill scales were reduced with hydrogen at 800-1200 °C for 1-3 hours. The products were characterized using with XRD method.

1. Introduction

In 2020, an average of 1.891 tons of carbon dioxide (CO_2) was released into the atmosphere for every tonne of steel produced. With a total steel production of 1,860 million tonnes (Mt) in the same year, direct emissions from the industry reached 2.6 billion tonnes, accounting for 7% to 9% of all anthropogenic CO_2 emissions worldwide (1). In light of these striking figures, global environmental policies and sustainability goals have undergone a significant transformation process aimed at making industrial production processes more environmentally friendly.

Especially, the European Commission unveiled the EU (European Union)'s intermediate 2040 climate target in February 2024. The EU could fulfil its goal of becoming climate neutral by 2050 if net greenhouse gas emissions were reduced by 90% by 2040 compared to 1990 levels (2). Additionally, imports of specific precursors, such as steel and iron (whose manufacturing is C-intensive and most at risk of C leakage, will initially be subject to the CBAM. The CBAM will guarantee that the C price of imports equals the C price of domestic production and that the EU's climate goals are not compromised by verifying that a price has been paid for the embedded C emissions produced in some goods imported into the EU (3). Similarly, the Paris Climate Agreement has prioritized reducing C emissions in line with limiting global warming to 1.5°C. Greenhouse gas emissions need to fall by 43 percent by 2030 (4).

Within this framework, the iron and steel industry is under strong pressure to adopt innovative and energy-efficient solutions. Industrial wastes such as scale and slag, which are rich in Fe oxides, represent an important secondary raw material source. However, conventional recycling methods are both energy-intensive and environmentally harmful. Therefore, developing environmentally friendly and economically feasible alternatives is essential. One promising approach is the recovery of Fe from industrial wastes and its potential use in advanced manufacturing, such as 3D printing technologies, where high-purity Fe powders are required. This strategy not only supports circular economy goals but also contributes to sustainability by reducing emissions and resource consumption.

2. Experimental Procedure

In this study, hydrogen was employed as the reductant gas. The hydrogen flow rate was controlled via a flowmeter according to calculated parameters and introduced into the tube furnace. To evaluate the reduction behavior of different feedstocks, mill scale and slag were utilized in separate experiments. Before each experiment, the tube furnace was purged with argon gas to eliminate residual air. Hydrogen flow was then initiated under specified experimental conditions to carry out the reduction process. Upon completion, the hydrogen supply was ceased, and argon was passed through the system during furnace cooling to prevent oxidation. Gaseous by-products exited the furnace through a water-cooled system to ensure safe handling. This experimental setup enabled controlled investigation of hydrogen's effectiveness as a reductant in metallurgical applications.

A single slag sample and two different mill scale samples were used in the experiments. Tables 1 and 2 show the XRF analyses of the slag and mill scale samples used throughout the experiments.

Table 1. XRF Analysis of Slag Sample.

Content (Wt. %)	FeO	SiO_2	Al_2O_3	CaO	MgO	MnO
Slag	35.08	11.77	8.67	25.78	6.15	4.41

Table 2. XRF Analysis of Mill Scale Samples.

Content (Wt. %)	Fe_T	Fe_2O_3	Fe_3O_4	FeO	Fe
Mill Scale 1	71.72	-	35.14	36.58	-
Mill Scale 2	68.71	63.54	-	-	5.07

In the conducted studies, reduction experiments were carried out on slag sample under a hydrogen gas atmosphere at various temperature and duration conditions. Specifically, the slag specimens were subjected to reduction at 1100 °C and 1200 °C for 2 hours each. Additionally, further reduction experiments were performed at 1250 °C for 3 hours and at 1350 °C for 2 hours. For the Mill scale 1 raw material, two separate reduction experiments were conducted at 900 °C for durations of 1 hour and 2 hours, respectively. In the case of the mill scale 2 raw material, reduction processes were carried out at 800 °C and 900 °C, both with a duration of 2 hours.

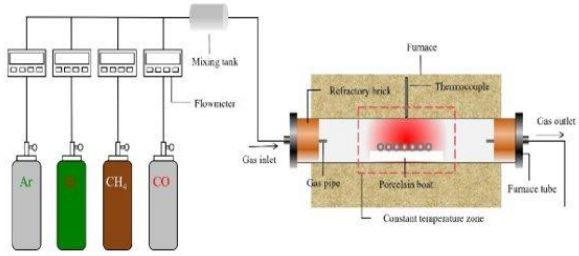

Figure 1. Schematic diagram of a horizontal tube furnace.

Figure 1 illustrates the schematic representation of the laboratory setup used for the reduction experiments. A tube furnace was employed to reduce the samples under controlled conditions. The gas flow was regulated using a flowmeter to maintain a constant and accurate flow rate throughout the experiments. During the reduction process, hydrogen reacted with Fe oxides and formed water vapor by combining with the released oxygen. As a result, metallic Fe was obtained from Fe oxides. Additionally, argon gas was used to provide an inert atmosphere during the experiments. Argon helped prevent unwanted side reactions by diluting or displacing residual oxygen in the system. In this way, it ensured a more efficient and controlled reduction process.

3. Results and Discussion

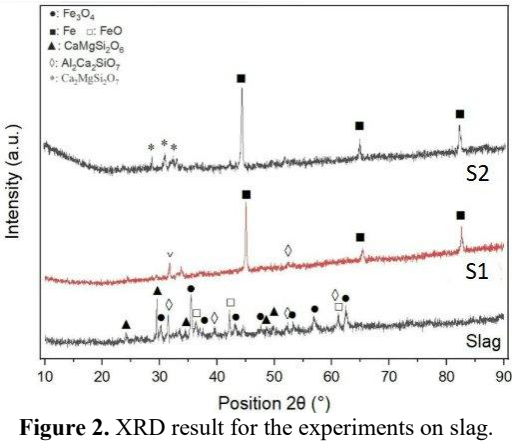

Figure 2. XRD result for the experiments on slag.

In Figure 2, XRD analysis demonstrated that untreated slag mainly exhibited amorphous characteristics with crystalline phases of Fe oxides and silicates, while no metallic Fe was detected. Following hydrogen reduction, Fe peaks were observed in all treated samples, varying their intensity according to temperature, duration, and sample preparation. The S1 sample (1200 °C, 2 h, ground) showed the onset of Fe formation. In contrast, S2 (1100 °C, 2 h, ground) exhibited weaker Fe peaks, indicating limited reduction efficiency at lower temperatures. These results highlight that both thermal conditions and pre-treatment strongly influence the reduction behavior of slag, underlining the potential of hydrogen-based processes for efficient Fe recovery.

Figure 3. Adhesion problem at 1350°C.

Figure 4. Adhesion problem at 1250°C.

According to Figures 3 and 4, in slag samples, high temperatures caused structural issues such as sintering and adhesion, which in turn limited reduction performance.

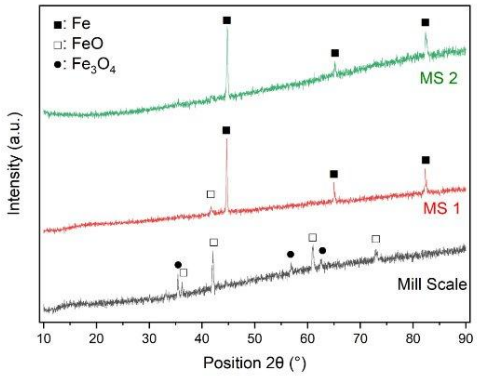

Figure 5. XRD result for experiments of mill scale 1.

In Figure 5, the untreated mill scale sample, distinct peaks corresponding to typical Fe oxide phases, Fe_3O_4 (magnetite) and FeO (wüstite), formed during high-temperature steel processing were observed. In the sample MS-1 obtained after 1 hour of hydrogen reduction, a noticeable decrease in the intensities of these oxide peaks was detected, while new and distinct peaks corresponding to Fe emerged. This indicates that the Fe oxides were partially reduced to metallic Fe. In contrast, in the MS-2 sample, which was reduced for 2 hours, the peaks corresponding to oxide phases almost completely disappeared, while the peaks associated with elemental Fe became significantly sharper and more intense. This suggests that as the reduction time increases, the phase transformation progresses further, resulting in the formation of high-purity metallic Fe.

The direct relationship between the increase in mass loss and the formation of metallic phases is evident: as the reduction proceeds, oxygen is removed from the oxides, combines with hydrogen to form water vapor, and escapes from the system, leading to a decrease in the total mass of the sample. Overall, both the mass analysis and XRD data clearly demonstrate that the hydrogen reduction process becomes more effective with longer treatment durations, enabling the successful conversion of industrial mill scale waste into metallic Fe under moderate thermal conditions.

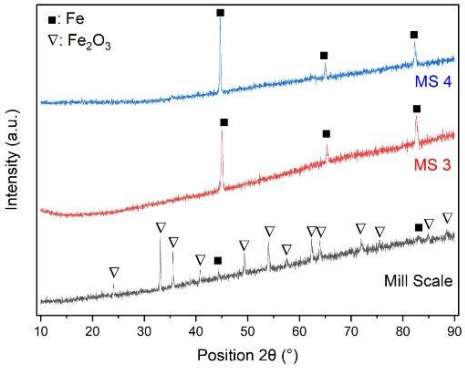

Figure 6. XRD result for experiments of mill scale 2.

The XRD analysis results of Experiments of MS-3 and MS-4 are presented in Figure 6. In the untreated mill scale sample, numerous distinct peaks corresponding to the Fe_2O_3 phase are observed. This phase indicates the presence of highly oxidized Fe within the mill scale. Additionally, a few peaks associated with metallic Fe are also present.

The MS-3 sample was subjected to hydrogen reduction at 800 °C for 2 hours. In this sample, a noticeable decrease in the intensity of Fe_2O_3 peaks was observed. Simultaneously, the peaks corresponding to metallic Fe became more prominent. These results indicate that the reduction process was effective. Indeed, the high percentage of mass loss also confirms that the reduction reactions were actively taking place.

Although the temperature applied to the MS-4 sample was increased to 900 °C, resulting in the near-complete disappearance of Fe_2O_3 peaks and the emergence of sharp, high-intensity metallic Fe peaks in the XRD pattern, it is noteworthy that the corresponding mass loss is slightly lower than that of the MS-3 sample. This difference can be attributed to the onset of sintering of the mill scale at elevated temperatures. Sintering is a process in which the particle surfaces partially melt, leading to increased density and reduced porosity. This densification can hinder the penetration of hydrogen gas into the interior of the particles, thereby limiting the depth of reduction reactions. As a result, although the oxide phases on the surface may be fully reduced, the inner regions might experience only partial reduction. Consequently, while XRD indicates a high purity of metallic Fe on the surface, the total amount of oxygen removed from the system may be slightly reduced, leading to a lower overall mass loss.

Table 3. Mass Analysis of Experiments Slag.

Sample	Temp. (°C)	Gas Flow (L/min)	Time (h)	Initial Mass (g)	Final Mass (g)	Mass Loss (%)
Slag	1200	0.21	2	10	8.29	17.10
Slag	1100	0.21	2	10	8.75	12.50

In Table 3, mass analysis of experiments on slag. The efficiency of experiments is 51.4% and 70.32%, respectively.

Table 4. Mass Analysis of Experiments Mill Scale 1.

Sample	Temp. (°C)	Gas Flow (L/min)	Time (h)	Initial Mass (g)	Final Mass (g)	Mass Loss (%)
Mill Scale 1	900	0.21	1	10	8.65	13.50
Mill Scale 1	900	0.21	2	10	8.54	14.60

In Table 4, mass analysis of experiments on mill scale 1. The efficiency of experiments is 75.5% and 81.66%, respectively.

Table 5. Mass Analysis of Experiments Mill Scale 2.

Sample	Temp. (°C)	Gas Flow (L/min)	Time (h)	Initial Mass (g)	Final Mass (g)	Mass Loss (%)
Mill Scale 2	800	0.21	2	10	7	30
Mill Scale 2	900	0.21	2	10	7.17	28.28

In Table 5, mass analysis of experiments on mill scale 2. The efficiency of experiments is 98.16% and 95.83%, respectively.

4. Conclusion

In this study, the hydrogen-based reduction of Fe-containing industrial wastes, such as mill scale and slag, was investigated as a sustainable alternative to conventional methods. The results showed that higher temperatures and longer reaction durations significantly enhanced the reduction efficiency, particularly in the case of mill scale. Reduction at 900 °C for 2 hours proved more effective than shorter durations or lower temperatures, underlining the importance of thermal activation and sufficient reaction time. However, in slag samples, temperatures at or above 1200 °C caused issues such as melting and adhesion to the crucible, which not only reduced reduction performance but also hindered accurate structural analysis using techniques like XRD. This highlights the need for careful process optimization tailored to the specific characteristics of each material. Overall, hydrogen-assisted reduction demonstrated clear advantages in terms of material recovery and CO_2 emission reduction, supporting the principles of the circular economy. The proposed method offers an environmentally responsible and scalable approach to waste valorization. Future research should focus on optimizing the process and exploring its integration into existing metallurgical systems.

Acknowledgment

We would like to thank Prof. Dr. Onuralp Yücel, Res. Ass. Dr. Kağan Benzeşik, Res. Ass. Selçuk Kan, Res. Ass. Çağdaş Ekin Zöhra and Metallurgical and Materials Engineer Ayşe Deniz for their contributions and guidance to our study.

References

[1] worldsteel. (2024, October 22*). Climate change and the production of iron and steel* - worldsteel.org. worldsteel.org. https://worldsteel.org/climate-action/climate-change-and-the-production-of-iron-and-steel/

[2] *Climate action and the Green Deal.* (n.d.). European Commission. https://commission.europa.eu/strategy-and-policy/priorities-2019-2024/european-green-deal/climate-action-and-green-deal_en

[3] *Carbon Border Adjustment Mechanism.* (n.d.). Taxation and Customs Union. https://taxation-customs.ec.europa.eu/carbon-border--adjustment-mechanism_en#iron-and-steel

[4] *The Paris Agreement.* (n.d.). United Nations Climate Change. Retrieved December 26, 2024, from https://unfccc.int/process-and-meetings/the-paris-agreement

HYDROMETALLURGICAL METAL RECOVERY FROM LITHIUM ION BATTERY THROUGH CO-PROCESSING OF NMC AND LFP

Oğulcan Güngör, Elif Güloğlu and Gökhan Orhan

Istanbul University-Cerrahpaşa, Department of Metallurgical and Materials Engineering, 34320 Avcılar, Istanbul, Turkey

Keywords: Lithium-ion batteries, Battery recycling, Synergistic leaching, Citric acid

Abstract

State-of-the-art recycling of end-of-life (EoL) lithium-ion batteries (LIBs) pose severe environmental and economic challenges, with conventional recycling methods being energy-intensive and polluting. This study pioneers a synergistic hydrometallurgical process using eco-friendly citric acid to co-recycle NMC111 and LFP cathode active powders. We synergize Fe (II) in LFP as a reductant for high-valency transition metals such as Ni, Co, Mn in NMC, systematically optimizing leaching parameters including leaching time, acid concentration and solid-to-liquid ratio for maximizing metal recovery. The method not only eliminates toxic and expensive reductants, it also offers potentially sustainable and efficient alternative for critical metal leaching. The study represents a critical midpoint towards industrial recycling of NMC111 and LFP cathode materials.

1. Introduction

The demand for energy has increased substantially due to the expanding global population and the advancements in modern living. Over 80% of the world's current energy consumption comes from fossil fuels, which are limited and environmentally harmful [1]. This necessitates a transition from fossil fuels to greener, renewable, and sustainable energy utilization and storage methods to reduce the carbon footprint. LIBs are critical energy storage systems due to their high energy density, high cycle rates and long lifespan. These properties have contributed to their widespread adoption, mainly in modern devices, including electric vehicles, portable electronic devices, and stationary storage systems. Preliminary findings from market research conducted in the current literature indicate that under the LFP scenario, the market share of LFP chemistry will increase linearly from approximately 30% in 2019 to 60% in 2030 and remain at that level until 2050 [2]. This contrasts with other battery chemistries that have proportionally lost market share compared to the NMC scenario. Regarding the NMC scenario, it is estimated that nickel-rich NMCs will be introduced to the market in 2030, gradually replacing other previous chemistries, and reaching one-third of the market share by 2050 [2]. LIBs, which have a lifespan of approximately 8-10 years, are considered to have reached the end of their lifespan when their capacity drops to at least 80%. The waste generated when batteries reach the end of their lifespan, coupled with the sharp increase expected in the coming years, poses significant environmental and economic challenges.

EoL LIBs contain Li, Co, Ni, and Mn, which are considered critical metals by European countries due to strategic and supply risks. Additionally, the primary environmental concern associated with EoL LIBs is the potential for critical metals and chemically reactive lithium compounds to leach into soil and groundwater. These compounds can cause toxic effects if not disposed properly. The state-of-the-art recycling processes involve the application of pyrometallurgical, hydrometallurgical, and direct recycling, either independently or in an integrated manner [3]. Pyrometallurgical methods are techniques that aim to recover metals through melting and reduction which are carried out at high temperatures [4]. Hydrometallurgical methods involve the application of leaching processes using acid or base solutions, followed by the recovery of metallic values from the metal-rich solution [5]. Hydrometallurgical methods are increasingly preferred due to their low energy requirements, potential environmental compatibility compared to pyrometallurgy, and selective metal separation capability [5,6]. However, effective hydrometallurgical processing requires careful classification and pretreatment of EoL LIBs. This is primarily to prevent foreign metals (Al, Cu, Fe) and compounds such as residual carbon, electrolyte, and binders from inhibiting reaction kinetics [7]. As a result, the requirement for a single cathode input remains a significant constraint in state-of-the-art hydrometallurgical recycling, hindering scalability and economic viability potential.

Due to these technical challenges, the vast majority of today's industrial-scale hydrometallurgical recycling plants prefer to process only LFP or only NMC containing waste batteries in order to ensure efficiency and process control. However, there are laboratory and pilot-scale studies in the literature on the co-leaching of LFP and NMC cathode chemistries [8–10]. Inorganic acids such as sulfuric acid (H_2SO_4) [8], hydrochloric acid (HCl) [7,10], nitric acid (HNO_3), or phosphoric acid (H_3PO_4) [11] have been extensively studied in the literature and have the capacity to leach valuable metals from cathode materials. Guimarães et

al. applied a leaching process using sulfuric acid to dissolve valuable metals in NMC cathode materials. In their study, under optimized conditions of 1 M H_2SO_4, 90 °C, and a 10:1 liquid to solid ratio, 100% of Co, Li, and Ni, and 93% of Mn were enriched in the solution [12]. Organic acids such as citric acid ($C_6H_8O_7$), formic acid (CH_2O_2), oxalic acid ($C_2H_2O_4$) are considered more environmentally friendly than inorganic acids [13–16]. They also demonstrate the ability to form complexes with cathode metals and can add selectivity to the leaching process by enriching only the target metals in the solution. Rouquette et al. applied a leaching process using oxalic acid on NMC cathode material, and the optimized conditions were found to be 60 °C, 60 minutes, and 0.6 M oxalic acid, resulting in a leaching yield of 98.8% for Li, while Ni, Co, and Mn were recovered as oxalate salts [13]. Although high leaching yields and selectivity were achieved, the high liquid/solid ratios used negatively impacted the environmental effects and industrial feasibility of the proposed studies [13]. The use of reducing agents to reduce acid consumption and enhance leaching efficiency has been extensively studied. Swain et al. found that when H_2O_2 was added to the cathode material containing Li and Co in the presence of H_2SO_4, the leaching efficiency of Li improved significantly from 75% to 94%, Co from 35% to 93%. In addition, their study emphasized that approximately 1.6 tons of H_2O_2 would be required for the hydrometallurgical recycling of 1 ton of EoL LIBs [17]. The cost and secondary waste of reducing agents have increased interest in alternative approaches.

Similar studies provide a foundation for future research into the use of Fe already present in LFP as a reducing agent. In the study conducted by Ning et al., the effect of Fe (II) released by the rapid dissolution of LFP in H_2SO_4 without the need for an additional reducing agent. Under optimal conditions of 0.7 M H_2SO_4, 60 minute leaching time, 90 g/L solid-to-liquid ratio, and an NMC:LFP weight ratio of 1:2, leaching efficiencies of approximately 99% for Li, Ni, and Mn, and 95.57% for Co were achieved [8]. The resulting solution was recovered as $FePO_4$ at a pH of approximately 2.5 using NaOH under thermodynamic conditions. However, while the leaching kinetics and reaction mechanism were investigated, the effects of using industrial cathode powders and different acid types under these conditions were not examined. Zou et al. investigated the effects of acid concentration, LFP powder amount, and additional H_2O_2 amount as a reducing agent in a system where industrially obtained NMC cathode material was reduced with synthetic LFP powder in the presence of H_2SO_4. Under conditions of 2 M H_2SO_4, 60 °C temperature, and a leaching time of 3 hours, leaching efficiencies of 100%, 87.6%, 100%, and 91.1% were achieved for Li, Ni, Co, and Mn, respectively [9]. However, the synergistic effects of NMC and LFP in citric acid solutions were not investigated in these studies, and no method was proposed for the recovery of metals from the solution obtained after the leaching process.

This study addresses gaps in existing literature by investigating the co-leaching process of citric acid using synthetic NMC111 and LFP powders. The study examines parameters such as acid concentration, leaching time, solid-to-liquid ratio, and uses stoichiometrically controlled ratio of synthetic powder to investigate the chemical reaction mechanisms governing the behavior of high-value metals in NMC111 within citric acid solutions. The findings from this synthetic experimental design serve as a cornerstone, demonstrating significant potential for developing scalable, sustainable, and environmentally friendly industrial processes for the recycling of complex mixed cathode waste streams.

2. Experimental Procedure

2.1. Materials and reagents

In this study, synthetic NMC111 (CAS 346417-97-8) and LFP (CAS 15365-14-7) cathode powders was purchased from Nanografi NanoTechnology, Turkey. Mass percentage of elements in synthetic cathode powders were determined via ICP-OES analysis and results shown in Table 1. Citric acid (anhydrous, 99%, Sigma Aldrich) solutions were used as the lixiviant at different concentrations.

Table 1. Chemical analyses of synthetic cathode powders.

%	Li	Co	Ni	Mn	Fe	P
NMC111	7.37	19.48	18.24	16.65	-	-
LFP	3.87	-	-	-	29.8	25.64

2.2. Leaching experiments

Leaching experiments were conducted in a three-neck cylindrical borosilicate flask with a capacity of 100 ml. The reactor was equipped with a magnetic stirrer positioned at its center, operating at a constant speed of 450 rpm to ensure sufficient agitation and overcome liquid film resistance. Precise temperature control during leaching was achieved using an oil bath equipped with a temperature sensor. A cooling system was incorporated to minimize evaporation losses and maintain a constant solid-to-liquid ratio throughout the process.

For each leaching experiment, the citric acid solution was first heated to the target temperature of 40 °C within the reactor. A calculated amount of synthetic NMC111 and LFP cathode powders with a mole ratio of LFP:NMC111 1:1 were individually added to the heated lixiviant under continuous stirring. The leaching conditions were investigated at different solid-to-liquid ratio and different leaching times.

3. Results and Discussion

The effect of citric acid concentration on the leaching efficiency of high-valency transition metals were investigated. Redox mechanisms during co-leaching of NMC111 and LFP have been previously hypothesized in the literature and proposed reactions are given in Eq. (1) and Eq. (2) [8,9]. However, in this study, it is challenging to assume a proper reaction due to the complexation properties of citric acid.

$$LiFePO_4 + 2H^+ \rightarrow Li^+ + Fe^{2+} + H_2PO^-_4 \quad (1)$$

$$Li(Ni_xCo_yMn_z)O_2 + 4H^+ + Fe^{2+} \rightarrow Li^+ + xNi^{2+} + yCo^{2+} + zMn^{2+} + Fe^{3+} + 2H_2O \quad (2)$$

In the reaction between NMC111 and LFP, Fe^{2+} was initially released from $LiFePO_4$ in presence of citric acid. This served as a reducing agent, thereby facilitating a redox reaction with high valence metals in NMC111, which consequently resulted in the leaching of NMC in the form of Ni^{2+}, Co^{2+}, Mn^{2+}, and Li^+ [8]. The co-leaching of synthetic LFP and NMC111 cathode materials using citric acid demonstrated high efficiencies under the conditions of 40 °C and 30 minutes. A systematic variation in acid concentration has shown a critical threshold value for optimal metal recovery as demonstrated in Figure 1. The use of 1 M citric acid has demonstrated efficiencies of 95% and 74% for Li and P respectively while complete dissolution of target metals was achieved. In contrast, citric acid concentration of 0.5 M has yielded recoveries of 71.45%, 76.15%, 78.6%, 81.74%, 90.26%, 56.73% for Li, Co, Ni, Mn, Fe and P respectively.

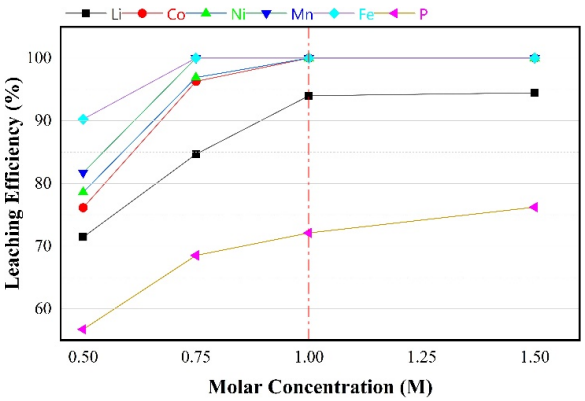

Figure 1. The effect of acid concentration on leaching efficiency (50 g/L, 40 °C, 30 mins).

The efficacy of this organic acid system was further demonstrated when compared with NMC111-only leaching, which yielded recovery for Li, Ni, Co, and Mn of 17%, 10.12%, 9.72%, 10.89% respectively. This outcome indicates that Fe^{2+} released from LFP plays a role for the reduction of high-valency transition metals (Ni^{3+}, Co^{3+}, Mn^{4+}) to soluble divalent states [9,11]. The comparison of these two systems in time-dependent leaching efficiencies was illustrated in Figure 2.

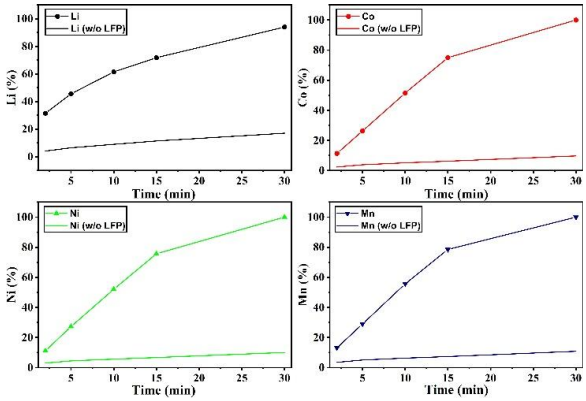

Figure 2. Leaching efficiencies of Li, Ni, Co, and Mn from NMC111 with and without LFP in citric acid (1 M, 40°C, 50 g/L).

The effect of solid-to-liquid ratio was investigated under conditions of 0.5 M citric acid concentration at 40 °C with leaching time of 30 minutes and 10 g/L solid-to-liquid ratio, the results are shown in Figure 3. In comparison to experiments conducted at a solid-to-liquid ratio of 50 g/L, experiments conducted at 10 g/L about 100% of Li and Fe while relatively high leaching efficiencies of 84.3%, 87.17%, 86% and 88.92% for Co, Ni, Mn and P were achieved respectively.

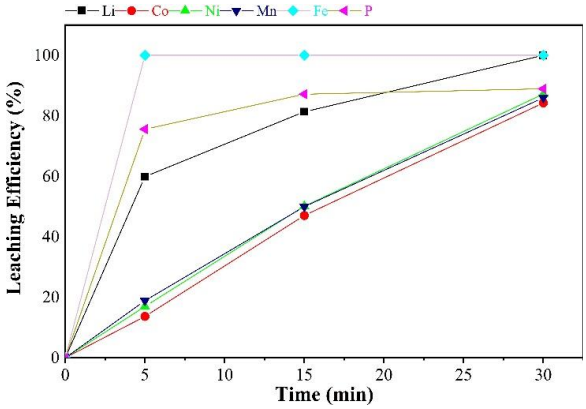

Figure 3. The leaching efficiency of metals at 10 g/L (0.5 M, 40°C).

4. Conclusion

This study successfully demonstrates the applicability of a hydrometallurgical process using environmentally friendly citric acid for the co-leaching of valuable metals from mixed NMC and LFP cathode materials. The effect of acid concentration, leaching time, and solid-to-liquid ratio on the leaching efficiencies of NMC111 metals were investigated.

Under the conditions of 1 M citric acid, 40 °C, 30 minutes leaching time and 50 g/L solid-liquid ratio, Li efficiency was found to be 95% and nearly complete dissolution of Ni, Co, and Mn was achieved. The high recovery efficiencies and the clear understanding of the effect of using LFP as a reducing agent indicate that the process is highly promising towards the development of a more sustainable, economical, and scalable recycling solution for the growing problem of mixed lithium-ion battery waste.

Acknowledgment

This study was funded by Scientific Research Projects Coordination Unit of İstanbul University-Cerrahpasa Rectorate. Project number: 38483

References

[1] J. Wang and W. Azam, "Natural resource scarcity, fossil fuel energy consumption, and total greenhouse gas emissions in top emitting countries," *Geoscience Frontiers*, vol. 15, no. 2, p. 101757, 2024.

[2] C. Xu, Q. Dai, L. Gaines, M. Hu, A. Tukker, and B. Steubing, "Future material demand for automotive lithium-based batteries," *Commun Mater*, vol. 1, no. 1, p. 99, 2020.

[3] A. Cornelio, A. Zanoletti, and E. Bontempi, "Recent progress in pyrometallurgy for the recovery of spent lithium-ion batteries: A review of state-of-the-art developments," *Current Opinion in Green and Sustainable Chemistry*, vol. 46, 2024.

[4] B. Makuza, Q. Tian, X. Guo, K. Chattopadhyay, and D. Yu, "Pyrometallurgical options for recycling spent lithium-ion batteries: A comprehensive review," *Journal of Power Sources*, vol. 491, p. 229622, 2021.

[5] K. Binnemans and P. T. Jones, "The Twelve Principles of Circular Hydrometallurgy," *Journal of Sustainable Metallurgy*, vol. 9, no. 1, pp. 1–25, 2023.

[6] W. Liu, K. Li, W. Wang, Y. Hu, Z. Ren, and Z. Zhou, "Selective leaching of lithium ions from LiFePO4 powders using hydrochloric acid and sodium hypochlorite system," *The Canadian Journal of Chemical Engineering*, vol. 101, no. 4, pp. 1831–1841, 2023.

[7] A. Porvali *et al.*, "Mechanical and hydrometallurgical processes in HCl media for the recycling of valuable metals from Li-ion battery waste," *Resources, Conservation and Recycling*, vol. 142, pp. 257–266, 2019.

[8] Y. Ning, Y. Zhang, B. Zhu, G. Wei, Q. Wang, and J. Qu, "Reducing the environmental impact of lithium-ion battery recycling through co-processing of NCM and LFP," *Process Safety and Environmental Protection*, vol. 187, pp. 810–819, 2024.

[9] Y. Zou, A. Chernyaev, M. Ossama, S. Seisko, and M. Lundström, "Leaching of NMC industrial black mass in the presence of LFP," *Sci Rep*, vol. 14, no. 1, p. 10818, 2024.

[10] H. Tang, Y. Qiao, X. Dai, F. Tan, and Q. Li, "Preparation of FePO4•2H2O from LiFePo4 mixed with LiNixCoyMn1-x-yO2 waste material," *J Serb Chem Soc*, vol. 85, no. 5, pp. 671–685, 2020.

[11] X. Zhou *et al.*, "One-step selective separation and efficient recovery of valuable metals from mixed spent lithium batteries in the phosphoric acid system," *Waste Management*, vol. 155, pp. 53–64, 2023.

[12] L. F. Guimarães, A. B. Botelho Junior, and D. C. R. Espinosa, "Sulfuric acid leaching of metals from waste Li-ion batteries without using reducing agent," *Minerals Engineering*, vol. 183, 2022.

[13] L. M. J. Rouquette, M. Petranikova, and N. Vieceli, "Complete and selective recovery of lithium from EV lithium-ion batteries: Modeling and optimization using oxalic acid as a leaching agent," *Separation and Purification Technology*, vol. 320, 2023.

[14] M. Bruno, C. Francia, and S. Fiore, "Closed-loop recycling of lithium iron phosphate cathodic powders via citric acid leaching," *Environ Sci Pollut Res*, 2024.

[15] T. Zhao *et al.*, "A clean and sustainable method for recycling of lithium from spent lithium iron phosphate battery powder by using formic acid and oxygen," *Science of The Total Environment*, vol. 920, p. 170930, 2024.

[16] X. Chai *et al.*, "Study on green closed-loop regeneration of waste lithium iron phosphate based on oxalic acid system," *Waste Management*, vol. 181, pp. 168–175, 2024.

[17] B. Swain, J. Jeong, J. Lee, G.-H. Lee, and J.-S. Sohn, "Hydrometallurgical process for recovery of cobalt from waste cathodic active material generated during manufacturing of lithium ion batteries," *Journal of Power Sources*, vol. 167, no. 2, pp. 536–544, 2007.

CIRCULAR ECONOMY APPROACH FOR EAF SLAG VIA CARBOTHERMIC REDUCTION

Onur Uçar[1], Gizemnur Sülün[1], Rümeysa Korkmaz[1], Süleyman Esen[1], Onuralp Yücel[1],

1. Istanbul Techical University

Electric Arc Furnace (EAF) slag, a by-product of steelmaking, contains high levels of FeO and CaO but is often discarded or underutilized. The objective of this study is to apply a circular economy approach by using carbothermic reduction to recover metallic iron and convert the remaining slag into a secondary material that can be used in other industries. This approach seeks to reduce waste, lower environmental impact, and offer cost-effective resource recovery.

Carbothermic reduction experiments were performed using an induction furnace and graphite crucibles. The process temperature was maintained at approximately 1450–1470 °C to ensure effective slag reduction. Graphite served as the carbon source for reduction. EAF slag samples were charged into the crucibles and heated under controlled conditions. After processing, the metallic phase and the secondary slag were separated and analyzed. The chemical compositions of both products were determined using X-ray fluorescence (XRF), and metallic purity was measured to assess recovery efficiency. A mass balance was conducted to calculate iron recovery rates and changes in slag composition.

The experimental results indicated a high efficiency in metallic iron recovery. On average, 95% of the iron present in the EAF slag was successfully recovered, with the metallic phase reaching a purity of up to 89.3%. The FeO content in the secondary slag dropped significantly, from an initially high percentage to as low as 0.94%, indicating effective separation of iron from the slag. Additionally, the secondary slag showed a high CaO content, around 50%, which suggests its potential reuse as a supplementary cementitious material (SCM) in construction. These findings highlight the dual benefit of resource recovery and potential secondary applications.

This study demonstrates that carbothermic reduction is a viable and effective method for the valorization of EAF slag within a circular economy framework. By recovering high-purity metallic iron and producing a reusable secondary slag, the process not only minimizes industrial waste but also supports the development of sustainable materials. The use of low-cost carbon sources and existing furnace infrastructure contributes to the economic feasibility of the method. Overall, this approach promotes environmental sustainability and resource efficiency in metallurgical processes.

Keywords: Carbothermic, Metal Recovery, Circular Economy

Nanomaterials and Advanced Materials

TUNABLE MAGNETIC-LUMINESCENT Tb:SiO_2@Fe_3O_4 NANOPARTICLES FOR THERANOSTIC APPLICATIONS

Mehmet Fatih AKYEL [1] and Fatma UNAL [1,2*]

[1]Samsun University, Faculty of Engineering and Natural Sciences, Biomedical Eng. Dep., Samsun. Turkiye

[2]Samsun University, Vocational School of Technical Sciences, Samsun, Turkiye

*corresponding author: fatma.unal@samsun.edu.tr

Keywords: Core–shell nanostructures, magnetic-luminescent nanoparticles, photoluminescence, superparamagnetic, terbium doping

Abstract

Magnetic-luminescent Tb-doped SiO_2@Fe_3O_4 core@shell nanoparticles were synthesized via a two-step approach and evaluated for biomedical applications. Photoluminescence (PL) analysis showed broad emissions from the SiO_2 matrix and distinct Tb^{3+}-related peaks at 543–621 nm, corresponding to $^5D_4$-^7F_j (j=5,4,3) transitions. Increasing Tb content led to enhanced PL intensity and crystallinity. Vibrating sample magnetometer (VSM) confirmed superparamagnetic behavior, with high saturation magnetization values—45.53 emu/g for 1% and 36.93 emu/g for 3 mol. % Tb-doped samples—exceeding values reported in prior studies. The inverse relationship between Tb concentration and magnetization is attributed to 3d–4f orbital interactions and enhanced magneto-crystalline anisotropy. These multifunctional nanoparticles, combining high magnetic responsiveness and optical traceability, demonstrate strong potential for use in non-invasive, image-guided therapies, marking a significant advancement in multifunctional nanomedicine.

1. Introduction

In recent years, there has been growing scientific interest in in situ therapeutic strategies, particularly those enabling the direct delivery of functional particles to diseased tissues. This approach has gained prominence in the treatment of infections and cancer, where site-specific targeting is critical. Magnetic nanoparticles—including Fe_3O_4[1], γ-Fe_2O_3[2], $CoFe_2O_4$[3], $MnFe_2O_4$[4], $NiFe_2O_4$[5], $BaFe_{12}O_{19}$[6]—have been extensively investigated for their ability to be guided to target regions under an external magnetic field. These materials serve critical functions across diverse biomedical applications, including magnetic drug delivery, magnetic resonance imaging (MRI), cancer diagnosis and therapy, biosensing, and magnetic cell labeling [7–9]. Among these candidates, Fe_3O_4 has emerged as the most widely preferred magnetic material, owing to its unique combination of superparamagnetic properties, excellent biocompatibility, high chemical stability, and its proven capacity to stimulate osteoblastic activity and bone regeneration [10–13]. The ability to guide magnetic particles to specific anatomical regions using an external magnetic field necessitates the verification of their successful localization. To achieve this, rare earth (lanthanide) elements are frequently incorporated into magnetic particles, endowing them with luminescent properties that enable their non-invasive tracking under visible light illumination [13–15]. This luminescent feature facilitates real-time monitoring of particle distribution, thereby allowing treatment to be precisely confined to the target site. As a result, invasive surgical procedures can be circumvented, significantly reducing collateral damage to healthy tissues, and potentially eliminating the need for invasive procedures. Materials that simultaneously exhibit magnetic responsiveness and luminescence are commonly referred to as magnetic-luminescent nanoparticles [13–16]. Lanthanide-doped systems have attracted considerable interest not only for their applications in bioimaging and cellular labeling, but also for their multifunctionality in fields such as osteoporosis treatment, photodynamic and photothermal therapies, drug and gene delivery platforms, and as contrast agents in magnetic resonance imaging [17–21]. Although several studies have explored Fe_3O_4/terbium (Tb)/SiO_2-based magnetic-luminescent nanoparticles for biomedical applications, the reported saturation magnetization (σ_s) values remain relatively low, potentially limiting their efficiency in magnetic targeting. For instance, Shiyong et al. reported an σ_s of 18.48 emu/g for YF_4/Fe_3O_4@SiO_2@Tb(DBM)$_3$.2H_2O/SiO_2 nanostructures [14], while Sun et al. obtained an σ_s of 15.8 emu/g for Fe_3O_4@SiO_2@SiO_2-Tb(PABA)$_3$) nanoparticles [22]. Similarly, Fernández-Ramos et al. documented σ_s values of 11.33 emu/g for ($Y_{0.9}Tb_{0.1}VO_4$/Fe_3O_4)@SiO_2 and 18.08 emu/g for [($Y_{0.9}Tb_{0.1}VO_4$@SiO_2)/Fe_3O_4@SiO_2] hybrid systems [23]. In contrast, significantly lower values were reported by Khan et al. (3.01 emu/g for Fe_3O_4@SiO_2-(TTATb-AB)[1]) and Li et al. (0.075 emu/g for Fe_3O_4@SiO_2-TbDPA[15]). These findings highlight a

common challenge: the substantial reduction in magnetization due to multilayer coatings or low Fe_3O_4 content. Unlike previous approaches, the present study introduces a novel design in which Fe_3O_4 nanoparticles are deposited onto Tb-doped SiO_2 particles, resulting in significantly enhanced saturation magnetization values. This configuration offers improved magnetic responsiveness, making it a promising candidate for effective magnetic targeting in biomedical applications.

2. Materials And Method

The core@shell nanoparticles were synthesized via a two-step approach involving the modified Stöber method for silica core formation, followed by surface deposition of Fe_3O_4. In the first stage, both un-doped and terbium-doped silica (SiO_2 and Tb:SiO_2) particles were prepared. For the synthesis of SiO_2-based cores, a mixture of absolute ethanol and deionized water was prepared in a 1.5:1 (v/v) ratio and stirred magnetically at room temperature for 20 min to ensure homogeneity. Tetraethyl orthosilicate (TEOS), serving as the silica precursor, was then added dropwise under continuous stirring. For Tb-doped samples, a predetermined amount of terbium nitrate hexahydrate ($Tb(NO_3)_3.6H_2O$) was dissolved in the ethanol – water mixture after TEOS addition to introduce luminescent centers into the silica matrix. This mixture was designated as the first solution. In a separate vessel, a base-catalyzing agent was prepared by mixing ethanol and ammonium hydroxide (NH_4OH) in a 5:1 (v/v) ratio to form the second solution. The first solution was added dropwise into the second under vigorous magnetic stirring to initiate the hydrolysis and condensation of TEOS. The resulting colloidal suspension was stirred continuously for 3 hours at ambient conditions to allow the formation of silica particles. Upon completion of the reaction, the formed particles were separated by centrifugation and washed several times with absolute ethanol and deionized water to remove residual reactants and byproducts. The purified particles were then dried in an oven at 60 ºC for 24 hours. A subsequent calcination step was performed in a muffle furnace at 700 ºC for 6 hours in air to enhance the structural stability and remove any remaining organic components.

3. Results and Discussion

3.1. XRD Analysis and Crystallinity Index (CI)

All synthesized samples were subjected to crystallographic analysis using an X-ray Diffractometer (PANalytical) equipped with monochromatic CuKα radiation (λ=1.5406 Å), operated at a step size of 0.03º and a scanning rate of 2º/min. The XRD patterns of $SiO_2@Fe_3O_4$, 1Tb:$SiO_2@Fe_3O_4$, 2Tb:$SiO_2@Fe_3O_4$, and 3Tb:$SiO_2@Fe_3O_4$ particles are illustrated in Figure 1. The diffraction profiles of all samples exhibited characteristic peaks at 2θ≈30.2º, 35.6º, 43.3º, 53.7º, 57.2º, and 62.9º, which correspond to the (220), (311), (400), (422), (511), and (440) crystallographic planes of cubic magnetite (Fe3O4), respectively. These reflections are in excellent agreement with the standard JCPDS card no. #075-0449, thereby confirming the successful formation of the magnetite phase in all samples.

Table 1. Sample codes and corresponding chemical compositions of synthesized particles (mol. %).

Sample codes	SiO_2	Tb_2O_3
$SiO_2@Fe_3O_4$	100	0
1Tb:$SiO_2@Fe_3O_4$	99	1
2Tb:$SiO_2@Fe_3O_4$	98	2
3Tb:$SiO_2@Fe_3O_4$	97	3

Notably, no additional peaks indicative of secondary phases or impurity products—such as maghemite (γ-Fe_2O_3), hematite (α- Fe_2O_3), or terbium-related crystalline species—were detected in the XRD patterns. This observation suggests that the Tb dopant was either homogeneously incorporated into the amorphous silica matrix or present in quantities below the detection threshold of the XRD instrument. The structural coherence across all doped and un-doped samples indicates that the Fe_3O_4 deposition process retained phase purity and crystallinity, regardless of terbium incorporation. These results validate the effectiveness of the synthesized protocol in producing single-phase, magnetically active Fe_3O_4 coatings on both un-doped and doped silica cores, with no adverse effects on crystallographic structure.

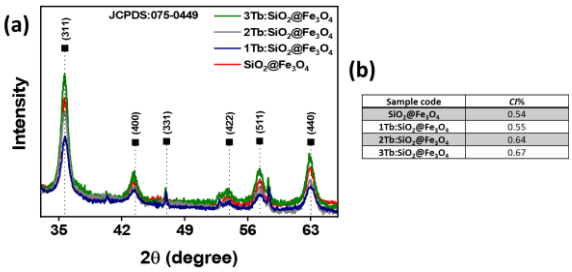

Figure 1. XRD patterns (a) and, Crystallinity index (CI%) values of $SiO_2@Fe_3O_4$, 1Tb:$SiO_2@Fe_3O_4$, 2Tb:$SiO_2@Fe_3O_4$ and, 3Tb:$SiO_2@Fe_3O_4$ samples (b).

The degree of crystallinity of the synthesized particles was quantitatively assessed through the calculation of the Crystallinity Index (CI%) based on X-ray diffraction data. The CI% was determined by evaluating the ratio of the area under the crystalline peaks (Acrystalline) to the total area of the diffractogram (Atotal), using the following equation (Eq. 1) [24]:

$$CI\% = (A_{crystalline}/A_{total}) \times 100 \quad (1)$$

This method allows the relative quantification of the crystalline portion in partially amorphous or nanocrystalline materials. The integrated areas were obtained via baseline subtraction and peak fitting applied to the XRD patterns using appropriate analytical software. The calculated CI% values were found to be 0.54 for SiO_2@Fe_3O_4, 0.55 for 1Tb: SiO_2@Fe_3O_4, 0.64 for 2Tb: SiO_2@Fe_3O_4,The progressive increase in crystallinity with higher Tb content may be attributed to the influence of terbium on the nucleation and growth kinetics of Fe_3O_4 nanocrystals during the coating process. This trend suggests that Tb incorporation does not hinder, and may even enhance, the formation of ordered crystalline domains within the magnetite shell. These findings further support the structural integrity and quality of the magnetic coating, indicating a successful synthesis approach capable of tuning crystallinity via dopant concentration.

3.2 Luminescence and Magnetic Properties of Core@Shell Nanoparticles

The photoluminescence (PL) and magnetic behaviors of the synthesized core@shell nanostructures were systematically investigated to evaluate their suitability for magnetically guided and optically traceable biomedical applications. PL emission spectra, acquired at room temperature under 349 nm excitation using an ANDOR SR500i-BL spectrometer, are presented in Figure 2a. As expected, Fe_3O_4 control sample exhibited negligible luminescence due to the lack of optically active centers. In contrast, all SiO_2-containing particles exhibited a broad emission band ranging from 400 to 700 nm. Deconvolution of this band using a Gaussian fitting model revealed two distinct peaks at 493 nm (~2.51 eV) and 569 nm (~2.17 eV), attributed to oxygen-deficient (≡Si–Si≡) and hydrogen-passivated (≡Si–H) centers in the silica network, respectively [25,26]. In the 3 mol. % Tb-doped sample, additional sharp emission peaks appeared at 543, 549, 585, and 621 nm. These peaks correspond to the intra-4f electronic transitions of Tb^{3+} ions: $^5D_4$-$^7F_5$ (543 and 549 nm, green emission), $^5D_4$-$^7F_4$ (585 nm, green-orange), and $^5D_4$-$^7F_3$ (621 nm, red). The emergence of a broad band between 360 and 390 nm, assigned to ligand-mediated transitions, further confirmed the successful incorporation and activation of Tb ions within the silica matrix. The PL intensity was found to increase proportionally with the Tb doping level, which is indicative of a higher population of optically active Tb^{3+} centers contributing to the emission. Moreover, this trend exhibited a strong correlation with the crystallinity index (CI%), suggesting that improvements in structural order enhance the radiative recombination efficiency. Complementary to the optical findings, magnetic characterization via vibrating sample magnetometer (VSM) revealed superparamagnetic behavior in all samples, as indicated by the absence of hysteresis in the magnetization–field (M–H) curves (Figure 2b). The saturation magnetization (σ_s) values for SiO_2@Fe_3O_4, 1Tb:SiO_2@Fe_3O_4, 2Tb:SiO_2@Fe_3O_4, and 3Tb:SiO_2@Fe_3O_4 were determined to be 45.53, 42.31, 44.26, and 36.93 emu/g, respectively. Although all samples retained sufficient magnetic responsiveness for external field-guided applications, a notable decrease in σ_s was observed with increasing Tb content. This decline in magnetization can be attributed to the magnetic dilution effect and electronic interactions between Fe^{3+} (3d orbitals) and Tb^{3+} (4f orbitals), which perturb the magnetic exchange interactions and contribute to increased magneto-crystalline anisotropy. Such interactions may disrupt the long-range magnetic ordering within the Fe_3O_4 shell, leading to reduced net magnetization.

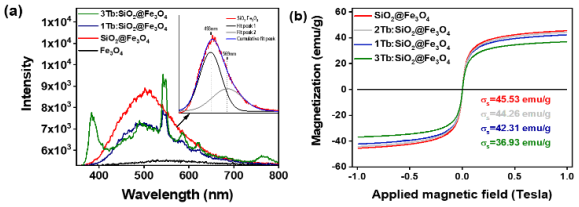

Figure 2. PL spectra of Fe_3O_4, SiO_2@Fe_3O_4, 1Tb:SiO_2@Fe_3O_4 and, 3Tb:SiO_2@Fe_3O_4 particles (a), Magnetization curves of SiO_2-Fe_3O_4, 1Tb:SiO_2@Fe_3O_4, 2Tb:SiO_2@-Fe_3O_4 and, 3Tb:SiO_2@Fe_3O_4 samples (b).

Taken together, these findings demonstrate the successful synthesis of magnetic-luminescent core@shell nanoparticles that combine the desirable attributes of high luminescence yield, superparamagnetic behavior, and tunable optical-magnetic responses via Tb doping. These multifunctional characteristics establish their potential utility in targeted drug delivery, multimodal imaging, and other theranostic biomedical applications.

4. Conclusion

In this study, magneto-luminescent core@shell nanoparticles based on Tb-doped silica coated with Fe_3O_4 were successfully synthesized via a two-step process and systematically characterized for their structural, optical, and magnetic properties. The synthesized particles demonstrated promising features for biomedical applications such as bioimaging, cell labeling, and targeted delivery.

References

[1] L. U. Khan, D. Muraca, H. F. Brito, O. Moscoso-Londono, M. C. F. C. Felinto, K. R. Pirota, E. E. S. Teotonio, and O. L. Malta, "Optical and magnetic nanocomposites containing Fe_3O_4@SiO_2 grafted with Eu^{3+} and Tb^{3+} complexes," J. Alloys Compd., vol. 686, pp. 453–466, 2016.

[2] A. Curcio, A. K. A. Silva, S. Cabana, A. Espinosa, B. Baptiste, N. Menguy, C. Wilhelm, and A. Abou-Hassan, "Iron oxide nanoflowers@CuS hybrids for cancer tri-therapy: Interplay of photothermal therapy, magnetic

hyperthermia and photodynamic therapy," Theranostics, vol. 9, no. 5, pp. 1288–1302, 2019.

[3] S. Sabale, V. Jadhav, S. Mane-Gavade, and X. Y. Yu, "Superparamagnetic $CoFe_2O_4$@Au with high specific absorption rate and intrinsic loss power for magnetic fluid hyperthermia applications," Acta Metall. Sin. (English Lett.), vol. 32, pp. 719–725, 2019.

[4] F. D. Heikham and D. S. Thiyam, "Fabrication of spherical magneto-luminescent hybrid $MnFe_2O_4$@YPO_4:$5Eu^{3+}$ nanoparticles for hyperthermia application," ChemistrySelect, vol. 2, pp. 10010–10019, 2017.

[5] A. M. Abu-Dief, I. F. Nassar, and W. H. Elsayed, "Magnetic $NiFe_2O_4$ nanoparticles: Efficient, heterogeneous and reusable catalyst for synthesis of acetylferrocene chalcones and their anti-tumour activity," Appl. Organomet. Chem., vol. 30, pp. 917–923, 2016.

[6] N. Shrivastava, N. A. Shad, M. M. Sajid, A. Duong, and S. K. Sharma, Design of Magnetic-Luminescent Nanoplatforms: Applications in Theranostics and Drug Delivery. Springer, 2020.

[7] C. Mi, J. Zhang, H. Gao, X. Wu, M. Wang, Y. Wu, Y. Di, Z. Xu, C. Mao, and S. Xu, "Multifunctional nanocomposites of superparamagnetic (Fe_3O_4) and NIR-responsive rare earth-doped up-conversion fluorescent ($NaYF_4$:Yb,Er) nanoparticles and their applications in biolabeling and fluorescent imaging of cancer cells," Nanoscale, vol. 2, pp. 1141–1148, 2010.

[8] S. Hu, Y. Zhou, Y. Zhao, X. Yang, F. Zhang, N. Gu, J. Ma, M. A. Reynolds, Y. Xia, and H. H. K. Xu, "Enhanced bone regeneration and visual monitoring via superparamagnetic iron oxide nanoparticle scaffold in rats," J. Tissue Eng. Regen. Med., vol. 12, pp. e2085–e2098, 2018.

[9] S. Khashan, S. Dagher, S. Al Omari, N. Tit, E. Elnajjar, B. Mathew, and A. Hilal-Alnaqbi, "Photo-thermal characteristics of water-based Fe_3O_4@SiO_2 nanofluid for solar-thermal applications," Mater. Res. Express, vol. 4, p. 055701, 2017.

[10] S. Mortazavi-Derazkola, M. Salavati-Niasari, H. Khojasteh, O. Amiri, and S. M. Ghoreishi, "Green synthesis of magnetic Fe_3O_4/SiO_2/HAp nanocomposite for atenolol delivery and in vivo toxicity study," J. Clean. Prod., vol. 168, pp. 39–50, 2017.

[11] J. Meng, B. Xiao, Y. Zhang, J. Liu, H. Xue, J. Lei, H. Kong, Y. Huang, Z. Jin, N. Gu, and H. Xu, "Super-paramagnetic responsive nanofibrous scaffolds under static magnetic field enhance osteogenesis for bone repair in vivo," Sci. Rep., vol. 3, p. 2655, 2013.

[12] G. Kandasamy and D. Maity, "Recent advances in superparamagnetic iron oxide nanoparticles (SPIONs) for in vitro and in vivo cancer nanotheranostics," Int. J. Pharm., vol. 496, pp. 191–218, 2015.

[13] F. Unal, "Production and characterization of magnetic-luminescent Fe_3O_4@ZnO:RE composite nanoparticles for biomedical application," Phys. Status Solidi A, p. 2300149, 2023.

[14] Y. Shiyong, Z. Renfei, Z. Jing, G. Xuechuan, L. Zhao, T. Zhibing, and S. Haiquan, "Synthesis and characteristic of the $NaYF_4$/Fe_3O_4@SiO_2@Tb(DBM)$_3$·$2H_2O$/SiO_2 luminomagnetic microspheres with core–shell structure," J. Nanosci. Nanotechnol., vol. 16, pp. 3791–3795, 2016.

[15] X. Li, Q. Wen, J. Chen, W. Sun, Y. Zheng, C. Long, and Q. Wang, "Lanthanide molecular species generated Fe_3O_4@SiO_2-TbDPA nanosphere for the efficient determination of nitrite," Molecules, vol. 27, p. 4431, 2022.

[16] L. U. Khan, L. F. M. Zambon, J. Santos, R. V. Rodrigues, L. S. Costa, D. Muraca, K. R. Pirota, M. C. F. C. Felinto, O. L. Malta, and H. F. Brito, "Red-emitting magnetic nanocomposites assembled from Ag-decorated Fe_3O_4@SiO_2 and Y_2O_3:Eu^{3+}: Impact of iron-oxide/silver nanoparticles on Eu_{3+} emission," ChemistrySelect, vol. 3, pp. 1157–1167, 2018.

[17] K. Zhao, J. Sun, F. Wang, A. Song, K. Liu, and H. Zhang, "Lanthanide-based photothermal materials: Fabrication and biomedical applications," ACS Appl. Bio Mater., vol. 3, no. 7, pp. 3975–3986, 2020.

[18] V. V. Bakhmetyev, T. S. Minakova, S. V. Mjakin, L. A. Lebedev, A. B. Vlasenko, A. A. Nikandrova, I. A. Ekimova, N. S. Eremina, M. M. Sychov, and A. Ringuede, "Synthesis and surface characterization of nanosized Y_2O_3:Eu and YAG:Eu luminescent phosphors which are useful in photodynamic therapy of cancer," Eur. J. Nanomedicine, vol. 8, no. 4, pp. 173–184, 2016.

[19] K. Wieszczycka, K. Staszak, M. J. Woźniak-Budych, and S. Jurga, "Lanthanides and tissue engineering strategies for bone regeneration," Coord. Chem. Rev., vol. 388, pp. 248–267, 2019.

[20] Y. Bu, B. Cui, W. Zhao, and Z. Yang, "Preparation of multifunctional Fe_3O_4@$ZnAl_2O_4$:Eu^{3+}@mSiO_2-APTES drug-carrier for microwave controlled release of anticancer drugs," RSC Adv., vol. 7, pp. 55489–55495, 2017.

[21] J. Zhou, Y. Sun, X. Du, L. Xiong, H. Hu, and F. Li, "Dual-modality in vivo imaging using rare-earth nanocrystals with near-infrared to near-infrared (NIR-to-NIR) upconversion luminescence and magnetic resonance properties," Biomaterials, vol. 31, pp. 3287–3295, 2010.

[22] D.-H. Sun, P. Lu, J.-L. Zhang, Y.-L. Liu, and J.-Z. Ni, "Synthesis of the Fe_3O_4@SiO_2@SiO_2–Tb(PABA)$_3$ luminomagnetic microspheres," J. Nanosci. Nanotechnol., vol. 11, pp. 9774–9779, 2011.

[23] M. Fernandez-Ramos, J. Isasi, M. Alcolea, T. Munoz-Ortiz, and E. Ortiz-Rivero, "New magnetic-fluorescent bifuntional ($Y_{0.9}Ln_{0.1}VO_4$/Fe_3O_4)@SiO_2 and [($Y_{0.9}Ln_{0.1}VO_4$@SiO_2)/Fe_3O_4@SiO_2] materials," Ceram. Int., vol. 48, pp. 22006–22017, 2022.

[24] H. Cakmak and F. Unal, "Reinforcement of Na-alginate based films with carrot juice processing wastes," Hittite J. Sci. Eng., vol. 7, p. 173, 2020.

[25] R. Salh, Crystalline Silicon – Properties and Uses: Silicon Nanocluster in Silicon Dioxide: Cathodoluminescence, Energy Dispersive X-ray Analysis and Infrared Spectroscopy Studies. IntechOpen, 2011.

[26] Y. D. Glinka, S. H. Lin, and Y. T. Chen, "The photoluminescence from hydrogen-related species in composites of SiO_2 nanoparticles," Appl. Phys. Lett., vol. 75, pp. 778–780, 1999.

Electrochemical Analysis and Investigation of Energy Storage Capacity of Wo3 with Active Carbon Additives with Different Morphologies

Serkan KILIÇTEK[1],

1. YILDIZ TECHNICAL UNIVERSITY

Supercapacitors are a class of energy storage technology that has significant potential in the contemporary energy landscape. These devices are notable for their environmentally friendly nature, short charge–discharge times, high power density, long cycle life, and high reliability. The design and fabrication of advanced electrode materials enables the effective utilization of these systems in strategic sectors, including electric vehicles, the defense industry, unmanned aerial vehicles (UAVs), and aerospace applications. Regardless of the type of energy source, enhancing storage capacity and ensuring the efficient utilization of stored energy are critical requirements for the development of sustainable energy systems.In this study, WO_3 powders with different morphologies were mixed with activated carbon to prepare an electrode slurry. Nickel foams with dimensions of 1 × 1.5 mm were subsequently cut and coated with the prepared slurry, rendering them suitable for electrochemical analyses. The electrochemical performance of the prepared electrodes was evaluated in a 6 M KOH electrolyte solution. According to the analysis results, the highest specific capacitance value was determined as 124.72 F/g at a scan rate of 5 mV/s, while the lowest specific capacitance value was recorded as 44.78 F/g at a scan rate of 100 mV/s.

Keywords: Supercapacitor, energy storage, tungsten

Impact of Surface Pre-Treatment on Electrochemical Performance of B_4C-Coated Nickel Foam Electrodes

Vecihe Elif İMAMOGLU[1], Suna AVCIOGLU [1], Figen KAYA[1] and Cengiz KAYA[1]

[1]Yıldız Technical University, Faculty of Chemistry and Metallurgy, Department of Metallurgical and Materials Engineering, 34210, Istanbul/TURKEY

Keywords: Boron Carbide (B_4C), Nickel Foam, Supercapacitors

Abstract

In this study, the influence of surface pre-treatment conditions on the electrochemical behavior of boron carbide (B_4C)-coated nickel foam electrodes for supercapacitor applications was systematically investigated. Nickel foam substrates were subjected to surface cleaning in 2M hydrochloric acid (HCl) treatment to effectively eliminate surface contaminants to enhance their conductivity and electrochemical activity. Two different techniques were employed: the first involved magnetic stirring for 30 minutes, while the second consisted of magnetic stirring followed by high-power probe ultrasonication for 10 minutes. Post-treatment, the nikel foam substrates were coated with 40µl B_4C slurry using drop casting technique.

The resulting composite electrodes were characterized using cyclic voltammetry (CV) and electrochemical impedance spectroscopy (EIS) to assess their capacitive performance. The findings reveal that the nature of the acid-cleaning process significantly affects the adhesion, uniformity, and electrochemical efficacy of the B_4C layer, thereby impacting the overall performance of the electrode. Application of the treatment led to an increase of 163.8783 F/g in specific capacitance relative to the untreated nickel foam, accompanied by a minor rise of 0.032 Ω in internal resistance as revealed by electrochemical impedance spectroscopy (EIS). These results underscore the critical role of optimizing surface modification parameters prior to active material deposition in the development of high-performance electrode architectures for advanced energy storage systems.

1. Introduction

The performance and reliability of supercapacitor electrodes are significantly influenced by the choice and surface treatment of the underlying substrate materials. Nickel foam, carbon cloth, stainless steel, and other conductive supports are commonly employed as current collectors and mechanical frameworks for active materials due to their high electrical conductivity, chemical stability, and porous structures that facilitate electrolyte diffusion [1,2]. Among these, nickel foam has gained widespread attention owing to its three-dimensional interconnected porous network, which offers large surface area and excellent electron transport pathways, enhancing the electrochemical activity of the deposited active materials [3].

However, the electrochemical behavior of electrodes is not solely dependent on the active material but also critically on the substrate's surface condition and its interaction with the coating layer. Surface pre-treatment methods such as acid cleaning, ultrasonication, and thermal annealing are widely adopted to remove impurities, increase surface roughness, and improve adhesion between the substrate and the active material, thereby optimizing the charge storage capabilities and cycling stability of the electrode [4,5]. Recent studies have demonstrated that variations in substrate preparation protocols can lead to significant differences in capacitive performance and impedance characteristics, highlighting the necessity of systematic optimization for each substrate-active material system [6,7].

In this context, boron carbide (B_4C)-coated nickel foam electrodes present a promising candidate for supercapacitor applications, combining the unique properties of B_4C with the conductive and porous nature of nickel foam [8]. This study aims to investigate the effect of different surface pre-treatment conditions on nickel foam substrates and their subsequent impact on the electrochemical performance of B_4C-coated electrodes, emphasizing the critical role of substrate preparation in achieving high-performance energy storage devices.

2. Experimental Procedure

2.1 Synthesis of B4C Powder (Active Material)

The synthesis of boron carbide was performed following the procedures previously established in our research group [9].

2.2 Production of Electrode

For process optimization, nickel foams intended for subsequent coating were subjected to three distinct pre-treatment protocols. In the first protocol, the foam was utilized without any surface modification. In the second, the substrate was immersed in a 2 M HCl solution and exposed to ultrasonic probe agitation for 10 minutes. In the third, the foam was initially conditioned on a magnetic stirrer at ambient temperature for 30 minutes, followed by ultrasonic probe treatment for an additional 10 minutes. Upon completion of the pre-treatment procedures, cyclic voltammetry (CV) analyses were conducted in a 6 M KOH electrolyte for all prepared samples. Thereafter, the substrates were uniformly coated with electrode slurries comprising boron carbide powders as the active material, after which the electrochemical characterizations were performed.

2.3 Electrochemical Measurements

Electrochemical analyses of the synthesized electrode material were carried out at room temperature (approximately 25 °C) using a Metrohm/VIONIC potentiostat/galvanostat system. A three-electrode configuration was employed, in which 6 M KOH served as the electrolyte. In this arrangement, the nickel foam coated with the active material acted as the working electrode, a platinum plate was used as the counter electrode, and an Hg/HgO electrode functioned as the reference.

3. Results and Discussion

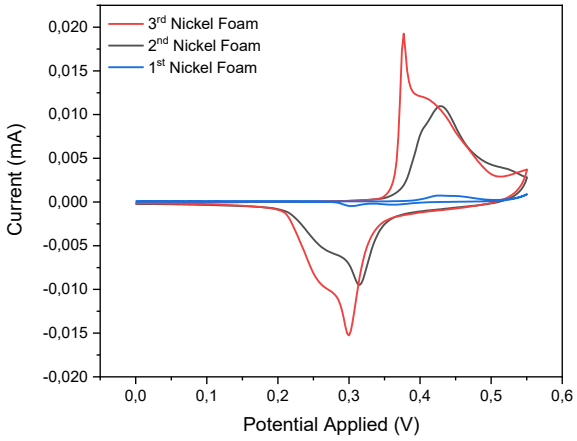

Figure 1. Cyclic voltammetry results measured using nickel foams subjected to three different treatments.

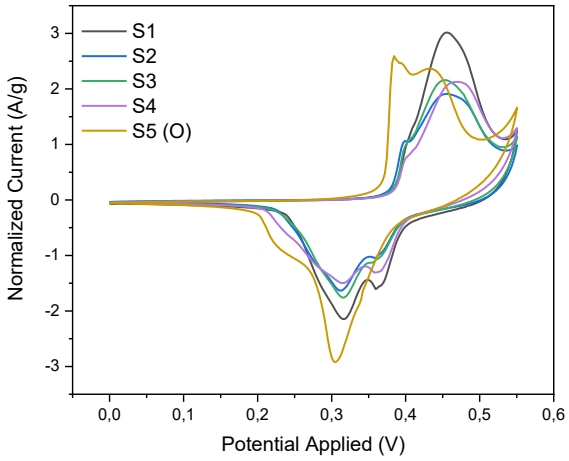

Figure 2. Cyclic voltammetry measurements of six samples analyzed for sample optimization.

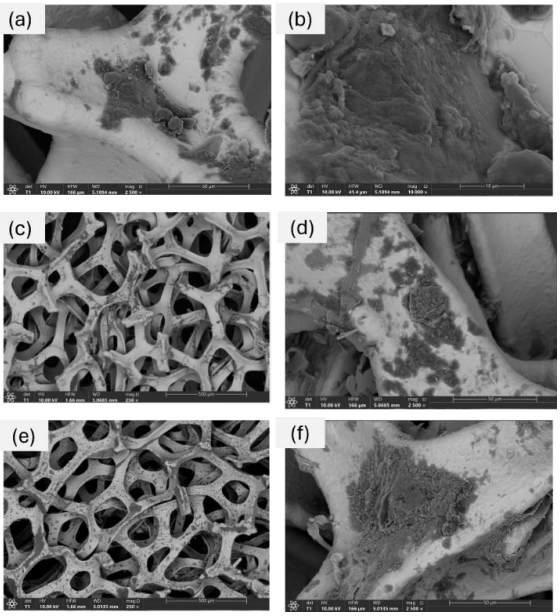

Figure 3. (a, b) correspond to the FE-SEM images of nickel foam No. 1, (c, d) correspond to those of nickel foam No. 2, and (e, f) correspond to those of nickel foam No. 3, recorded after measurements in 6 M KOH.

Based on the cyclic voltammetry (CV) profiles presented in Figures 1 and 2, the production method associated with the second nickel foam was selected for further use. For the first sample, the CV curves were found to enclose a relatively small area, indicating limited electrochemical activity, and it was determined that surface impurities generated during the manufacturing process required removal. While a well-defined curve shape was obtained for the second sample, prolonged exposure of the third sample to the HCl solution resulted in distortions of the CV curves. Distortions similar to those observed in the third nickel foam were also detected in the coated electrode material labeled as sample S5 (O) in Figure 2. Accordingly, the production method of the second nickel foam was adopted in subsequent measurements. Moreover, analysis of the peak and trough positions of the CV curves, corresponding to the reduction and oxidation peaks, revealed that their close proximity indicated a homogeneous and uniform distribution of the active material on the nickel foam surfaces.

An examination of the FE-SEM images obtained at different magnifications reveals that the nickel surface of Sample 1, measured in 6 M KOH and presented in Figure 3(a, b), exhibited no pronounced cracks; however, some residues adhered to the surface during measurement were detected. For Sample 2, shown in Figure 3(c, d), although the crack density was low, the amount of surface residues was found to be higher compared to Sample 1. In contrast, Sample 3, illustrated in Figure 3(e, f), displayed a markedly higher crack density than the other samples, accompanied by a correspondingly greater amount of surface residues.

4. Conclusion

During the preparation of nickel foams, the optimal cyclic voltammetry (CV) profiles were observed for the second nickel foam sample. Furthermore, after coating with boron carbide, the

second nickel foam demonstrated a homogeneous and uniform active material distribution. In contrast, the third nickel foam, which exhibited a high oxide content, showed distortions in its electrochemical response similar to those observed in its uncoated state. The average specific capacitance of boron carbide powders coated onto the electrode substrates was determined to be 203.306 F/g, demonstrating the material's promising capacitive performance. These findings highlight the critical importance of substrate selection and surface condition in achieving reliable and high-performance supercapacitor electrodes.

Acknowledgment

The authors are grateful for the financial support from The Scientific and Technological Research Council of Turkey (TUBITAK) under the contract number of 123C836.

References

[1] You, P., Tang, G., & Yan, F. (2019). Two-dimensional materials in perovskite solar cells. *Materials today energy*, *11*, 128-158.
[2] Ohashi, H., Hagiwara, M., & Fujihara, S. (2017). Solvent-assisted microstructural evolution and enhanced performance of porous ZnO films for plastic dye-sensitized solar cells. *Journal of Power Sources*, *342*, 148-156.
[3] Negro, E., Nale, A., Vezzù, K., Pagot, G., Polizzi, S., Bertoncello, R. & Di Noto, V. (2018). Hierarchical oxygen reduction reaction electrocatalysts based on FeSn0. 5 species embedded in carbon nitride-graphene based supports. *Electrochimica Acta*, *280*, 149-162.
[4] He, Y., Zhang, Y., Li, X., Lv, Z., Wang, X., Liu, Z., & Huang, X. (2018). Capacitive mechanism of oxygen functional groups on carbon surface in supercapacitors. *Electrochimica Acta*, *282*, 618-625.
[5] Fan, Y., Jiao, W., & Huang, C. (2018). Effect of the noncovalent functionalization of graphite nanoflakes on the performance of MnO2/C composites. *Journal of Applied Electrochemistry*, *48*(2), 187-199.
[6] Okwundu, O. S., Ugwuoke, C. O., & Okaro, A. C. (2019). Recent trends in non-faradaic supercapacitor electrode materials. *Metallurgical and Materials Engineering*, *25*(2), 105-138.
[7] Shang, Z., Huang, S., Xu, X., & Chen, J. (2009). Mo/MgO from avalanche-like reduction of MgMoO4 for high efficient growth of multi-walled carbon nanotubes by chemical vapor deposition. *Materials Chemistry and Physics*, *114*(1), 173-178.
[8] Li, Q., Sun, X., Lozano, K., & Mao, Y. (2016). Dependence of photoelectrochemical properties on geometry factors of interconnected "Caterpillar-like" ZnO networks. *Electrochimica Acta*, *222*, 232-245.
[9] Avcıoğlu, S., Kaya, F., & Kaya, C. (2021). Morphological evolution of boron carbide particles: Sol-gel synthesis of nano/micro B4C fibers. *Ceramics International*, *47*(19), 26651-26667.

Special Topics

INVESTIGATION OF HOT CORROSION RESISTANCE OF HIGH MANGANESE STEELS

Mustafa Guven Gok*

*Gaziantep University, Metallurgical and Materials Eng. Dep., Gaziantep, Turkiye

Keywords: Hadfield steel, Hot corrosion, Na_2SO_4–V_2O_5, AlTiB, Oxidation resistance

Abstract

In this study, hot corrosion resistance of Hadfield steel alloys (GX120Mn13) having high manganese (Mn 12–14%) content and containing Al5Ti1B (AlTiBor) at rates varying between 0.1 and 1 wt.% was investigated. In experimental studies hot corrosion salts (sodium sulfate (Na_2SO_4) and vanadium oxide (V_2O_5)) were used. These salts were applied to the surface of the samples at 30 mg/cm^2 and kept in open atmosphere at 950°C for a total of 12 hours. Weight losses and both cross-sectional and surface microstructures of the cooled samples were investigated. The findings showed that the hot corrosion resistance of the samples was improved by the formation of mixed protective oxide film layers such as Al_2O_3 and TiO_2 thanks to the AlTiBor addition.

1. Introduction

High-manganese austenitic steels (Hadfield steels) are widely used in applications involving severe impact and wear owing to their outstanding work-hardening capacity and toughness [1–4]. However, their resistance to high-temperature corrosion, particularly in environments containing sulfate/vanadate deposits, is comparatively limited. In such service conditions, molten salt deposits formed on hot components can react with the substrate and significantly accelerate degradation beyond simple dry oxidation.

Hot corrosion caused by alkali sulfates and vanadates is recognized as a distinct damage mechanism, especially in boilers and turbine hot sections. Fundamentally, low-melting oxyanion melts dissolve or disrupt protective oxide scales and may penetrate through microcracks, exposing large surface areas of the alloy to aggressive attack. In particular, Na_2SO_4 (sodium sulfate) reacts with V_2O_5 (vanadium pentoxide) to form eutectic mixtures that melt below about 600 °C, producing a continuous liquid film on the surface that penetrates cracks. This accelerates damage through basic/acidic fluxing reactions and/or internal sulfidation/oxidation [5–8]. At elevated temperatures, the molten Na_2SO_4-V_2O_5 mixture dissolves chromia/spinel scales, acts as a transport medium for cations/anions, and promotes the formation of non-protective, porous, exfoliating surface morphologies, thereby facilitating spallation. Altogether, these phenomena result in severe corrosion damage [9–12].

In contrast to Cr-rich stainless steels and alumina-forming alloys, conventional Hadfield-type high-Mn steels tend to form Mn-rich oxides (MnO/Mn_3O_4) and (Fe, Mn)-spinels at 900–1100 °C. However, such Mn-rich oxides and spinels are porous, loosely adherent, and thus non-protective. During the outward diffusion of Mn and Fe, subsurface decarburization occurs, generating porosity and a weak structure that reduces the adhesion of the oxide scale to the substrate. Moreover, the relatively high vapor pressure of MnO at 900–1100 °C can lead to volatilization, further accelerating decarburization and weakening the oxide adherence [13–15].

Therefore, alloy design strategies that promote the formation of more adherent oxides such as Al_2O_3 (alumina) and TiO_2 (titania) appear to be promising solutions to mitigate corrosion in salt-laden high-temperature environments. This rationale has been demonstrated in alumina-forming austenitic steels, where continuous alumina layers significantly improve high-temperature oxidation performance [16–19].

Table 1. Chemical composition of Hadfield steel (wt.%)

Specimen Code	C	Si	Mn	P	S	Cr	AlTiBor
Ref.	1.1 - 1.3	0.3 - 0.5	12 - 14	<0.1	<0.4	<0.04	-
01ATB							0.1
02ATB							0.2
05ATB							0.5
10ATB							1.0

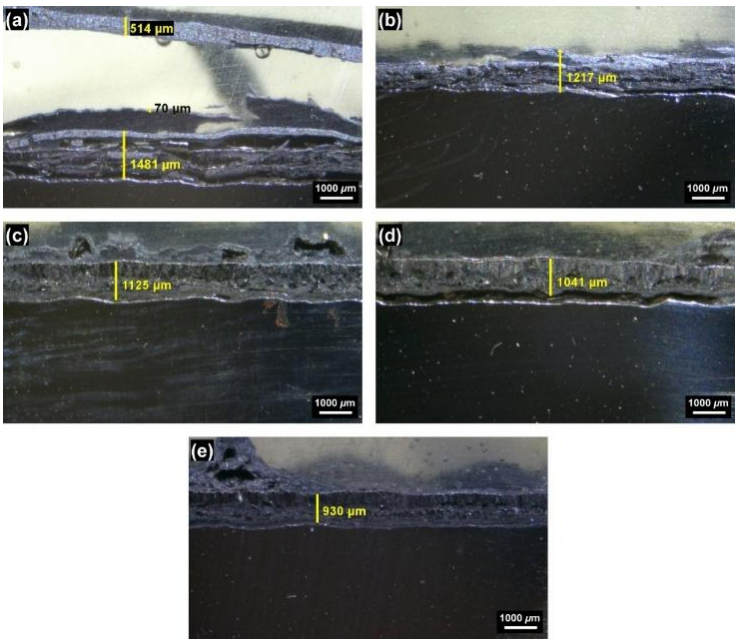

Figure 1. Images taken from the cross-sectional surface of the samples using a SOM. (a) ref., (b) 01ATB, (c) 02ATB, (d) 05ATB and (e) 10ATB.

From a thermodynamic perspective, Al_2O_3 and TiO_2 are much more stable than Fe-oxides within the temperature range relevant to hot corrosion. Across nearly all relevant temperatures, the standard Gibbs free energies of formation ($\Delta G°$) of Al_2O_3 and TiO_2 are lower (more negative) than those of $FeO/Fe_3O_4/Fe_2O_3$ and MnO. Consequently, enriching the near-surface region with Al and Ti can favor the preferential formation of alumina and/or titania, suppress the rapid growth of non-protective Fe/Mn oxides, and limit flux penetration by molten sulfate/vanadate [20–22].

Based on these considerations, the present study aims to evaluate the effect of varying Al_5Ti_1B (AlTiBor) additions (0.1–1 wt.%) on the hot corrosion resistance of Hadfield steel (GX120Mn13, containing 12–14 wt.% Mn) when exposed to aggressive Na_2SO_4–V_2O_5 salt mixtures at elevated temperature. The hypothesis of this study is that AlTiBor additions will (i) improve the adherence and continuity of the oxide scale and (ii) reduce subsurface damage beneath the scale. As a result, mass-change rates are expected to decrease and the development of non-protective Mn/Fe-oxide scales to be suppressed. In the study, stereo optical microscopy and FE-SEM/EDS were employed to characterize corrosion products and oxide morphologies, while mass-change measurements were used to help elucidate the underlying mechanisms.

2. Experimental Procedure

First, Hadfield steel was induction melted and alloyed by adding 0.1, 0.2, 0.5 and 1 wt.% AlTiBor (chemical composition of Hadfield steel and specimen codes were given in Table 1).

The resulting compositions were cast into Y-block sand molds. After casting, solution heat treatment was applied to the samples at 1050°C. The cooled samples were cut with the precision cutting method and then the surfaces of the cut samples were polished up to 800 mesh sandpaper level. For hot corrosion test, 30 mg/cm² of 50% Na_2SO_4 + 50% V_2O_5 salt mixture was applied to the polished surface. Coated specimens were exposed to temperatures at 950 °C for 3, 6 and 12 h in a muffle furnace without any inert or vacuum atmosphere. Samples that were kept in the furnace for the specified periods were cooled in the furnace. Mass change measurements were taken by using a precision scale (Precisa XB 220A) after each 3, 6 and 12 h intervals. Post-test characterization included stereo optical microscopy (SOM, SOIF SZM45-T2/L) and field emission scanning electron microscopy (FESEM, ZEISS - Gemini FESEM 300) with energy-dispersive X-ray spectroscopy (EDS) on cross-sections and surfaces. In order to obtain microstructure images from the cross-sectional surface, the samples were first cold-mounted. Then, they were cut with a precision cutting method and the cut surfaces were polished with a wet sanding method.

3. Results and Discussion

In the images taken with SOM in Figure 1 (a-e), the oxidation layers formed on the surface of the Hadfield steel after the hot corrosion test are clearly seen. In fact, the severe corrosion formed on the surface of the reference (ref.)

sample without AlTiBor addition is remarkable (see Figure 1 (a)). There was also a lot of spallation in the oxidation layer in this sample. On the other hand, as seen in Figure 1 (b-e), the thickness of the oxidation layer decreased regularly as the AlTiBor addition increased. It also took on a more homogeneous and continuous morphology (more tightly adhering to the metal). This showed that Al and Ti elements slowed down the corrosion rate by forming protective oxide layers (especially Al_2O_3 and TiO_2) at high temperatures. Therefore, the addition of AlTiBor to Hadfield steel up to 1% significantly improved the hot corrosion resistance by reducing the oxidation layer thickness by up to 37% (1481→930µm). The thicknesses of the formed oxidation layers for each specimen are given in Figure 2.

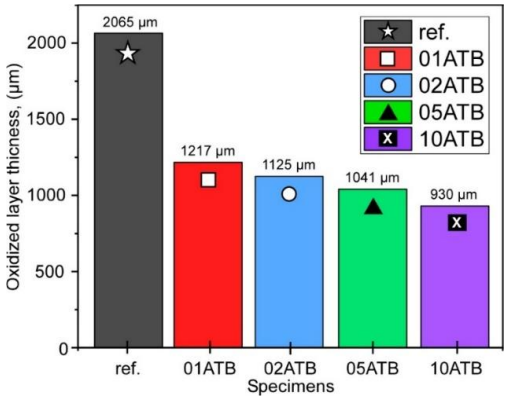

Figure 2. Oxidation layer thicknesses of all samples.

In addition, the FESEM cross-sectional images given in Figure 3 (a and b) confirmed the previous SOM results at higher magnification and resolution. Accordingly, in the microstructure of the reference sample without AlTiBor addition in Figure 3 (a), the penetration of corrosion products was probably noticeable along the spallation zone and the bifurcated cracks in the spalled oxidation layer. It was also seen that the metal surface remaining as a result of spallation had a dense rough morphology. On the other hand, it was seen that the oxide layer-metal boundary of the sample containing 1 wt% AlTiBor was flatter and the oxidation layer was denser. The cracks and pores along the oxidation layer were less compared to the reference sample. Thus, FESEM images supported that AlTiBor addition not only reduced the oxidation layer thickness but also dramatically improved the bond strength and integrity, thus providing more effective protection against high temperature corrosion.

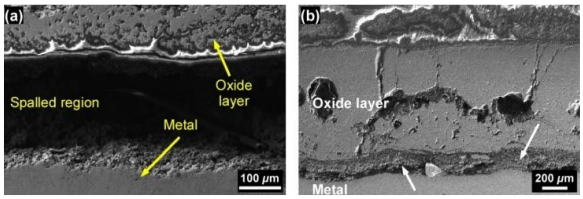

Figure 3. Images taken from the cross-sectional surface of the samples using a FESEM. (a) ref. and (b) 10ATB.

In Figure 4 (a-d), FESEM images of the surface morphology of the corrosion layer are given. When the general surface appearance given in Figure 4 (a) is examined, three different morphology regions are seen. A large part of the general surface consisted of finely structured acicular (needle-like) oxide crystals (Figure 4 (d)). On the right side of the general surface image, there were granular oxide nodules in a porous morphology (Figure 4 (b)). It was understood that the strength of this morphology was weak and prone to spallation. In Figure 4 (c), rod-like oxide lamellae were seen. These morphologies are generally the morphologies formed as a result of hot corrosion and are compatible with the studies in the literature [6–8,23,24].

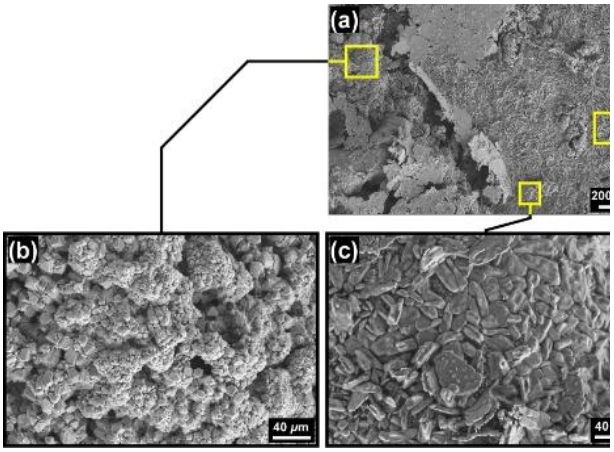

Figure 4. Images taken from the top surface of the reference sample using a FESEM. (a) general surface, (b) granular oxide nodules, (c) lamellar oxide rods and (d) acicular oxide crystals.

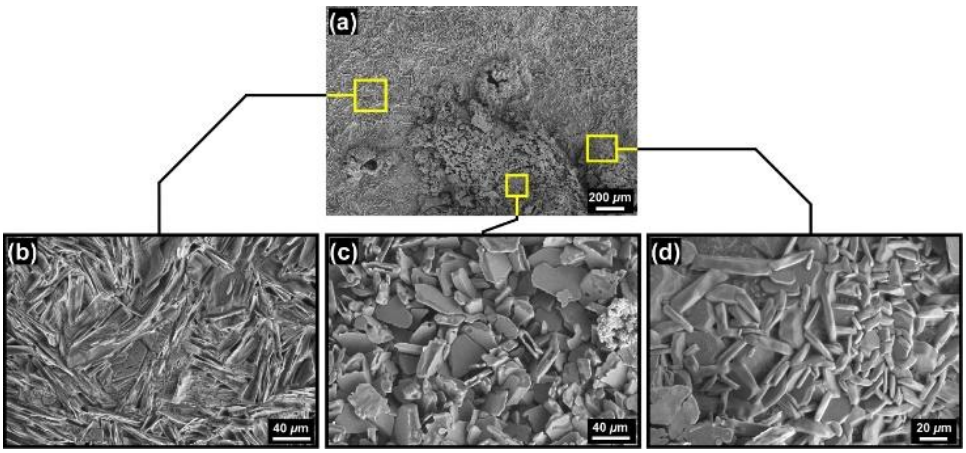

Figure 5. Images taken from the top surface of the 10ATB sample using a FESEM. (a) General surface, (b) acicular oxide crystals, (c) plate-like oxide crystals and (d) lamellar oxide rods.

The oxide layer surface morphology of the 10ATB sample is given in Figure 5 (a-d). When Figure 5 (a) was examined, it was seen that the general surface was dominantly acicular (needle-like). Unlike the reference sample without AlTiBor addition, the general surface was more homogeneous and consisted of needle-like oxide crystals. It was also noticed that this needle-like structure was in a more frequent form (Figure 5 (b)). As seen in Figure 5 (c and d), there were also plate-like and rod-like oxide crystal regions, respectively. However, unlike the reference sample, these occupied narrower areas on the general surface. Therefore, Al_2O_3/TiO_2 based acicular morphology and tighter oxide crystals formed a structure resistant to spallation and further V_2O_5+Na_2SO_4 penetration.

As a result of hot corrosion tests, the mass changes of the samples are summarized as percentages in Table 2 and Figure 6. As seen in Figure 6, the reference sample (ref.) reached the highest mass gain (4.26%), while the mass gains generally decreased as the AlTiBor addition increased.

Table 2. Weight changes in samples after hot corrosion tests at different times

Time (h)	Weight gain (%)				
	ref.	01ATB	02ATB	05ATB	10ATB
0	0.00	0.00	0.00	0.00	0.00
3	1.14	0.72	0.60	0.45	0.71
6	1.65	2.55	1.27	1.23	1.49
12	4.26	3.99	4.13	2.96	2.30

In general, the weight gain in the first 3 hours in the AlTiBor added samples was lower compared to the reference. This suggested that a thin, tight layer with Al_2O_3 and TiO_2 film was rapidly formed in the first oxidation stage in the 05ATB samples containing AlTiBor. At the end of 6 hours, an unexpected increase (2.55%) was observed in the 01ATB sample. This situation can be explained by the local protection weakness due to insufficient amount/distribution of AlTiBor. The lowest mass increase at 12 hours was recorded in the 10ATB (1 wt.%) sample with 2.30%. The high amount of AlTiBor in this sample provided the continuity and integrity of the protective oxide layer in the most efficient way. These results, in agreement with the shape and thickness analyses, show that the increase in the Al_2O_3/TiO_2 ratio strengthens the mechanical adhesion and reduces the penetration of V_2O_5-Na_2SO_4.

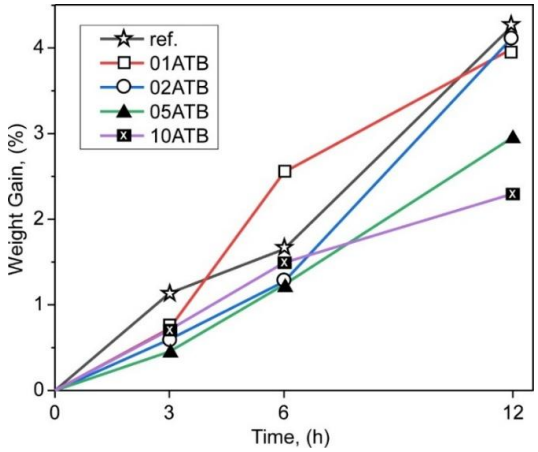

Figure 6. Weight change graph of samples after hot corrosion test at different times.

Accordingly, oxidation layers probably formed according to the following reactions (Equation 1-3).

$4/3\ Al + O_2 \rightarrow 2/3\ Al_2O_3$ (Equation 1)
$Ti + O_2 \rightarrow TiO_2$ (Equation 2)
$2\ Fe + O_2 \rightarrow 2\ FeO$ (Equation 3)

Thermodynamic data are critical in determining which oxide phases will form first. According to this, when Ellingham

diagrams [25,26] showing the standard Gibbs formation energies (ΔG°) of formation of metal oxides as a function of temperature are examined or when ΔG° values are calculated thermodynamically, it can be easily understood that the ΔG° values for the oxidation of Al, Ti, and Fe to form Al_2O_3, TiO_2, and Fe_2O_3 at 950 °C are approximately -900, -650, and -350 kJ/mol, respectively. Moreover, the order of ΔG° for the oxidation of Al, Ti and Fe is the same at all temperatures, not just at 950°C. Therefore, the presence of Al and Ti additives thermodynamically supports the formation of first Al_2O_3 and then TiO_2 layers on the metal surface. These oxidation layers limit the oxidation of iron and salt penetration.

4. Conclusion

- AlTiBor addition supported the in-situ formation of Al_2O_3, the most thermodynamically stable oxide, and then TiO_2 on the surface, creating a tight, homogeneous and adhesive oxidation layer.
- Compared to the reference sample, the oxide layer thickness decreased by 37% (1481 → 930 µm) in the sample containing 1 wt.% AlTiBor and spallation was significantly prevented.
- The lowest mass gain (2.30%) at the end of 12 hours was measured in the 10ATB (%1 wt. AlTiBor) sample; the high addition rate provided the continuity and integrity of the oxide layer in the most efficient way.
- In future studies, it is recommended to further support the chemical properties of the oxide layer (with XRD and EDS analyses), determine its mechanical properties and add tests longer than 12 hours.

Acknowledgment

The authors would like to thank the Gaziantep University Scientific Research Projects Coordination Unit.

References

[1] J.S. Park, S.C. Lee, J.K. Choi, S.J. Kim, Advanced Hadfield steel with Cr-optimization resists against corrosion and erosion-corrosion, Appl Surf Sci 637 (2023) 157875. https://doi.org/https://doi.org/10.1016/j.apsusc.2023.157875.

[2] S. Hu, H. Finklea, X. Liu, A review on molten sulfate salts induced hot corrosion, J Mater Sci Technol 90 (2021) 243–254. https://doi.org/https://doi.org/10.1016/j.jmst.2021.03.013.

[3] R. Zellagui, L. Hemmouche, H. Bouchafaa, R. Belrechid, H. Aitsadi, A. Chelli, M. Touil, N. Djalleb, Effect of Heat Treatments on the Microstructure, Mechanical, Wear and Corrosion Resistance of Casted Hadfield Steel, International Journal of Metalcasting 16 (2022) 2050–2064. https://doi.org/10.1007/s40962-021-00751-z.

[4] M. Sabzi, M. Farzam, Hadfield manganese austenitic steel: A review of manufacturing processes and properties, Mater Res Express 6 (2019). https://doi.org/10.1088/2053-1591/ab3ee3.

[5] T.A. Badea, D. Batalu, N. Constantin, A. Paraschiv, D. Pătroi, L.C. Ceatra, Assessment of Hot Corrosion in Molten Na2SO4 and V2O5 of Inconel 625 Fabricated by Selective Laser Melting versus Conventional Technology, Materials 15 (2022). https://doi.org/10.3390/ma15124082.

[6] M.G. Gok, G. Goller, Microstructural characterization of GZ/CYSZ thermal barrier coatings after thermal shock and CMAS+hot corrosion test, J Eur Ceram Soc 37 (2017) 2501–2508. https://doi.org/https://doi.org/10.1016/j.jeurceramsoc.2017.02.004.

[7] F. Kirbiyik, M.G. Gok, G. Goller, Application of thermal gradient and thermal cycling tests to Al2O3/CYSZ functionally graded TBC in the presence of simultaneous hot corrosion and CMAS effects, Surf Coat Technol 444 (2022) 128688. https://doi.org/https://doi.org/10.1016/j.surfcoat.2022.128688.

[8] G. Goller, M.G. Gok, State of the Art of Gadolinium Zirconate Based Thermal Barrier Coatings: Design, Processing and Characterization, in: L. Nanai, A.K. Samantara, S. Ratha, L. Fabian (Eds.), Methods for Film Synthesis and Coating Procedures, IntechOpen, Rijeka, 2019. https://doi.org/10.5772/intechopen.85451.

[9] S.A. Shaikh, A.J. Keche, C.D. Kuthe, Study of cyclic oxidation and hot corrosion of 310 SS under the environmental impurities of Na2SO4+V2O5 at different temperatures, in: IOP Conf Ser Mater Sci Eng, Institute of Physics Publishing, 2018. https://doi.org/10.1088/1757-899X/377/1/012066.

[10] L. Li, L. Li, G. Zhang, H. Xue, M. Cui, W. Wang, D. Liu, Hot Corrosion Behavior of Inconel 625 in Na2SO4 and V2O5 Molten Salt System, Metals (Basel) 13 (2023). https://doi.org/10.3390/met13061069.

[11] P. Huilgol, K.R. Udupa, K.U. Bhat, Hot Corrosion Resistance of Hot-Dip-Aluminized AISI 321 Stainless Steel in a Salt Mixture of 60%V2O5 + 40% Na2SO4 at 700 °C, Transactions of the Indian Institute of Metals 72 (2019) 1613–1616. https://doi.org/10.1007/s12666-019-01653-9.

[12] D. Deb, S.R. Iyer, V.M. Radhakrishnan, A comparative study of oxidation and hot corrosion of a cast nickel base superalloy in different corrosive environments, Mater Lett 29 (1996) 19–23. https://doi.org/https://doi.org/10.1016/S0167-577X(96)00109-7.

[13] M. Sangsuwan, S. Pokvitidkul, P. Wiman, Y. Tanaka, T. Thublaor, Manganese Constituent in Stainless Steels Oxidized in Oxygen Containing Water Vapor at 800 oC: High Temperature Oxidation and Volatilization, in: E3S Web of Conferences, EDP Sciences, 2023. https://doi.org/10.1051/e3sconf/202342802012.

[14] R.M. El-Shorbagy, L.Z. Mohamed, A. Abdelfatah, Effect of Chloride Salt Bath on Electrochemical Behavior and Morphology of 304L and 316L Stainless steels, Egypt J Chem 68 (2025) 343–354. https://doi.org/10.21608/EJCHEM.2024.302136.9963.

[15] C.-J. Wang, Y.-C. Chang, NaCl-induced hot corrosion of Fe–Mn–Al–C alloys, Mater Chem Phys 76 (2002) 151–161.

https://doi.org/https://doi.org/10.1016/S0254-0584(01)00515-6.
[16] Q. Gao, Z. Liu, H. Li, H. Zhang, C. Jiang, A. Hao, F. Qu, X. Lin, High-temperature oxidation behavior of modified 4Al alumina-forming austenitic steel: Effect of cold rolling, J Mater Sci Technol 68 (2021) 91–102. https://doi.org/https://doi.org/10.1016/j.jmst.2020.08.013.
[17] Y. Yamamoto, M.P. Brady, M.L. Santella, H. Bei, P.J. Maziasz, B.A. Pint, Overview of Strategies for High-Temperature Creep and Oxidation Resistance of Alumina-Forming Austenitic Stainless Steels, Metallurgical and Materials Transactions A 42 (2011) 922–931. https://doi.org/10.1007/s11661-010-0295-2.
[18] L. Liu, C. Fan, H. Sun, F. Chen, J. Guo, T. Huang, Research Progress of Alumina-Forming Austenitic Stainless Steels: A Review, Materials 15 (2022). https://doi.org/10.3390/ma15103515.
[19] N.M. Yanar, B.S. Lutz, L. Garcia-Fresnillo, M.P. Brady, G.H. Meier, The Effects of Water Vapor on the Oxidation Behavior of Alumina Forming Austenitic Stainless Steels, Oxidation of Metals 84 (2015) 541–565. https://doi.org/10.1007/s11085-015-9581-0.
[20] Z. Zhu, T. Jiang, G. Li, Y. Guo, Y. Yang, Thermodynamics of Reactions Among Al2O3, CaO, SiO2 and Fe2O3 During Roasting Processes, in: J.C. Moreno Piraján (Ed.), Thermodynamics - Interaction Studies - Solids, Liquids and Gases, IntechOpen, Rijeka, 2011. https://doi.org/10.5772/21545.
[21] G. Obulan Subramanian, C. Kim, W. Heo, C. Jang, Corrosion behaviour of alumina-forming heat resistant alloy with Ti in high temperature steam, Corros Sci 195 (2022) 110000. https://doi.org/https://doi.org/10.1016/j.corsci.2021.110000.
[22] Y.-B. Kang, J.-H. Lee, Reassessment of Oxide Stability Diagram in the Fe–Al–Ti–O System, ISIJ International 57 (2017) 1665–1667. https://doi.org/10.2355/isijinternational.ISIJINT-2017-182.
[23] A.R. Kannan, V. Rajkumar, C.D. Prasad, N.S. Shanmugam, J. Yoon, Microstructure and hot corrosion performance of stainless steel 347 produced by wire arc additive manufacturing, Vacuum 210 (2023) 111901. https://doi.org/https://doi.org/10.1016/j.vacuum.2023.111901.
[24] Q. Zhou, T. An, K. Zhang, C. Zhou, H. Qian, D. Ying, Y. Li, L. Zhang, Effect of microstructure on hot corrosion behavior of new superalloy Ad 730 in 75 wt% Na2SO4 + 25 wt% NaCl molten salt, Mater Lett 341 (2023) 134231. https://doi.org/https://doi.org/10.1016/j.matlet.2023.134231.
[25] H.J.T. Ellingham, Reducibility of Oxides and Sulphides in Metallurgical Processes, Journal of the Society of Chemical Industry 63 (1944) 125–160. https://doi.org/10.1002/jctb.5000630501.
[26] M. Hasegawa, Ellingham Diagram, in: S. Seetharaman (Ed.), Treatise on Process Metallurgy, Elsevier, Stockholm, 2014: pp. 507–516. https://doi.org/10.1016/B978-0-08-096986-2.00032-1.

Integration of Cold Stretch Testing and FEM Analysis in the Development of a Cryogenic Tank for Industrial Storage of Cryogenic Fluids

Marian Staicu[1], Viorica Ghisman [1], Gabriel Bogdan Carp [1], Daniela Buruiană[1],

1. Interdisciplinary Research Centre in the Field of Eco-Nano Technology and Advance Materials CC-ITI, Faculty of Engineering, "Dunarea de Jos" University of Galati

The paper presents the design, analysis, and testing of a cryogenic tank intended for industrial applications, aiming to optimize mechanical performance and enhance operational safety. The assembly, consisting of an inner vessel, outer vessel, and vaporizer, is designed to ensure the safe and efficient storage of cryogenic fluids in industrial environments.To increase the usable volume and improve the mechanical behavior of the inner vessel, cold stretching was applied to induce strain hardening. The tank was subjected to a test pressure of 57 bar, resulting in controlled plastic deformation with diameter expansion, confirming structural integrity under high mechanical stress.To validate the design and prevent structural deficiencies, a finite element method (FEM) analysis was performed before experimental testing. The strong correlation between simulation and experimental results confirmed the model's accuracy and the methodology's effectiveness, supporting the development of reliable cryogenic storage solutions.

Keywords: cryogenic storage,hydraulic reinforcement,plastic

Deep Learning and Novel Sensor Architectures for Structural Health Monitoring

Mohammad Ikhsan BIN ZAKARIA[1], Prof. Tarik OZKUL[2]
[1] Department of Computer Science and Engineering, Istanbul Sabahattin Zaim University
[2] Department of Computer Science and Engineering, Istanbul Sabahattin Zaim University

Abstract

This study explores state-of-the-art technologies in predictive maintenance, with a focus on the deployment of Structural Health Monitoring (SHM) systems for fatigue failure detection. The research aims to develop novel algorithms that enhance the accuracy and reliability of damage identification in high-stress engineering structures. A comprehensive literature review was conducted to examine the core components of SHM, including advanced sensing technologies, artificial intelligence models—particularly deep learning architectures—and the supporting network infrastructure required for scalable and effective system integration.

Keywords: structural health monitoring, artificial intelligence, predictive maintenance

1. Introduction

Manual monitoring of infrastructure is a laborious task that can lead to fatigue, thereby increasing safety risks. Essential systems, such as aircraft, buildings, and bridges, require constant supervision to avoid unexpected failures. For example, a bridge collapse that occurs without any apparent damage prompts immediate inquiries regarding responsibility and the underlying cause.

Structural Health Monitoring (SHM) combines sensors, edge devices, RF modules, and cloud systems to enable predictive maintenance. Its effectiveness relies on analyzing collected data to detect early damage. AI—especially deep learning—boosts this by extracting insights from complex datasets. Hoon et al. identified four SHM pillars: operational evaluation, data acquisition/cleaning, feature extraction, and statistical modeling [1][21][22].

Predictive maintenance research enhances SHM systems and deep learning models to improve repair strategies. Aircraft and bridges face repeated stress, demanding fatigue-resistant materials. Paris' law is a key tool for modeling crack growth and failure risk in civil engineering.

Structural maintainability is vital for risk management, but ongoing human oversight is demanding. IoT and fast connectivity now allow small teams to monitor efficiently. Combining physical variables with IT advances enables self-sensing, self-diagnostic structures.

Examples of SHM systems include vibration-based monitoring using magnetostrictive sensors and accelerometers [11], aircraft pipeline fault detection resembling helicopter tail booms [25], wireless power transfer influenced by moisture and coil placement [26], and bridge crack detection using ADXL345 accelerometers with RF modules [27]. See Figure 5 for system layout.

This paper is organized as follows: Section 2 reviews current Structural Health Monitoring (SHM) methods. Section 3 focuses on failure detection and structural integrity. Section 4 outlines data acquisition techniques. Section 5 explores relevant deep learning algorithms. Section 6 concludes with key findings and future research directions.

2. SHM Methodologies

SHM methods include model-driven approaches that refine finite element models [20], and data-driven techniques that track structural changes via statistical patterns. Mariani linked temperature data to structural responses using regression [1]. Bridge damage detection often relies on these two strategies. Xiangli et al. enhanced feature separation with adversarial training and circle loss [3].

Generally predictive maintenance methodologies are divided into three methods:

- Physic-based method.
- Data-driven method.
- Hybrid-based method.

Physic-based predictive maintenance is a well-established methodology that uses the fundamental laws of physics to model how systems degrade over time. Unlike purely data-driven approaches, it focuses on understanding the physical failure mechanisms and stress-response behavior of components under real-world oper-

ation conditions.

Figure 1: Big data platform structure

Banavara et al. used Digital Twin technology for accurate aircraft damage detection under varied flight conditions [4]. Yang et al. developed a big data–driven bridge monitoring platform with four modules: storage, display, export, and warning [18]. Wang et al. reviewed GNSS/BDS-based bridge deformation tracking, showing how 3D time series reveal modal characteristics [19]. Zonzini et al. combined IoT and multi-source monitoring in the MAC4PRO SHM framework. Dimitrios et al. introduced a damage estimation model using multi-linear summation to simulate nonlinear accumulation [14]. Federica et al. proposed a sensor cloud architecture with three layers, integrating hardware and software for signal acquisition and structural assessment [24].

3. Key Components

Huia et al. emphasized the importance of sensing technologies in SHM, such as piezoelectric ceramics, fiber Bragg gratings, and ultrasonic methods [2]. Damage detection approaches include probabilistic analysis and information fusion to address structural and environmental uncertainties. John et al. introduced vibration-based techniques to identify functional changes and detect issues through vibrational data [7].

3.1. Finite Elements

Yu et al in their research concentrated on the foundational theoretical aspects of intelligent systems for structural health monitoring, examining the acquisition of the stress intensity factor (SIF) through macro fiber composite (MFC) sensors to assess the lifespan of crack propagation as influenced by SIF. The Paris formula provides a means to establish the correlation between crack length, the stress intensity factor, and the remaining lifespan of a material [17]. Moreover the extended finite element method is employed to address the constraints of the empirical formula concerning the crack failure model, thereby broadening the applicability of the empirical formula.

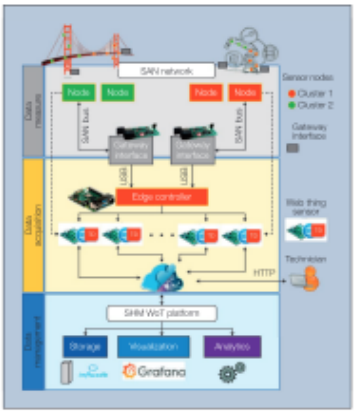

Figure 2: Federica proposed architecture

3.2. Fatigue Strength

Fatigue strength is defined as the capacity of a material to endure repeated or cyclic loads without experiencing failure attributed to fatigue. Fatigue failure arises when a material is exposed to varying stress levels over an extended period, even if these stress levels are below the material's ultimate tensile strength. A crucial aspect to consider is that, when subjected to repeated loading, a material may fail at significantly lower stress levels compared to those encountered in static loading conditions.

3.2.1. Stress-Life (S-N)

This illustration depicts the correlation between the number of cycles until failure (N) and the stress amplitude (S). The graph indicates that with an increase in the number of cycles, the maximum permissible stress diminishes. The material continues to be extensively utilized in design applications where the stress experienced remains predominantly within the elastic range, resulting in extended lifespans (cycles to failure).

3.2.2. Fatigue Limit

Certain materials, such as steel, possess a stress threshold beneath which they can theoretically endure an unlimited number of cycles without experiencing failure. This

phenomenon is referred to as the endurance limit. However, not all materials demonstrate a distinct endurance limit; for instance, aluminum and various polymers lack a clearly defined fatigue limit.

3.2.3. Fatigue Strength Factors

Fatigue Strength Factors play a critical role in determining a material's resistance to failure under cyclic loading. These factors influence how long a structure can endure repeated stress before cracks initiate or propagate. Key contributors include surface finish, temperature, environmental conditions, geometry, and material properties. Understanding and optimizing these variables is essential for designing durable components in aerospace, civil, and mechanical engineering applications.

- **Surface Finish**. Smoother surfaces improve fatigue strength by reducing stress concentrators.
- **Temperature**. High temperatures weaken material integrity, especially metals.
- **Environment**. Corrosive conditions accelerate fatigue through stress corrosion.
- **Size and Geometry**. Larger or complex shapes with sharp features increase stress and reduce fatigue strength.

4. Sensing Technologies

Dan et al. used a multi-functional sensor network with flexible piezoelectric and microfiber composite (MFC) sensors to detect failures in inflatable Softgoods structures [5]. These sensors support long-term SHM and RUL assessments. John et al. introduced the steel slit damper (SSD) to monitor fatigue and reduce seismic damage by dissipating energy [7]. Sensor technologies continue to evolve, including dielectric resonator and fiber Bragg grating (FBG) systems, each with distinct applications and research backing.

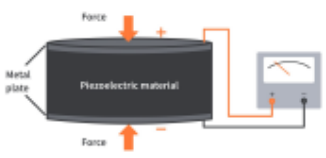

Figure 3: Piezoelectonic Example

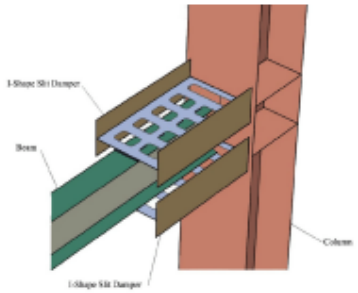

Figure 4: Steel Slit Damper

The cylindrical dielectric resonator (CDR) sensor detects cracks by tracking resonant frequency shifts, showing high sensitivity to crack depth [13][16][15]. Chien developed a low-cost IoT node with an organic pressure sensor using polyurethane film for SHM data collection and processing [6]. Charles et al. introduced a flexible Smart Skin temperature sensor for localized monitoring [12]. Koganezawa et al. designed a self-powered vibration sensor using magnetostrictive material, leveraging magnetic flux changes for accurate, long-term SHM without manual recharging [11].

Wang et al. studied Fiber Bragg Grating (FBG) sensors, derived from 1990s optical fiber technology, highlighting their principles and SHM applications [8]. First proposed by Morey, FBG sensors expanded fiber use beyond communication. They offer key advantages: EMI immunity, compact size (125 μm), lightweight, high thermal resistance (400–600°C), strong multiplexing, long-range transmission, corrosion resistance, and high sensitivity.

4.1. Sensing Technology Categories

Sensing technologies include a diverse array of instruments, techniques, and tools designed to identify and quantify physical, chemical, and environmental variables. These technologies are essential across multiple domains, including industrial automation, healthcare, environmental surveillance, and consumer electronics.

- Physical Sensing Technologies.
- Chemical and Gas Sensing Technologies.
- Optical Sensing Technologies.
- Biosensing Technologies.
- Environmental Sensing Technologies.
- Position and Proximity Sensing Technologies.
- Acoustic and Ultrasonic Sensing Technologies.
- Motion and Force Sensing Technologies.

- Smart Wearable Sensors.
- Integrated and Multimodal Sensing Technologies.

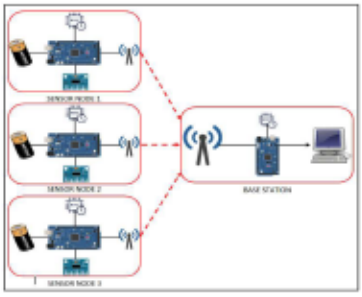

Figure 5: Rolando proposed architecture

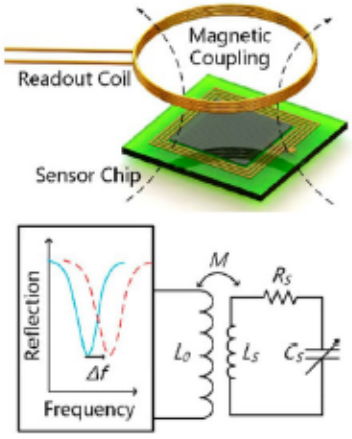

Figure 6: Wireless Sensor Example

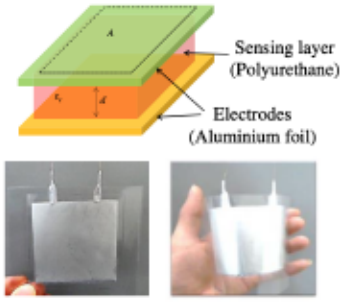

Figure 7: Pressure Sensor Example

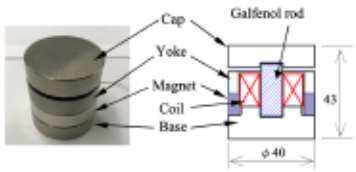

(a) A picture of the device (b) Cross-sectional view of the device

Figure 8: A vibration sensor

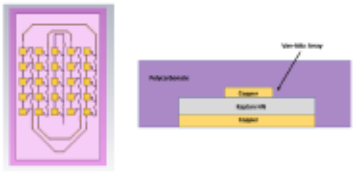

Figure 9: Smart Skin Temperature Sensor

A separate study conducted by Cai et al. focused on structural health monitoring (SHM) through vibration analysis to detect structural failures in multimotor unmanned aerial vehicles (UAVs). In their investigation, they integrated multiple sensors, including gyroscopes, accelerometers, and motion sensors. Their analysis of the motion sensor and vibration measurement modules identified faults in the assembly components[9].

5. Data Acquisition Techniques

The effectiveness of Structural Health Monitoring (SHM) can be greatly improved by integrating Internet of Things (IoT) devices and infrastructure, which utilize diverse data acquisition techniques. Nevertheless, depending on IoT for data gathering introduces several challenges, such as risks of data loss, corruption, and synchronization difficulties. As a result, the stages of data acquisition, along with subsequent data cleaning and processing, become essential elements in the monitoring methodologies applied in SHM applications.

Malekloo et al added optimization of two critical components in data acquisition is imperative: (1) the quantity of sensors and (2) their strategic placement. Excessive and superfluous data can overload the data acquisition system, thereby impeding the subsequent operations of the Structural Health Monitoring (SHM) system. Furthermore, given that these sensors are generally installed in a permanent manner, a haphazard approach to the design of a data acquisition system could lead to further

complications [22]. Machine learning models are generally modified to optimize the placement of current sensor locations, thereby enhancing the overall efficacy of the system in detecting damage. This approach provides straightforward, flexible, and cost-effective alternatives compared to conventional methods.

5.1. Blind source separation

Blind source separation (BSS) is a technique designed to isolate distinct signal sources from a collection of mixed signals, utilizing minimal to no prior information. The development of machine learning algorithms for blind source separation (BSS) applications is aimed at resolving a range of challenges, including the complexities associated with modeling and the variability inherent in heterogeneous environments. These algorithms are effectively utilized in practical applications, such as structural health monitoring (SHM) within the field of civil infrastructure.

5.2. Data Loss

Data-driven SHM faces challenges from missing or lost data [28][10]. Deng et al. addressed this with a deep learning framework combining imputation and damage detection using an LSTM-based autoencoder, where dropout simulates data loss and reconstruction error signals damage [28]. Tested on cable tension data from a cable-stayed bridge, the method proved effective. Shruti et al. used orthogonal matching pursuit (OMP) to recover lost ultrasonic sensor data by exploiting signal sparsity and applying a Hanning window [10]. Transmission losses—due to attenuation, collisions, or hardware faults—can hinder SHM reliability, but adaptive signal processing and interpolation offer recovery solutions.

6. Deep Learnings

Malekloo et al. identify a variety of machine learning algorithms employed in Structural Health Monitoring (SHM), including Decision Trees (DT), Support Vector Machines (SVM), Random Forests (RF), k-Nearest Neighbors, Bayesian methods, Neural Networks, K-means clustering, Gaussian Mixture Models, and Association Analysis, with some being categorized as supervised and others as unsupervised or semi-supervised [22]. Their research suggests that relying on supervised learning algorithms for analysis in SHM is often impractical, as fully labeled datasets are seldom available in real-world applications.

To accomplish data-driven technique SHM application in predictive maintenance system, it must follow 8 important steps:

- Detecting the existence of damage (Excitation methods)
- Data acquisition
- Data normalization
- Data cleaning
- Data compression
- Feature extraction
- Data fusion
- Pattern recognition

Yang proposed a novel algorithm combining Graph Neural Networks (GNNs) and Reinforcement Learning (RL) to address urban infrastructure challenges, enabling intelligent monitoring and adaptive maintenance decisions [23]. The GNN-based model captures structural node relationships, while RL optimizes maintenance strategies. Barthorpe et al. applied support vector machines for pattern recognition in damage detection, using a feature-rich experimental database to train their classifier [29].

7. Experiment

This review article underscores the importance of investigating experimental methodologies related to data-driven strategies in predictive maintenance applications. Researchers such as Chen et al. have implemented data-driven approaches to enhance predictive accuracy [30]. Additionally, deep learning techniques have been employed to reduce the substantial expenses linked to fatigue testing, particularly in the creation of training datasets for the multiaxial fatigue life of metallic materials. Chen et al. assembled a comprehensive dataset consisting of 1167 samples derived from 40 distinct materials referenced in existing literature. This dataset aims to facilitate researchers in utilizing deep learning for predicting fatigue life, thereby tackling the ongoing issue of limited data availability and fostering progress at the intersection of artificial intelligence and metal fatigue studies. The dataset is categorized into two distinct groups: the first group comprises data points obtained from stress-controlled experiments, while the second group includes

data points derived from strain-controlled experiments. To guarantee the technical integrity and relevance of our dataset, we utilized a range of established deep learning algorithms, such as GRU (Gated Recurrent Unit), LSTM (Long Short-Term Memory Networks), and 1D CNN (One-Dimensional Convolutional Neural Network), in conjunction with fully connected layers (FCL) to assess the dataset's validity.

Bruno et al employed machine learning techniques to facilitate predictive maintenance, focusing on real-time anomaly detection and forecasting of potential failures[31]. A variety of analog sensor signals, including pressure, temperature, and current consumption, alongside digital signals such as control and discrete signals, as well as GPS data encompassing latitude, longitude, and speed, establish a comprehensive framework that facilitates the advancement of novel machine learning techniques. The predictive maintenance system applied to the Air Production Unit (APU) located on the roofs of Metro vehicles supplies units that carry out various functions. Bruno demonstrated the predictive maintenance on MetroPT rail way using IoT and machine learning. It revealed to us that using IoT and machine learning and deep learning methods can be implemented. As we the data is collected in certain period of time. We can not gather data in short time and take conclusion based on that. It must have support data and AI model that support our decision.

Used model	MAE	MSE	R^2
CNN + FCL	0.181932	0.146262	0.155936
LSTM + FCL	0.116249	0.059000	0.056612
GRU + FCL	0.826342	0.911863	0.915431

8. Discussion

In the context of Structural Health Monitoring (SHM) technology, our literature review and research indicate several critical considerations. Firstly, it is essential to determine the type of structure that requires monitoring, which will subsequently inform the selection of appropriate sensing technologies. This initial step is crucial for effective implementation. Secondly, the choice of an IoT gateway or communication method must be made, ensuring that it is well-suited for the specific application. While wireless network sensing technology is advantageous for stationary structures such as bridges and buildings, it may not be the best option for aircraft, which are in constant motion. Thirdly, a robust data loss recovery methodology should be integrated into the system to manage the time series data collected. The establishment of warning or alert systems must be calibrated according to the significance of the detected anomalies. Lastly, the selection of forecasting models utilizing artificial intelligence should prioritize those that yield the most accurate and reliable results.

References

[1] S. Mariani, A. Kalantari, R. Kromanis, A. Marzani, Data-driven modeling of long temperature time-series to capture the thermal behavior of bridges for SHM purposes, Mechanical Systems and Signal Processing 206 (2024) 110934

[2] LI Huia, OU Jinping, Structural Health Monitoring: From Sensing Technology Stepping to Health Diagnosis, 1877–7058 © 2011 Published by Elsevier Ltd

[3] Xiangli Yanga, Xijie Denga, Hanwei Zhangb, Yang Zoud, Jianxi Yang, Enhancing robustness of data-driven SHM models: adversarial training with circle loss

[4] Banavara R. Seshadr, Structural Health Management of Damaged Aircraft Structures Using the Digital Twin Concept, American Institute of Aeronautics and Astronautics

[5] Dan Xiang, Carson Willey, A Multi-Functional Sensor Network System for Health Monitoring of Inflatable Softgoods Structures, 2023 Prognostics and Health Management Conference (PHM), DOI 10.1109/PHM58589.2023.00022

[6] Chien Khong Duc, Toan Thanh Dao, Anh Bui Tien, Van-Phuc Hoang, "An IoT Node with Organic Pressure Sensor for Structural Health Monitoring System", 2020 International Conference on Green and Human Information Technology (ICGHIT), DOI 10.1109/ICGHIT49656.2020.00012

[7] John Mark G. Payawal, Dong-Keon Kim, A Review on the Latest Advancements and Innovation Trends in Vibration-Based Structural Health Monitoring (SHM) Techniques for Improved Maintenance of Steel Slit

Damper (SSD), Received 28 February 2024, accepted 19 March 2024, date of publication 25 March 2024, date of current version 29 March 2024.

[8] Limin Wang, Chuncheng Xiao, Wenqi Ding, Jiayi Wu, Chunlin Shi, Application Overview of Fiber Bragg Grating Sensors in Structural Health Monitoring, 978-1-6654-5864-1/22/31.00 ©2022 IEEE.

[9] Jiandong Cai,Menglong Ding,Xufie Yan,Yiren Hu,Anhuan Xie,Xian Su, "Preliminary Study of Vibration-based Structural Health Monitoring for Multirotor Unmanned Aerial Vehicle", 2022 8th International Conference on Mechanical Engineering and Automation Science(ICMEAS), DOI 10.1109/ICMEAS57305.2022.00036

[10] Shruti Sawant,Sauvik Banerjee,Siddharth Tallur, Compressive sensing based data-loss recovery enables robust estimation of damage index in ultrasonic structural health monitoring, 978-1-7281-6801-2/20/31.00 ©2020 IEEE

[11] Shinji Koganezawa, Tomotake Ishii, Hiroshi Tani, Renguo Lu, Norio Tagawa, Development of Vibration Sensor Using Giant Magnetostrictive Material for Self-Powered Structural Health Monitoring System, 978-1-7281-6801-2/20/31.00 ©2020 IEEE

[12] Charles A. Lynch III, Ajibayo O. Adeyeye, Bijan Tehrani, Manos M. Tentzeris, Flexible Passive Smart Skin Temperature Sensor for Remote Sensing in Structural Health Monitoring Applications, 2021 IEEE International Symposium on Antennas and Propagation and USNC-URSI Radio Science Meeting (APS/URSI), 978-1-7281-4670-6/21/31.00 ©2021 IEEE, DOI: 10.1109/APS/URSI47566.2021.9704071

[13] J. Zhang, H. Huang, C. Huang, B. Zhang, Y. Li, K. Wang, D. Su, and G. Y. Tian, A configurable dielectric resonator-based passive wireless sensor for crack monitoring, IEEE Trans. Antennas Propag., vol. 67, no. 8, pp. 5746–5749, Aug. 2019, doi: 10.1109/TAP.2019.2916672.

[14] Dimitrios Pavlou, A deterministic algorithm for nonlinear, fatigue-based structural health monitoring, DOI: 10.1111/mice.12783

[15] Peter Edge, Hossein Akarinejad, Zhongwei Zhang, On Standards for Wireless Sensor Networks in the application of Structural Health Monitoring, 2023 Congress in Computer Science, Computer Engineering, Applied Computing (CSCE), 979-8-3503-2759-5/23/31.00 ©2023 IEEE, DOI: 10.1109/CSCE60160.2023.00440

[16] Atharva Ajgaonkar, Shriniket Vichare,Rohan Badgujar,Manisha Bansode, Deepak Karia,Abhay Bambole, Remote Structural Health Monitoring, 2020 IEEE International Conference on Convergence to Digital World – Quo Vadis (ICCDW 2020)

[17] Changli Yu, Runfa Ge, MyungHyun Kim, Xiaobo Gong, Zhen Xin Yang, Research on Structural Health Monitoring of Pressure Cabin Based on Stress Intensity Factor.

[18] Di Yang, Lianfa Wang, Yufeng Zhang, Research on the Application of Computer Big Data Technology in the Health Monitoring of the Bridge Body of Cross-river Bridge, 2022 IEEE Asia-Pacific Conference on Image Processing, Electronics and Computers (IPEC)

[19] Xinpeng Wang, Qingzhi Zhao, Ruijie Xi, Chengeng Li, Review of Bridge Structural Health Monitoring Based on GNSS: From Displacement Monitoring to Dynamic Characteristic Identification, Digital Object Identifier 10.1109/ACCESS.2021.3083749

[20] Mohsen Azimi, Armin Dadras Eslamlou, Gokhan Pekcan, Data-Driven Structural Health Monitoring and Damage Detection through Deep Learning: State-of-the-Art Review, Sensors 2020, 20, 2778; doi:10.3390/s20102778

[21] Hoon Sohn, Charles R. Farrar Francois Hemez, Jerry Czarnecki, A Review of Structural Health Monitoring Literature 1996 – 2001, LA-UR-02-2095

[22] Arman Malekloo, Ekin Ozer, Mohammad AlHamaydeh, Mark Girolami, Machine learning and structural health monitoring overview with emerging technology and high-dimensional data source highlights, Structural Health Monitoring 2022, Vol. 21(4) 1906–1955

[23] Rujun Yang, Structural Health Monitoring and Intelligent Maintenance Algorithm of Building Engineering Based on Graph Neural Networks and Reinforcement Learning, 2024 International Conference on Electrical Drives, Power Electronics and Engineering (EDPEE)

[24] Federica Zonzini, Cristiano Aguzzi, Lorenzo Gigli, Luca Sciullo, Nicola Testoni, Luca De, Marchi, Marco Di Felice, Tullio Salmon Cinotti, Canio Mennuti, and Alessandro Marzani, Structural Health Monitoring and Prognostic of Industrial Plants and Civil Structures: A Sensor to Cloud Architecture, IEEE Instrumentation and Measurement Magazine, December 2020

[25] Shuai Ren, Guoqing Pan, Hongwei Ma, Yong Liu, Hongzheng Fang, Jian Sun, Structural Health Monitoring System and Experiment Study of Aircraft Tapered Pipeline Structure, 2020 International Conference on Sensing, Diagnostics, Prognostics, and Control (SDPC), 978-1-7281-7050-3/20/$31.00 ©2020 IEEE, DOI: 10.1109/SDPC49476.2020.9353154

[26] Zhiming Sun, Kexue Cui, Dashan Wang, Study on Wireless Power Transfer Techniques in Structural Health Monitoring Applications, 2023 International Conference on Power Energy Systems and Applications (ICoPESA), 979-8-3503-4560-5/23/$31.00 ©2023 IEEE, DOI: 10.1109/ICoPESA56898.2023.10140328

[27] Rolando Dll. De La Torre, Garnet Amor E. Pasobillo, Maricris F. Rebueno, Donnabel P. Suñga, Bennyvic Joyce J. Esguerra, Ronnie Concepcion II, Vibration-based Structural Health Monitoring System for Bridges using ADXL345 Accelerometer with MATLAB Standalone Application, 2020 IEEE 12th International Conference on Humanoid, Nanotechnology, Information Technology, Communication and Control, Environment, and Management (HNICEM), 978-1-6654-1971-0/20/$31.00 ©2020 IEEE, DOI: 10.1109/HNICEM5

[28] Deng, F.,Tao, X., Wei, P., Wei, S., "A Robust Deep Learning-Based Damage Identification Approach for SHM Considering Missing Data". Appl. Sci. 2023,13,5421. https://doi.org/ 10.3390/app13095421

[29] R J Barthorpe, K Worden, "Classification of multi-site damage using support vector machines", 9th International Conference on Damage Assessment of Structures (DAMAS 2011), Journal of Physics: Conference Series 305 (2011) 012059,doi:10.1088/1742-6596/305/1/012059

[30] Shuonan Chen, Yongtao Bai, Xuhong Zhou, ao Yang1, "a deep learning dataset for metal multiaxial fatigue life prediction", www.nature.com/scientificdata/, https://doi.org/10.1038/s41597-024-03862-4

[31] Bruno Veloso, Rita P. Ribeiro, João Gama, Pedro Mota Pereira, "The MetroPt dataset for predictive maintenance",www.nature.com/scientificdata, https://doi.org/10.1038/s41597-022-01877-3

Compositional Diversity in Medieval Glass Bracelets from Yumuktepe: A Broader Sample Perspective

Zeynep Atasayar[a], Gülgün Köroğlu[b], Fatma Şişman Tükel[c], Özden Ormancı[a]*

[a]Mimar Sinan Fine Arts University, Department of Conservation and Restoration of Cultural Property, Cumhuriyet Mahallesi Silahşör Caddesi No:71, Şişli, İstanbul, Türkiye

[b]Mimar Sinan Fine Arts University, Department of Art History, Cumhuriyet Mahallesi Silahşör Caddesi No:71, Şişli, İstanbul, Türkiye

[c]İstanbul University – Cerrahpasa, Engineering Faculty, Deptartment of Geological Engineering, İstanbul, Türkiye

Keywords: LA-ICP-MS, Middle Age glass, material characterization, archaeometry.

Abstract

Forty-eight glass bracelet samples from the Medieval (12th-13th century AD) Yumuktepe excavation in Mersin, located on the Mediterranean coast of southern Anatolia, were analyzed to identify the raw materials used and to shed light on glass-making technology in Medieval Asia Minor. The major and trace element composition of the glass materials were obtained by LA-ICP-MS (laser ablation-inductively coupled plasma-mass spectrometry). As regard to the values analyzed with LA-ICP-MS and hierarchial cluster analysis, two distinctive glass groups appeared: soda-lime-silica, plant ash-based Na-Al glasses including natron, and only one sample found that contains high-Al glass with wood ash.

1. Introduction

The examination of ancient glass species through material characterization, puts forward technological and industrial development and cultural traditions of the old civilizations. Anatolian (Asia Minor) antiquities in glass in Medieval Age hides crucial informations of how the glass has been made, the raw materials used or if the raw glass was recycled or not.

This study aims to investigate the elemental composition of 48 glass bracelet samples from the 12th–13th century Yumuktepe excavation in order to identify local variations in glass production practices in Asia Minor. This study seeks to clarify whether the glass was locally produced or imported, and to shed light on the technological choices made by medieval glassmakers in this region. These findings contribute to filling a gap in the literature on medieval Anatolian glass production, which has so far remained understudied.

2. Experimental Procedure

A Perkin Elmer NexION 2000 mass spectrometer coupled with an ESI NWR-213 solid-state laser ablation system was used to conduct elemental analyses. This instrument is located at the Geochronology and Geochemistry Laboratory of Istanbul University-Cerrahpaşa in Istanbul, Turkey. The analytical conditions comprised an 80 µm laser spot size, a 20-second background acquisition period, a 30-second ablation period and a 50-second washout period for each spot analysed. The laser operated at a repetition rate of 10 Hz with an energy density of 5 J/cm². Helium was used as the carrier gas at a flow rate of 0.6 L/s.

Prior to analysis, the instrument was calibrated by monitoring the ThO/Th ratio, which was consistently maintained below 0.05%. The quadrupole ion deflector (QID) parameters were optimised to maximise signal intensities across light, medium and heavy mass ranges. NIST SRM 610 and 612 glass standards were analysed for calibration and drift correction. BCR-2g and GSP-2g standards were also used as quality control materials. Data reduction was performed using the ICPMSDATACALL software package, following the methodology outlined by [1].

3. Results and Discussion

3.1. Base Glass Composition

According to the major element composition results, 29 samples can be defined as soda-lime-silica glass since the SiO_2, Na_2O and CaO concentration ranges between 53.94-71.95 wt%, 13.33-24.65 wt% and 5.61-13.80 wt% respectively. On the other hand, as the concentration of Na_2O and Al_2O_3 varies between 20.19-32.07 wt.% and 3.91-9.64 wt.% respectively, 18 samples can be described as Na-Al glasses. Lastly, B9 differs from Na-Al glasses since Na_2O concentration was detected as 0.74 wt.% while Al_2O_3 amount examined as 9.64 wt.% and can be identified as high-Al glass. Figure 1 shows the discrimination between these groups as their Na_2O-Al_2O_3 (wt.%) content. The hierarchical cluster analysis separate our glasses into two groups: first one includes soda-lime-silica and the other consists Na-Al

and soda-lime-silica glasses divided into subgroups. The sample B9 is clearly differ from each groups. Although it was analyzed on a freshly cut surface, it is the only example exhibiting high Al_2O_3 and low Na_2O contents. Given this limited evidence, it is premature to define high-alumina glass as a distinct compositional group. Therefore, further investigation is required.

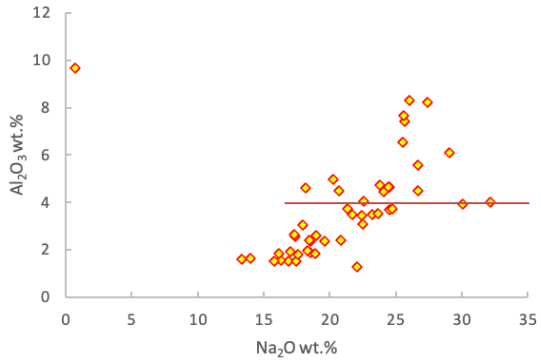

Figure 1. Discrimination between Na-Al glasses and soda-lime-silica glasses as their Na_2O-Al_2O_3 (wt.%) content.

In this study, the samples were divided into three groups according to their MgO and K_2O concentration: Low Magnesium-Low Potassium (Natron), High Magnesium-High Potassium (HMHK), High Magnesium-Low Potassium (HMLK). Figure 2 represents the MgO and K_2O contents of the glass samples. The Natron-group includes 5 samples that can be characterized as natron-glass since MgO and K_2O contents are quite low, below 1.55 wt.%, indicating that they were produced using a mineral source of soda as flux. The samples of High Magnesium-High Potassium group (HMHK) (33 samples) show both MgO and K_2O, suggesting the use of plant ash as a flux agent as their concentration were both above 1.55 wt.%. The last group High Magnesium-Low Potassium (HMLK) (10 samples) includes the samples of "mixed natron-plant ash glass" that presents a variability of MgO (ranging from 1.56 wt.% to 6.93 wt.%), K_2O (ranging from 1.16 wt.% to 1.54 wt.%) and P_2O_5 (ranging from 0.12 wt.% to 1.10 wt.%), suggesting the addition of some organic material to a natron mixture, perhaps a soda-rich plant ash. Elevated levels of P_2O_5, along with significant amounts of K_2O and CaO and low concentrations of Na_2O, are indicative of the use of wood ash as a fluxing agent in glass production [2]. In sample B9, which has elevated levels of Al_2O_3 (9.64 wt.%), despite the notably low Na_2O content (0.72 wt.%), relatively high concentrations of K_2O (7.10 wt.%) and P_2O_5 (2.06 wt.%) were observed. The CaO content, however, was relatively low (3.05 wt.%), which is reflected in the CaO/K_2O ratio of approximately 0.43. This low ratio suggests that the ash used likely derived from the trunk rather than the twigs or bark, as calcium content is known to vary between different parts of the tree [2]. The data implies the intentional use of higher-quality hardwoods, such as beech, which are characterized by lower calcium content and thus result in reduced CaO levels in the final glass composition. To sum up, the sample coded B9 can be described as high-Al glass made of wood ashes. Besides, all natron and HMLK groups consist of soda-lime-silica glasses. The remaining of soda-lime-silica and all Na-Al glasses classified as plant ash-based group (HMHK). In addition to being plant ash based, all Na-Al glasses contain exceptionally high amounts of Na_2O (18.10-32.07 wt.%). Plant ash-based Na-Al glasses mostly include up to 20 wt.% Na_2O, just a sample found 26 wt.% from Al-Andulus dated to 12th century [3]. The Na_2O concentrations in the Yumuktepe Na-Al glasses, reaching up to 32.07 wt.%, represent the highest values reported among all comparable Medieval glasses. Although there are limited studies on this type of glasses as the higher values of Na, this high concentration of Na_2O could be an implication of type of plant ash [4], [5].

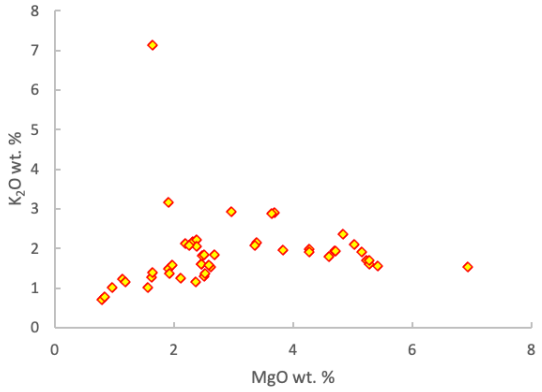

Figure 2. MgO and K_2O contents of the glass samples.

Al_2O_3 introduces to the glass matrix with sand source as impurities (feldspar and clay) or in some cases non-purified ashes as flux source and makes the glass more stable [6], [7]. Although high-Al glasses are known as rarely occur in ancient world, relatively common in South Asia region is known. Archaeometric studies conducted at Byzantine-period sites such as Ḥiṣn al-Tīnāt, [8] Pergamon, [9] and Sagalassos [10] suggest the production of diverse types of high-alumina glasses in Anatolia. The Group 1 glass bracelets from Ḥiṣn al-Tīnāt exhibit compositional similarities to the soda-lime-silica glasses identified at Yumuktepe. Specifically, all purple samples in the Ḥiṣn al-Tīnāt glasses, along with Yumuktepe samples P1 and P2, display comparable elemental profiles. Nevertheless, the Yumuktepe Na-Al glasses can be distinguished from the Group 2 Ḥiṣn al-Tīnāt bracelets by their relatively lower B concentrations [8]. Pergamon glasses differs from Yumuktepe samples as mostly produced from mineral soda from evaporatic lakes around West Anatolia instead of plant ashes [9]. The elevated Na_2O and Al_2O_3 levels in Sagalassos plant ash glasses suggest mixing with Roman natron glass.

While Yumuktepe Na-Al glasses show similar base compositions, the absence of elevated Sb, Zn, Cr, Cu, and Pb indicates a lack of recycling, unlike the Sagalassos samples [10]. In the Western Mediterranean, ancient glassmakers commonly melted raw glass together with cullet. Both raw and recycled glass were traded from the Near East to Europe, as evidenced by cargoes recovered from several Mediterranean shipwrecks [11]. Although glass recycling was a common practice during the Middle Ages, the Yumuktepe samples appears to have been primarily produced from raw glass.

Like Al_2O_3, TiO_2 is commonly associated with the discrimination of sand raw materials. For all samples, the correlation coefficient calculated between Al_2O_3-TiO_2 increase from 0.06 to 0.87 when the samples G9, Bl12, B4, B6, B9, B10 and B11 were excluded from the calculation. The samples coded G9, BlA12, B4, B6, B9, B10 and B11 clearly distinct from the others. These glass bracelets also characterized with higher Al_2O_3 (>6 wt.%) and Na_2O (>25 wt.%) (B9 not included as its Na_2O content is 0.72 wt.%).

To achieve better understanging of compositional variation of Yumuktepe glasses, we compared our samples with other glasses from Middle East in Medieval Age.

The distribution of MgO/CaO versus Al_2O_3 for glasses from al-Raqqa (11th century AD) [12], Samarra (9th century AD) [13], Nishapur (9th century AD) [14], Wadi al-Tur (6th–13th century AD) [15], Tyre (10th–12th century AD) [16], Banias (9th–11th century AD) [16], Damascus (12th–14th century AD) [17], Beirut (9th–14th century AD) [17], and Yumuktepe highlights the differentiation between Mesopotamian, Levantine, and Egyptian types of glass production [13]. Most soda-lime-silica glasses correspond to Levantine and Egyptian types, except for samples G2, G4, G8, BlA1, BlA2, BlA6, BlA7, and BlA13, which align with the Mesopotamian tradition and resemble glasses from Wadi al-Tur and Nishapur. All Na-Al glasses also show strong affinities with the Mesopotamian type. It is clearly observed from that all Mesapotamian glasses consist of blue (B4, B6, B9, B10, B11), green, and black appearing samples. All red, turquoise, purple and only G1, G3, BlA5, and BlA11 from green and black appearing glasses are associated with Levantine and Egypt type.

Comparative analysis with contemporary sites indicates the use of two different sand raw material: one related to the Egyptian/Levantine tradition, and two linked to Mesopotamian production, distinguished primarily by differences in Al_2O_3 and Na_2O content. Most soda-lime-silica glasses reflects the Levantine type while Na-Al glasses and the remaining of soda-lime-silica glasses could indicate the Mesopotamian type. This variation implies that one subgroup of Mesopotamian type -especially the higher Na-Al glasses as their rare amounts in Na_2O- may represent local glass production with local plant ash that contain elevated content of Na_2O.

4. Conclusion

The chemical composition of glass bracelets from the 12th-13th century AD Yumuktepe (Mersin) excavations, determined by LA-ICP-MS analysis, provides significant insights into the base glass composition, raw materials used in their production. The results show that the glasses are classified as soda-lime-silica and Na-Al glasses, with the majority produced using plant ash as a flux. In Na-Al glasses from Yumuktepe, the detected Na_2O levels are higher than those reported in comparable studies. Glass bracelets classified as their major element distribution and compared with regional variations of chemical compositions. The elevated Na_2O content observed in certain Na-Al glasses may indicate local production, whereas the remaining Na-Al glasses correspond to the Mesopotamian type, with others showing affinities to Egyptian and Levantine traditions.

Overall, this study contributes to a broader archaeometric understanding of medieval glass production technologies in the Eastern Mediterranean and sheds light on the raw material procurement strategies of the period.

ACKNOWLEDGMENT

This work was supported by the Research Fund of Mimar Sinan Fine Arts University (MSGSÜ) under Project Number 24/BAP/26.

References

[1] Liu Y, Hu Z, Gao S, Günther D, Xu J, Gao C, Chen H (2008) In situ analysis of major and trace elements of anhydrous minerals by LA-ICP-MS without applying an internal standard. Chemical Geology, 257(1–2), 34–43 https://doi.org/10.1016/j.chemgeo.2008.08.004

[2] Wedepohl KH, Simon K (2010) The chemical composition of medieval wood ash glass from Central Europe. Chemie Der Erde, 70(1), 89–97 https://doi.org/10.1016/j.chemer.2009.12.006

[3] Carmona, N., Villegas, M. A., Jiménez, P., Navarro, J., & García-Heras, M. (2009). Islamic glasses from Al-Andalus. Characterisation of materials from a Murcian workshop (12th century AD, Spain). *Journal of Cultural Heritage*, *10*(3), 439-445. https://doi.org/10.1016/j.culher.2008.12.005

[4] Henderson, J (2016) Ancient glass: an interdisciplinary exploration. Cambridge University Press, Cambridge

[5] Barkoudah, Y., & Henderson, J. (2006). Plant ashes from Syria and the manufacture of ancient glass: ethnographic and scientific aspects. *Journal of glass studies*, 297-321.

[6] Biron, I., & Chopinet, M. H. (2013). Colouring, decolouring and opacifying of glass. *Modern methods for analysing archaeological and historical glass*, *1*, 49-65.

[7] van Ham-Meert A, Dillis S, Blomme A, Cahill N, Claeys P, Elsen J, Eremin K, Gerdes A, Steuwe C, Roeffaers M, Shortland A, Degryse P (2019) A unique recipe for glass beads at Iron Age Sardis. Journal of Archaeological Science, 108 https://doi.org/10.1016/j.jas.2019.104974

[8] Swan CM, Rehren T, Dussubieux L, Eger AA (2018) High-boron and High-alumina Middle Byzantine (10th–12th Century ce) Glass Bracelets: A Western Anatolian Glass Industry. Archaeometry, 60(2), 207–232 https://doi.org/10.1111/arcm.12314
[9] Schibille N, Meek A, Wypyski MT, Kröger J, Rosser-Owen M, Haddon RW (2018) The glass walls of Samarra (Iraq): Ninth-century Abbasid glass production and imports. PLoS ONE, 13(8) https://doi.org/10.1371/journal.pone.0201749
[10] Lauwers, V., Degryse, P., Waelkens, M., Drauschke, J., & Keller, D. (2010). Middle Byzantine (10th to 13th century AD) glass bracelets at Sagalassos (SW Turkey). *Glass in Byzantium-production, usage, analyses.*, 145-152.
[11] Janssens K (2013) Modern methods for analysing archaeological and historical glass. Wiley, New York
[12] Henderson J, Adams P, Mann J (2005) Medieval and Post-Medieval Glass Finewares from Lincoln: an Investigation of the Relationships between Technology, Chemical Compositions, Typology and Value. Archaeological Journal, 162(1), 256–322. https://doi.org/10.1080/00665983.2005.11020626
[13] Schibille, N., Meek, A., Wypyski, M. T., Kröger, J., Rosser-Owen, M., & Wade Haddon, R. (2018). The glass walls of Samarra (Iraq): Ninth-century Abbasid glass production and imports. *PLoS One*, *13*(8), e0201749.
[14] Wypyski MT (2015) Chemical Analysis of Early Islamic Glass from Nishapur. Journal of Glass Studies, 57 https://about.jstor.org/terms
[15] Kato N, Nakai I, Shindo Y (2010) Transitions in Islamic plant-ash glass vessels: On-site chemical analyses conducted at the Raya/al-Tur area on the Sinai Peninsula in Egypt. Journal of Archaeological Science, 37(7), 1381–1395 https://doi.org/10.1016/j.jas.2009.12.042
[16] Degryse P, Freestone I, Jennings S, Schneider J (2010) Technology and provenance study of Levantine plant ash glass using Sr-Nd isotope analysis. In: Drauke J, Keller D (ed) Glass in Byzantium–Production, Usage, Analyses, pp. 83-9, Römisch-Germanisches Zentralmuseum: Mainz, Germany
[17] Henderson J, Ma H, Evans J (2020) Glass production for the Silk Road? Provenance and trade of islamic glasses using isotopic and chemical analyses in a geological context. Journal of Archaeological Science, 119 https://doi.org/10.1016/j.jas.2020.105164

Micro-Arc Oxidation-induced Surface Modification of Znmg-Zr Alloys

Ramona Cimpoeșu[1], Alexandra Tamara Șutic[1], Romeu Chelariu[1], Sorin Moga[2], Ana -Maria Roman, Bogdan Istrate[3], Fabian Cezar Lupu[3], Gheorghe Bădărău[1] and Nicanor Cimpoeșu[1]

[1]Faculty of Materials Science and Engineering, Gheorghe Asachi Technical University of Iasi, 67 Dimitrie Mangeron str., 700050 Iasi, Romania
[2]Regional Center of Research and Development for Materials, Processes, and Innovative Products Dedicated to the Automotive Industry, National University of Science and Technology Politehnica Bucharest, Pitesti University Centre, Targu din Vale, No. 1, 110040, Pitesti, Romania
[3]Mechanical Engineering Faculty,"Gheorghe Asachi" Technical University of Iasi, 700050 Iasi, Romania

Electrolytic plasma oxidation (PEO) technology has been applied to obtain oxide layers on Zn-based alloys in order to improve functional performance in corrosive environments. The anodic discharges at high voltages favoured the in-situ formation of dense, adherent, multiphase layers, confirmed by XRD and EDS analyses. The layers exhibited a characteristic porous morphology, the pore distribution and thickness being controlled by optimising PEO process parameters including current density, frequency and electrolyte composition. Electrochemical impedance spectroscopy (EIS) revealed a significant increase in the total impedance modulus, indicating superior barrier properties of the PEO treated surfaces. Potentiodynamic polarisation tests demonstrated a considerable reduction in corrosion current density (I_corr) and an increase in polarisation resistance (R_p), reflecting improved passivation and suppression of anodic dissolution. The integration of microstructural, compositional and electrochemical data allowed the understanding of the protective mechanisms conferred by PEO coatings, highlighting their potential in extending the corrosion lifetime of zinc-based substrates in aggressive environments.

Acknowledgment: This work was supported by a National Research Grants of the TUIASI, project number GNaC2023_285/2024.

INVESTIGATION OF THE EFFECTS OF LASER PARAMETERS ON SURFACE ROUGHNESS IN THE LASER TURNING OF AISI 308L AUSTENITIC STAINLESS STEEL

Emin Orhun Bastekeli[1], Haci Abdullah Tasdemir, Buse Ortac Bastekeli

Istanbul Technical University, Faculty of Mechanical Eng., Mechanical Eng. Dep., 34437, İstanbul, Turkiye

Keywords: Laser turning, Surface roughness, AISI 308L austenitic stainless steel

Abstract

Austenitic stainless steels are widely used today in various fields such as chemical processing, food industry, biomedical applications, and energy systems due to their excellent corrosion resistance and mechanical properties. However, the machinability of these types of stainless steels is generally more challenging compared to other steel materials and often requires special considerations. Conventional machining methods typically lead to issues such as rapid tool wear and machine vibrations, which can be mitigated through laser-based machining techniques. In this study, for the first time in the literature, laser turning of AISI 308L austenitic stainless steel was performed without the use of a cutting tool, utilizing direct laser beam application. The effects of laser scanning speed and the number of passes on surface roughness were systematically investigated. As a result, the relationship between laser parameters and surface roughness was clearly established and mathematically formulated. The developed mathematical model enables the prediction and control of surface roughness values in the laser turning of AISI 308L austenitic stainless steel, providing a valuable reference for future studies and researchers working in the field.

1. Introduction

Austenitic stainless steels constitute a distinguished class of alloys recognized for their excellent corrosion resistance, superior formability, and significant work-hardening capability [1-3]. Among commercially available alloys, they offer exceptional strength, toughness, and formability over a broad temperature range. Beyond their functional performance, these alloys are also valued for their aesthetic appearance and environmental sustainability [4]. Thanks to these advantageous properties, austenitic stainless steels have gained widespread application across various sectors. This alloy family comprises numerous grades, each specifically developed to address the requirements of diverse fields, including household and public infrastructure, biomedical devices, transportation, food processing, industrial machinery, chemical and energy systems, cryogenics, and the construction industry [5-8]. Despite their outstanding mechanical and corrosion-resistant characteristics, austenitic stainless steels present challenges in machinability when conventional methods are employed. This is primarily due to their tendency to work-harden and their relatively low thermal conductivity [9,10].

Recent studies have increasingly emphasized laser processing technologies as viable alternatives to conventional machining techniques [11,12]. In addition to their well-established role in precision-critical applications such as microscale sensor manufacturing [13-15], these technologies have also proven effective in the accurate processing of materials with limited machinability and stringent tolerance requirements [16-20].

Laser beams can be utilized for various material removal operations such as turning, milling, high-speed cutting, and other high-value manufacturing processes [21]. Moreover, they are also applicable to surface modification techniques including texturing, melting, and hardening, enabling both functional and structural enhancements of component surfaces [22].

Although both laser-assisted turning and direct laser turning involve the integration of laser technology with turning processes, they represent fundamentally different approaches and should not be used interchangeably. Laser-assisted turning (LAT) is a sophisticated hybrid machining method that combines traditional turning operations with a concentrated laser beam to enhance material removal efficiency. In LAT, a high-power laser is accurately focused on the surface of the workpiece during machining, inducing localized heating. This thermal softening reduces the material's hardness, thereby facilitating the cutting process. As a result, cutting forces are minimized, tool wear is decreased, and surface finish is significantly improved [16]. Numerous studies have explored the effectiveness of LAT [19,23,24], particularly in the machining of stainless steels, which typically exhibit low thermal conductivity and high work hardening behavior [20,25,26]. Additionally, favorable results have been reported in the laser-assisted turning of composite materials [27-29].

Direct laser turning (DLT), on the other hand, is a technique that incorporates laser technology directly into the turning process to improve both material removal and surface quality. While LAT has been widely investigated, studies focused specifically on DLT remain limited. DLT is a non-contact subtractive manufacturing method in which concentrated laser energy is used to thermally ablate material from the surface of a rotating workpiece with high accuracy [30]. This process is gaining increasing attention in fields such as micromanufacturing and the machining of hard-to-cut materials, owing to its ability to eliminate tool wear and offer enhanced control over surface characteristics [31-33].

In this study, the emerging topic of laser turning, which has gained popularity in recent years but has been the subject of relatively few investigations, was explored. Using a laser power of 50 W and a frequency of 50 kHz, the relationship between increasing number of passes and surface roughness was examined at two different laser scanning speeds. The aim of this study is to investigate the effect of varying laser scanning speeds and number of passes on surface roughness in the laser turning process.

2. Experimental Procedure

The laser turning experiments were conducted on AISI 308L stainless steel rods (Ø1.6 mm×20 mm), supplied by Gitanjali Industrial Mart Pvt. Ltd., using an Nd:YAG fiber laser system. Figure 1 illustrates both the specimen geometry and a schematic view of the turned and non-turned regions of the workpiece. The chemical composition and mechanical properties of the AISI 308L stainless steel used in the experiments are presented in Table 1 and Table 2, respectively, based on the manufacturer's specifications.

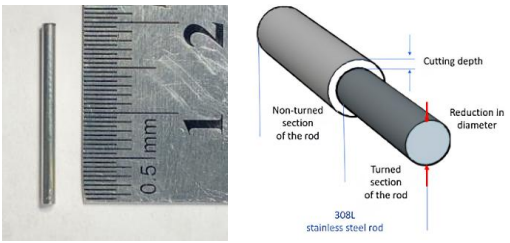

Figure 1. AISI 308L sample rod d=1.6 mm, l=20 mm and schematic representation of the turned and non-turned sections of the AISI 308L stainless steel rod.

Table 1. Chemical composition of AISI 308L stainless steel.

Element	Fe	Cr	Ni	Mn
Min. (%)	63.8	19.5	9	1
Max. (%)	70.5	22	11	2.5
Element	Si	C	P	S
Min. (%)	0.25	-	-	-
Max. (%)	0.6	0.08	0.03	0.03

Table 2. Mechanical properties of the AISI 308L stainless steel.

Tensile Strength (MPa)	Yield Strength (MPa)	Modulus of Elasticity (GPa)	Poisson's Ratio	Elongation (%)
593	207	190-210	0.27-0.30	48

The laser turning operations were carried out using a Raycus QB50 pulsed Nd:YAG fiber laser system. A schematic illustration of the direct laser turning setup is provided in Figure 2. The laser operates at a wavelength of 1064 nm with pulse durations in the nanosecond range. The laser spot diameter is 0.05 mm. Technical specifications of the laser source are summarized in Table 3. During the experiments, a servo motor was employed to rotate the workpiece at a constant speed of 2 rpm.

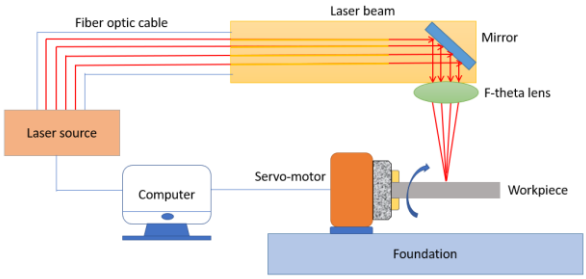

Figure 2. Schematic representation of the fiber laser setup employed in the laser turning process.

Table 3. Technical specifications of the laser source.

Laser source type	Pulsed Nd:YAG fiber laser
Pulse duration (ns)	120~150@50 kHz
Wavelength (nm)	1060~1085
Average output power (W)	50

Throughout the experiments, the laser's average output power was maintained at 50 W, and the pulse frequency was kept constant at 50 kHz. The stainless steel specimens, each cut to a length of 20 mm, were grouped for processing at two laser scanning speeds: 3200 mm/s and 6400 mm/s. For both scanning speeds, the laser turning operation was performed with 1, 4, 16, and 32 passes. To ensure repeatability, three specimens were processed under identical conditions and laser parameters for each set of experiments. After the laser turning operations, the surface roughness of each specimen was measured using a Mitutoyo 178-561-02A Surftest SJ-210 surface roughness tester and a Zeiss Smartproof 5 optical profilometer. Measurements were taken from 10 different locations on each specimen, and the arithmetic mean of these values was calculated.

Pulse frequency denotes the number of laser pulses generated per unit of time, commonly expressed in kilohertz (kHz). The use of pulsed laser processing is crucial as it governs the amount of energy imparted to the material over time, thereby affecting thermal impacts, the rate of material removal, and the overall efficiency of the process. The number of passes refers to how many times the laser beam traverses the rod, effectively subjecting it to repeated diameter reduction. In other words, this parameter indicates the total count of laser scans over the identical region of the specimen. It significantly impacts the depth of material ablation, heat build-up, and the surface quality achieved. Employing multiple passes is typical when a single pass does not suffice to accomplish the targeted modification, especially in processing hard materials or when gradual and controlled material removal is required.

3. Results and Discussion

In this section, surface roughness measurements were plotted against varying laser scanning speeds and numbers of passes and the results were interpreted. The measured surface roughness values are presented in Table 4. The relationship between the number of passes and surface roughness is plotted in Figure 3.

Table 4. Surface roughness variation at laser speeds of 3200 and 6400 mm/s for different pass counts.

Laser scanning speed of 3200 mm/s				
Number of passes	1	4	16	32
Surface roughness (µm)	0.52	0.90	1.77	3.39
Laser scanning speed of 6400 mm/s				
Number of passes	1	4	16	32
Surface roughness (µm)	0.55	0.80	1.23	1.8

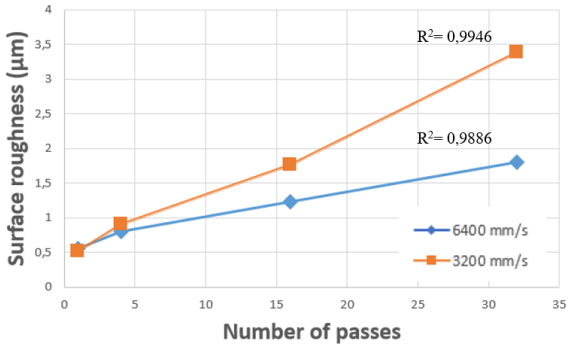

Figure 3. Surface roughness variation with number of passes at 3200 mm/s and 6400 mm/s

First-degree equations have been obtained as follows:

$y=0.0903x + 0.4479$ (Eq.1)
$y=0.0387x + 0.5827$ (Eq.2)

As shown in Figure 3, the difference in surface roughness between the scanning speeds of 6400 mm/s and 3200 mm/s increases with the number of passes. While higher numbers of passes result in a more significant increase in surface roughness at the lower speed of 3200 mm/s, the surface roughness at 6400 mm/s shows only a slight increase. This can be attributed to the fact that lower scanning speeds allow more laser energy to be delivered to a specific area, thereby enhancing the laser–material interaction. Overall, although increasing the number of passes generally leads to higher surface roughness values, the rate of increase varies depending on the scanning speed. As the number of passes increases, the gap in surface roughness between the two scanning speeds becomes more pronounced.

Nanosecond laser ablation is characterized by intricate interactions between laser pulses and material surfaces, predominantly driven by photothermal effects. When a material is exposed to a nanosecond laser pulse, the absorbed energy is rapidly converted into heat, causing a sharp temperature increase that can lead to melting, followed by vaporization or material expulsion [34]. Because of the relatively long pulse duration compared to ultrafast lasers such as femtosecond or picosecond systems, significant thermal diffusion occurs in the surrounding areas, often producing a wider heat-affected zone (HAZ) and increasing the risk of thermal damage [35]. Moreover, the generation of plasma and the associated recoil pressure play a role in displacing the molten material, thereby affecting both the efficiency of ablation and the final surface characteristics.

Due to the aforementioned laser–material interaction mechanisms, phenomena such as resolidification of the material and localized accumulation caused by recoil pressure may occur. During laser processing, a reduction in the rod diameter, the formation of undercut regions, and the presence of debris (burr) can be observed, as illustrated in Figure 4.

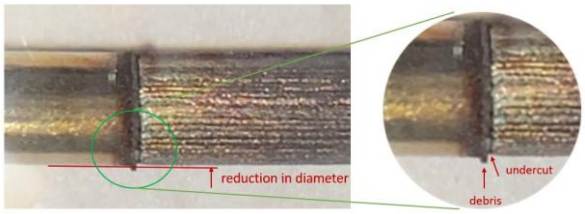

Figure 4. Geometric and material alterations induced by laser processing: diameter reduction, undercuts, and debris.

4. Conclusion

The AISI 308L stainless steel samples were processed using the laser turning technique with a 1064 nm Nd:YAG nanosecond laser, without the use of any external cooling methods. During the experiments, the laser power and

frequency were kept constant at 50 W and 20 kHz, respectively, while the laser scanning speed and number of passes were systematically varied. For the two selected scanning speeds, 3200 mm/s and 6400 mm/s, the number of passes was set to 1, 4, 16, and 32. Surface roughness measurements were carried out using both a contact-type surface roughness tester and an optical profilometer. Graphs were plotted to illustrate the correlation between the number of passes and the corresponding surface roughness values obtained from the measurements. The key findings of this study can be outlined as follows:

1.An increase in the number of passes resulted in higher surface roughness values at both laser scanning speeds.

2.At lower scanning speeds, the increase in surface roughness with a higher number of passes is more pronounced compared to higher speeds.

3.An increase in the number of passes leads to a reduction in rod diameter and results in the enlargement of undercut and debris regions on the rod.

Acknowledgment

This work was financially supported by Istanbul Technical University Scientific Research Projects Coordination Unit (ITU BAP Koordinasyon Birimi, No. MGA-2023-45222).

References

[1] M. A. Ibrahim, S. S. Abd El Rehim, and M. M. Hamza, "Corrosion behavior of some austenitic stainless steels in chloride environments," Materials Chemistry and Physics, vol. 115 (1), pp. 80-85, 2009.

[2] A. Järvenpää, M. Jaskari, A. Kisko, and P. Karjalainen, "Processing and properties of reversion-treated austenitic stainless steels," Metals, vol. 10 (2), p. 281, 2020.

[3] L. P. Karjalainen, T. Taulavuori, M. Sellman, and A. J. S. R. I. Kyröläinen, "Some strengthening methods for austenitic stainless steels," Steel Research International, vol. 79 (6), pp. 404-412, 2008.

[4] T. Michler, "Austenitic stainless steels," Reference Module in Materials Science and Materials Engineering, vol. 1 (6), 2016."

[5] G. George and H. Shaikh, "Introduction to austenitic stainless steels," In Corrosion of austenitic stainless steels, Woodhead Publishing, pp. 1-36, 2002.

[6] M. Talha, C. K. Behera, and O. P. Sinha, "A review on nickel-free nitrogen containing austenitic stainless steels for biomedical applications," Materials Science and Engineering: C, vol. 33 (7), pp. 3563-3575, 2013.

[7] K. J. Lee, M. S. Chun, M. H. Kim, and J. M. Lee, "A new constitutive model of austenitic stainless steel for cryogenic applications," Computational Materials Science, vol. 46 (4), pp. 1152-1162, 2009.

[8] A. Saha Podder and A. Bhanja, "Applications of stainless steel in automobile industry," Advanced Materials Research, vol. 794, pp. 731-740, 2013.

[9] S. Dolinšek, "Work-hardening in the drilling of austenitic stainless steels," Journal of Materials Processing Technology, vol. 133 (1-2), pp. 63-70, 2003.

[10] D. T. Llewellyn, "Work hardening effects in austenitic stainless steels," Materials Science and Technology, vol. 13(5), pp. 389-400, 1997.

[11] G. Eberle, S. C. D. Huber, B. Frei, and C. Pluess, "Ultrashort-pulsed laser processing of hard and ultrahard helical cutting tools," 10th CIRP Conference on Photonic Technologies [LANE 2018], 2018.

[12] S. Marimuthu, J. Dunleavey, and B. Smith, "High-power ultrashort pulse laser machining of tungsten carbide," Procedia CIRP, vol. 94, pp. 829-833, 2020.

[13] M. Razeghi, S. Slivken, A. Tahraoui, A. Matlis and Y. S. Park, "High power 3–12 μm infra-red lasers: recent improvements and future trends," Physica E: Low-dimensional Systems and Nanostructures, vol. 11 (2-3), pp. 233-239, 2001.

[14] W. K. Pitts and M. D. Martin, "Experience with laser microfabricated detectors at the University of Louisville," Nuclear Instruments and Methods in Physics Research Section A: Accelerators, Spectrometers, Detectors and Associated Equipment, vol. 471 (1-2), pp. 268-271, 2001.

[15] L. Lu, Y. Zhao, N. Lin, and Y. Xie, "Skin-inspired flexible pressure sensor with hierarchical interlocked spinosum microstructure by laser direct writing for high sensitivity and large linearity," Sensors and Actuators A: Physical., vol. 366, p. 114988, 2024.

[16] F. Zhao, W. Z. Bernstein, G. Naik, and G.J. Cheng, "Environmental assessment of laser assisted manufacturing: case studies on laser shock peening and laser assisted turning," Journal of Cleaner Production, vol. 18 (13), pp. 1311-1319, 2010.

[17] D. Przestacki, "Conventional and laser assisted machining of composite A359/20SiCp," In:Procedia CIRP 14, p.229-233, 2014.

[18] F. A. Khatir, M. H. Sadeghi, and S. Akar, "Investigation of surface roughness in laser-assisted hard turning of AISI 4340," Materials Today: Proceedings, vol. 38, pp. 3085-3090, 2021.

[19] K. You, G. Liu, W. Wang, and F. Fang, "Laser assisted diamond turning of silicon freeform surface," Journal of Materials Processing Technology, vol. 322, p. 118172, 2023.

[20] C. Naresh, P. S. C. Bose, C. S. Rao, and N. Selvaraj, "Prediction of cutting force of AISI 304 stainless steel during laser-assisted turning process using ANFIS," Materials Today: Proceedings, vol. 38, pp. 2366-2371, 2021.

[21] K. E. Hazzan, M. Pacella, and T. L. See, "Understanding the surface integrity of laser surface engineered tungsten carbide," The International Journal of Advanced Manufacturing Technology, vol. 118 (3), pp. 1141-1163, 2022.

[22] J. Marczak, "Micromachining and pattering in micro/nano scale on macroscopic areas," Archives of Metallurgy and Materials, vol. 60, 2015.

[23] F. A. Khatir, M. H. Sadeghi, and S. Akar, "Investigation of surface roughness in laser-assisted hard turning of AISI 4340," Materials Today: Proceedings, vol. 38, pp. 3085-3090, 2021.

[24] N. Deswal and R. Kant, "Machinability and surface integrity analysis of magnesium AZ31B alloy during laser assisted turning," Journal of Manufacturing Processes, vol. 101, pp. 527-545, 2023.

[25] F. Yasmin, K. F. Tamrin, N. A. Sheikh, P. Barroy, A. Yassin, A. A. Khan, and S. Mohamaddan, "Laser-assisted high speed machining of 316 stainless steel: The effect of water-soluble sago starch based cutting fluid on surface roughness and tool wear," Materials, vol. 14 (5), p. 1311, 2021.

[26] M. Szymański and M. Kukliński, "Geometrical structure of surface after turning of 316L stainless steel in laser assisted conditions," Archives of Mechanical Technology and Materials, vol. 39, pp. 66-73, 2019.

[27] C. Wei, W. Guo, B. Gao, Y. Wang, Z. Sun, and L. Li, "Understanding the behaviour of workpieces bulk temperature during laser-assisted turning of Ti6Al4V alloy and heating of Al-SiC metal-matrix composite rods," Optics & Laser Technology, vol. 139, p. 106951, 2021.

[28] R. Abedinzadeh, E. Norouzi, and D. Toghraie, "Study on machining characteristics of SiC–Al2O3 reinforced aluminum hybrid nanocomposite in conventional and laser-assisted turning," Ceramics International, vol. 48 (19), pp. 29205-29216, 2022.

[29] R. Bejjani, B. Shi, H. Attia, and M. J. C. A. M. T. Balazinski, "Laser assisted turning of titanium metal matrix composite," CIRP annals, vol. 60 (1), pp. 61-64, 2011.

[30] E. O. Bastekeli, H. A. Tasdemir, A. Yucel and B. Ortac Bastekeli, "Experimental and Numerical Analyses of Diameter Reduction via Laser Turning with Respect to Laser Parameters," Journal of Manufacturing and Materials Processing, 2025.

[31] G. Kibria, B. Doloi, and B. Bhattacharyya, "Experimental analysis on Nd: YAG laser micro-turning of alumina ceramic," The International Journal of Advanced Manufacturing Technology, vol. 50 (5), pp. 643-650, 2010.

[32] D. Sriram, G. Jayaprakash, D. Arulkirubakaran, M. Prabu, and A. Ajithkumar, "Laser turning of alumina (Al_2O_3) ceramic by Nd: YAG laser technique," Materials Today: Proceedings, vol. 39, pp. 731-735, 2021.

[33] D. Dhupal, B. Doloi, and B. Bhattacharyya, "Pulsed Nd: YAG laser turning of micro-groove on aluminum oxide ceramic (Al_2O_3)," International Journal of Machine Tools and Manufacture, vol. 48 (2), pp. 236-248, 2008.

[34] C. Chu, Q. Zhang, H. Zhuo, Z. Zhang, Y. Zhu, and Y. Fu, "Investigation on the ablation behavior of cemented tungsten carbide by a nanosecond UV laser," Journal of Manufacturing Processes, vol. 71, pp. 461-471, 2021.

[35] B. Nagarajan, J. Han, S. Huang, J. Qian, J. Vleugels, and S. Castagne, "Femtosecond laser processing of cemented carbide for selective removal of cobalt," Procedia CIRP, vol.113, pp. 576-581, 2022.

Advancing Hydrogen Permeation Testing: in Situ Xrd Microscopy for Mapping Diffusivity and Concentration in Complex Microstructures

Cem Örnek[1], Ammar Aksoy[1], Ulrich Lienert[2], Steve Ooi[3],

1. Istanbul Technical Universirty

2. DESY German Electron Synchrotron

3. Ovako Corporate R&D

To develop and demonstrate an in-situ synchrotron X-ray diffraction (XRD) microscopy technique for quantitatively mapping hydrogen-induced lattice strain and diffusivity in complex microstructures, enabling improved understanding and modelling of hydrogen transport and its interaction with material features like carbides.

A high-strength hybrid martensitic steel was tested using a custom electrochemical cell compatible with in-situ synchrotron X-ray diffraction (XRD) microscopy. Hydrogen charging was applied via a Devanathan–Stachurski–type setup under controlled cathodic polarisation. High-energy XRD data were collected during simultaneous hydrogen charging and tensile loading, capturing time-resolved lattice strain with micrometre spatial resolution and ~1 × 10^{-5} strain sensitivity.2D diffraction data were processed using pyFAI to extract time-lapse series, which were then azimuthally integrated into 1D patterns. Peak fitting was performed using xrdfit or OriginLab to quantify lattice strain. The resulting spatially and temporally resolved strain data were visualised in OriginLab to construct strain maps. The experimental strain was correlated to hydrogen concentration via DFT-based calibration, enabling the mapping of hydrogen and refinement of finite element models of hydrogen diffusion in the martensitic microstructure.

Hydrogen-induced lattice strain was mapped in space and time using in-situ XRD microscopy.Local hydrogen uptake was quantified indirectly by linking strain data to hydrogen concentration using density functional theory (DFT) calibration.The method achieved a strain sensitivity of 10^{-5}, corresponding to a minimum detectable hydrogen concentration of ~10 wt.-ppm.Spatially resolved hydrogen diffusivity was determined across different microstructural regions.In carbide-containing steel, hydrogen diffusivity was measured at ~3 × 10^{-13} m^2/s.In carbide-free steel, diffusivity was ≥5 × 10^{-12} m^2/s, indicating much faster hydrogen transport.Carbides were observed to act as hydrogen traps, confining strain evolution to near-surface regions.Strain evolution revealed how hydrogen transport and mechanical response varied with microstructure.

This study demonstrates that in-situ synchrotron XRD microscopy enables spatial and temporal mapping of hydrogen-induced lattice strain in complex microstructures, such as high-strength steels, with a strain sensitivity corresponding to ~10 wt.-ppm hydrogen, marking the lower detection limit. By linking strain data with DFT calibration, we quantified local hydrogen uptake

and diffusivity, revealing that carbides significantly reduce hydrogen mobility and confine strain to near-surface regions. These observations provide direct evidence of how microstructural features control hydrogen transport and mechanical response. The approach offers a robust framework for designing steels with improved resistance to hydrogen embrittlement through microstructural optimisation.

Keywords: In-Situ-XRD-Microscopy; Hydrogen-embrittlement Lattice-strain-mapping; Hydrogen-diffusion

INVESTIGATION OF THE INFLUENCE OF TARTARIC ACID QUANTITY AND CALCINATION TEMPERATURE ON THE MORPHOLOGY, CRYSTAL STRUCTURE, AND PHOTOCATALYTIC ACTIVITY OF ZINC OXIDE NANOPARTICLES

Mücahid Özcan[1], Serra Ersoy[2,3], Figen Kaya[2], Cengiz Kaya[2]

[1]Oak Ridge National Laboratory, Oak Ridge/(US) United States

[2]Yıldız Technical University, Faculty of Chemistry and Metallurgy, Department of Metallurgical and Materials Engineering, Istanbul/Türkiye

[3]Sabanci University, Faculty of Engineering and Natural Sciences, Department of Materials Science and Nano Engineering, Istanbul/Türkiye

Keywords: Nanomaterials, Tartaric Acid, Sol-gel, Photochemistry

Abstract

In this study, zinc oxide (ZnO) nanoparticles were synthesized via the sol-gel method with varying amounts of tartaric acid (0.01, 0.05, and 0.1 mol), followed by calcination at 400, 500, and 600°C. The effects of tartaric acid content and calcination temperature on morphological, structural, and photocatalytic properties were investigated. Results showed that increasing tartaric acid concentration led to finer, more uniform particles with reduced porosity, negatively affecting photocatalytic performance. ZnO synthesized with 0.05 mol tartaric acid exhibited the highest activity, achieving 94.51% methylene blue degradation in 90 minutes. Due to their efficiency, stability, and biocompatibility, the synthesized ZnO nanoparticles show potential for use in surface coatings.

1. Introduction

Photocatalysis, a light-induced chemical reaction mechanism, has gained increasing attention due to its potential in addressing environmental pollution and promoting sustainable energy solutions [1]. Among various photocatalysts, ZnO nanoparticles have emerged as a promising material owing to their wide bandgap 3.37 eV, high exciton binding energy, UV absorption capability, excellent thermal and chemical stability, non-toxicity, and biocompatibility [2]. These properties make ZnO highly suitable for diverse applications such as UV protection, antibacterial coatings, optoelectronics, and environmental remediation. Notably, porous ZnO nanoparticles offer advantages such as high surface area, enhanced surface activity, and structural uniformity, which improve photocatalytic and sensing performances [3]. Given these benefits, the synthesis method plays a crucial role in tailoring ZnO's properties. Among various techniques, the sol-gel method stands out due to its simplicity, low-temperature processing, control over particle size and morphology, and superior chemical homogeneity, making it widely preferred in nanoparticle fabrication [4].

2. Experimental Procedures

2.1. Materials

Zinc acetate dihydrate ($(CH_3COO)_2Zn * 2 H_2O$, Merck KGaA /Germany) as the zinc source, tartaric acid ($C4H6O6$, Merck 100804 L(+)-Tartaric Acid for Analysis Emsure®) as the acid and distilled water (DW) were used while preparing the solution with sol-gel method.

2.2. Synthesis of ZnO nanoparticles

In the experimental study, the synthesis of six different powders, shown in *Table 1*, was carried out. In the experimental study, two different groups were carried out to examine the morphological and structural effects of tartaric acid and calcination temperature on the ZnO nanoparticle. In the initial set of Exp. 1.0 group to understand the effect of calcination temperature, zinc acetate dihydrate, and tartaric acid were meticulously weighed using a precision scale, maintaining a mole-to-mole ratio of 1:1. In this experimental procedure, adding tartaric acid to the beaker followed the initial addition and dissolution of zinc acetate dihydrate in 100 ml of DW on a magnetic stirrer. The solution was subjected to a thorough mixing process utilizing a magnetic stirrer for 30 minutes while maintaining a constant rotational speed of 450 revolutions per minute (rpm). This meticulous

agitation continued until the solution's temperature reached a level of 90 °C. The specimen was subjected to thermal treatment within an oven operating at a controlled temperature of 80 °C for precisely 24 hours. A series of experiments were meticulously devised to investigate the influence of temperature, encompassing three distinct temperature levels: 400, 500, and 600 °C. In the subsequent phase, a series of meticulously designed experiments were conducted to thoroughly investigate the influence of tartaric acid on the intricate nanostructure. These experiments were carried out at three distinct moles of tartaric acid to provide a comprehensive understanding of its effects. In the experiments, the substances under investigation were zinc acetate dihydrate and tartaric acid. These substances were carefully measured in weight-to-weight ratios of 1:1 (Exp. 1.1), 2:1 (Exp. 1.2), and 10:1 (Exp. 1.3), respectively. Other experimental steps were repeated as in the first experiment.

Table 1. Chemical ratios of raw materials and different calcination parameters for different ZnO NPs.

Experiment Code	Zinc Source and Moles	Tartaric Acid Moles	Mixing	Drying	Calcination
Exp. 1.0-a	Zinc Acetate Dihydrate (0.15 mole)	0.15	90 °C, 3 hours	80 °C, 24 hours	400 °C, 1 hour
Exp. 1.0-b	Zinc Acetate Dihydrate (0.15 mole)	0.15	90 °C, 3 hours	80 °C, 24 hours	500 °C, 1 hour
Exp. 1.0-c	Zinc Acetate Dihydrate (0.15 mole)	0.15	90 °C, 3 hours	80 °C, 24 hours	600 °C, 1 hour
Exp. 1.1	Zinc Acetate Dihydrate (0.1 mole)	0.1	90 °C, 3 hours	80 °C, 24 hours	500 °C, 1 hour
Exp. 1.2	Zinc Acetate Dihydrate (0.1 mole)	0.05	90 °C, 3 hours	80 °C, 24 hours	500 °C, 1 hour
Exp. 1.3	Zinc Acetate Dihydrate (0.1 mole)	0.01	90 °C, 3 hours	80 °C, 24 hours	500 °C, 1 hour

The experimental stages depicted in *Figure 1* were implemented according to the schematic representation.

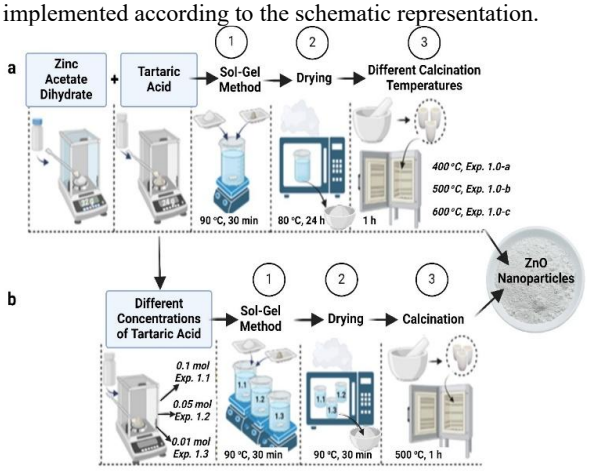

Figure 1. Experiments were carried out by keeping the zinc source constant and changing the **a)** calcination temperatures like 400, 500 and 600°C and **b)** tartaric acid moles like 0.1, 0.05 and 0.01.

3. Results and Discussion

In the results section, Fourier Transform Infrared Spectroscopy (FT-IR), Scanning Electron Microscope (SEM), X-Ray Diffraction (XRD), Thermogravimetry Differential Thermal (TG/DTA) and photocatalytic activity tests were performed on the powders.

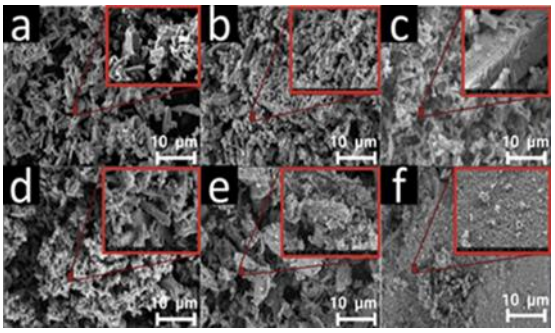

Figure 2. SEM images **a)** for Exp. 1.0-a, calcination at 400 °C in 4 µm and 10 µm; **b)** for Exp. 1.0-b, calcination at 500 °C in 4 µm and 10 µm; **c)** for Exp. 1.0-c, calcination at 600 °C in 2 µm and 10 µm; **d)** for Exp. 1.1, (0,1) mole tartaric acid in 3 µm and 10 µm; **e)** for Exp. 1.2, (0,05) mole tartaric acid in 3 µm and 10 µm; **f)** for Exp. 1.3, (0,01) mole tartaric acid in 3 µm and 10 µm.

Morphological images of six different powders are added in SEM images in *Figure 2*. It was determined that the best porosity and rod-like structure were seen in the powder calcined at 600°C.

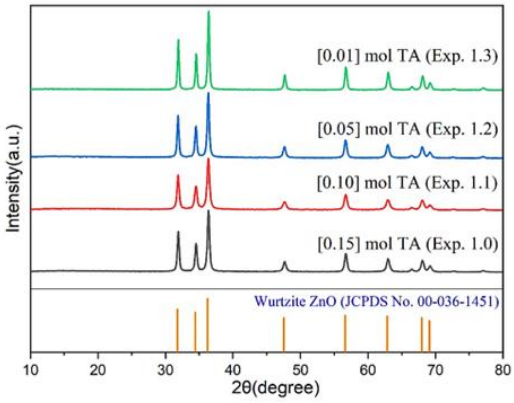

Figure 3. XRD patterns of ZnO nanoparticles synthesized with different tartaric acid moles.

The X-ray diffraction (XRD) patterns obtained for the synthesized zinc oxide (ZnO) nanoparticles have been presented in *Figure 3*. X-ray diffraction (XRD) analysis

provides compelling evidence supporting the hexagonal wurtzite structure in the synthesized ZnO nanoparticles [5].

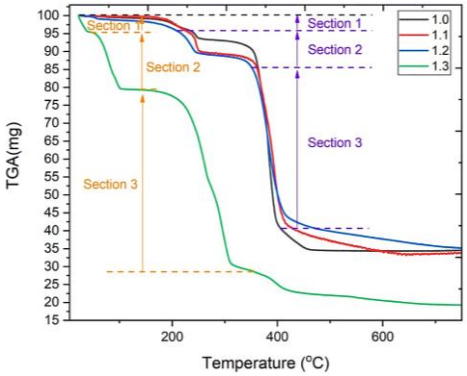

Figure 4. TGA analysis for ZnO nanoparticles with different tartaric acid moles before the calcination process.

TGA is a technique in which the mass of a sample is monitored as a function of temperature (thermal) or time (equilibrium) under a controlled temperature program in a controlled atmosphere in *Figure 4*. During the initial decomposition stage, occurring within the 25 to 250°C temperature range, moisture, salt, and impurities decomposition is observed at a specific temperature of 50°C for Exp. 1.3. However, for other tartaric acid rates, this decomposition process takes place at temperatures exceeding 200°C. Subsequently, commencing at temperatures ranging from 250 to 350°C, a substantial reduction in mass is observed, coinciding with the onset of ZnO transformations. Conversely, at temperatures exceeding 350°C, both the mass decrease and alteration exhibit a diminishing trend, reaching minimal values as the formation of ZnO commences. Consequently, carbon dioxide (CO_2) and carbon monoxide (C.O.) effectively eliminated the structure's carbon components. The experimental investigation observed that a mere 18 % of the initial mass was retained. Notably, this reduction was determined to be approximately 35 % in the case of different moles of tartaric acid.

The present study investigates the efficacy of highly reactive radicals in the oxidation of organic pollutants, resulting in the formation of benign byproducts, namely carbon dioxide (CO_2) and water (H_2O). The utilization of nanoscale ZnO particles in photocatalytic reactions is of significant interest due to their remarkable surface area/volume ratio. This unique characteristic offers more active sites, thereby enhancing the efficiency of photocatalytic reactions. Moreover, the nanosize of these particles facilitates improved dispersion and interaction with organic pollutants, further augmenting their photocatalytic performance. According to the photocatalytic analyses, while the amount of degradation does not reach 9 % in the absence of UV, the amount of pigment degradation of ZnO nanoparticles in the presence of UV is observed to be at least 86 %. It is known that Exp. 1.0-b particles exposed to UV light for 90 minutes cause 89.89 %, Exp. 1.1 particles cause 86.4 %, Exp. 1.2 particles cause 94.51 %, and Exp. 1.3 particles cause 90.47 % of dye degradation.

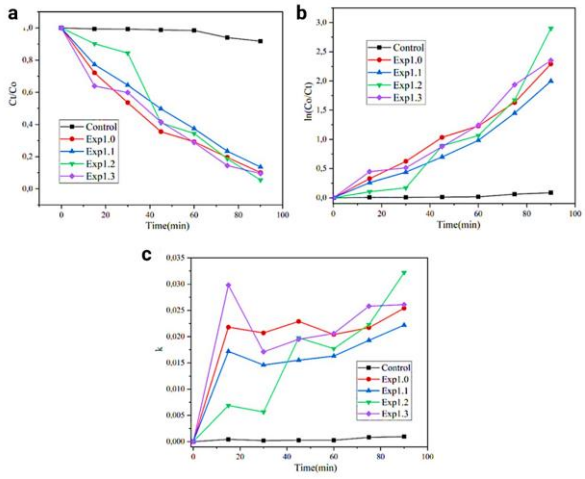

Figure 5. a) Ct/Co ratio of the M.B. dye degradation at different tartaric acid mole ZnO nanoparticles, **b)** first-order kinetic plots of the M.B. dye degradation, **c)** and dye degradation rate constants(k).

Figure 5 illustrates the degradation constant and first-order kinetic calculations and results to aid in comprehending the methylene blue degradation mechanism of ZnO nanoparticles. *Figure 5 (a)* displays the Ct/Co ratio, where Ct represents the dye mole after a specified period and Co represents the initial mole before degradation.

Moreover, the experimental results demonstrate that Exp. 1.2 ZnO nanoparticles exhibit the most pronounced photocatalytic activity. The effect of the morphology change on the photocatalytic activity is depicted in the Ct/Co curves by the extremely high degradation rate of Exp. 1.3 at the 15th minute with a value of 0.6392, while the low degradation rate of Exp. 1.2 at the 30th minute is 0.8438, which is very close to 1. As depicted in *Figure 6*, ZnO nanoparticles containing methylene blue degraded when exposed to ultraviolet light, resulting in color differences. After 90 minutes, the degradation of approximately 9 percent in the control samples does not result in a significant color change. When exposed to ultraviolet light, the ZnO nanoparticles generated with varying moles of tartaric acid degrade methylene blue and their colors approach white. After 90 minutes, it is believed that the methylene blue of Exp. 1.2 ZnO nanoparticles, which degraded the most, became completely transparent.

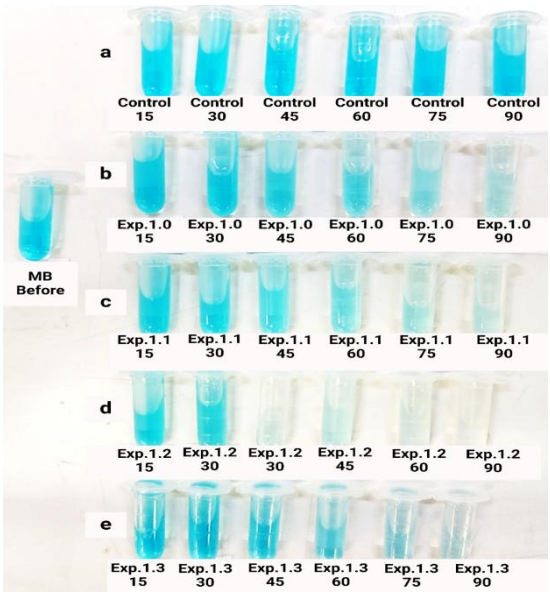

Figure 6. Methylene blue before analysis in UV-visible spectrophotometer to get a baseline and to understand the color change of the ZnO nanoparticle in all experimental groups and the control group at different time intervals **a)** Control group, **b)** Exp. 1.0-b group, **c)** Exp. 1.1 group, **d)** Exp. 1.2 group, and **e)** Exp. 1.3 group.

4. Conclusion

In conclusion, this study examined the effect of tartaric acid on ZnO nanoparticles in a systematic manner, casting light on the modification of their morphological, structural, and photocatalytic properties. The Zn-O bond at a wavelength of 453 cm^{-1} and the wurtzite crystal structure of ZnO nanoparticles are evidence of their formation. 600°C is believed to be the optimal calcination temperature for ZnO nanoparticles produced with tartaric acid. Low tartaric acid (0.01 $mole.L^{-1}$) prevents the production of prismatic forms because it cannot provide sufficient substrate for crystallization. While increasing tartaric acid mole results in forming ZnO nanoparticles with a finer and more uniform prismatic shape, it also decreases photocatalytic activity by reducing porosity. Therefore, ZnO nanoparticles produced with 0.05 mole tartaric acid have the highest photocatalytic activity and induce the degradation of nearly 94.51 % of methylene blue within 90 minutes.

Acknowledgment

The authors also acknowledge the financial support from Yıldız Technical University under contract numbers FBA-2024-6093, FDK-2019-3742 and FBA-2023-5301, respectively. TG/DTA and UV-visible analyses were carried out at Sabancı University Nanotechnology Application and Research Center (SUNUM).

References

[1] Cho, J., Lin, Q., Yang, S., Simmons, J.G., Cheng, Y., Lin, E., Yang, J., Foreman, J.V., Everitt, H.O., Yang, W., Kim, J., Liu, J.: Sulfur-doped zinc oxide (ZnO) Nanostars: Synthesis and simulation of growth mechanism. Nano Res. (2012). https://doi.org/10.1007/s12274-011-0180-3

[2] Kondal, N.: Effect of high temperature annealing on structural and defect associated properties on ZnO nanoparticles. Materials Today: Proceedings (2021). https://doi.org/10.1016/j.matpr.2020.09.009

[3] Sowri Babu, K., Ramachandra Reddy, A., Sujatha, C., Venugopal Reddy, K., Mallika, A.N.: Synthesis and optical characterization of porous ZnO. J Adv Ceram (2013). https://doi.org/10.1007/s40145-013-0069-6

[4] Hasnidawani, J.N., Azlina, H.N., Norita, H., Bonnia, N.N., Ratim, S., Ali, E.S.: Synthesis of ZnO Nanostructures Using Sol-Gel Method. Procedia Chemistry (2016). https://doi.org/10.1016/j.proche.2016.03.095

[5] Deepty, M., Srinivas, C., Kumar, E.R., Mohan, N.K., Prajapat, C.L., Rao, T.C., Meena, S.S., Verma, A.K., Sastry, D.L.: XRD, EDX, FTIR and ESR spectroscopic studies of co-precipitated Mn–substituted Zn–ferrite nanoparticles. Ceramics International (2019). https://doi.org/10.1016/j.ceramint.2019.01.029

DEVELOPMENT OF NANOFIBER MEMBRANES FOR GAS SEPARATION AND PURIFICATION

Bilge Betul Ozcelik[1,2], Melek Erol Taygun[1]

[1]Istanbul Technical University, Chemical & Metallurgical Engineering Faculty, Department of Chemical Engineering, 34469, İstanbul, Türkiye

[2]TÜBİTAK Marmara Research Center, Materials and Process Technologies Vice Presidency, P.O. Box 21, 41470 Gebze, Kocaeli, Türkiye

Keywords: Cellulose Acetate, Electrospinning, Nanofiber Membrane, CO_2 Capture

Abstract

Electrospinning enables a straightforward and adaptable method for obtaining nanofibrous polymer membranes with elevated specific surface area. This work involved the electrospinning of cellulose acetate (CA) solutions under systematically changed processing settings to optimize nanofiber morphology for potential carbon dioxide (CO_2) separation and purification applications. A three-factor Box–Behnken design (BBD) was utilised to assess the influence of polymer content (9–11 wt%), solvent ratio (a binary solvent system of acetone and dimethylacetamide, AC/DMAC, with acetone mass fraction varying from 0.33 to 0.67), and mixing duration (6–24 h) on the diameter of nanofibers and their structural integrity. Scanning electron microscopy (SEM) was used to evaluate nanofiber homogeneity, bead formation, and overall morphological quality using quantitative mean nanofiber diameter (MeanDia) analysis and a semi-quantitative morphology score (MorphScore). The analysis of variance (ANOVA) revealed that the solvent ratio (AC/DMAC) was the predominant factor, succeeded by polymer concentration, but mixing time had negligible impacts, primarily through interactions. Response surface approach optimization indicated an optimum at 11% CA, AC/DMAC ratio of 0.667, and 24 hours of mixing, resulting in nanofibers with an average diameter of approximately 123 nm and a MorphScore of about 8.8. The results highlight the critical influence of solvent composition in electrospinning, offering a solid foundation for the design of CA nanofiber membranes with improved gas separation and purification performance.

1. Introduction

Carbon dioxide (CO_2) emissions from extensive industrial activities, including fossil fuel combustion, cement production, and fermentation, surpass 30 billion tones each year and are recognized as a significant contributor to global climate change [1]. CO_2, a significant greenhouse gas, has garnered considerable attention in terms of mitigation strategies and technological advancements. Mature technologies for CO_2 separation, such as absorption, adsorption, and cryogenic distillation, are well-established. However, membrane-based processes have garnered significant interest in recent decades owing to their reduced energy requirements, operational simplicity, and cost-effectiveness [2]. Electrospinning has emerged as a significant method for the fabrication of polymer nanofiber membranes, characterized by tunable morphology, high porosity, and extensive specific surface area [3]. The structural characteristics directly affect transport properties and separation and purification efficiency. Cellulose acetate (CA) is a promising material for electrospun membranes due to its biodegradability, chemical stability, and cost-effectiveness [4]. The morphology and fiber diameter of CA nanofibers are significantly influenced by electrospinning parameters, including polymer concentration, solvent composition, and solution preparation duration [5]. Optimizing these variables is crucial for generating bead-free, uniform nanofibers that possess the required properties for gas separation and purification. This study employed a statistical Design of Experiments (DoE) framework utilizing the BBD design to systematically assess the impact of critical electrospinning parameters on the morphology of CA nanofibers. This study integrates quantitative fiber diameter measurements with a semi-quantitative morphology score, thereby establishing a solid basis for optimizing electrospinning conditions and enhancing the design of CA-based nanofiber membranes for CO_2 separation, purification, and related applications.

2. Experimental Procedure

2.1 Materials

Cellulose acetate (CA, Mn ≈ 50,000 as determined by GPC, Sigma-Aldrich) served as the polymer in this study. The solvent system comprised acetone (AC, ≥99.5%, ISOLAB Chemicals) and dimethylacetamide (DMAC, ≥99%, Sigma-Aldrich). All chemicals utilized were of analytical grade and employed without additional purification.

2.2 Experimental Design

A three-factor, three-level BBD design was utilized to assess the influence of solution and processing variables on the morphology of electrospun nanofibers. The factors that were independent included (Table 1). The design included 15 runs (Table 2), incorporating replicated center points to enhance statistical reliability. Throughout all experiments, voltage was maintained at 20–24 kV, flow rate at 2 mL h^{-1}, and tip-to-collector distance at 215 mm.

Table 1. Experimental Factors and Levels Used in the Box–Behnken Design

Factor	Level (−1)	Level (0)	Level (+1)
CA%	9	10	11
AC/DMAC	0.33	0.50	0.67
Mixing time (h)	6	15	24

Table 2. 15 Runs in the Box–Behnken Design

Run	Polymer	Conc. (%)	AC/DMAC	Mixing time (h)
1	CA	10%	0.667	24
2	CA	9%	0.5	6
3	CA	9%	0.667	15
4	CA	11%	0.5	24
5	CA	9%	0.333	15
6	CA	11%	0.333	15
7	CA	10%	0.333	24
8	CA	10%	0.667	6
9	CA	10%	0.5	15
10	CA	11%	0.5	6
11	CA	10%	0.333	6
12	CA	10%	0.5	15
13	CA	9%	0.5	24
14	CA	11%	0.667	15
15	CA	10%	0.5	15

2.3 Electrospinning Procedure

CA solutions were formulated at specified concentrations and solvent ratios, and were homogenized through magnetic stirring for the required mixing durations. Each solution was introduced into a syringe pump and electrospun onto a grounded collector under regulated environmental conditions (temperature ~23 ± 2 °C, relative humidity 40–50%).

2.4 Morphological Characterization

The morphology of the electrospun membranes was analyzed through scanning electron microscopy (SEM, Philips XL30 SFEG). Fiber diameters were quantified from a minimum of 100 individual fibers per sample utilizing ImageJ software, and the mean fiber diameter (MeanDia) was determined. Morphological integrity was assessed using a semi-quantitative morphology score (MorphScore, 0–10), which considers bead formation, fiber continuity, and overall network homogeneity.

2.5 Statistical Analysis

Statistical modelling and analysis were conducted using Minitab 16. Quadratic regression models were applied to the experimental data, and an analysis of variance (ANOVA) was conducted to evaluate factor significance. Model adequacy was assessed using the coefficient of determination (R^2, adjusted R^2, predicted R^2), residual analysis, and lack-of-fit testing. Response optimizer tools were utilized to determine the optimal electrospinning conditions for reducing MeanDia and enhancing MorphScore.

3. Results and Discussion

3.1 Morphological Observations

SEM analysis revealed that the morphology of nanofibers was strongly dependent on the solution composition. At a low CA concentration (9%) combined with low AC/DMAC ratios (≤0.33), the electrospinning process predominantly yielded bead-like or particle-shaped structures, indicative of insufficient chain entanglement and unstable jet dynamics. In contrast, increasing the CA concentration to 11% and employing higher solvent fractions (0.50–0.67) resulted in the formation of continuous nanofiber networks with substantially fewer structural defects (Figure 1). The mixing time primarily influenced solution homogeneity, with minimal direct effect on nanofiber morphology.

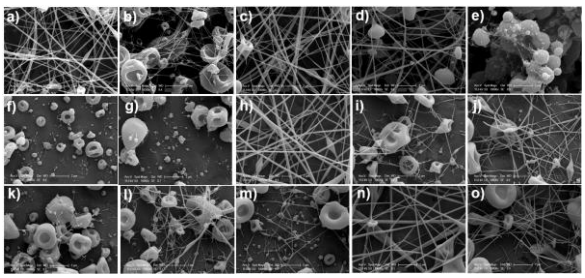

Figure 1. SEM micrographs of electrospun CA nanofiber membranes under different Box–Behnken runs: (a) Run-1, (b) Run-2, … (o) Run-15

A semi-quantitative Morphology Score (0–10) was utilised, evaluating fibre density, bead formation, and structural homogeneity in SEM images to qualitatively assess fibre formation and integrity, as similarly employed in prior electrospinning studies [6]. The average nanofiber diameters (MeanDia) ranged from about 60 to 145 nm, depending on the conditions.

3.2 Statistical Analysis and Model Adequacy

The ANOVA findings showed that the AC/DMAC ratio was the most important factor for both MeanDia (Table 3) and MorphScore ($p < 0.05$) (Table 4). Polymer

concentration was significant for MorphScore ($p = 0.045$) and marginally significant for MeanDia ($p \approx 0.053$). Mixing time didn't matter on its own, but it did have an effect when combined with solvent ratio, showing that it had an indirect effect.

Table 3. ANOVA Summary for MeanDia

Source	DF	Seq SS	Adj SS	Adj MS	F	P
Regression	8	9031.41	9031.41	1128.93	16.67	0.058
Linear	3	6135.71	7371.32	2457.11	36.29	0.027
CA%	1	1009.05	1186.39	1186.39	17.52	0.053
AC/DMAC	1	5090.00	5187.31	5187.31	76.60	0.013
Mixing time, h	1	54.26	997.61	997.61	14.73	0.062
Square	2	516.84	516.64	258.32	3.81	0.208
CA%*CA%	1	431.86	504.99	504.99	7.46	0.112
Mixing time, h*Mixing time, h	1	84.78	84.78	84.78	1.25	0.380
Interaction	3	2361.46	2361.46	787.15	11.62	0.08
CA%*AC/DMAC	1	217.14	217.14	217.14	3.21	0.215
CA%*Mixing time, h	1	182.78	182.78	182.78	2.70	0.242
AC/DMAC*Mixing time, h	1	1961.53	1961.53	1961.53	28.97	0.033
Residual Error	2	135.43	135.43	67.72		
Pure Error	2	135.43	135.43	67.72		
Total	10	9166.85				

Table 4. ANOVA Summary for MorphScore

Source	DF	Seq SS	Adj SS	Adj MS	F	P
Regression	9	94.5667	94.5667	10.5074	16.59	0.003
Linear	3	84.0000	89.0000	29.6667	46.84	0.000
CA%	1	4.5000	4.5000	4.5000	7.11	0.045
AC/DMAC	1	84.5000	84.5000	84.5000	133.42	0.000
Mixing time, h	1	0.0000	0.0000	0.0000	0.00	1.000
Square	3	0.8167	0.8167	0.2722	0.43	0.741
CA%*CA%	1	0.2333	0.3141	0.3141	0.50	0.513
AC/DMAC*AC/DMAC	1	0.2692	0.3141	0.3141	0.50	0.513
Mixing time, h*Mixing time, h	1	0.3141	0.3141	0.3141	0.50	0.513
Interaction	3	4.7500	4.7500	1.5833	2.50	0.174
CA%*AC/DMAC	1	2.2500	2.2500	2.2500	3.55	0.118
CA%*Mixing time, h	1	2.2500	2.2500	2.2500	3.55	0.118
AC%/DMAC*Mixing time, h	1	0.2500	0.2500	0.2500	0.39	0.557
Residual Error	5	3.1667	3.1667	0.6333		
Lack-of-Fit	3	0.5000	0.5000	0.1667	0.13	0.937
Pure Error	2	2.6667	2.6667	1.3333		
Total	14	97.7333				

The model fits were quite good: for MeanDia, $R^2 = 98.52\%$, and adj $R^2 = 92.61\%$; for MorphScore, $R^2 = 96.76\%$, adj $R^2 = 90.93\%$, and pred $R^2 = 85.68\%$. The lack of fit was not significant for MorphScore ($p = 0.937$), which confirmed that the model was good enough. MeanDia could not be properly tested because there were no runs (fiberless circumstances). The regression model for the mean fiber diameter (MeanDia) was expressed as Equation (1), while the regression model for the morphological quality score (MorphScore) was formulated as Equation (2). Both equations were obtained using uncoded units of the experimental factors.

$$MeanDia_{nm} = 683.17 - 238.60 \cdot CA\% + 1418.29 \cdot \left(\frac{AC}{DMAC}\right) + 9.15 \cdot t_{mix} + 14.14 \cdot (CA\%)^2 - 0.07 \cdot (t_{mix})^2 - 76.42 \cdot \left(CA\% \times \frac{AC}{DMAC}\right) + 0.75 \cdot (CA\% \times t_{mix}) - 25.52 \cdot \left(\frac{AC}{DMAC} \times t_{mix}\right) \quad \textbf{(Eq.1)}$$

$$MorphScore = 51.7351 - 8.5788 \cdot CA\% - 33.4122 \cdot \left(\frac{AC}{DMAC}\right) - 0.8582 \cdot t_{mix} + 0.2917 \cdot (CA\%)^2 + 10.4581 \cdot \left(CA\% \times \frac{AC}{DMAC}\right) + 4.4910 \cdot (CA\% \times t_{mix}) - 0.1663 \cdot \left(\frac{AC}{DMAC} \times t_{mix}\right) \quad \textbf{(Eq.2)}$$

The residuals were normally distributed and didn't indicate any systematic bias (Figure 2, Figure 3).

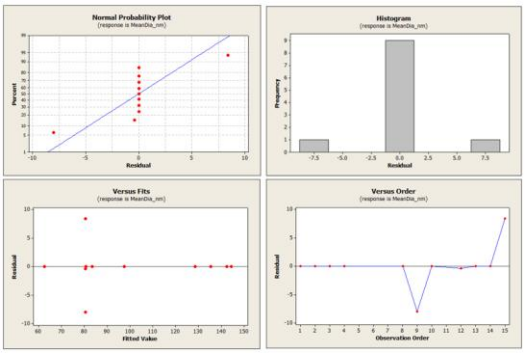

Figure 2. Residual plots for MeanDia including normal probability, histogram, residuals vs fits, and residuals vs order

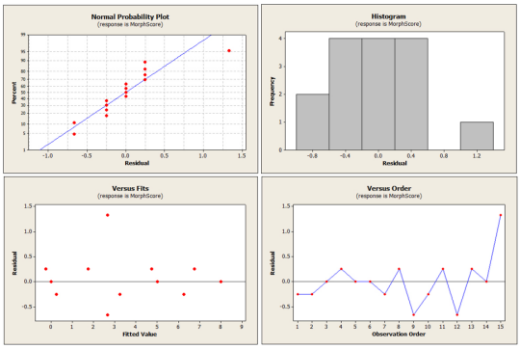

Figure 3. Residual plots for MorphScore including normal probability, histogram, residuals vs fits, and residuals vs order

3.3 Surface and Contour Plot Analysis

Surface plots showed that the solvent ratio was the most important element, with CA concentration being a minor influence and mixing time having only small effects (Figure 4). Contour plots indicated that lowering the AC/DMAC ratio lowered the MeanDia (Figure 5a), while raising the CA concentration and solvent proportion increased the MorphScore (Figure 5b).

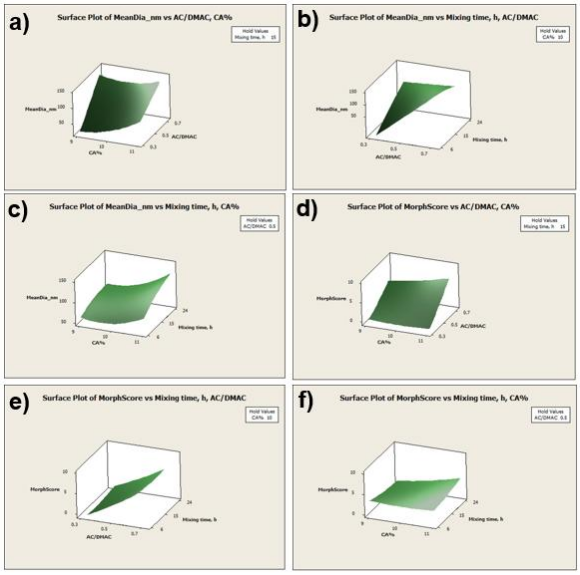

Figure 4. Surface Plot of MeanDia and MorphScore

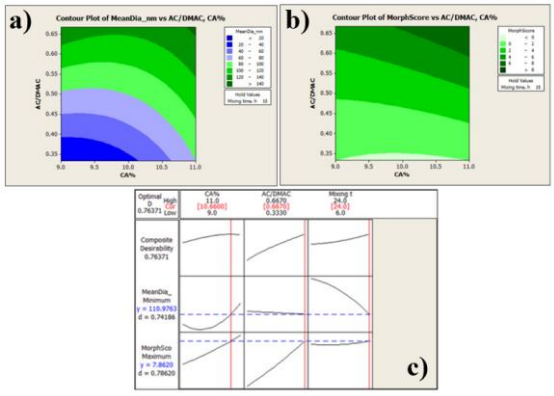

Figure 5. Contour plot of MeanDia (a) MorphScore (b) vs CA concentration and AC/DMAC ratio, (c) Response Optimizer Plot

3.4 Multi-Response Optimization

The analysis of the response optimizer indicated that the optimal electrospinning conditions were CA = 11%, AC/DMAC = 0.667, and a mixing time of 24 hours (Figure 5c). Under these conditions, the predicted mean fiber diameter was 122.8 nm (95% CI: 77–168 nm; 95% PI: 65–180 nm), and the MorphScore was 8.8 (95% CI: 6.4–11.2; 95% PI: 5.6–11.9). The composite desirability of 0.76 showed that both objectives, MeanDia minimisation and MorphScore maximisation, were effectively attained.

4. Conclusion

This study systematically fabricated and optimized cellulose acetate (CA) nanofiber membranes through electrospinning, utilizing a Box–Behnken experimental design. The findings indicated that the solvent ratio was the primary factor influencing both fiber diameter and structural homogeneity, whereas polymer concentration had a secondary yet notable impact. The influence of mixing time was minimal, mainly through its interaction with solvent composition. The statistical analysis validated the robustness of the quadratic models, evidenced by high coefficients of determination (R^2 > 95%) and an insignificant lack-of-fit for MorphScore. Response surface methodology was employed for optimization, revealing optimal electrospinning conditions: CA = 11%, AC/DMAC = 0.667, and a mixing time of 24 hours. Under these conditions, the predicted average fiber diameter was approximately 123 nm, and the MorphScore attained a value of 8.8, indicating bead-free fiber networks. A composite desirability value of 0.76 reflects a balanced optimization outcome. The findings underscored the significant influence of solvent composition on nanofiber morphology and provide a robust framework for the optimization of CA membranes with superior morphological quality. The optimized structures showed significant potential for applications in CO_2 separation and purification.

References

[1] Li, B., Duan, Y., Luebke, D., & Morreale, B. (2013). Advances in CO_2 capture technology: A patent review. *Applied Energy*, *102*, 1439-1447.

[2] Valappil, R. S. K., Ghasem, N., & Al-Marzouqi, M. (2021). Current and future trends in polymer membrane-based gas separation technology: A comprehensive review. *Journal of Industrial and Engineering Chemistry*, *98*, 103-129.

[3] Heidari, Y., Noroozian, E., & Maghsoudi, S. (2023). Electrospun nanofibers of cellulose acetate/metal organic framework-third generation PAMAM dendrimer for the removal of methylene blue from aqueous media. *Scientific Reports*, *13*(1), 4924.

[4] Oldal, D. G., Topuz, F., Holtzl, T., & Szekely, G. (2023). Green electrospinning of biodegradable cellulose acetate nanofibrous membranes with tunable porosity. *ACS Sustainable Chemistry & Engineering*, *11*(3), 994-1005.

[5] Toro-Gallego, M., Valencia, C., Sánchez, M. C., Martín-Alfonso, J. E., & Franco, J. M. (2025). Use of Electrospun Cellulose Acetate/Silica Composites as Multifunctional Ingredients in Eco-Friendly Semisolid Lubricant Formulations. *Journal of Applied Polymer Science*, *142*(7), e56489.

[6] Amores de Sousa, M. C., Rodrigues, C. A., Ferreira, I. A., Diogo, M. M., Linhardt, R. J., Cabral, J. M., & Ferreira, F. C. (2020). Functionalization of electrospun nanofibers and fiber alignment enhance neural stem cell proliferation and neuronal differentiation. *Frontiers in Bioengineering and Biotechnology*, *8*, 580135.

POSTER PRESENTATIONS

Advanced Ceramics and Composites

INVESTIGATION OF ELECTROCALORIC PROPERTIES OF PVDF-BCZT COMPOSITES

Sinem Saclioglu[1], Ebru Mensur[1],

1. Gebze Technical University, Department of Materials Science and Engineering, Kocaeli.

Solid state cooling has gained significant importance nowadays due to developments in the energy sector, efforts to improve living standards, and concerns like climate change. There is an urgent need to develop energy efficient cooling technologies that do not negatively affect the environment. In this context, solid state cooling systems using caloric effects have come to the forefront as alternatives to conventional vapor-compression systems. Especially with increasing energy costs and need to reduce CO_2 emissions, these technologies are becoming more attractive.Regulations such as RoHS, which restrict the use of lead-based materials, have increased the focus on lead-free compositions in solid-state cooling applications. These systems are also valuable for cooling miniaturized electronic circuits.In this study, lead-free BCZT ceramic based on barium titanate containing Ca and Zr were combined with P(VDF-TrFE) polymer to produce 0–3 type composite film. The effect of different BCZT volume ratios in P(VDF-TrFE) matrix was examined, focusing on electrocaloric, dielectric, and ferroelectric properties. Thanks to its lead-free nature and good electrical characteristics, BCZT stands out as a promising material for sustainable cooling technologies. The final goal is to apply these eco-friendly electrocaloric composites in various fields that use electronic circuitry.

Firstly, $(Ba_{1-x}Ca_x)(Zr_YTi_{1-Y})O_3$ (BCZT) ceramics were synthesized by a solid-state reaction using $BaCO_3$, $CaCO_3$, ZrO_2, and TiO_2 powders. Powder mixture was calcined at 1200°C for 6h and sintered at 1440°C for 4h. Phase analysis of the BCZT powder was performed using XRD.BCZT powders at different volume ratios were mixed with various molar ratios of P(VDF-TrFE) polymer in DMF to form a homogeneous mixture. The 0–3 piezocomposite films were prepared via solution casting and dried in furnace. Then, the dried films were heat treated at 135°C for 3h. Structural characterizations were carried out using XRD, FTIR, and SEM.For electrical measurements, both sides of the films were coated with silver electrodes. Temperature-dependent P–E hysteresis measurements were conducted to investigate electrocaloric behavior. Electrocaloric temperature change (ΔT) was calculated indirectly using the Maxwell relation. Also, the temperature-dependent dielectric constant and dielectric loss of the samples were also measured. Finally, the mechanical strength of the films with BCZT additive was evaluated.

XRD and FTIR results showed that thermal treatment formed the polar β-phase in P(VDF-TrFE), and BCZT addition increased crystallinity.The dielectric constant of pristine P(VDF-TrFE) was15, which increased to 20 with the addition of 10 vol.% BCZT at room temperature.When P-E curves are examined, the +Ec (coercive field) of the pristine P(VDF-TrFE) polymer is measured to be approximately 730 kV/cm, whereas the composite with 10 vol.% BCZT sample exhibited a

significantly reduced value of ~450 kV/cm.Electrocaloric measurements showed −11 K ΔT at 1200 kV/cm for pristine P(VDF-TrFE), and −4.2 K ΔT at 700 kV/cm with 10 vol.% BCZT.

This study demonstrates the potential of BCZT addition P(VDF-TrFE)-based composite films for environmentally friendly solid-state cooling applications. The combination of BCZT ceramic with P(VDF-TrFE) matrix significantly enhanced the dielectric and electrocaloric properties of the composites. Thermal treatment promoted the formation of the polar β-phase, while BCZT addition improved crystallinity, dielectric constant, and breakdown strength. A notable decrease in the coercive field with BCZT addition enabled significant ΔT values at lower electric fields. These findings suggest that high energy-efficient cooling systems can be achieved through such composite designs. Overall, P(VDF-TrFE)-based lead-free composites are promising candidates for next-generation cooling technologies, especially in applications where compactness, efficiency, and environmental safety are essential, such as in modern miniature electronic systems.

Keywords: Solid-state cooling, Electrocaloric effect, Lead-free compositions.

INVESTIGATION OF THE EFFECT OF SAMARIUM DOPING ON THE MICROSTRUCTURAL AND ELECTRICAL PROPERTIES OF PMN-PZT CERAMICS

Maral Kervancı[1], Sedat Alkoy[1], Ayşe Berksoy Yavuz [2],

1. Gebze Technical University

2. Istanbul Gedik University

PMN-PZT ceramics [(1-x)Pb($Mg_1/_3Nb_2/_3$)O_3–xPb(Zr,Ti)O_3] are of significant importance in transducers due to high dielectric constant, strong piezoelectric response, and stable phase transition behaviour. Samarium, a rare earth element, can substitute A- or B-site cations in the perovskite structure due to its ionic radius and electronic configuration, potentially inducing notable changes in the microstructural evolution, grain growth, and electrical properties of PMN-PZT.This study aims to investigate the effects of samarium doping on the structural and electrical properties of the 0.40PMN-0.25PZ-0.35PT composition.

This particular composition was selected due to its proximity to the morphotropic phase boundary (MPB) region, which is known for its enhanced piezoelectric and dielectric properties. Samarium was substituted into the PMN-PZT ceramics in varying amounts via the conventional solid-state reaction method. After the powder preparation steps, the obtained powders were mixed with binders, uniaxially pressed into pellets using steel molds, and sintered at 1200°C for 6 hours, followed by microstructural and electrical characterization.

The findings revealed that samarium doping leads to modifications in the crystal structure of the ceramics and causes significant variations in electrical conductivity, dielectric behavior, and piezoelectric performance.

Consequently, this study demonstrates the potential of samarium doping in enhancing the piezoelectric properties of PMN-PZT-based ceramic materials.

Keywords: 0.40PMN-0.25PZ-0.35PT, Samarium,Doping,Piezoelectric properties

SYNTHESIS OF KNN TEMPLATE PARTICLES WITH NEEDLE-LIKE MORPHOLOGY VIA THE MOLTEN SALT METHOD AND STRUCTURAL CHARACTERIZATION

Emirhan Ersoy[1], Sedat Alkoy[1], Ayşe Berksoy Yavuz[2],

1. Gebze Technical University & STEM Sensor Technologies and Electronic Materials Ltd.

2. Istanbul Gedik University

Environmental and health concerns over lead led to research on lead-free piezoceramics with enhanced piezoelectric properties. Enhancement is usually done by texturing the lead-free piezoceramics through tape casting and templated grain growth, which requires anisometric single crystalline template particles with plate-like morphology. Textured piezoceramic fibers, on the other hand, requires needle-like template particles.

This study focuses on synthesizing needle-like potassium sodium niobate (KNN) template particles to texture KNN fibers. A two-step molten salt synthesis (MSS) process with $K_2Nb_4O_{11}$ (KN) precursors was used.

KN particles were prepared at various salt/oxide ratios and heat-treated at 1000°C for 6 hours. These precursors were then used to form needle-like KNN particles through further heat treatment at 950°C for 0.5–3 hours.

Phase composition and microstructure were investigated using X-ray diffraction (XRD) and scanning electron microscopy (SEM). SEM analysis revealed a morphological change from a needle shape to a cubic form with longer heat treatment.

Keywords: Lead-free piezoceramics,(KNN),Textured ceramics

TOWARDS SINGLE-CRYSTAL-LIKE PROPERTIES: HIGHLY TEXTURED LEAD-FREE KNN-LT CERAMICS

Burak DAĞAŞAN[1], Sedat ALKOY[1], Ayşe BERKSOY YAVUZ[2],

1. Gebze Teknik Üniversitesi & STEM Sensor Technologies and Electronic Materials Ltd.

2. Istanbul Gedik University

Development of superior lead-free systems is necessary to replace piezoceramics that contain heavy metals such as lead, which threaten human health and the environment. Lead-free (K0.5Na0.5)NbO3 (KNN) stands out as one of the best alternatives due to its high Curie temperature and easily improved piezoelectric response through doping. A key challenge of undoped untextured KNN systems, is achieving stable piezoelectric and dielectric properties. Developing textured ceramics with properties similar to single crystals remains a focus of research.

In this study, a textured KNN system was produced using $KNbO_3$, $NaNbO_3$, and $LiTaO_3$ precursor powders, along with $NaNbO_3$ template particles, and sintered at 1100–1200°C.

Highly textured KNN-LT ceramics without any secondary phase were obtained and a through structural and electrical characterization was carried out. Temperature-dependent dielectric measurements were taken at various frequencies within the range of 25°C to 500°C.

Piezoelectric charge coefficient (d33) measurements indicate a drastic improvement with texture development.

Keywords: Lead-free ceramics,KNN,texture,piezoelectric properties,dielectric properties,$NaNbO_3$ template

INVESTIGATION OF THE EFFECT OF THE MORPHOLOGY AND ORIENTATION OF THE ACTIVE PHASE ON THE PROPERTIES OF 0-3 PIEZOCOMPOSITE TACTILE SENSORS

Mehmet Alkan[1], Sedat Alkoy[1],

1. Gebze Technical University

Tactile sensors imitate the sense of touch, one of the five human senses, and detect the hardness, surface roughness and temperature of the objects. With this feature, they are used in areas such as prosthetic limbs, robots and virtual reality. Piezoelectricity is the one of most popular mechanism in tactile sensor world.In this study, 0-3 piezocomposites having BaTiO3 active phase with different morphologies distributed in polymer matrix were produced. Anisometric BaTiO3 powders in plate-like morphology were synthesized with three step molten salt synthesis (MSS), and BaTiO3 powders in equiaxed spherical morphology were synthesized with single step MSS and solid-state reaction. BaTiO3 particles were mixed in polymer matrix at the ratios of 5%, 10%, 15%, 20%, 30% by volume and cast on glass with the help of “doctor blade” by tape casting method. As a result, highly flexible 0-3 piezocomposites with a thickness of 120-150 microns were obtained.

Keywords: Tactile Sensor, Piezocomposite, Barium Titanate

MAGNESIA BASED CASTABLE REFRACTORIES

İrem Nur Karadeniz[1], Yıldız Elmaz[1], Suat Yılmaz[1],

1. İstanbul Üniversitesi- Cerrahpaşa

The aim of this study is to investigate the structure, production, and performance of magnesia-based castable refractories. These materials are widely used in high-temperature industrial processes, especially in the iron-steel and cement industries. This work focuses on the components, physical and chemical properties, and industrial applications of magnesia castables.

In this study, technical literature and industrial data were reviewed. Different types of magnesia-based castables were examined based on their raw materials, binder systems, additives, and production methods. Performance tests such as thermal shock resistance, chemical corrosion resistance, and mechanical strength were evaluated and compared for various commercial products.

The study shows that magnesia-based castables have excellent resistance to basic slags, high thermal stability, and strong mechanical strength. Low-cement and self-flowing types offer better performance. Test results indicate that magnesia refractories with proper additives can improve durability and reduce cost in industrial applications.

Magnesia-based castable refractories are highly effective materials for extreme conditions. Their properties can be tailored with additives and production techniques. These materials are a strong alternative to traditional shaped refractories and offer significant benefits in modern industry.

Keywords: magnesia, castable refractories

INVESTIGATION OF THE PRODUCTION OF ZRB_2 POWDERS FROM ULTRA-HIGH TEMPERATURE CERAMICS

Nisa Soylu[1], Esra Kaya[1], Ali Osman Kurt[1],

1. Sakarya University

The primary objective of this research project is to develop a novel, cost-effective method for synthesizing zirconium diboride (ZrB_2) powders—a member of the ultra-high temperature ceramics (UHTCs) family—at significantly lower temperatures than those reported in the literature. Conventional production methods for ZrB_2 require temperatures between 1600–1800°C and rely on expensive boron sources such as elemental boron or boron carbide (B_4C). This study aims to utilize more affordable and readily available raw materials, namely zirconium oxide (ZrO_2) and boron oxide (B_2O_3), in combination with both solid and gaseous carbon sources within a dynamic carbothermal reduction (DCTR) process. The goal is to achieve high-purity, fine-grained ZrB_2 powder at temperatures as low as 1450–1550°C. Success in this endeavor would not only reduce production costs but also facilitate broader application of these materials in high-tech industries such as aerospace, defense, and nuclear energy.

The synthesis of ZrB_2 powder was carried out using a Dynamic Carbothermal Reduction (DCTR) method. The starting materials—ZrO_2, B_2O_3, and solid carbon powder—were weighed in stoichiometric ratios according to the reaction:**$ZrO_2 + B_2O_3 + 5C \rightarrow ZrB_2 + 5CO$**The powder mixtures were homogenized and granulated to improve reactivity and ensure efficient gas removal during the reaction. The process was conducted in a specially designed rotary reactor furnace under an controlled argon atmosphere. The dynamic movement of the reactor, driven by a DC servo motor, enhanced mixing homogeneity and reaction efficiency by increasing contact surfaces and promoting the continuous removal of CO gas—a key factor in shifting the reaction equilibrium toward product formation.To support the experimental approach, thermodynamic simulations were performed using FactSage 7.0 software. These calculations confirmed the feasibility of ZrB_2 formation at the target temperatures. The synthesized powders were subsequently characterized using X-ray diffraction (XRD) for phase identification and scanning electron microscopy (SEM) equipped with energy-dispersive X-ray spectroscopy (EDS) for morphological and compositional analysis.

Experimental results confirmed the successful synthesis of ZrB_2 powder at temperatures as low as 1500°C, which is notably lower than the typical range of 1600–1800°C cited in the literature. XRD analysis revealed high-purity ZrB_2 with minimal secondary phases, indicating efficient reduction and conversion. SEM imaging showed that the produced powders exhibited fine and uniform particle morphology, with grain sizes in the submicrometer range—consistent with the project's objectives.The use of B_2O_3 as a boron source proved to be economically advantageous, reducing raw material costs by more than 20% compared to conventional boron sources. The introduction of a gaseous carbon source (e.g., propane) in addition to solid carbon further

enhanced reduction efficiency and contributed to the completion of the reaction at lower temperatures. The dynamic nature of the reactor played a critical role in maintaining reaction homogeneity and facilitating the rapid removal of gaseous by-products.

This study demonstrates that ZrB_2 powders can be successfully synthesized at significantly reduced temperatures (1500–1550°C) via a dynamic carbothermal reduction process using low-cost oxide precursors and a mixed solid/gas carbon reducing atmosphere. The method offers a economically viable and scalable alternative to conventional high-temperature synthesis routes, with clear benefits in terms of energy savings and material cost reduction.The findings hold considerable promise for industrial applications, particularly in sectors requiring high-performance refractory materials. The successful implementation of this process may also be extended to other UHTCs such as HfB_2 and TaB_2. Future work will focus on optimizing process parameters for large-scale production and further investigating the mechanical and thermal properties of sintered components produced from the synthesized powders. This project provides a strong foundation for subsequent applied research and potential technology transfer initiatives supported by national funding agencies.

Keywords: ZrB_2, B_2O_3, ZrO_2, UHTC

Coatings

ANALYSIS OF THE MECHANICAL AND MICROSTRUCTURAL PROPERTIES OF PLASMA JET THERMAL SPRAYED COATINGS ON METALLIC MATERIALS INTENDED FOR THE BALLISTIC PROTECTION OF BULLETPROOF VESTS

Corneliu Munteanu [1], Adrian Ropotoae [1], Fabian Cezar Lupu[1], *Bogdan Istrate*[1], Gelu Ianuș [1], Marcelin Benchea [1], Cristian Molder[2],

1. Mechanical Engineering Faculty "Gheorghe Asachi" Technical University of Iasi - Romania

2. Military Technical Academy Ferdinand I of Bucharest

Military equipment such as bulletproof vests must provide effective ballistic protection; thus, modern methods for surface coating ballistic plates used in the construction of these vests can contribute to achieving enhanced protection levels. In this study, thermal spray depositions using plasma jet were performed on materials intended for ballistic protection, employing both metallic and ceramic powders. The powders were selected from the catalogs of established manufacturers in the field of thermal spraying and are identified as Metco 42C and Metco 111. According to the manufacturer, these types of materials used for the coatings exhibit high impact resistance, and elevated resistance to wear, abrasion, and corrosion. The samples coated with these powders were analyzed from a microstructural perspective and for mechanical property evaluation in order to assess the improvement in ballistic protection levels. The paper concludes with the experimental results obtained for the two types of coatings.

Keywords: APS, Mechanical properties, Microstructural properties

CHITOSAN-ENHANCED PHOTOCURABLE COATINGS: A SUSTAINABLE APPROACH FOR IMPROVED MECHANICAL PERFORMANCE, FLAME RETARDANCY, AND UV-CURING EFFICIENCY

Recep Furkan Turan[1],

1. İZEL KİMYA R&D CENTER

Chitosan has attracted growing interest for functional coatings; however, its incorporation into photocurable systems remains limited due to solubility and compatibility challenges. In this study, we developed a novel photocurable coating formulation by directly dissolving chitosan (up to 4 wt%) in an acrylic acid/water mixture without the need for chemical modification. The resulting formulations were applied as coatings and cured under UV light. Coating performance was systematically evaluated in terms of surface hardness, gloss, curing and drying time, impact resistance, and flame retardancy. The chitosan-containing coatings exhibited rapid UV-curing and drying behavior, with enhanced flame-retardant properties compared to conventional acrylic systems. A balanced formulation containing 4 wt% chitosan demonstrated improved hardness and impact resistance, while maintaining good gloss and optical clarity. This work highlights the potential of chitosan as a multifunctional additive for eco-friendly, high-performance photocurable coatings, paving the way for its broader use in protective and decorative applications.

In this study, we developed a novel photocurable coating formulation by directly dissolving chitosan (up to 4 wt%) in an acrylic acid/water mixture without the need for chemical modification.The resulting formulations were applied as coatings and cured under UV light.

A balanced formulation containing 4 wt% chitosan demonstrated improved hardness and impact resistance, while maintaining good gloss and optical clarity.

This work highlights the potential of chitosan as a multifunctional additive for eco-friendly, high-performance photocurable coatings, paving the way for its broader use in protective and decorative applications.

Keywords: photo curable coatings, chitosan ,uv-curing

DEVELOPMENT AND CHARACTERIZATION OF BORON-BASED FLAME-RETARDANT POLYUREA COATINGS

Kubilay Özçalkap[1],

1. İZEL KİMYA R&D CENTER

Polyaspartic polyurea coatings, first introduced in the 1990s, have gained increasing industrial attention due to their superior UV resistance, color stability, and mechanical durability. These coatings are typically formed by the reaction of a polyisocyanate with an aliphatic diamine, such as a polyaspartic ester. In this study, novel methacrylic monomers containing cyclic borate esters (BOMs) were synthesized and incorporated into polyaspartic formulations at varying concentrations (1%, 2%, and 4%).

The resulting polymers were characterized using FTIR, DSC, GPC. The coatings were applied to metal substrates including sheet metal, galvanized steel, and aluminum

Physical properties such as contact angle, gloss, hardness, drying time, pot life, yellowing resistance, and gloss retention after UV exposure were evaluated

The influence of borate ester groups on hardness and drying time was investigated. Additionally, Limiting Oxygen Index (LOI) analysis was conducted to determine whether the boron groups enhanced the flame-retardant properties of the polyaspartic resins.

Keywords: FLAME RETARDANT,POLYUREA COATINGS,Polyaspartic

ENHANCING BALLISTIC PERFORMANCE THROUGH ADVANCED COATING

Georgiana Ghisman [1], Gabriel Bogdan Carp[1], Daniela Buruiană[1], Tudor Viorel Țigănescu[2],

1. Interdisciplinary Research Centre in the Field of Eco-Nano Technology and Advance Materials CC-ITI, Faculty of Engineering, "Dunarea de Jos" University of Galati

2. Military Technical Academy "Ferdinand I"

Advanced coatings play a key role in improving the ballistic performance of protective materials such as Kevlar, UHMWPE, and ceramic composites. By applying nanostructured layers—like graphene, carbon nanotubes, or nano-silica—or polymeric systems such as polyurea, materials gain improved impact resistance, durability, and energy absorption. These coatings enhance inter-fiber friction, reduce degradation, and maintain flexibility while decreasing overall weight. Recent developments show that tailored coatings significantly influence material behavior under high-velocity impacts. This work shows current coating strategies and highlights their potential in creating next-generation armor systems that are lighter, more efficient, and adaptable to evolving threats.

Keywords: graphene, inter-fiber friction, carbon nanotubes

INFLUENCE OF MANGANESE PHOSPHATE BATH CONDITIONS ON CRANKSHAFT SURFACE PROPERTIES AND WEAR BEHAVIOR

Simge Tarkuç[1], Emre Yavuz Türk[1], Berfin Kaya[2], Rıdvan Gecü[2],

1. Arçelik

2. Yıldız Technical University

The impact of manganese phosphate (MnP) bath parameters on the surface characteristics and wear resistance of crankshaft components were examined.

Specimens were coated using MnP treatments under systematically varied bath conditions, including temperature, pH, immersion time, and accelerator concentration. Post-coating surface analysis was conducted using scanning electron microscopy (SEM), energy-dispersive X-ray spectroscopy (EDS), and surface roughness measurements. Tribological performance was assessed through semi-lubricated sliding wear tests to evaluate the effect of coating conditions on wear behavior.

The findings reveal that optimized MnP bath parameters lead to improved surface morphology and a marked reduction in wear rate.

Overall, this work offers valuable insights into the role of MnP coating processes in improving the durability and performance of the components.

Keywords: wear resistance, semi-lubricated sliding, tribology

SURFACE CHARACTERIZATION OF THE COPPER COATINGS ON DIFFERENT METALLIC SUBSTRATES

Spanu Iulian[1], Antoniac Aurora[1], Ciocoiu Robert[1], Streza Alexandru[1], Robu Alina[1], Popescu Larisa[1], Antoniac Iulian[1],

1. National University for Science and Technical POLITEHNICA Bucharest,

This study aims to characterize copper coatings applied on various metallic substrates using the Thermal Spraying technique with an arc wire spray system (AWS400). The substrates investigated were Ol 316L, Ol 304, Ol 37, and aluminum (Al).

Characterization methods used for surface characterization was scanning electron microscopy for morphological aspects coupled with EDS for elemental composition measurements, profilometry for roughness measurements, and contact angle measurements for surface free energy.

The reason for coatings these different metallic substrates was to establish a reliable method for antibacterial copper coatings on different metallic substrates used for manufacturing metallic furniture and equipment used in hospitals and medical clinics.

Surface properties are very important from this point of view. As a conclusion, the selected coating method assures similar surface properties without any interference of the substrate properties. This means that the methods are reliable for our purpose.

Keywords: coatings, copper, SEM, profilometry, surface

Composite Materials

EFFECT OF INORGANIC FILLERS ON THE MULTIFUNCTIONAL PROPERTIES OF POLYURETHANE COMPOSITES

Tuçe FİDAN[1], *Aykut AYKAÇ*[2], Cem YİĞİT[2], Ece ONARAN[3],

1. Istanbul Technical University

2. Pimsa Automotive R&D Center

3. Yıldız Technical University

Polyurethane is widely used in applications such as soundproofing, automotive interiors, and thermal insulation due to its low density and excellent sound absorption properties. The morphology and physical properties of polyurethane can be tailored by incorporating various fillers during production. In this study, the influence of different inorganic filler types and concentrations on the acoustic, mechanical, and thermal performance of polyurethane was investigated

Inorganic fillers, including talc, nanoclay, silica, and silicon oxide, were initially incorporated at a concentration of 1 wt%. Based on the preliminary acoustic and mechanical results, talc and nanoclay were selected for further analysis at 3 wt.% and 5 wt.% concentrations. The effects of filler type and content on the sound absorption behaviour, thermal stability, and mechanical strength of the polyurethane composites were systematically evaluated

The results revealed that the polyurethane composite containing 5 wt.% talc exhibited the most favourable combination of mechanical strength and acoustic performance.

Keywords: Polyurethane, Fillers, Acoustic, Mechanical, Thermal

DEVELOPMENT OF SUSTAINABLE COMPOSITE MATERIALS FOR AUTOMOTIVE ROOF PANELS USING FLY ASH PARTICLES FROM THERMAL POWER PLANTS AND WOVEN ROVING STRUCTURED NATURAL VISCOSE FIBER REINFORCED POLYMER MATRIX

Ayşe Telligözoğlu[1], *Betül Öncü*[1], Safa Sercan Güven[1],

1. Yıldız Technical University

Environmental concerns in the automotive industry have increased the demand for sustainable alternatives to conventional synthetic materials. Automotive interior components like roof panels are dominated by petroleum-based polymers such as PVC and polyurethane, which are non-recyclable and persist in nature for extended periods.This study aims to develop a sustainable composite material for automotive roof panels. The goal is to design eco-friendly composites by combining biodegradable matrices with natural fiber reinforcement and industrial waste-based fillers. Specifically, natural woven roving structured viscose fiber was selected as the reinforcement, with polylactic acid (PLA) and epoxy resin as matrices, and fly ash particles from thermal power plants as a functional additive. The target is to achieve composites that are lightweight, durable, and support circular economy goals while maintaining required performance.

Two different matrix systems were employed in this study: the thermoplastic polylactic acid (PLA) and the thermoset epoxy resin. Natural viscose fibers in woven roving form were selected as the reinforcement material due to their renewable origin, high flexibility, and mechanical properties. Additionally, fly ash particles rich in silica and alumina—collected from thermal power plant emissions—were introduced at a 5% volume ratio into the composite structures to enhance mechanical strength and thermal resistance.PLA-based composites were manufactured using the hot press technique. PLA pellets were first melted and shaped into thin films, which were then layered alternately with woven viscose fabric to form a sandwich structure. Epoxy-based composites were produced via the hand lay-up method, in which epoxy resin and hardener were mixed in a 100:40 weight ratio and applied over woven viscose fabrics.To improve interfacial adhesion and material performance, surface modification processes were applied to both the fibers and fly ash particles. Viscose fibers were treated using alkali (NaOH) and silane coupling agents (TEOS, TMCS), while fly ash underwent alkaline activation and aluminum phosphate coating. All composite specimens—both filled and unfilled—were subjected to FTIR analysis for chemical characterization, as well as tensile and impact testing to assess mechanical behavior.

FTIR analysis confirmed the successful surface modification of both viscose fibers and fly ash particles. Treated viscose fibers showed reduced –OH peaks and new Si–O–C and Si–CH_3 bonds, indicating strong covalent attachment. For fly ash, NaOH treatment introduced Si–OH and CO_3^{2-} groups, enhancing surface reactivity.Tensile test results showed that fly ash addition reduced

mechanical strength. PLA-based sandwich composites without fly ash had an average tensile strength of 40.99 MPa, which dropped to 30.13 MPa with 5% fly ash. Epoxy-based composites reached 107.13 MPa without fly ash but decreased to 84.00 MPa with fly ash. The strength loss is linked to particle agglomeration and poor interfacial bonding.Impact tests supported this trend. Fly ash-free PLA composites absorbed ~147 kJ/m^2, while fly ash-containing ones absorbed only 71–91 kJ/m^2, reflecting lower toughness.In conclusion, while fly ash improves sustainability, it weakens mechanical performance in PLA composites. In epoxy systems, better compatibility helps mitigate this issue when particles are surface-modified.

This study successfully demonstrates that environmentally friendly and mechanically robust composite materials can be fabricated by combining biodegradable matrices, natural fiber reinforcements, and industrial waste-derived fillers. Among the tested systems, epoxy-based composites exhibited the highest mechanical performance, while PLA-based composites offered superior biodegradability and environmental compatibility.The use of woven roving structured viscose fiber significantly improved tensile and impact resistance, while surface-modified fly ash particles contributed to thermal stability and structural integrity.These findings highlight the potential of integrating renewable and recycled materials into functional automotive components. The resulting composites are not only suitable for interior trim applications but also align with global goals for sustainability, resource efficiency, and circular economy practices.

Keywords: Sustainable composite Automotive interior panels

Electronic, Magnetic and Optical Materials

STUDY OF (LIFP6)ELECTROLYTE REACTION WITH CATHODE MATERIAL TO IMPROVE LI-ION BATTERY PERFORMANCES.

Merzougui Amina [1], Azzedine Kabouche[1]

[1] *Institute of Technology, Ain M'lila, Oum El Bouaghi University*

Email : merzougui.amina@univ-oeb.dz

Several researchers are interested in the field of batteries in order to improve their performances, namely, increasing their storage capacity, reducing their charging time, increasing their life time and avoiding the parasitic effects that disturb the proper functioning of these systems.

In this context, the aim of this work is to improve the performance of lithium-ion batteries through the combined choice of the electrolyte and the cathode material of a Li-ion battery. In fact, the choice of electrolyte is crucial to ensure optimal operation. The electrolyte, must be chemically stable with cathode and anode materials. Good compatibility between the electrolyte and the cathode limits undesirable reactions, such as material degradation or formation of resistive layers, which can affect battery performance and service life. In addition, the electrolyte must allow good ionic conductivity to ensure efficient transport of lithium ions during charge and discharge cycles. Thus, the adequacy between electrolyte and cathode is essential to maintain the safety, capacity, and stability of the Li-ion battery.

In this work, we will present concentration, potential and conductivity curves of the electrolyte (LiFP6) in three cases of cathode material: LCO, LMO and LFP. The obtained results lead us to choose LMO as the best cathode material, compared to LCO and LFP. The curves are from numerical simulation using COMSOL multiphysics 6.0 software.

Glass and Glass-Ceramics

COMPREHENSIVE INDUCTIVELY COUPLED PLASMA-REACTIVE ION ETCHING (ICP RIE) INVESTIGATION OF GLASS ETCHING FOR MICROFLUIDICS

Duygu NUHOĞLU[1], Meryem SARIGÜZEL[2], Cihat TAŞALTIN[2], Ilke GÜROL[2], Esra ZAYIM[3],

1. Department of Physics Engineering, Istanbul Technical University

2. TUBITAK, Marmara Research Center, Materials Technologies

3. Department of Physics Engineering, Istanbul Technical University

Separation of particles such as platelets, erythrocytes and, leukocytes from blood to obtain human serum is essential for medical diagnostics. The deterministic lateral displacement (DLD) microfluidics are composed of pillar arrays lined up horizontally and tilted with a defined angle vertically, so, sort and, separate particles based on size from small fluid volumes in a short period. The manufacturing methods of DLD depend on microfabrication. Inductively coupled plasma-reactive ion etching (ICP RIE) is one of the etching techniques in the production process which used reactive ions such as SF6, C4F8 gases.

In this study, DLD principle-based microfluidic device has three different separation zones, which separate shaped elements and plasma, was produced on glass substrates by planning to add a sensor array in order to capture cardiac biomarkers. Sacrificial metallic layers were coated with e-beam deposition and electroplating methods such as Cr, Au, Ti, and Ni. The DLD pattern was transferred to silicon and pyrex surfaces with the maskless photolithography technique. Then, the etching of the substrates was carried out with the ICP RIE method using plasma etching techniques. To obtain a high aspect ratio of pillar, different etching recipes were tested and etching speed, depths, and surface roughness were investigated in detailed.

Four different prescriptions were tested in plasma etching and the surface profiles of the etched samples were examined. It has been observed that the argon gas in the recipes used causes plasma-induced damage on the surface. Gas flows of various concentrations were tested, and it was determined that the etching was dominantly driven by C4F8 gas.

The effects of different plasma etching parameters on etch rate, surface quality, and pillar aspect ratio were systematically investigated. Among the tested recipes, those with higher C4F8 gas concentrations provided stable etch rate and smoother surfaces while argon-rich plasmas led to significant surface damage. The optimized etching conditions enabled the production of well-defined pillar arrays suitable for particle separation, with potential integration of sensor arrays for cardiac biomarker detection in future applications.

Keywords: glass etching, microfluidic fabrication, photolithography

Materials Characterization and Computational Modeling

DESIGN AND THERMAL ANALYSIS OF METALLIC CPU COOLERS VIA FEM

Sevilay Gok[1], Mustafa Guven Gok[2],

1. Karatas Anadolu Lisesi (Karatas High School), Gaziantep İl Milli Eğitim Müdürlüğü (Gaziantep Provincial Directorate of National Education)

2. Gaziantep University

Rapid advances in semiconductor technology and AI applications demand that computer CPUs (Central Processing Unit) sustain rising computational loads at low operating temperatures. This study investigates the effect of different topologies on the thermal performance of aluminum-alloy CPU coolers.

Solid models of a computer CPU cooler with reference and different designs were created in SolidWorks software and imported into Ansys Workbench for finite-element thermal modelling (FEM). Separate steady-state simulations were conducted for each geometry, with Al-alloy material properties assigned. Temperature and heat-flux data were sampled at 40 equally spaced points across the external surface, and the average surface temperature was computed for each design.

All lattice designs reduced the average surface temperature by up to 3.1 % relative to the solid reference and increased heat flux accordingly, owing to their larger effective surface areas.

Lattice-based CPU cooler geometries demonstrably outperform solid counterparts in steady-state thermal management. Among the configurations tested, cubic lattice designs yield the greatest temperature reductions and heat-flux enhancements, offering a lightweight, high-efficiency solution for next-generation CPU cooling.

Keywords: CPU, Computer, Aluminum, FEM

Metallurgy

MODELING AND SIMULATION OF THE EFFECT OF SCANDIUM ADDITION TO Al-7Si-0.5Mg ALLOY USING INTEGRATED COMPUTATIONAL MATERIALS ENGINEERING

Süleyman Berk Hakyol[1], Cevat Bora Derin[1], Havva Kazdal Zeytin[2], Aydın Karaömer[2], Alihan Yılmaz[2], Yağız Akyıldız[3],

1. Istanbul Technical University

2. Unimetal Investment Casting

3. Alpomet Mühendislik Danışmanlık Yazılım İmalat Sanayi ve Ticaret Limtied Şirketi

Al-Si-Mg alloys hold critical importance in the automotive, aerospace, and defence industries due to their superior properties such as low density, high specific strength, corrosion resistance, and excellent thermal conductivity. Increasing service demands render the performance of existing Al-Si-Mg alloys insufficient, thereby necessitating the development of new-generation alloys. In this context, Integrated Computational Materials Engineering (ICME) methods emerge as powerful tools for alloy design, phase diagram calculations, and optimization of heat treatment processes.

In this study, Scandium was added to the Al-7Si-0.5Mg alloy for its grain-refining and strengthening potential, and its effects were investigated in detail through numerical modeling and simulation techniques. Using phase diagrams, critical transformation temperatures, intermetallic precipitates, phase fractions, and elemental distributions were determined.

Furthermore, the formation temperatures of intermetallic phases were calculated, providing insights into potential heat treatment strategies.

The results aim to contribute to the scientific literature and offer guidance for industrial applications.

Keywords: Aluminum alloys, Scandium, Simulation

EFFECT OF NANO-SIZED Y2O3 ADDITIONS ON THE WEAR BEHAVIOR OF NANOCRYSTALLINE 304L STAINLESS STEEL SYNTHESIZED VIA MECHANICAL ALLOYING

Hasan KOTAN[1], Cantekin KAYKILARLI[1], *Selin ARAS*[1],

1. Bursa Teknik Üniversitesi

In the current study, experimental studies will be conducted using commercially pure 304L stainless steel powder with a particle size range of 45-75 µm. Nano-sized Y2O3 (20-50 nm) will be used as the reinforcing material and added to the 304L stainless steel at varying weight percentages, specifically between 1.0% and 2.0%.The mechanical alloying process will be carried out for 20 hours at room temperature using a high-energy ball mill. The ball-to-powder ratio will be 10:1 (by weight), and the process will be performed under an argon atmosphere. After mechanical alloying, the obtained powder mixtures will be compacted into bulk samples using a uniaxial cold pressing method.The compacted samples will subsequently be sintered in an atmosphere-controlled tube furnace at 1273 K for 1.5 hours,with a heating and cooling rate of 5°C/minute. Structural and microstructural characterizations of the as-milled and sintered samples will be performed using X-ray diffraction (XRD) and scanning electron microscopy (SEM) techniques. Density analyses will be conducted using the Archimedes principle. Mechanical properties will be determined through Vickers hardness tests and reciprocating wear tests. Wear surfaces will be examined in detail using SEM and energy dispersive X-ray spectroscopy (EDS) analyses to identify the dominant wear mechanisms.

Keywords: 304L, Y2O3, mechanical alloying

Nanomaterials

FUNCTIONALIZED NANOPARTICLES IN INTELLIGENT SENSORS FOR ACTIVE FOOD PACKAGING

Andrei Ivanov [1], Viorica Ghisman[1], Georgiana Ghisman[1], Daniela Buruiană[1], Iulian Antoniac [2],

1. Interdisciplinary Research Centre in the Field of Eco-Nano Technology and Advance Materials CC-ITI, Faculty of Engineering, "Dunarea de Jos" University of Galati

2. Natl Univ Sci & Technol Politehn Bucharest

Incorporation of nanotechnology in food-contact materials has opened new avenues for the creation of intelligent and active packaging systems that monitor product quality and safety continuously. This review provides an overview of recent advances in the synthesis, surface functionalization, and embedding of metallic (Au, Ag) and metal-oxide (TiO_2, ZnO) nanoparticles into biodegradable polymer matrices (e.g., chitosan, gelatin, PLA) to create intelligent sensing platforms. Experimental considerations for scaling up are also discussed: nanoparticle dispersion techniques, film-casting versus coating techniques, and integration with automated packaging systems. Finally, we identify key challenges—e.g., long-term reproducibility of sensors, regulatory, and environmental fate of nano-enabled materials—and propose avenues for future research toward multiplexed sensing, wireless data transmission, and circular-economy approaches. By synthesizing conclusions throughout multidisciplinary research, this review aims to help researchers and industry experts implement nanoparticle-enhanced sensors to enhance food safety and reduce waste.

Keywords: nanoparticle functionalization; intelligent sensors

EFFECTS OF NANO-IRON OXIDE ON PHYSIOLOGICAL TRAITS, GENE EXPRESSION AND IRON UPTAKE IN SOYBEAN

Ahmet Buğrahan AKBIYIK[1], Ayten Kübra YAĞIZ[2],

1. Duzce University

2. Nigde Omer Halisdemir University

The objective of this study was to evaluate the impact of nano-iron oxide (nFe_2O_3) on physiological responses, gene expression patterns, and iron uptake efficiency in two soybean (Glycine max) cultivars differing in iron deficiency tolerance. Specifically, the study aimed to determine whether nFe_2O_3 application under hydroponic conditions could alleviate iron deficiency chlorosis (IDC) by modulating key iron homeostasis genes, enhancing photosynthetic performance, and increasing iron accumulation in plant tissues.

Two soybean (Glycine max) cultivars, Arısoy (IDC-tolerant) and Atakişi (IDC-susceptible), were grown hydroponically under controlled conditions. Plants were subjected to Fe-deficient and Fe-sufficient Hoagland solution, with three concentrations of nano-iron oxide (nFe_2O_3): 0, 100, and 200 ppm. Gene expression of Ferritin, GMOPT3, IRT-like, FRO2, and NRAMP (DMT1) was quantified using real-time PCR (qPCR), with 18sRNA as the reference gene. Chlorosis symptoms were visually scored, photosynthetic rates were measured using a portable gas exchange system, and iron concentrations of leaves and roots were determined via ICP-OES.Data obtained from the experiments were subjected to variance analysis and differences between means were evaluated using the Tukey test in Minitab statistical software.

Nano-iron oxide (nFe_2O_3) application led to noticeable improvements in both soybean cultivars. Chlorosis symptoms were reduced, and photosynthetic rates increased, especially at higher nFe_2O_3 concentrations. Gene expression analysis showed changes in iron-related genes, with cultivar-specific responses. In general, treated plants had higher iron accumulation, confirmed by ICP-OES measurements. These results suggest that nFe_2O_3 supports iron uptake and helps plants better tolerate iron deficiency.

Findings from the study highlight the potential of nano-iron oxide to enhance iron nutrition through both genetic and physiological pathways, offering a sustainable strategy to alleviate IDC in soybean.

Keywords: Soybean, nano-ironoxide, geneexpression, ICP-OES, IDC.

CURV, DYNEEMA, KEVLAR & NOMEX: INTEGRATION OF HIGH-PERFORMANCE FIBERS INTO COMPOSITE MATERIALS

Gabriel Cristescu[1],

1. Politehnica Bucharest

Combining four high-performance fibers (Curv, Dyneema, Kevlar and Nomex) to obtain a new hybrid material that can pave the ways for industries like protective gear, aerospace components or defense.

Fiber matrix adhesion.

An optimized fabrication technique is required along with a special technique for fiber stacking.

Keywords: Curv, Dyneema, Kevlar and Nomex

Polymers

SYNTHESIS AND ADHESION PERFORMANCE OF SILANE-FUNCTIONALIZED POLYUREA COATINGS

Emirhan Ramazanoğlu [1],

1. İzel Kimya

Polyaspartic resins are increasingly used in the coating industry due to their excellent mechanical strength, UV resistance, solvent-free nature, and flexibility. However, their limited adhesion to metal and plastic substrates presents a challenge.

In this study, PACM-silane compounds were synthesized by incorporating silane acrylate-containing monomers and subsequently reacted with polyaspartic esters to form modified resins. These resins were applied to various metal surfaces, including sheet metal, galvanized steel, and aluminum

The coatings were evaluated for physical properties such as contact angle, gloss, hardness, drying time, yellowing resistance, and gloss retention after UV exposure. Adhesion performance was assessed using standardized pull-off and cross-cut tests. The results demonstrated a significant improvement in adhesion to both metal and plastic substrates due to silane modification.

This study suggests that silane-functionalized polyaspartic resins offer promising potential for expanding their application in high-performance protective coatings across a wide range of industrial surfaces.

Keywords: Coating, polyaspartic, silane

SYNTHESIS AND DEVELOPMENT OF PVA-BASED ADHESIVES WITH HIGH ADHESION STRENGTH AND REUSABLE PROPERTIES

Ali Asgharian[1], Oykunaz Duranlar[2], Ayda Yari ilkchi[2], Fatma Seniha Guner[2],

1. Istanbul Technical University, Faculty of Chemical and Metallurgical Engineering, Department of Materials Science and Engineering

2. Istanbul Technical University, Faculty of Chemical and Metallurgical Engineering, Department of Chemical Engineering

Polymers with the ability to adhere to surfaces and being able to be rehydrated after drying are a major subject to investigate. For this reason, reversible adhesives using lignin, Polyvinyl Alcohol (PVA), Tannic Acid (TA), and Polyethyleneimine (PEI) were synthesised.

Briefly, the PVA, TA, and lignin solutions were prepared and mixed. The effect of different amounts of PVA was investigated on the performance of the adhesives. The synthesised samples were characterised by Fourier Transform Infrared (FTIR), thermogravimetric analysis (TGA), and contact angle measurements. Furthermore,adhesion strength was measured by lap shear tests.

The Formula with 1 g PVA,0.6 g TA,0.6 g PEI, 0.8 g lignin exhibited superior adhesive properties compared to 0.75 g PVA and 2 g PVA with the same amount of other polymers. Also, the adhesive with 1 g PVA maintained its adhesion properties after drying and rehydration.

Thus, the mentioned adhesive have efficient potential to be used in the adhesive industry

Keywords: Lap shear, PVA, Adhesive, reversibility

PERFORMANCE IMPROVEMENT OF RECYCLED ABS COMPOSITES VIA ELASTOMERIC MODIFIERS

Zeynep KAYA[1], Leila POUDEH[2],

1. Yıldız Technical University

2. Beko Corporate

The increasing demand for environmentally sustainable materials has highlighted the importance of utilizing recycled polymers in engineering applications. Among these, recycled acrylonitrile butadiene styrene (r-ABS) stands out due to its wide industrial usage. However, the mechanical properties of r-ABS, particularly its impact resistance, are generally inferior to those of virgin ABS, limiting its application in products requiring toughness and durability. To address this limitation, this study focuses on the formulation of r-ABS compounds modified with elastomeric additives to enhance their impact performance. The objective is to identify optimal additive content and evaluate its influence not only on mechanical properties such as impact strength, tensile strength, and flexural behavior but also on structural and thermal characteristics. By doing so, the study aims to establish a cost-effective, scalable, and sustainable route for upgrading the performance of recycled thermoplastics to meet industrial requirements.

In this study, recycled acrylonitrile butadiene styrene (r-ABS) granules were compounded with elastomeric modifiers at different weight ratios ranging from 1 wt.% to 15 wt.% using a co-rotating twin-screw extrusion process. Prior to compounding, all materials were pre-dried to prevent moisture-induced degradation. The extruded materials were then pelletized and injection molded into standard specimens for mechanical testing. Tensile, flexural, and impact strength tests were conducted in accordance with ASTM standards to evaluate the mechanical behavior. Additionally, Differential Scanning Calorimetry (DSC) and Fourier Transform Infrared Spectroscopy (FTIR) were employed to assess the thermal properties and interfacial interactions between the r-ABS matrix and the elastomeric modifiers. The mechanical test results were statistically analyzed to determine the optimal additive concentration that balances improved toughness without significantly compromising stiffness or strength.

The experimental results revealed that the mechanical performance of recycled ABS composites was significantly influenced by the type and concentration of elastomeric modifiers. Among the formulations tested, the composition containing 5 wt.% modifier exhibited the most favorable balance between impact resistance and structural integrity, achieving approximately a 30% improvement in impact strength compared to unmodified r-ABS. While higher modifier contents (>10 wt.%) led to further improvements in toughness, they also resulted in reduced stiffness and dimensional stability. Tensile and flexural strength values slightly decreased with increasing elastomeric content, indicating a trade-off between ductility and rigidity. DSC analyses confirmed thermal compatibility between the matrix and the modifiers, while FTIR spectra

revealed physical rather than chemical interactions at the interface. These findings suggest that with optimized additive levels, it is possible to tailor the mechanical performance of r-ABS composites to meet the requirements of various engineering applications.

This study demonstrates that the impact resistance of recycled ABS can be significantly improved through the incorporation of elastomeric additives. Among the tested formulations, the composition containing 5 wt.% modifier was identified as the optimal blend, providing a favorable balance between toughness and structural performance without compromising processability. Although higher additive contents further enhanced ductility, a decline in stiffness was observed, emphasizing the need for careful optimization. Thermal and spectroscopic analyses confirmed that the modifiers did not adversely affect the thermal stability of the composites. These results highlight the feasibility of using tailored modification strategies to upgrade the performance of r-ABS, thereby expanding its applicability in various engineering fields. Overall, this study contributes to the development of sustainable material solutions by promoting the functional reuse of recycled plastics in value-added applications.

Keywords: r-ABS, Toughening, Polymer Composites

Recycling and Sustainability

PRODUCTION OF CHELATED MICRONUTRIENT FERTILIZER FROM ELECTRIC ARC FURNACE SLAG

Oğuz Işık[1], Çetin Bağlan[1], Sencer Moral[1], Sinan Aras[1]

[1]MATİL Materials Testing and Innovation Laboratories Inc., 34450, Istanbul, Turkiye

Keywords: EAF Slag Fertilizer, Chelation and Nutrient Bioavailability, Soil Amendment, Circular Economy, Sustainable Agriculture

Abstract

Electric Arc Furnace (EAF) slag, a by-product of steelmaking, contains valuable nutrients such as Fe, Ca, Zn, and Mn, yet their bioavailability is limited in alkaline soils. This study explored a two-step valorisation strategy: (i) mild acid extraction using H_2SO_4 and H_3PO_4 to solubilize Fe and co-nutrients, followed by (ii) chelation with Fe-EDDHA to stabilize Fe bioavailability under high pH conditions. Slag samples were dried, milled (<1 mm), and characterized by XRF and ICP-OES. Leaching was conducted under controlled liquid/solid ratios, temperature, and time. Chelate formation was confirmed by UV–Vis spectroscopy.

Complementary pilot-scale pot and field trials with wheat and lettuce showed that EAF slag applications improved soil pH regulation, chlorophyll status, biomass accumulation, and root development compared with non-chelated controls. Fine-particle slags (0–2 mm) demonstrated higher efficiency than coarse fractions (0–4 mm), due to greater solubility and nutrient release. Particularly in acidic soils, positive effects on plant growth and yield were more pronounced, highlighting the potential of slag-based fertilizers to correct nutrient deficiencies.

Heavy metal monitoring and leaching tests confirmed safety and compliance with the EU Fertilising Products Regulation (EU 2019/1009). Overall, this approach illustrates how EAF slag can be transformed into a sustainable fertilizer, supporting circular economy principles and reducing dependence on conventional mineral fertilizers.

1. Introduction

In raw Electric Arc Furnace (EAF) slag, most micronutrients are locked in poorly soluble oxide and silicate phases, making direct application inefficient, particularly under alkaline soil conditions. Conventional Fe sources such as $FeSO_4$ and Fe-EDTA tend to precipitate as soil pH increases, thereby losing their effectiveness. Thus, a two-step approach is required: (i) controlled dissolution of Fe from the slag matrix and (ii) stabilization of dissolved Fe to prevent re-precipitation at high pH [1].

From a regulatory perspective, the EU Fertilising Products Regulation (EU 2019/1009) mandates compliance with heavy metal limits, leaching behavior, and batch-to-batch product consistency as prerequisites for CE marking. Current technical assessments emphasize that slag-derived fertilizers must demonstrate both agronomic efficiency and environmental safety through quantitative evidence [2,3]. Within this framework, opportunities arise for innovative solutions that support circular economy strategies while meeting regulatory standards.

In this study, a two-step valorisation of EAF slag was investigated: (i) mild acid extraction (H_2SO_4/H_3PO_4) to solubilize Fe and accompanying nutrients, followed by (ii) chelation with Fe-EDDHA to maintain bioavailability under high pH conditions. Based on preliminary characterization and pot trials, leaching and chelation parameters were optimized, compared with commercial Fe-EDDHA, and assessed through ICP-based heavy metal monitoring and leaching tests. The objective is to develop a CE-compliant, field-ready micronutrient fertilizer that contributes to circular bioeconomy goals [4,5,6].

2. Experimental Procedure

2.1. Materials and Pre-treatment

Electric Arc Furnace (EAF) slags were sourced from two different steelmaking plants, one intended for base fertilizer formulations and the other for foliar/top-dressing applications. Approximately 300 kg of composite slag was sampled from multiple points in three-year-old stockpiles. In the laboratory, the slags were subjected to crushing and sieving (0–8 mm), followed by magnetic separation to remove metallic Fe residues. Samples were then dried at 105 °C in an oven, ground to <100 µm using a ring mill, and prepared as pressed pellets for X-ray fluorescence (XRF) analysis.

Figure 1. EAF slag pile at factory site

2.2. Characterization

Initial characterization included XRF for bulk oxide composition (e.g., Fe_2O_3, CaO, SiO_2, MgO, MnO), X-ray diffraction (XRD) for phase identification, and scanning electron microscopy with energy-dispersive spectroscopy (SEM-EDS) for microstructural and compositional validation. Results confirmed that the EAF slag was particularly rich in Fe and Ca, consistent with its potential as a micronutrient source.

Table 1. Elemental analysis of slag samples

Element, %	1-EAF Slag	2-EAF Slag	BOF Slag	Binding Clay	Water Glass
Al2O3	10,47	15,12	9,64	29,25	
SiO2	15,17	15,1	10,05	61,85	28
CaO	28,01	32,3	42,46	0,92	
Cr2O3	1,84	0,04		0,03	
Fe2O3	37,42	26,3	23,95	3,17	
MnO	3,73				
K2O	0,01			2,83	
MgO	1,78	1,77	1,7	0,63	
Na2O	0,42	0,25			9
P2O5	0,5	0,02	0,08		
S	0,09				
TiO2	0,43	0,46	0,23	1,16	
ZnO2				0,02	

2.3. Mild Acid Leaching

A systematic leaching study was carried out using H_2SO_4 and H_3PO_4 (0.5–1.0 M). Experiments were conducted at liquid-to-solid (L/S) ratios of 10–20 L/kg, temperatures of 25–60 °C, and agitation rates of 300–500 rpm in jar-test setups. Reaction times varied between 2–4 h. After leaching, slurries were vacuum-filtered through 0.45 µm membranes. Filtrates were analyzed by ICP-OES/ICP-MS, while the solid residues were characterized by XRF/XRD. Considering the tendency of phosphoric acid to form insoluble $FePO_4$ phases, subsequent chelation was designed to retain Fe in soluble form.

2.4. Chelation with Fe-EDDHA

To maintain Fe in a plant-available form under high pH conditions, chelation with Fe-EDDHA was performed. Leachate pH was adjusted to 6.5–7.5, and commercial Fe-EDDHA (with emphasis on the o,o isomer) was added at Fe:EDDHA molar ratios of 1:1.2–1.5. Chelation reactions were carried out at 25–40 °C for 30–60 minutes under continuous stirring. Chelate formation was confirmed both visually—by the characteristic red-purple coloration—and analytically via UV–Vis spectroscopy with an absorption peak around 505 nm. This step successfully stabilized slag-derived Fe in solution for agronomic use.

2.5. Product Formulation

Two product formats were explored: liquid and solid. For liquid formulations, Fe concentrations of 1–3% (w/v) were targeted, and compatibility with irrigation fertilizers was tested using jar methods. For solid formulations, slag powders (<300 µm) were blended with binding clay and sodium silicate (water glass) as a binder, then granulated and dried at low temperature. Granules were tested for mechanical strength and friability to ensure handling stability.

2.6. Pot and Soil Incubation Trials

Complementary agronomic trials were conducted under both acidic and alkaline soil conditions. Different slag fractions (0.5–2.0% doses; 0–2 mm and 0–4 mm particle sizes) were tested. Soil incubation experiments revealed that slag application increased soil pH in acidic soils, while higher doses of fine slag fractions led to increased electrical conductivity (EC). DTPA extractions confirmed elevated levels of available Fe and Zn.

Pot experiments with wheat demonstrated significant improvements in chlorophyll content (SPAD index), root development, and biomass compared with controls and non-chelated treatments. Leaf Fe and Zn concentrations were also higher in chelated treatments. Field and garden trials indicated that excessively high slag doses could reduce yield parameters such as spike weight; however, acid-treated and chelated slag formulations consistently outperformed raw slag applications. These findings underline the effectiveness of the mild acid extraction–Fe-EDDHA chelation strategy.

Figure 2. Soil incubation experiments

Figure 3. Visual gradient of wheat growth under increasing slag fertilizer treatments (left to right)

3. Results and Discussion

Mild acid extraction significantly enhanced the solubility of Fe and accompanying micronutrients from EAF slag, while subsequent Fe-EDDHA chelation ensured their stability under high-pH conditions. Pot experiments with wheat and lettuce demonstrated clear agronomic benefits, including improved chlorophyll status (SPAD values), enhanced root development, and greater biomass accumulation. Leaf tissue analyses confirmed increased Fe and Zn uptake compared with non-chelated controls. Soil incubation studies further indicated that fine particle fractions and higher application doses elevated DTPA-extractable Fe and Zn, highlighting the agronomic potential of the proposed treatment.

Heavy metal monitoring (Cr, Ni, Pb, Cd, As) and leaching assessments (EN 12457-2 and TCLP protocols) confirmed compliance with the EU Fertilising Products Regulation (EU 2019/1009). Batch-to-batch consistency was validated through ICP-OES/ICP-MS analyses, with limits of detection (LOD), limits of quantification (LOQ), and measurement uncertainties documented. These findings provide robust evidence that slag-derived Fe-EDDHA formulations can meet both agronomic effectiveness and regulatory safety requirements.

Overall, the two-step approach—mild acid dissolution followed by Fe-EDDHA stabilization—offers a pathway to transform EAF slag into an efficient micronutrient input for calcareous soils. The development of both liquid and granular formulations provides flexibility for field use, thereby supporting sustainable agriculture and circular-economy objectives.

Future work should prioritize field-scale trials across calcareous and acidic soils to validate dose-response relationships, nutrient persistence, and crop yield impacts under real agronomic conditions. Parallel optimization of liquid versus granular formulations, combined with chelate stability testing, will identify the most practical delivery route. Cost-benefit analyses and pilot-scale production (100–500 L/batch) will be essential to demonstrate competitiveness with commercial products and to facilitate eventual farmer adoption.

4. Conclusion

This study demonstrated that Electric Arc Furnace (EAF) slag can be transformed into an agronomically valuable micronutrient fertilizer through a two-step process involving mild acid extraction followed by Fe-EDDHA chelation. Laboratory-scale experiments confirmed that Fe released from slag can be stabilized under high-pH conditions, ensuring its bioavailability for plant uptake. Pot trials with wheat and lettuce showed improved chlorophyll levels, enhanced root growth, and increased Fe/Zn accumulation in leaf tissues, validating the agronomic effectiveness of the developed formulation.

Heavy metal analyses and leaching tests confirmed compliance with the EU Fertilising Products Regulation (EU 2019/1009), ensuring environmental safety and regulatory suitability. The development of both liquid and granular formulations further provides flexibility for practical field applications under different soil conditions.

In conclusion, EAF slag-derived Fe-EDDHA formulations represent an innovative solution that can simultaneously enhance crop productivity and contribute to circular economy objectives. Future work should focus on field-scale trials and pilot production to validate commercial feasibility and support farmer adoption.

References

[1] Gao, D., Wang, F. P., Wang, Y. T., & Zeng, Y. N. (2020). Sustainable utilization of steel slag from traditional industry and agriculture to catalysis. Sustainability, 12(21), 9295.

[2] Branca, T. A., & Colla, V. (2012). Possible uses of steelmaking slag in agriculture: an overview. Material recycling–Trends and perspectives, 335-356.

[3] Pihl, (2021,16 June). Slag as a fertilizer with respect to current EU regulations, ESTEP Workshop, Building material Institute, Duisburg Germany

[4] Kimio, I. T. O. (2015). Steelmaking slag for fertilizer usage. Nippon Steel Sumitomo Metal Tech Rep, 109, 130-136.

[5] Tozsin, G., & Öztaş, T. (2023). Çelik cüruflarının tarımsal amaçlı kullanılması. Atatürk Üniversitesi Ziraat Fakültesi Dergisi, 54(1), 36-41.

[6] Delil, A., Yıldırım, D., Köleli, N., (2017), Çelikhane Cürufundan ve Tufalından Bitki Besin Elementlerinin Geri Kazanımı ve Bu Elementlerin Bitki Büyümesine Etkisi, Academic Platform Journal of Engineering and Smart Systems, 5-1 (2017) 01-07

USING FIRED GLAZED PORCELAIN TILE SCRAPS IN GLAZED PORCELAIN TILE BODY: A PRELIMINARY STUDY

İstem ŞENCAN[1], Ali KÜÇÜK[1], Levent ORHAN[1],

1. QUA GRANITE, R&D Laboratory, Aydın

As in many products, the demand for raw materials and the volume of production waste in ceramic tile production continue to increase worldwide due to the growing production volumes. This trend necessitates sustainable and natural resource-saving approaches such as waste use in production. "Glazed Porcelain Tiles (GPT)" are classified as Group BIa (Eb≤0.5%) tiles in the ISO 13006."Fired Glazed Porcelain Tile Scraps (FGPTS)" are formed when GPT are separated as waste due to various post-firing production defects, such as breakage.This study investigates the use of FGPTS instead of feldspar in GPT body for sustainable production. In the study, three samples, where feldspar was reduced and substituted with FGPTS, were prepared and compared to a standard GPT body. Results showed that FGPTS inclusion decreased firing shrinkage, increased modulus of rupture, and reduced deformation. These findings indicate that FGPTS can be effectively utilized in tile bodies for Group BIa tiles.

Keywords: using porcelain tile waste, sustainability

SUSTAINABLE COMPOSITES IN THE AUTOMOTIVE SECTOR: INNOVATIVE SOLUTIONS WITH FLAX FIBER AND SIO_2 PARTICLE REINFORCED POLYMER COMPOSITES

Kerem Günöz[1], *Manolya Gezgin*[1], Şükriye Göral[1], Zeynep Namal[1],

1. Yıldız Technical University, Department of Metallurgical and Materials Engineering, Istanbul

This project aimed to develop sustainable composite materials for the Turkish automotive sector by utilizing natural flax fibers and integrating SiO2 particles from both synthesized nano-silica and recycled foundry sand. The primary goal was to reduce moisture absorption, increase heat resistance, and obtain optimum mechanical performance, while simultaneously reducing the carbon footprint and promoting circular economy principles. The project's comprehensive design includes the investigation of both epoxy and polypropylene (PP) as matrix materials to evaluate their suitability for various automotive applications.

Flax fiber-reinforced polymer composites were designed with both epoxy and polypropylene matrices. For the currently completed experiments, epoxy resin-based composites were produced. Flax fiber-reinforced polymer composites without filler and 4% silica filler were produced with an epoxy resin matrix. 4% silica was incorporated from two distinct sources: nano-silica synthesized via the sol-gel method and recycled foundry sand. Surface modifications were applied to flax fibers, nano-silica, and foundry sand using Tetraethyl Orthosilicate (TEOS) to enhance interfacial bonding. The composites were fabricated using a combination of hand lay-up and vacuum bagging methods. For the nano-silica reinforced composites, particles were mixed directly into the epoxy. The foundry sand-reinforced composites were produced using an electrospinning technique to achieve a more uniform distribution of particles on the flax fabric, followed by hand lay-up and vacuum bagging. Mechanical properties were evaluated through tensile and impact tests according to ISO 527-4 and ISO 179 standards, respectively. Material characterization included XRD for silica crystallinity, SEM for morphological analysis and particle size distribution, and FTIR for confirming successful surface modifications. The project design also includes the production of flax-PP composites via the hot-pressing method, intended for future experimental phases.

XRD analysis revealed that the synthesized nano-silica remained amorphous, consistent with the sol-gel processing temperature being below the crystallization range (1000-1200◦°C). SEM images showed significant agglomeration of the nano-silica particles, resulting in an average particle size of 1.928 µm. FTIR analysis confirmed the successful surface modification of flax fiber, nano-silica, and foundry sand through the appearance of Si-O-Si bonds (1000-1100 cm−1), indicating improved compatibility.Mechanically, the unreinforced flax fiber-epoxy composite exhibited the highest tensile strength (93.57 MPa) and Young's modulus (5.71 GPa). The nano-silica reinforced composite showed a significant reduction in tensile strength (69.10 MPa) and

Young's modulus (4.69 GPa), primarily attributed to particle agglomeration and its negative impact on stress transfer. The foundry sand-reinforced composite performed better than the nano-silica samples, achieving a tensile strength of 73.48 MPa and a Young's modulus of 4.90 GPa, likely due to the more homogeneous particle dispersion achieved through electrospinning. Similar trends were observed in impact strength, with the unreinforced composite at 18.35 kJ/m2, nano-silica at 12.36 kJ/m2, and foundry sand at 15.42 kJ/m2.

The study highlights that the method of filler incorporation is crucial for the mechanical performance of particulate-reinforced composites, as evidenced by the epoxy-based results. Although nano-silica has theoretical potential, its practical application has led to a decrease in mechanical properties due to agglomeration. In contrast, the use of recycled waste foundry sand, effectively dispersed via electrospinning, showed promising results, validating its potential as a sustainable reinforcement. The ongoing project will further investigate flax-PP composites, which are expected to offer advantages in recyclability and processing speed inherent to thermoplastic matrices. Future work should focus on optimizing dispersion methods for nano-silica, investigating the effects of silica additive at different ratios and further refining the electrospinning process for waste foundry sand and extensively testing the flax-PP composites to achieve enhanced properties for automotive applications, ensuring alignment with Turkey's circular economy goals and the United Nations Sustainable Development Goals.

Keywords: Flax, Epoxy, Silica, Foundry Sand

INVESTIGATION OF THE USABILITY OF WASTE GREEN SODA BOTTLE GLASS AS AN ADDITIVE IN ARTISTIC CERAMIC PRODUCTION

Berfin Arikan[1],

1. Kocaeli University

This study investigates the integration of waste glass into artistic ceramic production and provides a solution to environmental problems caused by inorganic waste materials that do not decompose over time. The purpose of this research is to demonstrate that waste glass can be used as an aesthetic additive in ceramic art.

The study analyzed the behavior of a composite material made by adding waste green soda bottle glass to white ceramic clay in varying proportions (20%, 30%, 40%, and 50% by weight). Three different particle sizes were used. The material was fired at two different sintering temperatures (930°C and 1150°C). The samples were shaped using two different methods: mold pressing and hand shaping.

The findings reveal that the firing temperature changes the function of glass in the ceramic structure. At lower temperatures, no significant melting of the glass was observed, while at higher temperatures, the glass completely melted, triggering a vitrification reaction. The samples shaped by mold pressing maintained their shape at the higher temperature, while the hand-shaped samples with a higher glass content adhered to the surface and exhibited an unstable structure at the same temperature.

This research demonstrates that waste glass can be used as an aesthetic additive in ceramic art. According to the results, the sample containing 40% glass by weight, shaped by the mold pressing method and fired at 1150°C, exhibited the best visual effect.

Keywords: Waste Glass, Ceramic, Sustainability

Sintering and Advanced Sintering

EFFECT OF GNP ADDITION ON THE PROPERTIES OF SIC-TIB$_2$ COMPOSITES CONSOLIDATED BY SPARK PLASMA SINTERING

Demet Aydogmus[1], *Selen Erbay*[1], Damla Kilic[1], Esin Ceren Akca[1], Filiz Sahin[1],

1. Istanbul Technical University

The aim of this study is to improve the mechanical properties of SiC-based high-temperature structural ceramics. By incorporating TiB_2 and graphene nanoplatelets (GNPs) into the SiC matrix, it is intended to enhance the fracture toughness and oxidation resistance of the composite. The developed materials are targeted for potential use in systems operating under extreme conditions, particularly in the energy, aerospace, space, and defense industries. Through the use of the Spark Plasma Sintering (SPS) technique, it is possible to obtain high-performance, compact, and homogeneous structures at relatively lower sintering temperatures and within shorter durations. The study ultimately aims to improve the mechanical and thermal performance of the resulting composites.

In this study, SiC–30 vol.% TiB_2 composites were fabricated by the Spark Plasma Sintering (SPS) technique at 1780 °C with the addition of 0, 0.5, 1, and 2 vol.% graphene nanoplatelets (GNPs). Since the highest relative density was achieved at 1 vol.% GNP, an additional 1.5 vol.% B_4C was incorporated into that composition. Disk-shaped samples with a diameter of 50 mm were sandblasted, cut and subjected to density measurements. The crystalline phases of the produced composites were analyzed using X-ray diffraction (XRD). Microstructural analysis was performed using scanning electron microscopy (SEM) to determine the composition of the samples. The effects of GNP content on the composites were investigated through hardness and fracture toughness measurements using the Vickers indentation method. Additionally, oxidation tests were carried out at 1000 °C for 16 hours in order to determine the thermal oxidation characteristics of the composites.

High relative density values were achieved in all samples. The relative densities of the composites containing 0, 0.5, 1, and 2 vol.% GNP were determined to be 97.6%, 97.84%, 97.64%, and 97.00%, respectively. The addition of 1% GNP enhanced the hardness to 31.91 GPa compared to both the GNP-free and 2% GNP-containing samples, indicating that an optimal GNP content can improve load-bearing capacity and microstructural integrity of the matrix. In terms of fracture toughness (K_1c), the highest value of 4.6 MPa·m$^{1/2}$ was also obtained in the composite with 1% GNP. On the other hand, the addition of 2% GNP led to a decrease in mechanical properties, which may be attributed to poor dispersion and agglomeration at higher GNP contents. Oxidation tests were conducted on the samples at 1000 °C for 16 hours. The formation of volatile B_2O_3, which typically occurs at 400–900 °C, led to weight loss, whereas the oxidation of SiC, which exhibits passive oxidation behavior below 1800 °C, resulted in the formation of SiO_2 and contributed to weight gain. Although the addition of 1.5 vol.% B_4C did not enhance densification, it promoted the formation of stable oxides, thereby improving the oxidation resistance of the composite.

SiC–TiB_2–GNP ternary composites were successfully fabricated via SPS at 1780 °C, 50 MPa for 5 minutes using powders containing 30 vol.% TiB_2 and 0–2 vol.% GNP.Relative densities ranged between 97.00% and 97.84%, with the highest value (97.84%) observed in the composite containing 1 vol.% GNP.The 1 vol.% GNP composite exhibited the best mechanical performance, with a hardness of 31.91 GPa and a fracture toughness of 4.60 ± 0.37 MPa·$m^{1/2}$.Addition of 1.5 vol.% B_4C to the 1 vol.% GNP sample slightly decreased the density (96.6%) but improved oxidation resistance due to the formation of stable oxide phases.

Keywords: SiC, TiB2, GNP, SPS

Traditional, Clay-Based Ceramics

INVESTIGATION OF the EFFECTS of LUSTER GLAZES ON CHAMOTTE BODIES

Merve Öztorun [1], Doç.Dr. Nermin Demirkol[1],

1. Kocaeli Üniversitesi Sosyal Bilimler Enstitüsü

Luster is a thin film layer formed on the glaze surface. This thin film layer is formedwhen the metal ions in the glaze move towards thesurface in the reduction environment.

In this study, Silver Nitrate (AgNO3) salt was used to create luster on the surface of theglaze. Leaded and alkaline glaze recipescontaining Silver Nitrate and various metal oxideswere prepared and applied with the help of a brushon test tablets obtained from chamotte clay andfired at 1000oC. Glazed test tablets were fired in a gas oven at 1000oC. When the oven cooled downto 850oC, the test tablets were taken out of theoven with the help of tongs and subjected toreduction process.The luster glazes obtained at theend of the reduction process were analyzed byoptical microscope, SEM, EDS and XRD analysis.

The fired biscuit pieces (chamotte) in the chamotte clay caused the surface to have a rough structure. It was observed that the lustereffect increased when the glaze was appliedthicker.

In addition to the luster effect, a different artistic effect has also emerged due to thetextured appearance of the surfaces obtained.AcknowledgementsThis study was supported by Kocaeli University Scientific Research Projects Coordination Unitwith Project Number: SYL-2024-3781. As all authors, we would like to express our gratitude to Kocaeli University Scientific Research Projects Coordination Unit for their support.

Keywords: Luster, Glaze, Ceramic, Reduction, Chamotte

SUPPORTERS

METEM

TÜBİTAK

MAIN SPONSOR

ERDEMİR

PLATINUM SPONSOR

ATOMİKA TEKNİK

GOLD SPONSOR

ats

SILVER SPONSORS

ATLANTIS

ARTIMET

AVEKS

E-AUTOTREK

esan

FERINEKS

Hasçelik

niche glass

TATA STEEL